

Generation of exotic quantum states of a cold atomic ensemble

Stefan L. Christensen



PhD thesis

Stefan L. Christensen

Generation of exotic quantum states
of a cold atomic ensemble

Danish Center for Quantum Optics ([QUANTOP](#))
Niels Bohr Institute ([NBI](#))
Graduate School of Science
Faculty of Science
University of Copenhagen ([UCPH](#))

Stefan L. Christensen
Version 1.2 (defense version)
Copenhagen November 26, 2014
Cover design: Thomas Bræstrup
Copyright ©2014. All rights reserved.

Principal supervisor: Prof. Eugene S. Polzik

Additional supervisors: Assoc. Prof. Jürgen Appel
Assoc. Prof. Jörg H. Müller

PhD committee:

External experts: Prof. Markus Oberthaler (Uni. Heidelberg)
Asst. Prof. Monika Schleier-Smith (Stanford Uni.)

Local head: Assoc. Prof. Jan W. Thomsen ([NBI](#))

Submission date: September 1, 2014

Defense date: October 23, 2014

ABSTRACT

Over the last decades quantum effects have become more and more controllable, leading to the implementations of various quantum information protocols. These protocols are all based on utilizing quantum correlation. In this thesis we consider how states of an atomic ensemble with such correlations can be created and characterized.

First we consider a spin-squeezed state. This state is generated by performing quantum-nondemolition measurements of the atomic population difference. We show a spectroscopically relevant noise reduction of -1.7 dB, showing that the ensemble is in a many-body entangled state. Furthermore, the nonclassical properties of the created state is inferred through the use of atomic quadrature quasi-probability distributions.

The second generated state is a collective-single-excitation state — the atomic equivalent of a single photon. This state is created by the detection of a heralding photon and characterized using atomic homodyne tomography. Using this hybrid continues-discrete method we show a significant increase in the variance of the measurements conditioned on a click. A clear signature of the collective-single-excitation state.

Last we consider a new experimental venture — a nanofiber based light-atom interface. Using a dual-frequency probing method we measure and prepare an ensemble with a sub-Poissonian atom number distribution. This is a first step towards the implementation of more exotic quantum states.

RESUMÉ

Igennem de seneste årtier er flere og flere kvantemekaniske fænomener blevet kontrollerbare. Dette har gjort det muligt i kvanteinformation at implementere forskellige protokoller der alle er baseret på at udnytte kvantemekaniske korrelationer i systemet. I denne afhandling betragtes hvorledes et atomart ensemble kan bringes i tilstande med sådanne korrelationer.

Først gennemgås en klemt spintilstand. Denne skabes via ikke destruktive målinger af den atomare populations forskel. Vi viser at den skabte tilstand har en målingsrelevant støjreduktion på -1.7 dB og at ensemblet dermed er i en mange-legeme sammenfiltret tilstand. Desuden vises de ikke klassiske egenskaber af tilstanden ved brug af atomare kvasi-kvadratur sandsynlighedsfordelinger.

Den anden tilstand vi betragter er en kollektiv enkelteksitation tilstand — den atomare udgave af en enkelt foton. Skabelsen af en sådan tilstand varsles ved detektion af en enkelt foton og karakteriseres via atomare homodyn tomografi. Ved hjælp af denne hybrid kontinuere-diskrete metode finder vi en signifikant forøgelse af variansen hvis en foton blev detekteret i forhold til ingen detekteret foton. Dette er en klar signatur af en kollektiv enkelteksitation tilstand.

Sidst beskrives et nyt igangværende eksperiment baseret på en såkaldt optisk nanofiber. Ved hjælp af en to frekvens metode kan vi måle og lave et ensemble hvor antallet af atomer følger en sub-Poisson sandsynlighedsfordeling. Dette er et første skridt imod skabelsen af mere eksotiske kvantemekaniske tilstande.

PUBLICATIONS

- [Béguin et al. 2014] J. B. Béguin, E. Bookjans, S. L. Christensen, H. L. Sørensen, J. H. Müller, J. Appel, and E. S. Polzik (2014). „Generation and detection of a sub-Poissonian atom number distribution in a one-dimensional optical lattice.“ arXiv: [1408.1266v1](https://arxiv.org/abs/1408.1266v1).
- [Christensen et al. 2014] S. L. Christensen, J. B. Béguin, E. Bookjans, H. L. Sørensen, J. H. Müller, J. Appel, and E. S. Polzik (2014). „Quantum interference of a single spin excitation with a macroscopic atomic ensemble.“ *Physical Review A* **89**, p. 033801. DOI: [10.1103/PhysRevA.89.033801](https://doi.org/10.1103/PhysRevA.89.033801).
- [Christensen et al. 2013] S. L. Christensen, J. B. Béguin, H. L. Sørensen, E. Bookjans, D. Oblak, J. H. Müller, J. Appel, and E. S. Polzik (2013). „Towards quantum state tomography of a single polariton state of an atomic ensemble.“ *New Journal of Physics* **15.1**, p. 015002. DOI: [10.1088/1367-2630/15/1/015002](https://doi.org/10.1088/1367-2630/15/1/015002).
- [Kiesel et al. 2012] T. Kiesel, W. Vogel, S. L. Christensen, J. B. Béguin, J. Appel, and E. S. Polzik (2012). „Atomic nonclassicality quasiprobabilities.“ *Physical Review A* **86.4**, p. 042108. DOI: [10.1103/PhysRevA.86.042108](https://doi.org/10.1103/PhysRevA.86.042108).

PRESENTATIONS

- [Christensen 2012] S. L. Christensen (2012). *Engineering a non-Gaussian quantum state of an atomic ensemble*. Poster presentation at the ICAP Conference, Paris - France.
- [Christensen 2013a] – (2013a). *Interference of a single excited atom with an atomic ensemble*. Poster presentation at the Russian Quantum Center Summer School, Moscow - Russia.
- [Christensen 2013b] – (2013b). *Quantum Interference Between a Single Spin Excitation and a Macroscopic Atomic Ensemble*. Invited presentation at meeting on quantum information and application, Allahabad - India.
- [Christensen 2013c] – (2013c). *Towards realization and detection of a non-Gaussian quantum state in an atomic ensemble*. Poster presentation at the Winter School on Rydberg Physics and Quantum Information, Obergurgel - Austria.

*If you want my eyes, take my eyes, they're always true.
If you want my heart, take my heart, it's right here for you.
It's been so long, been so long, but I made it through.*

— [The Walkmen 2012]

ACKNOWLEDGMENTS

This account sums up work done in [QUANTOP](#) over the last four years. However, my working relationship with the group is almost twice as old. In the spring of 2007, I, as an unknowing undergraduate, opted for an experimental project co-supervised by Jörg H. Müller. As neither I nor the senior staff at [QUANTOP](#) were scared away by the experience, it made sense to stick around the basement at Blegdamsvej for my Bachelors project. Here I had the pleasure of working on a squeezed light source — my first encounter with nonclassicality. During a small detour to London from 2009-2010, my appreciation for the work of [QUANTOP](#) deepened, and in the late summer of 2010 I returned to start a PhD on the so-called “clock-experiment” under the supervision of Eugene Polzik. Over the last four years, countless hours have been spent in the lab in the hope of pushing our understanding further. Whether this has been successful or not is for others to decide; what I am certain of, however, is that I would never have made it through on my own, and I learned so much from others along the way.

First and foremost, I am indebted to Eugene Polzik for giving me the opportunity to carry out the work described here. His guidance, encouragement, and high standards set an admirable example for any scientist, young or old.

Starting out as part of a two-person team on the experiment, I could not have asked for a better teacher than Jürgen Appel – one of the most knowledgeable physicists I have met. He always (and I mean always) had a solution to whatever problem we were facing. In addition, he always kept an open door, making for an all-too-unusually supportive atmosphere for PhD students.

I also owe great thanks to Jörg H. Müller. I can not count the number of hours I have spent at his desk (piled up with papers) getting individual tuition. His knowledge and patience are immense and inspiring.

With Jürgen quickly progressing through the ranks, it was clear that more hands were needed in the lab. These came with Heidi Lundgaard Sørensen and Jean-Baptiste Béguin (JB) joining the team. Working closely with JB on the MZI setup, we shared all of its joys and sorrows. His persistent – and at times, magic – ways of increasing the atom number led to several key improvements and modifications of the setup. My collaboration with Heidi developed rapidly, and she is now my go-to person, whether this is to test out a new idea or simply share a morning coffee. The nanofiber experiments were also pushed forward by the addition of Eva Bookjans to the lab team.

It is also a pleasure to thank Vladan Vuletić for welcoming me into his group during my time at MIT. Here I joined Wenlan Chen and Kristi Beck working on a cavity-based light-atom interface. With a lot to learn, it was a privilege to work with such open-minded and dedicated physicists. While in Cambridge I also had countless discussions with Hao Zhang about implementing a similar scheme to the one presented here in their cavity experiment.

In addition to my closest collaborators mentioned above, QUANTOP has been filled with great people for as long as I can remember. Special thanks go to Nir Kampel and William H. P. Nielsen. In my early years, Nir always took the time to lend a hand or answer questions, no matter how simple. Having done my Bachelors project with William, it was a pleasure to have him “come back home” and even better having him as an office mate. My countless questions on optomechanics, LaTeX and Python, combined with William’s willingness to answer them, have meant that not a week has gone by without a major discussion.

Last (I promise) we come to the non-physicists – friends and family. Thanks for dealing with strange working hours, and for listening to complaints about such things as lasers not lasing, and atoms being there and then not. Without you I would never have made it to this stage.

CONTENTS

1	INTRODUCTION	1
i	THEORY	7
2	LIGHT	9
2.1	Quantum description	9
2.2	Light states	11
2.2.1	Quasi-probability distributions	13
2.3	Light propagation in an MZI	15
2.3.1	Real-life MZI	20
2.4	Summary	21
3	ATOMS	23
3.1	Cesium atoms	23
3.2	Atomic operators	25
3.2.1	Atomic quadrature operators	26
3.3	Coherent spin states	27
3.4	Spin-squeezed states	30
3.5	Atomic Fock states	32
3.6	Measurement outcomes	35
3.6.1	Coherent spin state	36
3.6.2	Spin-squeezed state	38
3.6.3	Collective-single-excitation state	39
3.7	Summary	40
4	LIGHT-ATOM INTERACTION	41
4.1	Maxwell-Bloch equations	41
4.1.1	Absorption and phase shift	44
4.2	State characterization	46
4.3	Microwave interaction	48
4.4	Summary	51
5	EXPERIMENTAL CONSIDERATIONS	53
5.1	Spin-squeezed state	53
5.1.1	Quantum-nondemolition measurement	53
5.1.2	QND measurements and squeezing	55
5.2	Collective-single-excitation state	58
5.3	Summary	61

CONTENTS

ii	EXPERIMENT	63
6	EXPERIMENTAL TECHNIQUES	65
6.1	Atom trapping	65
6.1.1	Magneto-optical trap	66
6.1.2	Far-off-resonant trap	68
6.2	State preparation	70
6.3	Population-difference measurement	72
6.3.1	Probes	72
6.3.2	Mach-Zehnder interferometer	74
6.3.3	Noise sensitivity	76
6.3.4	Locking	79
6.3.5	Shot noise limited operation	81
6.4	Acquisition and control	82
6.5	Summary	84
7	SPIN SQUEEZING	85
7.1	Experimental procedure	85
7.2	Decoherence	87
7.3	Squeezing	89
7.3.1	Projection noise	92
7.3.2	Noise reduction	94
7.4	Nonclassicality	96
7.5	Summary	100
8	COLLECTIVE-SINGLE EXCITATION	101
8.1	Experimental implementation	101
8.1.1	Excitation	104
8.1.2	Filtering	106
8.2	Gain estimation	107
8.3	Single excitation	110
8.3.1	Projection noise	111
8.3.2	Variance increase	114
8.4	Variance model	116
8.4.1	False positives	116
8.4.2	Finite efficiency	116
8.5	Multiple excitations	121
8.6	Nonclassicality and non-Gaussianity	124
8.7	Improvements	126
8.8	Summary	127
9	NANOFIBER-TRAPPED ATOMIC ENSEMBLE	129

9.1	Why a nanofiber?	129
9.2	Experimental setup	131
9.3	Atom number	134
9.3.1	Error estimate	137
9.4	Number squeezing	139
9.4.1	Variance estimator model	142
9.5	Projected single excitation purity	144
9.6	Summary	147
iii	CONCLUSION AND OUTLOOK	149
10	CONCLUSION	151
11	OUTLOOK	153
12	REVIEW OF RELATED WORK	155
iv	APPENDICES	159
A	EXPERIMENTAL CONSIDERATIONS	161
A.1	Parametric gain Hamiltonian	161
A.1.1	Excitation created in pairs	162
A.1.2	Expected photon number	162
B	EXPERIMENTAL TECHNIQUES	165
C	SPIN SQUEEZING	169
C.1	QND Master equation	169
C.1.1	Consistency check	172
D	SINGLE EXCITATION STATE	173
D.1	Hanle effect	173
D.2	n -point pulses	174
D.3	Error estimate	175
D.4	Collective single excitation state w. phase profile	177
E	NANOFIBER EXPERIMENT	179
E.1	Atom number	179
E.2	Squeezing estimation	180
	BIBLIOGRAPHY	183
	ACRONYMS	197

*... quantum phenomena do not occur in a Hilbert space,
they occur in a laboratory*

— [Peres 1995]



INTRODUCTION

Since the birth of quantum mechanics in the beginning of the last century a central aspect of the theory has been the interactions between light and matter. As photons only interact weakly with their environment these interactions were initially limited — the observation of *any* quantum effect was a success. However, with the development of new technologies, such as laser cooling and nanofabrication, quantum effects are now routinely observed. With the possibility to observe and study these effects a natural next step is to control and utilize them. This is the essence of quantum state engineering, the central topic of this thesis — more specific we will consider how states with distinct quantum correlations can be created and used.

“Exotic” quantum states are interesting for two reasons. First, increasing the size of the systems in which they are created and the “degree of quantumness” new insight into the fundamental aspects of quantum mechanics is gained. Second, the states have applications within quantum assisted metrology and quantum information processing. These exotic quantum states have been created in a wide range of systems ranging from photonic [Wu et al. 1986] to mechanical [O’Connell et al. 2010]. In this work our system of choice is a cold atomic ensemble coupled to light — a light-atom interface. To understand how we create, manipulate and characterize these states, we will touch on many of the central features of quantum mechanics such as Heisenberg’s uncertainty relation, quantum measurements, superposition states, and entanglement.

Within the field of light-atom interfaces two methods using either discrete or continuous variables, have been pursued successfully. The discrete method [Kimble 2008] is based on the probabilistic generation of collective atomic excitations through photon counting. This has allowed for the creation of highly non-Gaussian and nonclassical states (negative Wigner function) [Simon et al. 2007; Bimbard et al. 2014],

INTRODUCTION

quantum memories [Choi et al. 2008] and small quantum networks [Choi et al. 2010]. However, the discrete method has two drawbacks. First, the “low” characterization efficiency due to the loss in conversion from atomic to optical states. Second, the heralded (probabilistic) nature of the generation methods.

The continuous-variable method [Hammerer et al. 2010] on the other hand allow for high characterization efficiency and deterministic state generation. This has led to the creation of spin-squeezed states (SSSs) [Appel, Windpassinger, et al. 2009; Schleier-Smith et al. 2010] and their use in quantum-assisted metrology [Louchet-Chauvet et al. 2010; Leroux et al. 2010]. However, due to the linear and Gaussian nature of the method the nonclassical character of the created states has been limited.

So far the discrete and continuous variable methods have only been realized separately. Utilizing a hybrid discrete-continuous approach — as for photonic systems [Babichev et al. 2004; Neergaard-Nielsen et al. 2006; Ourjoumtsev et al. 2007] — we want to combine the discrete state generation method with the atomic tomography method of the continuous variables. With the atomic tomography done directly in the ensemble this method do not suffer from the loss in converting atomic to optical states. Furthermore, with the created state stored within the atomic ensemble (a quantum memory) it is readily available for further manipulation and on-demand readout using well-developed techniques.

THESES AND STRUCTURE

With this we are ready to state the main subjects that will be presented:

- Projection noise limited measurements on an ensemble of 10^5 atoms using a dual-color probing method.
- Creation and characterization of a SSS and its nonclassical properties through atomic quadrature quasi-probability (AQQP) distributions.
- Creation and characterization of a collective-single-excitation state using atomic tomography.
- Measurement and preparation of a nanofiber coupled ensemble with a sub-Poissonian atom number distribution.

The thesis is structured into three parts. In part one we develop the theoretical background required to understand and describe the experimental work. The two systems of interest, light (chap. 2) and atoms (chap. 3), are introduced and described using pseudo-spin and quadrature operators. This is followed by a discussion of their interactions (chap. 4). To bridge the theoretical descriptions to the experimental implementation we consider the methods used to create the two atomic states of interest (chap. 5). The main result shown is that by an appropriate parameter choice the light-atom interactions are described by the canonical quantum-nondemolition (QND) Hamiltonian. It can therefore be used for the creation and characterization of exotic atomic states.

Part two deals with the experimental work. We consider the general experimental techniques used for atom trapping, state manipulations and state characterization (chap. 6). The focus is especially on the implemented dual-color probing technique. We then describe three different experiments. First, we show the creation and characterization of a SSS with a spectroscopically relevant noise reduction of -1.7 dB (chap. 7). The nonclassical features of the state are unambiguously inferred using the concept of AQQP distributions. With this introduction to the method of atomic homodyne tomography we then consider the generation and characterization of a collective-single-excitation state (chap. 8). Following the protocol by Duan, Lukin, Cirac and Zoller (DLCZ), the state is created by the detection of a heralding photon. We show a statistically significant increase in the variance of the measured population difference conditioned on a click — a signature of the collective-single-excitation state. The last chapter of this part deals with our newest experimental setup — a nanofiber trapped atomic ensemble (chap. 9). We present a fast and robust way of determining the atom number and the preparation of an ensemble with a sub-Poissonian atom number distribution.

In part three we give concluding remarks on the work (chap. 10) and consider possible future directions (chap. 11). Finally, a review of related work (chap. 12) is presented.

MY CONTRIBUTION

Joining the group in 2010, I took over a setup operating at the projection noise level and capable of creating SSSs. Most relevant for the

work here is the creation and characterization of a [SSS](#) [Appel, Windpassinger, et al. 2009] and its use for quantum enhanced measurements [Louchet-Chauvet et al. 2010]. The work presented here, naturally builds upon these results. Especially the theoretical descriptions of light, atoms and their interactions given in the first part of the thesis build on the PhD theses by Windpassinger [2008] and Oblak [2010]. Furthermore, working in a collaborative environment helping hands were always close by. The presented results surely would not have been reached without the help from especially Jürgen Appel ([JA](#)), Jörg H. Müller ([JHM](#)), and Jean-Baptiste Béguin ([JB](#)) and the supervision of Eugene Polzik.

During my PhD I have had the main responsibility for our experiment using a dipole trapped atomic ensemble. In the following, my main contributions are detailed:

SETUP: With a power cut at the institute in the spring of 2011 our ion pump and vacuum broke. Taking a positive attitude to this unfortunate situation we decided to exchange the old dispensers. The vacuum setup was therefore completely rebuilt and pumped down in collaboration with [JB](#).

With another stroke of bad luck the fiber amplifier used for the far-off-resonant dipole trap ([FORT](#)) broke. This meant a complete realignment of the trapping beam when the new unit arrived.

Modifications of the Mach-Zehnder interferometer ([MZI](#)) were done towards the end of 2011 as a frequency dependent noise source was observed. After months of investigation the problem was solved by moving the glass cell a few mm. We now believe this was due to a small area of the cell having its anti-reflection coating burnt.

Furthermore the magneto-optical trap ([MOT](#)) control software was rebuilt from scratch due to incompatibilities with Windows 7.

SPIN-SQUEEZED STATE: When we were approached by Prof. W. Vogel and Dr. T. Kiesel in the fall of 2011 the timing was perfect. They had developed a test for nonclassicality and needed real data to test their criterion whereas [JB](#) and me had just done a long experimental run. Our joint work — they developed the theoretical framework and we supplied the data — was published in [Kiesel et al. 2012]. The data analysis and observation of squeezing in

the single-point measurements were done in collaboration with JA.

PROPOSAL: When I joined the group in 2010 several ideas on how the collective-single-excitation state could be created had been investigated. At the time the favorite scheme was based on the λ -system formed by the levels $|F = 3, m_F = 0\rangle$, $|F = 4, m_F = 1\rangle$ and $|F' = 4, m_{F'} = 0\rangle$. Experimental investigation of this idea with JA showed that due to optical pumping effects the setup was not projection noise limited. It was therefore back to the drawing board.

In collaboration with JA and JHM the currently used scheme was developed and published in [Christensen et al. 2013]. This is based on the λ -system $|F = 3, m_F = 0\rangle$, $|F = 4, m_F = 0\rangle$ and $|F' = 4, m_{F'} = 1\rangle$. Taking the probes and excitation beams to contain both linear and circular polarized light as well as a high magnetic field (details in sec. 8.1) allowed us to detect the heralding photons while at the same time being projection noise limited.

FILTER CAVITIES: To implement this proposal we needed a setup capable of filtering on both the frequency and polarization. Most crucial is the frequency filtering done by two cavities. These were needed to reject the excitation beam (co-propagating with the heralding single photon) and decays to other hyperfine ground states. The design of these cavities as well as control electronics and programs. This was done together with JA and is mainly presented in my progress report [Christensen 2012].

COLLECTIVE-SINGLE-EXCITATION STATE: To create this state several additions to the setup creating SSS were required. Most notable was the operation at a magnetic bias field of $|\mathbf{B}| = 20$ G together with implementing the excitation beam and the described filtering cavities. The data presented in [Christensen et al. 2014] and chap. 8 were mainly acquired by myself. The data analysis — n -point pulses (app. D.2) and the comparison of the click and no-click cases (creation of a collective single excitation state or a coherent spin state (CSS), see sec. 8.3.1) — was performed together with JA. The modeling of the observed variance (sec. 8.4) was done with JA and JHM. Last, the (unsuccessful) tests for non-Gaussianity and nonclassicality were made with JA.

INTRODUCTION

Besides the mentioned things our group has also been working towards performing similar experiments with a nanofiber trapped ensemble. The main work on this has been done by JB and will be presented in his PhD thesis [Béguin n.d.]. My contributions are as follows:

EXPERIMENTAL WORK: Assembling vacuum components, building coils and optics for the MOT — all done together with JB.

ATOM NUMBER: Development of the method and model to measure the atom number in collaboration with JHM. The data presented in [Béguin et al. 2014] and sec. 9.3 was acquired together with JB and Eva Bookjans. Furthermore, in collaboration with JA a model (not presented here) taking into account the full level structure of the atoms was developed.

BAYESIAN INFERENCE: The idea to use Bayesian inference was first put forward by JA, whereas I made the first implementation on the actual data. The data presented in [Béguin et al. 2014] and sec. 9.4 was acquired by JB and Eva Bookjans.

FIBER THERMAL EXPANSION: The strong beams required for trapping atoms around the nanofiber gives rise to the fiber expanding. This effect was observed and investigated, together with JB. As we could not develop a model in agreement with the observation and the publication by Wuttke et al. [2013] this was not investigated further and the results are not presented in this thesis.

Part I

THEORY

In this part we consider the theoretical background for the performed experiments. We first describe light and atoms individually and afterwards their interactions. We show how these interactions can be used to characterize the atomic spin-states through atomic homodyne tomography. Furthermore, we show that a suitable parameter choice leads to the interactions being of the QND type allowing for the creation of SSS. Last we consider a Raman process, and show that the detection of a single photon heralds the creation of the collective-single-excitation state.

LIGHT

With the large variety of quantum systems available the particular choice of using light might seem arbitrary, but the reasons are many. Light generated from lasers is stable and pure, and well-known techniques exist to precisely control its properties. Combined with an almost perfect detection efficiency, it is a marvelous system for designing controlled quantum-mechanical interactions. Before a detailed description of this can be made it is crucial that each individual part, light and atoms, is well-understood and described on its own. In this chapter we will focus on the quantum-mechanical description of light. Starting from the quantized field we describe its properties, its states and their description using quasi-probability distributions (QPDs). We then use Schwinger, or light pseudo-spin, operators to describe light propagating in a MZI — first for the simple case where losses are neglected followed by the experimentally relevant case where losses and non-perfect mode matching are taken into account. We will especially focus on the limit set by the shot noise of light and how this affects the achievable signal-to-noise ratio (SNR) — which will set the limit on any atomic-state characterization we will perform. The material in the first part of the chapter can be found in any quantum-optics textbook, for example [Steck 2012, chap. 8; Garrison et al. 2008, chap. 2-5; Mandel et al. 1995, chap. 10]; the second more specialized part is based on [Yurke et al. 1986; Oblak 2010, chap. 2].

2.1 QUANTUM DESCRIPTION

The electromagnetic vector potential is given by [Mandel et al. 1995, eq. 10.4-38]

$$\hat{A}(\mathbf{r}, t) = \frac{1}{\sqrt{V}} \sum_{\mathbf{k}, s} \sqrt{\frac{\hbar}{2\omega\epsilon_0}} \left[\hat{a}_{\mathbf{k}, s} \boldsymbol{\epsilon}_{\mathbf{k}, s} e^{i(\mathbf{k} \cdot \mathbf{r} - \omega t)} + \hat{a}_{\mathbf{k}, s}^\dagger \boldsymbol{\epsilon}_{\mathbf{k}, s}^* e^{-i(\mathbf{k} \cdot \mathbf{r} - \omega t)} \right]. \quad (2.1)$$

Here $\hat{a}_{\mathbf{k}, s}^\dagger$ ($\hat{a}_{\mathbf{k}, s}$) is the creation (annihilation) operator for a photon of frequency ω , \mathbf{k} is the wavevector, $\boldsymbol{\epsilon}_{\mathbf{k}, s}$ is the polarization vector, V is the

quantization volume, and ϵ_0 denotes the vacuum permittivity. The two summations are over all allowed wavevectors, \mathbf{k} and the orthogonal polarizations $s = 1, 2$. The creation and annihilation operators obey the commutation relation

$$[\hat{a}_{\mathbf{k},s}, \hat{a}_{\mathbf{k}',s'}^\dagger] = \hat{1} \delta(\mathbf{k} - \mathbf{k}') \delta(s - s'). \quad (2.2)$$

From the vector potential we find the electric field as

$$\hat{\mathbf{E}}(\mathbf{r}, t) = -\frac{\partial}{\partial t} \hat{\mathbf{A}}(\mathbf{r}, t), \quad (2.3a)$$

$$= i \sqrt{\frac{\hbar \omega}{2V \epsilon_0}} \left[\hat{a}_{\mathbf{k},s} \boldsymbol{\epsilon}_{\mathbf{k},s} e^{i(\mathbf{k} \cdot \mathbf{r} - \omega t)} - \hat{a}_{\mathbf{k},s}^\dagger \boldsymbol{\epsilon}_{\mathbf{k},s}^* e^{-i(\mathbf{k} \cdot \mathbf{r} - \omega t)} \right]. \quad (2.3b)$$

Summing up the energy in the electric and corresponding magnetic field for a single plane-wave mode gives the expected harmonic oscillator Hamiltonian

$$\hat{\mathcal{H}}_{\text{light}} \equiv \hbar \omega \left(\hat{a}_{\mathbf{k},s}^\dagger \hat{a}_{\mathbf{k},s} + \frac{1}{2} \right). \quad (2.4)$$

Identifying $\hbar \omega$ as the energy of a single photon it is suggestive to define

$$\hat{N}_{\text{ph},\mathbf{k},s} \equiv \hat{a}_{\mathbf{k},s}^\dagger \hat{a}_{\mathbf{k},s} \quad (2.5)$$

as the photon-number operator. For notational ease we will suppress the subscripts and write this as \hat{N}_{ph} . To describe the pulsed Gaussian beams used in the experiment, it is convenient to use a complete set of time-independent transverse mode functions¹ $u_{\mathbf{k}_\perp,s}(\mathbf{r}_\perp)$ such that

$$\hat{a}_{\mathbf{k},s}(\mathbf{r}, t) = u_{\mathbf{k}_\perp,s}(\mathbf{r}_\perp) \hat{a}_{\mathbf{k},s} \boldsymbol{\epsilon}_{\mathbf{k},s} e^{i(k_z z - \omega t)}. \quad (2.6)$$

Writing out the explicit time dependence of the creation and annihilation operators and introducing the quadrature operators

$$\hat{X}_L \equiv \frac{1}{\sqrt{2}} (\hat{a} + \hat{a}^\dagger), \quad (2.7a)$$

$$\hat{P}_L \equiv \frac{1}{\sqrt{2}i} (\hat{a} - \hat{a}^\dagger). \quad (2.7b)$$

¹ The mode functions will play an important role in atomic-state tomography. The atomic states of interest will have a spatial profile, i.e., an associated mode function. Characterizing the atomic state via light, we measure the overlap between the atomic and light mode functions (sec. 8.4).

We get

$$\hat{\mathbf{E}}(\mathbf{r}, t) = E_0 u_{\mathbf{k}_\perp, s}(\mathbf{r}_\perp) e^{ik_z z} [\hat{X}_L \sin(\omega t) - \hat{P}_L \cos(\omega t)], \quad (2.8)$$

where we have introduced the electric-field amplitude $E_0 \equiv \sqrt{\frac{\hbar\omega}{V\epsilon_0}}$. The two operators \hat{X}_L and \hat{P}_L are the sine and cosine components of the oscillating electromagnetic field and follow the commutation relation

$$[\hat{X}_L, \hat{P}_L] = i. \quad (2.9)$$

They are the optical analog of the position and momentum of a mechanical oscillator. A natural extension is to introduce the generalized quadrature operator

$$\hat{X}_L(\theta) = \hat{X}_L \cos(\theta) + \hat{P}_L \sin(\theta). \quad (2.10)$$

With this description of the quantized electromagnetic field in terms of the quadrature operators, we now describe its associated states.

2.2 LIGHT STATES

We consider two distinct set of states, the Fock, $|n\rangle_L$ and coherent states, $|\alpha\rangle_L$. The Fock states have a sharp photon number and are also referred to as number states. From the standard description of a harmonic oscillator we define them via

$$\hat{a}^\dagger |n\rangle_L = \sqrt{n+1} |n+1\rangle_L, \quad (2.11a)$$

$$\hat{a} |n\rangle_L = \sqrt{n} |n-1\rangle_L. \quad (2.11b)$$

Allowing us to identify them as energy eigenstates

$$\hat{\mathcal{H}}_{\text{light}} |n\rangle_L = E_n |n\rangle_L, \quad (2.12a)$$

where

$$E_n = \hbar\omega \left(n + \frac{1}{2} \right). \quad (2.12b)$$

With their intuitive interpretation, the Fock states are the most natural basis. They do however, have two drawbacks: first, they do not have a well-defined phase, and second, they are far from what a laser actually outputs.

The coherent states, on the other hand, have a well-defined phase and are close to the output of a laser. They can be defined as eigenstates of the creation and annihilation operators

$$\hat{a} |\alpha\rangle_L = \alpha |\alpha\rangle_L. \quad (2.13)$$

Here α is the coherent-state amplitude. Their average photon number is $\bar{n} = |\alpha|^2$ with a variance

$$\text{var}(\hat{N}_{\text{ph}})_{|\alpha\rangle_L} = \bar{n}. \quad (2.14)$$

The photon number in a coherent state is therefore, in contrast to the Fock states, not well-defined and the associated fluctuations are referred to as light shot noise. Using coherent states to measure the atomic ensemble, these fluctuations set the lower limit for our measurement precision. In terms of the quadrature operators (eq. (2.7)) their expectation values are

$$\langle \hat{X}_L \rangle_{|\alpha\rangle_L} = \sqrt{2} \text{Re}(\alpha), \quad (2.15a)$$

$$\langle \hat{P}_L \rangle_{|\alpha\rangle_L} = \sqrt{2} \text{Im}(\alpha). \quad (2.15b)$$

and more interestingly their variance

$$\text{var}(\hat{X}_L)_{|\alpha\rangle_L} = \text{var}(\hat{P}_L)_{|\alpha\rangle_L} = \frac{1}{2}. \quad (2.16)$$

Recall Heisenberg's uncertainty relation for two operators \hat{o} and \hat{u} ,

$$\text{var}(\hat{o}) \text{var}(\hat{u}) \geq \frac{1}{4} |\langle [\hat{o}, \hat{u}] \rangle|^2, \quad (2.17)$$

Considering the case of coherent states it is easily verified that they minimize the Heisenberg uncertainty relation — we refer to them as minimum uncertainty states. A second and equivalent way of defining the coherent states is as displaced vacuum states

$$|a\rangle_L = \hat{D}_\alpha |0\rangle_L, \quad (2.18)$$

where the displacement operator is defined as

$$\hat{D}_\alpha \equiv \exp(\alpha \hat{a}_L^\dagger - \alpha^* \hat{a}_L). \quad (2.19)$$

As the coherent states are eigenstates of the creation and annihilation operators, have a well-defined phase and minimize Heisenberg's uncertainty relation, they are interpreted as the most classical quantum states [Mandel et al. 1995, chap. 11]. One way of studying and distinguishing between classical and nonclassical states is through quasi-probability distributions (QPDs).

2.2.1 Quasi-probability distributions

The QPDs are the quantum mechanical analogue of the phase space description for a classical system. There exists a whole range of QPDs all contained in the s -parameterized QPD $W(s; X_L, P_L)$ introduced by Cahill et al. [1969]. Following [Leonhardt 1997, chap. 3]

$$W(s; X_L, P_L) \equiv \frac{1}{4\pi^2} \int_{-\infty}^{\infty} dv \int_{-\infty}^{\infty} du \tilde{W}(s; u, v) \exp(iuX_L + ivP_L). \quad (2.20)$$

Here X_L and P_L are the expectation values of the respective operators and $\tilde{W}(s; u, v)$ is the characteristic function of a state $\hat{\rho}$ given by

$$\tilde{W}(s; u, v) \equiv \text{Tr} \left(\hat{\rho} e^{-iu\hat{X}_L - iv\hat{P}_L} \right) \exp \left[\frac{s}{4} (u^2 + v^2) \right] \quad (2.21a)$$

$$= \langle -iu\hat{X}_L - iv\hat{P}_L \rangle \exp \left[\frac{s}{4} (u^2 + v^2) \right]. \quad (2.21b)$$

This is the “quantum Fourier transform” of the density operator $\hat{\rho}$, and u, v denotes the transformation variables.² The s -parameter has so far not been specified and the above definitions are valid for all $s \in \mathbb{R}$. To get a feel for these functions we consider the values of s giving the standard QPDs

$$s = \begin{cases} +1 : & P\text{-function} \\ 0 : & \text{Wigner function} \\ -1 : & Q\text{-function} \end{cases} \quad (2.22)$$

To understand the reason for introducing not one but a whole range of QPDs we consider $W(s; X_L, P_L)$ with $s = -1, 0, 1$ for a single photon state, $|1\rangle_L$. Starting with the P -function ($s = 1$), we find that $W(s = 1; X_L, P_L)$ is highly singular, containing derivatives of δ -functions [Leonhardt 1997, eq. (3.76)] which we ascribe to the nonclassicality of the single-photon state.³ This example shows the main features of the P -function; it has “abrupt” features for nonclassical states, making it a prime candidate for identifying them. However, its highly singular nature makes it impossible to reconstruct from experimental data.

² They are “time-variables”.

³ The term nonclassical is here used without a proper definition. In sec. 7.4 we define it and elaborate on what it actually means.

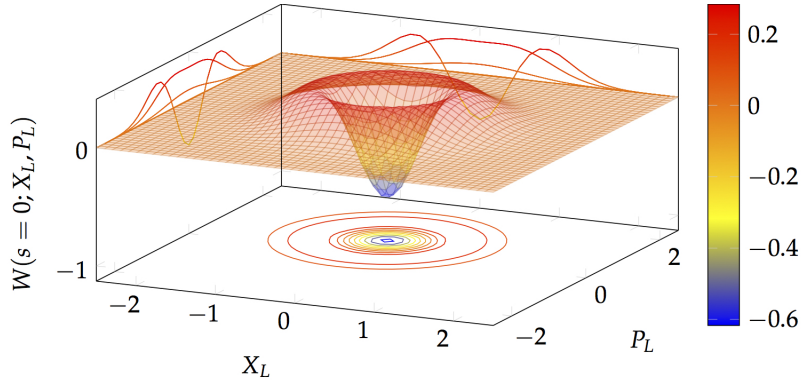


Figure 2.1.: Wigner function $W(s = 0, X_L, P_L)$ for a single-photon state. On each plane the respective contours are shown. We clearly see that the Wigner function takes on negative values, a unambiguous sign of nonclassical features.

The Wigner function ($s = 0$), on the other hand, has no singularities and can be visualized fig. 2.1. We see that $W(s = 0; X_L, P_L)$ has negative values. As this is not allowed for a classical probability distribution, we take it as a sign of nonclassical properties. In comparison to the P -function, the Wigner function can actually be reconstructed from an experiment. This makes it an ideal tool for certifying nonclassical properties.

Last we have the Q -function ($s = -1$) which is shown in fig. 2.2. As the Q -function is always positive (this is true for all states), it can be interpreted as a “classical” probability distribution, showing no distinct signs of nonclassicality.⁴ On the other hand, the Q -function is directly measurable since it can be written as $W(s = -1, X_L, P_L) = \langle \alpha | \hat{\rho} | \alpha \rangle$.

From this example we see a hierarchy between the QPDs; the smaller the s -parameter the fewer features due to nonclassical properties,⁵ but at the same time the easier it is to infer from experiments. This makes it clear that which QPD to use depends on the actual task at hand. With

⁴ The nonclassical features of the Q -function are actually “only” exponentially damped. This makes it practically impossible to directly detect nonclassicality via the Q -function. An example would be the difference between a Schrödinger cat-state and a classical statistical mixture of two coherent states; the nonclassical interference features of the Q -function are damped by $\exp(-\alpha)$, with α the coherent state amplitude, and therefore for all practical purposes negligible [Leonhardt 1997, sec. 3.3].

⁵ It can be shown that the s -parameter corresponds to a “smoothing” of $W(s; X_L, P_L)$ and its marginal distributions; the smaller the smoother [Leonhardt 1997, sec. 3.3.2].

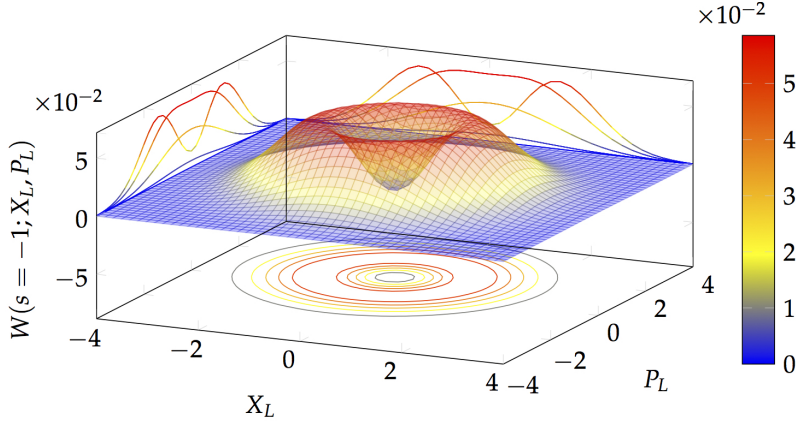


Figure 2.2.: Q-function $W(s = -1, X_L, P_L)$ for a single-photon state. On each plane the respective contours are shown. The Q-function is positive and has no distinct features from which we can identify the nonclassical properties of the single-photon state.

the description of light either in terms of their state vectors or their QPD, we now turn to the topic of light propagation in an interferometer and how this directly relates to the atomic state tomography.

2.3 LIGHT PROPAGATION IN AN MZI

To measure the atomic ensemble we consider the state-dependent phase shift imprinted on light passing through the atomic cloud. To measure such a phase shift we will use a Mach-Zehnder interferometer (MZI), which we describe through the Schwinger operators. The Schwinger operators can be used to describe any bosonic two mode-system and are defined as [Schwinger 1952]

$$\hat{S}_x \equiv \frac{1}{2} (\hat{a}^\dagger \hat{b} + \hat{b}^\dagger \hat{a}), \quad (2.23a)$$

$$\hat{S}_y \equiv -\frac{i}{2} (\hat{a}^\dagger \hat{b} - \hat{b}^\dagger \hat{a}), \quad (2.23b)$$

$$\hat{S}_z \equiv \frac{1}{2} (\hat{a}^\dagger \hat{a} - \hat{b}^\dagger \hat{b}). \quad (2.23c)$$

The most well-known example of such a two-mode system is the polarization of light, leading to the Stokes operators [Garrison et al. 2008,

sec. 2.4]. In the **MZI** the two modes are spatially separated and propagating in each arm of the interferometer (see fig. 2.3). The Schwinger operators have an angular-momentum-like commutation relation

$$[\hat{S}_x, \hat{S}_y] = i\hat{S}_z \quad (2.24)$$

and are referred to as pseudo-spin operators for light. We form the pseudo-spin vector

$$\hat{\mathbf{S}} = \begin{pmatrix} \hat{S}_x \\ \hat{S}_y \\ \hat{S}_z \end{pmatrix}, \quad (2.25)$$

which together with the total photon number operator $\hat{N}_{\text{ph,tot}} \equiv \hat{N}_{\text{ph},a} + \hat{N}_{\text{ph},b}$, (corresponding to $|\hat{\mathbf{S}}|$) completely defines the two-mode system. The connection to the Bloch-vector description of a spin-1/2 system (see sec. 3.3) is clear. We therefore expect that the propagation in the **MZI** can be described as rotations of $\hat{\mathbf{S}}$. Before this is done we consider how the light shot noise gives rise to fluctuations of $\hat{\mathbf{S}}$. Considering the coherent states, the shot noise of light will carry over to the Schwinger operators. Focusing on \hat{S}_z (what we shall measure) we have

$$\langle \hat{S}_z \rangle_{|\alpha_a, \beta_b\rangle_L} = \frac{\bar{n}_a - \bar{n}_b}{2}, \quad (2.26a)$$

$$\text{var}(\hat{S}_z)_{|\alpha_a, \beta_b\rangle_L} = \frac{N_{\text{ph,tot}}}{4}. \quad (2.26b)$$

Here $|\alpha\rangle_L$ and $|\beta\rangle_L$ are the coherent states in the modes \hat{a} and \hat{b} and $N_{\text{ph,tot}} = \langle \hat{N}_{\text{ph,tot}} \rangle$. With the Schwinger operators at hand we now consider the case of light propagating in a lossless **MZI**, and describe this as rotations of $\hat{\mathbf{S}}$.

The **MZI** is shown in fig. 2.3. The first element is a beam splitter with transmission and reflection coefficients for the electric field $t, r, \in \mathbb{C}$, such that $|t|^2 + |r|^2 = 1$ and $tr^* + rt^* = 0$ to ensure a unitary transformation. Using the standard beam-splitter relation we can write the output modes \hat{c}_1 and \hat{c}_2 (fig. 2.3) as

$$\begin{pmatrix} \hat{c}_1 \\ \hat{c}_2 \end{pmatrix} = \begin{pmatrix} t & r \\ r & t \end{pmatrix} \begin{pmatrix} \hat{a}_1 \\ \hat{a}_2 \end{pmatrix}. \quad (2.27)$$

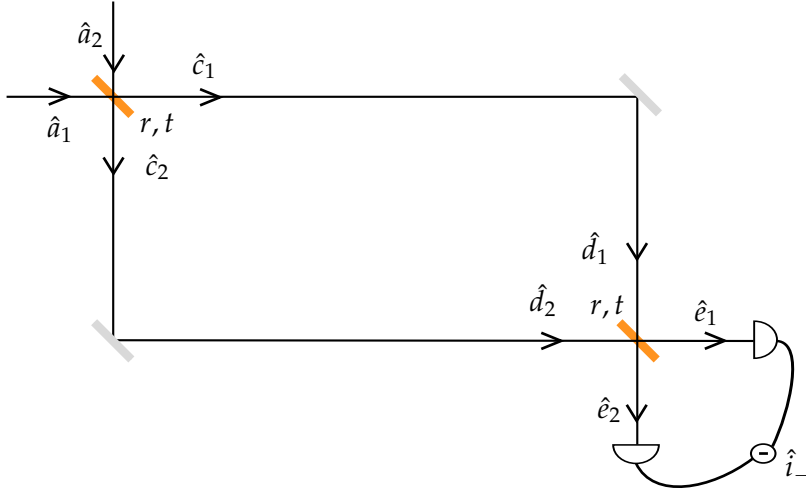


Figure 2.3.: A lossless MZI. The two inputs each split at the first beam splitter, then travel through the MZI and accumulate a phase shift difference. Then they are recombined and we detect the photocurrent output.

Converting this into a rotation of the light pseudo-spin vector using eq. (2.23) we get

$$\hat{\mathbf{S}}^{(c)} = M_{\Theta} \hat{\mathbf{S}}^{(a)} \quad (2.28a)$$

$$= \begin{pmatrix} 1 & 0 & 0 \\ 0 & \cos \Theta & \sin \Theta \\ 0 & -\sin \Theta & \cos \Theta \end{pmatrix} \begin{pmatrix} \hat{S}_x^{(a)} \\ \hat{S}_y^{(a)} \\ \hat{S}_z^{(a)} \end{pmatrix}, \quad (2.28b)$$

where the rotation angle Θ is given by

$$\Theta = \arctan \left(\frac{2rt}{r^2 - t^2} \right). \quad (2.29)$$

Taking the typical case of a 50/50 beam-splitter this corresponds to $\pi/2$ rotation around the x -axis (see fig. 2.4(a)).

Next the two modes propagate and accumulate a phase (see fig. 2.3). We will especially be interested in the *differential* phase shift between the two arms $\phi = |k| \Delta l$, where Δl is the path-length difference between the two arms. The annihilation operators change as

$$\begin{pmatrix} \hat{d}_1 \\ \hat{d}_2 \end{pmatrix} = \begin{pmatrix} e^{i\phi/2} & 0 \\ 0 & e^{-i\phi/2} \end{pmatrix} \begin{pmatrix} \hat{c}_1 \\ \hat{c}_2 \end{pmatrix}, \quad (2.30a)$$

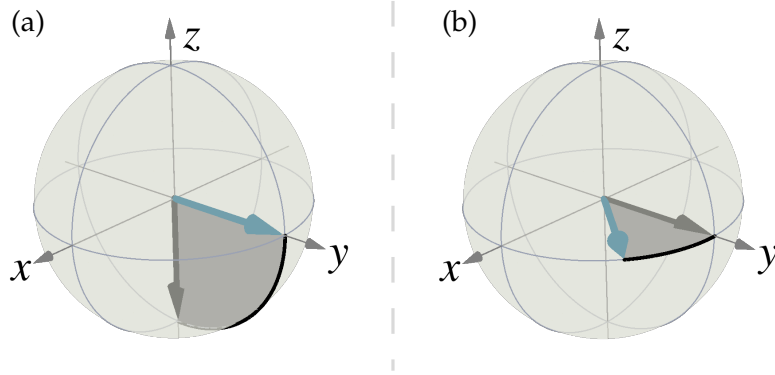


Figure 2.4.: Rotations of the pseudo-spin vector. (a) With all photons entering in one mode, the pseudo-spin vector points to the south pole and the 50/50 beam-splitter rotates it by an angle of $\pi/2$. (b) The free propagation in the MZI corresponds to a rotation of $\hat{\mathbf{S}}$ around the z-axis.

which in terms of the Schwinger operators becomes

$$\hat{\mathbf{S}}^{(d)} = \mathbf{M}_\phi \hat{\mathbf{S}}^{(c)} \quad (2.31a)$$

$$= \begin{pmatrix} \cos \phi & \sin \phi & 0 \\ -\sin \phi & \cos \phi & 0 \\ 0 & 0 & 1 \end{pmatrix} \begin{pmatrix} \hat{S}_x^{(c)} \\ \hat{S}_y^{(c)} \\ \hat{S}_z^{(c)} \end{pmatrix}. \quad (2.31b)$$

In our pictorial representation this corresponds to a rotation around the z-axis, which due to the first beam splitter is a rotation in the equatorial plane (see fig. 2.4(b)).

The two modes are then combined on a beam splitter and the number of photons in each mode is measured and subtracted from one another, allowing us to infer \hat{S}_z . With the description of how the individual components in the MZI affect the light, we can now write the total evolution as

$$\hat{\mathbf{S}}^{(\text{out})} = \mathbf{M}_{\Theta_2} \mathbf{M}_\phi \mathbf{M}_{\Theta_1} \hat{\mathbf{S}}^{(\text{in})}. \quad (2.32)$$

Taking a coherent light state in the mode \hat{a}_1 and vacuum in the mode \hat{a}_2 as the input at the first beam splitter (fig. 2.3) which we for simplicity take to be a 50/50, $\hat{\mathbf{S}}$ will be rotated into the equatorial plane. Here it rotates around the z-axis by an angle ϕ due to the path-length difference between the two interferometer arms. At the second beam-splitter

it is again rotated by $\pi/2$, effectively mapping $\cos \phi$ onto \hat{S}_z of the output pseudo-vector. The photocurrent difference at the output is then $\hat{i}_- = -2\epsilon \cos(\phi) \hat{S}_z^{(\text{in})}$, where ϵ is a conversion factor between photon numbers and photoelectrons. Scanning the phase difference between the two arms, using for example a piezo, the output oscillates and we observe an interference fringe. In the experiment We will detect small deviations $\delta\phi$ around a mean ϕ_0 and write the phase shift as $\phi = \phi_0 + \delta\phi$, which is then related to the photocurrent as

$$\delta\phi = \arcsin \left(\frac{\langle \hat{i}_- \rangle}{\epsilon \langle \hat{N}_{\text{ph}} \rangle} \right), \quad (2.33a)$$

$$\approx \frac{\langle \hat{i}_- \rangle}{\epsilon N_{\text{ph}}}. \quad (2.33b)$$

Here we have taken $\phi_0 = \pi/2$, leading to a linear relation between the phase shift and the detected photo-current difference as well as the highest phase sensitivity. To quantify how well we can measure the phase shift, we consider its variance due to the light shot noise affecting the photocurrent as

$$\text{var}(\hat{i}_-)_{\text{SN}} = 4\epsilon^2 \text{var}(\hat{S}_z^{(\text{out})})_{\text{SN}}, \quad (2.34a)$$

$$= \epsilon^2 N_{\text{ph,tot}}. \quad (2.34b)$$

This leads to a variance in the detected phase given by

$$\text{var}(\delta\phi)_{\text{SN}} = \frac{\text{var}(\hat{i}_-)_{\text{SN}}}{\epsilon^2 N_{\text{ph,tot}}^2}, \quad (2.35a)$$

$$= \frac{1}{N_{\text{ph,tot}}}. \quad (2.35b)$$

The SNR of the measurement is then

$$\text{SNR} = \frac{\langle \delta\phi^2 \rangle}{\text{var}(\delta\phi)_{\text{SN}}} \quad (2.36a)$$

$$= \langle \delta\phi^2 \rangle N_{\text{ph,tot}}, \quad (2.36b)$$

increasing linearly with the number of probe photons, as expected. In the experiment the upper limit for N_{ph} will depend on the type of experiment performed. For squeezing it is set by the reduction of Ramsey fringe contrast, whereas for atomic state-tomography it can

be much larger,⁶ leading to a negligible contribution of the light shot noise to $\text{var}(\delta\phi)$.

2.3.1 Real-life MZI

To push our description further than the textbook examples and closer to the actual experimental implementation, we first introduce the dual-color MZI, and second consider the effect of losses in the MZI.

In the experimental implementation we are using not one but two lasers to measure $\delta\phi$. An elaborate discussion of the reasons for this is given in sec. 6.3.3 and [Saffman et al. 2009]. The two lasers (referred to as orange and purple) are separated by 9 GHz. This allows us to propagate them individually through the MZI and sum them at the output:⁷

$$\hat{S}_z^{(\text{out})} = -\cos\phi \left(\hat{S}_z^{(\text{in},o)} + \hat{S}_z^{(\text{in},p)} \right). \quad (2.37)$$

We can thus reuse all the above formulas regarding phase sensitivity and SNR as long as we use

$$N_{\text{ph,tot}} = N_{\text{ph,tot}}^{(o)} + N_{\text{ph,tot}}^{(p)}. \quad (2.38)$$

The other thing to include in the description is inefficiencies of the MZI — we consider probe arm transmission and the finite mode overlap at the output. Modeling each loss mechanism as a beam splitter and knowing how this affects \hat{S} , the propagation in eq. (2.32) can be modified accordingly.

With the main derivation of the real-life MZI done before my time and as the result is a set of rather messy equations we refer to [Oblak 2010, chap. 2, appen. A] for the full description. The reason for the complication is that each beam-splitter adds an extra vacuum mode to the problem. This requires us to introduce new Schwinger operators to describe the system. Doing this and keeping track of all modes leads to the end result [Oblak 2010, eq. (2.31)]

$$\text{SNR} = \frac{\mathcal{T}^4 \tau^2 \sin^2(\phi_0) \sin^2(\Theta_1)}{1 - \rho^2 t_1^2} N_{\text{ph}} \langle \delta\phi^2 \rangle \quad (2.39)$$

⁶ We need to stay in the range where the detector and electronics are operating linearly.

⁷ For now we neglect that the two lasers have a different wavevector and therefore travel a different optical path-length. This will become important later and is described in sec. 5.1.

Table 2.1.: Parameters that are used in eq. (2.39) taken, from [Oblak 2010, Appen. A].

SYMBOL	MEANING
\mathcal{T}	Mode overlap, fields
τ	Probe arm transmission
Θ_1	Angle for first beam splitter
ϕ_0	Mean phase shift
$\delta\phi$	Deviations from the mean shift
ρ	Probe arm reflection
t_1	Transmission first splitter

where the relevant parameters are given in table 2.1. We again see that the SNR is highest for $\phi_0 = \pi/2$, and as the $1 - \rho^2 t_1^2$ term describes the photon loss it increases linearly with the detected number of photon. Furthermore, the SNR is maximized with $\Theta_1 = \pi/2$, corresponding to a 50/50 beam splitter which gives the maximum fringe contrast. As discussed the upper limit on the used photon number depends on the type of experiment performed. To have the detected photon number as high as possible it is favorable to take the first beam-splitter to be unbalanced. In this case we can have a strong beam in the reference arm whereas the photon number in the probe arm can be chosen accordingly. As a sanity check we see that the lossless MZI (where $\rho = t_1 = 0$ and $\mathcal{T} = \tau = 1$) with a 50/50 beam splitter reproduces eq. (2.36).

2.4 SUMMARY

In this chapter we have introduced the quantum-mechanical description of the electromagnetic field. Starting from the harmonic-oscillator Hamiltonian, we introduced two types of states, the Fock and coherent states. The concept of QPDs were described with a special focus on how these are used to infer nonclassical properties of the states. These considerations will be directly applicable when we infer the nonclassical properties of the states in chap. 7. We then considered the description of the MZI via the Schwinger, or light pseudo-spin, operators, and how this allows for phase measurements. This led to several key insights: first the path-length difference between the arms should be $\phi_0 = \pi/2$

LIGHT

(corresponding to measuring around a zero-crossing of the fringe). Second, to overcome the light shot noise we should use as many photons as possible. With the atoms limiting the used number of photons (scattering events reduces the Ramsey fringe contrast see sec. 7.2) it is desirable to have an unbalanced first beam-splitter effectively using the reference arm as a strong local oscillator (LO).

ATOMS

With the quantum-mechanical description of light we will in this chapter consider the second main player of the experiment, the atomic ensemble. More specifically we are interested in describing a dipole-trapped ensemble of approximately 10^5 cesium (Cs) atoms. As we later will be looking at the interactions between light and atoms, it is convenient to have comparable descriptions of the two systems. We will thus throughout this chapter emphasize the similarities between the descriptions of light and atoms in terms of pseudo-spin operators and harmonic oscillators. The chapter is organized as follows. Starting from the complex multilevel structure of a single Cs atoms we introduce the two-level system of interest and describe it using angular-momentum operators. This is then generalized to treat all the atoms in the ensemble. In connection to the previous chapter we introduce *atomic* quadrature operators, using the Holstein-Primakoff approximation. We then consider the three types of states that we will create in the experiment; the CSSs, spin-squeezed states (SSSs) and atomic Fock states (AFSs). These states will be characterized by measuring the population difference ΔN and we conclude the chapter by deriving probability distributions for the measurement statistics.

3.1 CESIUM ATOMS

Our atom of choice is the only natural isotope of Cs, with 133 nucleons in its core. Cs has a single electron in the outermost shell, the *s*-shell, making it an alkali atom. In the used wavelength range, the ground state $6S_{1/2}$ is coupled to the excited $6P_{1/2}$ and $6P_{3/2}$ states (see fig. 3.1). We will exclusively be dealing with the $6S_{1/2} \rightarrow 6P_{3/2}$ transition also known as the D_2 -line, with a transition wavelength of 852 nm. Each of these states is split due to different possible alignments of the electron and nuclear spins, and we distinguish these by the quantum number F . To add further to the complexity, an external magnetic field B lifts the

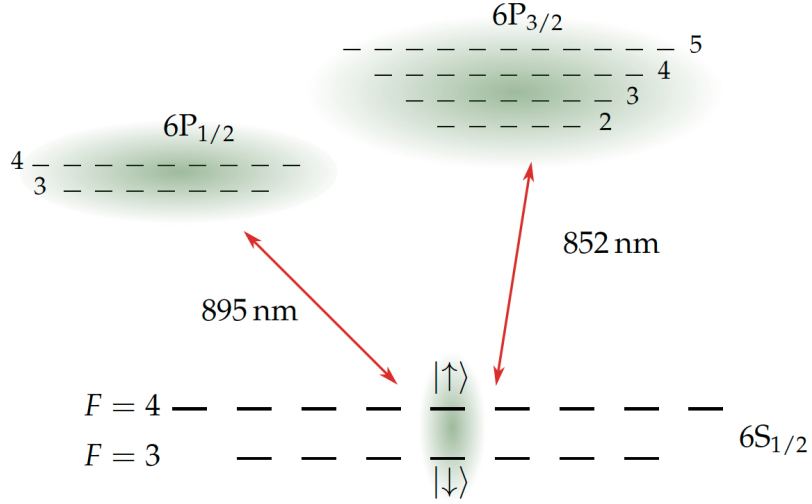


Figure 3.1.: Atomic level structure, showing the ground state $6S_{1/2}$ and the two excited states $6P_{1/2}$ and $6P_{3/2}$. The two-level system we will be using is formed by the hyperfine ground states, $|\downarrow\rangle_A$ and $|\uparrow\rangle_A$, and is highlighted.

degeneracy of the m_F states via the linear Zeeman shift (of the ground states) given by [Steck 2010]

$$\Delta\omega_{\text{Zeeman}} = \frac{\mu_B}{\hbar} g_F m_F |\mathbf{B}|, \quad (3.1a)$$

$$= 2\pi m_F |\mathbf{B}| \cdot 350 \text{ kHz G}^{-1}. \quad (3.1b)$$

Here μ_B is the Bohr magneton, g_F is the Landé factor for the corresponding hyperfine level and we have taken the quantization axis along \mathbf{B} . The atomic states can then be written as $|F, m_F\rangle_A$, and we will use a prime to denote the excited states.

We are interested in the clock levels,¹ i.e., the two hyperfine ground levels ($m_F = 0$) of the $6S_{1/2}$ manifold which we write as

$$|\downarrow\rangle_A \equiv |F = 3, m_F = 0\rangle_A, \quad (3.2a)$$

$$|\uparrow\rangle_A \equiv |F = 4, m_F = 0\rangle_A. \quad (3.2b)$$

¹ Termed so since the definition of the second, and thus time, is based on the energy difference between these levels.

Their are two reasons for this choice. First they are to first order insensitive² to magnetic-field fluctuations. Second, they are meta-stable, meaning they have long coherence times, which will allow for long lifetimes of the created states. Having introduced the two-level system of interest we now consider the operators required to describe it.

3.2 ATOMIC OPERATORS

To describe the two level system we, in analogy to a spin-1/2 system and the Pauli spin operators, introduce angular-momentum operators for the l^{th} atom. These are defined as

$$\hat{j}_x^{(l)} \equiv \frac{1}{2} (|\downarrow\rangle_l \langle \uparrow| + |\uparrow\rangle_l \langle \downarrow|), \quad (3.3a)$$

$$\hat{j}_y^{(l)} \equiv -\frac{i}{2} (|\downarrow\rangle_l \langle \uparrow| - |\uparrow\rangle_l \langle \downarrow|), \quad (3.3b)$$

$$\hat{j}_z^{(l)} \equiv \frac{1}{2} (|\uparrow\rangle_l \langle \uparrow| - |\downarrow\rangle_l \langle \downarrow|) \quad (3.3c)$$

we have the commutation relation

$$[\hat{j}_x^{(l)}, \hat{j}_y^{(l')}] = i \hat{j}_z^{(l)} \delta_{l,l'}, \quad (3.4)$$

with cyclic permutation. To complete the description of the single atom, we write the angular-momentum as a spin-vector

$$\hat{\mathbf{j}}^{(l)} \equiv \begin{pmatrix} \hat{j}_x^{(l)} \\ \hat{j}_y^{(l)} \\ \hat{j}_z^{(l)} \end{pmatrix}, \quad (3.5)$$

with a length of 1/2.

In the experiment we will be using an ensemble of atoms, and therefore need to extend the single-atom description. This is done by summing up the single-atom spin vectors and introducing collective operators

$$\hat{\mathbf{J}} \equiv \sum_{l=1}^{N_{\text{at}}} \hat{\mathbf{j}}^{(l)}, \quad (3.6)$$

² To second order the clock levels do experience a quadratic Zeeman shift of 427.45 Hz G⁻² [Steck 2010].

with a magnitude $N_{\text{at}}/2$. From eq. (3.4) it follows that

$$[\hat{J}_x, \hat{J}_y] = i\hat{J}_z, \quad (3.7)$$

with cyclic permutation. A central feature of the collective operators are their symmetry under particle exchange. This feature will be of particular importance when we consider the atomic Fock states in sec. 3.5. Forming the collective operators (eq. (3.6)), each atom is weighted equally. If required the definition could be expanded by introducing a spatial mode function, similar to the case of light, weighing each atom according to its position — see for example [Hammerer et al. 2010, sec. II.3; Oblak 2010, chap. 3].

3.2.1 Atomic quadrature operators

For many ensemble states of interest \hat{J} is aligned along a specific axis, which allows to simplify the description substantially as the Holstein-Primakoff approximation [Holstein et al. 1940; Kuzmich et al. 2000] can be made. We take the pseudo-spin vector to be aligned along the x -axis, i.e., $\langle \hat{J}_x \rangle \approx J = N_{\text{at}}/2$, where J is the length of the collective-spin vector. For a large atomic ensemble $J \gg 1$ we can substitute the operator \hat{J}_x with its expectation value [Hammerer et al. 2010], i.e., taking \hat{J}_x to be a classical quantity. Rescaling the two remaining collective-angular-momentum operators as

$$\hat{X}_A \equiv \frac{\hat{J}_y}{\sqrt{\langle \hat{J}_x \rangle}}, \quad (3.8a)$$

$$\hat{P}_A \equiv \frac{\hat{J}_z}{\sqrt{\langle \hat{J}_x \rangle}}, \quad (3.8b)$$

their commutation relation becomes

$$[\hat{X}_A, \hat{P}_A] = i. \quad (3.9)$$

This is the canonical commutation relation and analogous to the case of the quadrature operators for light (eq. (2.7)). In the Holstein-Primakoff approximation we therefore have a harmonic-oscillator-like description of the collective-angular-momentum operators. With this we have introduced a description of the atomic system identical to the case of a photonic system (see sec. 2.1).

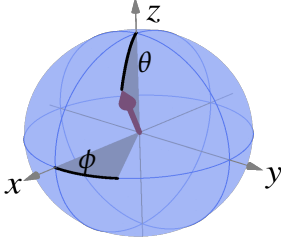


Figure 3.2.: Representation of the CSS $|\theta, \phi\rangle_A$ on the collective Bloch sphere. The angles ϕ and θ are given by eq. (3.12) and related to the single atom state through eq. (3.11).

3.3 COHERENT SPIN STATES

Having introduced the relevant operators to describe the atomic ensemble, we consider the coherent spin states (CSSs). These states are product states of single-atom states³

$$|\phi, \theta\rangle_A = \bigotimes_{l=1}^{N_{\text{at}}} |\psi\rangle_l. \quad (3.10)$$

Here each atom is in the state

$$|\psi\rangle_l = \cos\left(\frac{\theta}{2}\right) |\uparrow\rangle_l + \sin\left(\frac{\theta}{2}\right) e^{i\phi} |\downarrow\rangle_l, \quad (3.11)$$

parameterized by the angles $\theta \in [0, \pi]$ and $\phi \in [0, 2\pi]$. We calculate the expectation value for each of the collective spin operators

$$\langle \hat{J}_x \rangle = \frac{N_{\text{at}}}{2} \sin(\theta) \cos(\phi), \quad (3.12a)$$

$$\langle \hat{J}_y \rangle = \frac{N_{\text{at}}}{2} \sin(\theta) \sin(\phi), \quad (3.12b)$$

$$\langle \hat{J}_z \rangle = \frac{N_{\text{at}}}{2} \cos(\theta). \quad (3.12c)$$

This is exactly the description of a vector of length $N_{\text{at}}/2$ in spherical coordinates, with the polar angle θ and azimuthal angle ϕ . It is thus natural to use the picture of the generalized Bloch sphere [Dowling et al. 1994] to represent the pseudo-spin vector $\hat{\mathbf{J}}$ (see fig. 3.2).

An arbitrary CSS can be generated from the ground state

$$|0\rangle_A \equiv |\theta = \pi, \phi\rangle_A \quad (3.13a)$$

$$= \bigotimes_{l=1}^{N_{\text{at}}} e^{i\phi} |\downarrow\rangle_l, \quad (3.13b)$$

³ This is not true in general, as the CSS can also be formed by lower cooperativity Dicke states, [Mandel et al. 1995, sec. 16.7].

by a rotation. How such a rotation is implemented depends on the actual system of interest and in our experiment a low phase-noise microwave source is used, discussed in more detail in sec. 4.3. The CSS lives on the two dimensional surface of a sphere where rotations are the equivalent to displacement in the plane. This, once again, gives a clear analogy to the coherent states of light, namely as displaced vacuum states [Mandel et al. 1995, sec. 16.7].

To take the analogy to the coherent states of light a step further we consider the quantum fluctuations of the CSS, known as atomic shot noise or projection noise. The variance of each of the components for \hat{J} is for a CSS

$$\text{var}(\hat{J}_x) = \frac{N_{\text{at}}}{4} [1 - \sin^2(\theta) \cos^2(\phi)], \quad (3.14a)$$

$$\text{var}(\hat{J}_y) = \frac{N_{\text{at}}}{4} [1 - \sin^2(\theta) \sin^2(\phi)], \quad (3.14b)$$

$$\text{var}(\hat{J}_z) = \frac{N_{\text{at}}}{4} [1 - \cos^2(\theta)]. \quad (3.14c)$$

For the collective-angular-momentum operators Heisenberg's uncertainty relation (eq. (2.17)), is given by

$$\text{var}(\hat{J}_y) \text{var}(\hat{J}_z) \geq \frac{1}{4} \langle \hat{J}_x \rangle^2. \quad (3.15)$$

Using eq. (3.14) it is seen that the CSS minimize Heisenberg's uncertainty relation, and we refer to them as minimum-uncertainty states,⁴ again similar to the coherent states of light. Due to the associated uncertainty the initial picture of describing the ensemble as a point on the Bloch sphere is misleading, and we have to ascribe a corresponding uncertainty to the Bloch vector. Considering states in the Holstein-Primakoff approximation⁵ we can directly extend the concept of a quasi-probability distribution (QPD) — see sec. 2.2.1 — to atomic states.⁶ To depict this we will at the tip of the Bloch vector plot

-
- ⁴ Naively considering eqs. (3.12), (3.14) and (3.14), one can find values of ϕ and θ for which this is not the case. The reason for this is that Heisenberg's uncertainty relation *only* holds for the directions orthogonal to the mean spin. Therefore, an extra rotation would have to be performed after which sanity is restored and Heisenberg's uncertainty relation holds.
- ⁵ This is equivalent to neglecting the curvature of the Bloch sphere and simply using the two-dimensional tangential plane (fig. 3.3(b)).
- ⁶ The concept of Wigner function can also be used beyond the Holstein-Primakoff approximation; for the theoretical description see [Bizarro 1994; Dowling et al. 1994] and [Schmied et al. 2011] for an experimental reconstruction.

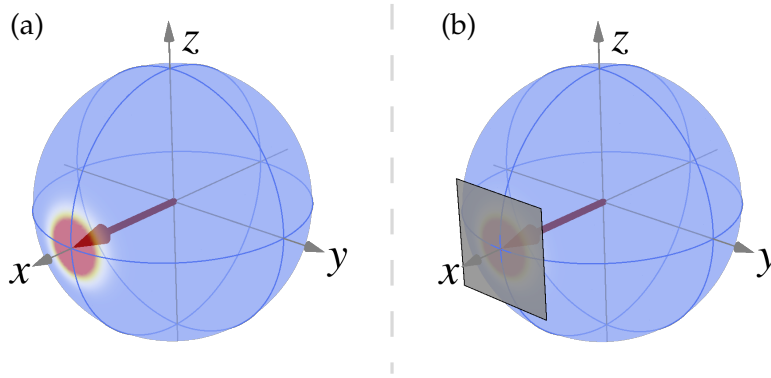


Figure 3.3.: The pseudo-spin vector \hat{J} describing the atomic ensemble can be visualized on the collective Bloch sphere. (a) The CSS pointing along the x -axis, $|\theta = \pi/2, \phi = 0\rangle_A$ with its associated error disk plotted as the Wigner function. (b) Same as (a) but with the tangential plane illustrating that for large spins, i.e., in the Holstein Primakoff approximation, we can neglect the curvature of the Bloch sphere and take \hat{J} to be constrained to the tangential plane.

the Wigner function for the corresponding state;⁷ an example for the $|\theta = \pi/2, \phi = 0\rangle_A$ state is shown in fig. 3.3(a).

We consider the interactions between a classical (external) field and an ensemble in the ground state. Taking the field to be uniform over the ensemble, it rotates all the individual pseudo-spins in an identical fashion. The ensemble is therefore still in a product state, i.e., a CSS. A full-blown derivation can be found in [Mandel et al. 1995, sec. 16.7.3]. This and the above properties allow us to identify the CSSs as the “most classical quantum states” [Arecchi et al. 1972; Combescure et al. 2012]. The CSS will play a crucial part in the remainder of this thesis. It will be our benchmark state to which we will always compare other states and we will use it in our definition and discussion of non-classicality in sec. 7.4.

⁷ The shape will be correct, but we will for visual clarity use a scale factor.

3.4 SPIN-SQUEEZED STATES

Having introduced the CSSs, a natural extension is the spin-squeezed states (SSSs). Considering Heisenberg’s uncertainty relation for the collective spin operators (eq. (3.15)), the thing to note is that only the product of the variance is limited. The variance of one spin component can be reduced if the variance of the other component increases accordingly, i.e., the area of the QPD is kept constant. This reduced variance is exactly what drives the intuition behind the SSSs. To define a SSS more rigorously and quantify the amount of squeezing, we consider two⁸ different squeezing criteria.

KITAGAWA CRITERION To specify the squeezing requirement, we follow [Kitagawa et al. 1993]. The error disk associated with a state is orthogonal to the direction of the mean spin \hat{J}_\perp with magnitude $|\langle \hat{J} \rangle|$ (see fig. 3.4). The standard quantum limit (SQL) found from Heisenberg’s uncertainty relation is then

$$\text{var}(\hat{J}_\perp)_{\text{SQL}} = \frac{|\langle \hat{J} \rangle|}{2}. \quad (3.16)$$

Introducing a squeezing parameter

$$\zeta_{\text{Kitagawa}} = \frac{\text{var}(\hat{J}_\perp)}{\text{var}(\hat{J}_\perp)_{\text{SQL}}} \quad (3.17a)$$

$$= \frac{2}{|\langle \hat{J} \rangle|} \text{var}(\hat{J}_\perp), \quad (3.17b)$$

a state is squeezed if $\zeta_{\text{Kitagawa}} < 1$. If only pure states are considered, this criterion ensures that there are correlations between the atoms. Expanding the class of considered states to also include mixed states, this is no longer the case and a second more stringent definition is required.

WINELAND CRITERION The most striking application of SSSs is their capability to increase measurement precision. In metrology applications, the parameter of interest is the phase associated with a state [Giovannetti et al. 2011]. Considering the example of Ramsey spectroscopy,

⁸ Many more can be found in [Ma et al. 2011, tab. 1].

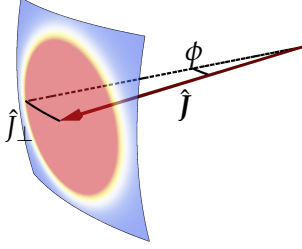


Figure 3.4.: In spectroscopy the parameter of interest is the atomic phase ϕ . Which can be related to the mean spin \hat{J} and the fluctuations in the orthogonal directions \hat{J}_\perp .

the variance of the “atomic” phase can be related to the pseudo-spin components (fig. 3.4) as

$$\phi = \arctan \left(\frac{\langle \hat{J}_\perp \rangle}{|\langle \hat{J} \rangle|} \right), \quad (3.18a)$$

$$\stackrel{N_{\text{at}} \gg 1}{\approx} \frac{\langle \hat{J}_\perp \rangle}{|\langle \hat{J} \rangle|}. \quad (3.18b)$$

Using eqs. (3.12) and (3.14) the SQL is found to be⁹

$$\text{var}(\phi)_{\text{SQL}} = \frac{1}{N_{\text{at}}}, \quad (3.19)$$

allowing us to introduce the Wineland squeezing parameter [Wineland et al. 1994]

$$\zeta_{\text{Wineland}} = \frac{\text{var}(\phi)}{\text{var}(\phi)_{\text{SQL}}}, \quad (3.20a)$$

$$= N_{\text{at}} \frac{\text{var}(\hat{J}_\perp)}{|\langle \hat{J} \rangle|^2}, \quad (3.20b)$$

and we term a state squeezed if $\zeta_{\text{Wineland}} < 1$. If a quantum state allows for a sensitivity beyond the SQL, it must have nonclassical correlations, i.e., entanglement. That this is the case was shown in [Sørensen et al. 2001].

⁹ This result can also be directly derived using the Fisher information and the Cramér-Rao bound [Giovannetti et al. 2011].

3.5 ATOMIC FOCK STATES

The last type of states we consider is the atomic Fock states (AFSs), which are the atomic equivalent of the photon number states. In analogy to the case of light, the vacuum state has no excitations:

$$|0\rangle_A \equiv \bigotimes_{l=1}^{N_{\text{at}}} |\downarrow\rangle_l, \quad (3.21a)$$

$$= |\theta = \pi, \phi\rangle_A. \quad (3.21b)$$

To create a higher-excited AFS we define the atomic creation operator [Hammerer et al. 2010] as

$$\hat{a}_A^\dagger \equiv \frac{\hat{X}_A + i\hat{P}_A}{\sqrt{2}}, \quad (3.22a)$$

$$= \frac{1}{\sqrt{N_{\text{at}}}} \sum_{l=1}^{N_{\text{at}}} |\uparrow\rangle_l \langle \downarrow |_l. \quad (3.22b)$$

As expected in the limit of large ensembles, we obtain similar commutation relations to the creation and annihilation operators for light

$$[\hat{a}_A, \hat{a}_A^\dagger] = 1, \quad (3.23)$$

fitting with the harmonic-oscillator description. The *collective-single-excitation* state¹⁰ can then be defined as

$$|1\rangle_A \equiv \hat{a}_A^\dagger |0\rangle_A, \quad (3.24a)$$

$$= \frac{1}{\sqrt{N_{\text{at}}}} \sum_{l=1}^{N_{\text{at}}} |\underbrace{\downarrow\downarrow \dots \downarrow \uparrow \downarrow \dots \downarrow\downarrow}_{l\text{-th atom}}\rangle_A. \quad (3.24b)$$

Subsequent application of \hat{a}_A^\dagger then allows us to define higher order AFS as

$$|n\rangle_A \equiv \left(\hat{a}_A^\dagger\right)^n |0\rangle_A \quad (3.25a)$$

$$= \frac{1}{\sqrt{\binom{N_{\text{at}}}{n}}} \sum_{\pi} \underbrace{|\uparrow\uparrow \dots \uparrow\downarrow \dots \uparrow\downarrow \dots \uparrow\rangle_A}_{\text{Total of } n \text{ atoms up}} \quad (3.25b)$$

¹⁰ Which we will also refer to as the first excited AFS or first excited Dicke state.

where the summation index π denotes a sum over all permutations and the normalization is given by the binomial coefficient $\binom{N_{\text{at}}}{n}$. The important thing to realize is that it is not a single atom in the ensemble that is excited — the excitation is shared among *all* the atoms. It is this point which will give rise to the many strange and peculiar properties that we will study throughout this thesis. To strengthen the connection to the case of optical number states we consider the action of the creation operator on the AFS

$$\hat{a}_A^\dagger |n\rangle_A = \frac{1}{\sqrt{\binom{N_{\text{at}}}{n} N_{\text{at}}}} \sum_{l=1}^{N_{\text{at}}} |\uparrow\rangle_l \langle \downarrow| \sum_{\pi} \underbrace{|\uparrow\uparrow \dots \uparrow\downarrow \dots \uparrow\downarrow \dots \uparrow\rangle_A}_{\text{Total of } n \text{ atoms up}} \quad (3.26a)$$

$$= \frac{1}{\sqrt{\binom{N_{\text{at}}}{n} N_{\text{at}}}} (n+1) \sum_{\pi} \underbrace{|\uparrow\uparrow \dots \uparrow\downarrow \dots \uparrow\downarrow \dots \uparrow\rangle_A}_{\text{Total of } n+1 \text{ atoms up}} \quad (3.26b)$$

$$= \sqrt{\frac{\binom{N_{\text{at}}}{n+1}}{\binom{N_{\text{at}}}{n} N_{\text{at}}}} (n+1) |n+1\rangle_A, \quad (3.26c)$$

$$= (n+1) \sqrt{\frac{N_{\text{at}} - 1}{N_{\text{at}}(n+1)}} |n+1\rangle_A, \quad (3.26d)$$

$$\stackrel{N_{\text{at}} \gg n}{\approx} \sqrt{n+1} |n+1\rangle_A. \quad (3.26e)$$

In the limiting case this is identical to the case of photonic Fock states — see eq. (2.11).

The reader familiar with the work of Dicke [1954] will have noted the connection to the so-called Dicke states. The angular-momentum states can also be described by the quantum numbers J and m_J such that

$$\hat{J}_z |J, m_J\rangle_A = m_J |J, m_J\rangle_A, \quad (3.27a)$$

$$\hat{J}^2 |J, m_J\rangle_A = J(J+1) |J, m_J\rangle_A, \quad (3.27b)$$

where the states $|J, m_J\rangle_A$ are referred to as Dicke states [Mandel et al. 1995, sec. 16.5]. The value of m_J is related to the number of excita-

tions,¹¹ and J is the pseudo-spin vector length vector proportional to the atom number. As for any angular momentum,

$$|m_J| \leq J \leq \frac{N_{\text{at}}}{2}. \quad (3.28)$$

Thus for an ensemble with N_{at} atoms the, n^{th} AFS is related to the Dicke state by

$$|n\rangle_A = \left| \frac{N_{\text{at}}}{2}, -\frac{N_{\text{at}}}{2} + n \right\rangle_A. \quad (3.29)$$

To better understand the AFS we first look at the variance of the vacuum state $|0\rangle_A$. Using the angular-momentum properties of the Dicke states, we calculate the variance of this state and show the consistency with the calculations in sec. 3.3. From the eigenvalue relation (eq. (3.27)) we have

$$\langle \hat{j}^2 \rangle = \frac{N_{\text{at}}}{2} \left(\frac{N_{\text{at}}}{2} + 1 \right), \quad (3.30a)$$

$$\langle \hat{j}_z^2 \rangle = \frac{N_{\text{at}}^2}{4}. \quad (3.30b)$$

As \hat{J}_x and \hat{J}_y are symmetric and $\langle \hat{J}_x \rangle = \langle \hat{J}_y \rangle = 0$ we directly find

$$\text{var}(\hat{J}_x) = \frac{\langle \hat{j}^2 - \hat{j}_z^2 \rangle}{2}, \quad (3.31a)$$

$$= \frac{N_{\text{at}}}{4} - \frac{1}{2} \quad (3.31b)$$

$$\stackrel{N_{\text{at}} \gg 1}{\approx} \frac{N_{\text{at}}}{4}, \quad (3.31c)$$

in agreement with eq. (3.14). We now consider the case where the projection onto the z-axis has changed by one leading, to $\left| J, -\frac{N_{\text{at}}}{2} + 1 \right\rangle_A$. The possible values of J are

$$J = \frac{N_{\text{at}}}{2} \quad (3.32a)$$

or

$$J = \frac{N_{\text{at}}}{2} - 1. \quad (3.32b)$$

¹¹ In his original work, Dicke referred to J as the *cooperation* number, since it plays a key role in determining the radiation properties of the atomic ensemble [Dicke 1954].

The first value corresponds to a coherent flip. Again using the symmetry between \hat{J}_x and \hat{J}_y and the eigenvalue equations, we find for the incoherent flip

$$\text{var}(\hat{J}_x) \stackrel{N_{\text{at}} \gg 1}{\approx} \frac{N_{\text{at}}}{4}. \quad (3.33)$$

In comparison, the variance of \hat{J}_x increases by a factor of three for the coherent flip:

$$\text{var}(\hat{J}_x) \stackrel{N_{\text{at}} \gg 1}{\approx} \frac{3N_{\text{at}}}{4}. \quad (3.34)$$

The difference comes from knowing or not knowing which atom was flipped, i.e., whether the excitation is shared or not. This increase in the variance will in chap. 8 be used to distinguish between a CSS and the created collective-single-excitation state. Continuing along the same lines, we now proceed with a calculation of the full probability distribution.

3.6 MEASUREMENT OUTCOMES

As will be explained in detail in chap. 4, the observable of interest is the population difference, $\Delta N = N_{\uparrow} - N_{\downarrow} = 2 \langle \hat{J}_z \rangle$. From the above we can easily find the corresponding mean value and variances. However to describe the actual measurements we will be interested in the full probability distributions of the outcomes, which we will derive in this section. Knowing the total number of atoms N_{at} , we can infer ΔN by measuring the number of atoms in the upper state. This is done by a projective measurement described by

$$\hat{\mathcal{P}}(n) \equiv \sum_{\pi} |n\rangle_A \langle n|, \quad (3.35a)$$

$$= \sum_{\pi} \underbrace{|\uparrow\uparrow \dots \uparrow\downarrow \dots \downarrow\rangle}_{n \quad N_{\text{at}} - n} \langle \uparrow\uparrow \dots \uparrow\downarrow \dots \downarrow|. \quad (3.35b)$$

With this we can consider each type of state and compare the variance of the derived distributions to eqs. (3.31) and (3.34).

3.6.1 Coherent spin state

We start by considering the CSS aligned along the x -axis of the Bloch sphere¹²

$$|\theta = \pi/2, \phi = 0\rangle_A = |\leftarrow\leftarrow \dots \leftarrow\rangle_A, \quad (3.36)$$

where we have introduced the equal superposition state

$$|\leftrightarrow\rangle_l \equiv \frac{|\uparrow\rangle_l \pm |\downarrow\rangle_l}{\sqrt{2}}. \quad (3.37)$$

The probability to detect n atoms in the upper state is

$$\tilde{p}_0(n) \equiv \langle \theta = \pi/2, \phi = 0 | \hat{P}(n) | \theta = \pi/2, \phi = 0 \rangle \quad (3.38a)$$

$$= \sum_{\pi} |\langle \leftarrow\leftarrow \dots \underbrace{|\uparrow\uparrow \dots \uparrow}_{n} \underbrace{|\downarrow\downarrow \dots \downarrow}_{N_{\text{at}} - n} \rangle|^2 \quad (3.38b)$$

$$= \sum_{\pi} \frac{1}{2^{N_{\text{at}}}} \quad (3.38c)$$

$$= \frac{1}{2^{N_{\text{at}}}} \binom{N_{\text{at}}}{n} \quad (3.38d)$$

$$= \binom{N_{\text{at}}}{n} \left(\frac{1}{2}\right)^n \left(1 - \frac{1}{2}\right)^{N_{\text{at}} - n}. \quad (3.38e)$$

Thus $\tilde{p}_0(n)$ is a binomial distribution with an equal probability of the two outcomes, corresponding to an atom being in either the upper or lower state. The physical interpretation is straightforward: performing the measurement on the state $|\theta = \pi/2, \phi = 0\rangle_A$, each atom is projected into either the upper or lower state with equal probability (see fig. 3.5). Since we are working with large ensembles, $N_{\text{at}} \gg 1$, we can approximate the binomial distribution with a normal distribution,¹³ allowing us to write

$$\tilde{p}_0(n) \stackrel{N_{\text{at}} \gg 1}{\approx} \sqrt{\frac{2}{\pi N_a}} \exp \left[-\frac{2}{N_a} \left(n - \frac{N_a}{2} \right)^2 \right]. \quad (3.39)$$

This is a normal distribution with a mean of $N_{\text{at}}/2$ and a variance of $N_{\text{at}}/4$. The last step is to recall that we will be measuring the popu-

¹² We consider a state with a pseudo-spin vector living in the equatorial plane, as it is such states we will be creating and characterizing in the remainder of this thesis.

¹³ This correspondence can be found via Stirling's formula: $\ln(x)! = x \ln(x) - x$.

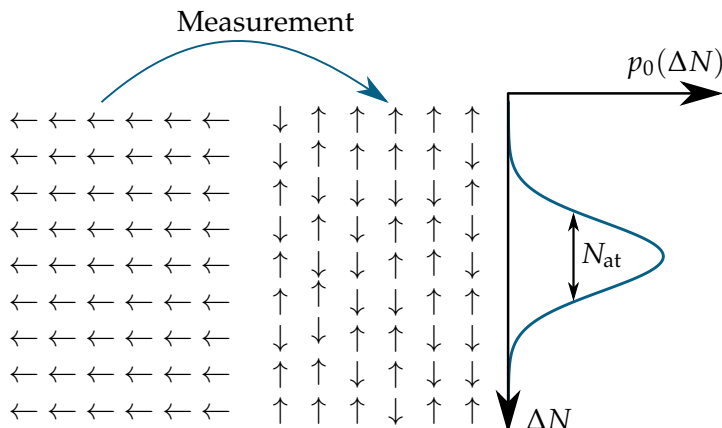


Figure 3.5.: Performing a projective measurement of ΔN on an atomic ensemble prepared in the CSS $|\theta = \pi/2, \phi = 0\rangle_{A'}$, each atom is projected onto $|\uparrow\rangle$ or $|\downarrow\rangle$ with equal probabilities. The distribution of measurement outcomes then follows a binomial distribution, which in the limit of $N_{\text{at}} \gg 1$ is well approximated by a Gaussian with a mean of zero and a variance of N_{at} .

lation difference ΔN . Assuming that N_{at} is fixed, this corresponds to changing the *domain* of $\tilde{p}_0(n)$ as follows:

$$\begin{aligned}
 n = 0 &\rightarrow \Delta N = -N_{\text{at}} \\
 n = 1 &\rightarrow \Delta N = -N_{\text{at}} + 2 \\
 &\vdots \\
 n = N_{\text{at}} &\rightarrow \Delta N = N_{\text{at}}.
 \end{aligned}$$

Performing these substitutions, one finds

$$p_0(\Delta N) = \frac{1}{\sqrt{2\pi N_{\text{at}}}} \exp\left(-\frac{\Delta N^2}{2N_{\text{at}}}\right). \quad (3.40)$$

This is a normal distribution with a mean of zero and a variance¹⁴ of N_{at} , which is plotted in fig. 3.6. Using eqs. (3.12) and (3.14) and the fact that $\Delta N = 2\hat{J}_z$, we see that this is in agreement with the previous calculation. A different derivation, based on expanding the coherent

¹⁴ The corresponding full width half maximum (FWHM) is $2\sqrt{2\ln 2}\sigma$

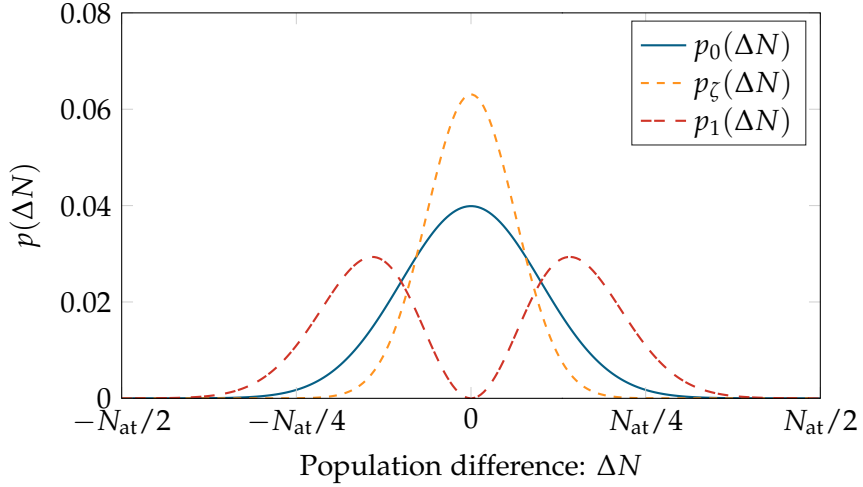


Figure 3.6.: Measurement outcomes for **CSS** (blue), **SSS** (orange) and collective-single-excitation state (red) calculated for $N_{\text{at}} = 100$. The variance of the **SSS** is reduced by a factor of $\zeta = 0.4$ in comparison to that of a **CSS**. The three states give rise to vastly different distributions of the measurement outcomes $p(\Delta N)$.

state $|\theta = \pi/2, \phi = 0\rangle_A$ onto the basis formed by the Dicke states with a given cooperativity number (as done in [Itano et al. 1993] and [Mandel et al. 1995, sec. 16.7]) gives an identical result.

3.6.2 Spin-squeezed state

With the above calculation and the definition of squeezing (see sec. 3.4), one easily generalizes the result of eq. (3.40) to the squeezed state $|\phi = \pi/2, \phi = 0, \xi\rangle_A$, by decreasing the variance by a factor of ζ . This yields

$$p_{\zeta}(\Delta N) = \frac{1}{\sqrt{2\pi\zeta N_{\text{at}}}} \exp\left(-\frac{\Delta N^2}{2\zeta N_{\text{at}}}\right), \quad (3.41)$$

which is shown in fig. 3.6. Here we have taken the squeezed spin component to be $\hat{J}_z \propto \hat{P}_A$.

3.6.3 Collective-single-excitation state

We now consider the collective-single-excited state $|1\rangle_A$ (eq. (3.24)) and are again interested in the distribution of the measurement outcomes. We first rotate the state $|1\rangle_A$ into the equatorial plane:

$$|1'\rangle_A = \frac{1}{\sqrt{N_{\text{at}}}} \sum_{l=1}^{N_{\text{at}}} |\leftarrow \leftarrow \dots \leftarrow \underbrace{\rightarrow \leftarrow}_{l\text{-th atom}} \dots \leftarrow \leftarrow \rangle. \quad (3.42)$$

Using the projector (eq. (3.35)), the probability to find n atoms in the upper state is

$$\tilde{p}_1(n) = \langle 1' | \hat{\mathcal{P}}(n) | 1' \rangle. \quad (3.43)$$

Reexpressing the l^{th} atom in the standard spin basis as

$$|1'\rangle_A = \frac{1}{\sqrt{N_{\text{at}}}} \sum_{l=1}^{N_{\text{at}}} \frac{1}{\sqrt{2}} [|\leftarrow \leftarrow \dots \leftarrow \underbrace{\downarrow \leftarrow}_{l\text{-th atom}} \dots \leftarrow \leftarrow \rangle - |\leftarrow \leftarrow \dots \leftarrow \underbrace{\uparrow \leftarrow}_{l\text{-th atom}} \dots \leftarrow \leftarrow \rangle] \quad (3.44)$$

and inserting this into eq. (3.43), we find

$$\tilde{p}_1(n) = \sum_{\pi} \left| \sum_{l=1}^{N_{\text{at}}} \frac{1}{\sqrt{2N_{\text{at}}}} \left(\langle \underbrace{\uparrow \uparrow \dots \uparrow}_n \underbrace{\downarrow \downarrow \dots \downarrow}_{N_{\text{at}}-n} | \leftarrow \leftarrow \dots \leftarrow \underbrace{\uparrow \leftarrow}_{l\text{-th atom}} \dots \leftarrow \leftarrow \rangle - \langle \underbrace{\uparrow \uparrow \dots \uparrow}_n \underbrace{\downarrow \downarrow \dots \downarrow}_{N_{\text{at}}-n} | \leftarrow \leftarrow \dots \leftarrow \underbrace{\downarrow \leftarrow}_{l\text{-th atom}} \dots \leftarrow \leftarrow \rangle \right) \right|^2. \quad (3.45)$$

The two inner products give Kronecker deltas dependent on the permutation

$$\tilde{p}_1(n) = \sum_{\pi} \left| \sum_{l=1}^{N_{\text{at}}} \frac{1}{\sqrt{2N_{\text{at}}}} \left[\frac{1}{2^{N_{\text{at}}/2}} \left(\delta_{l,\uparrow}^{\pi} - \delta_{l,\downarrow}^{\pi} \right) \right] \right|^2 \quad (3.46a)$$

$$= \frac{1}{2^{N_{\text{at}}}} \frac{1}{N_{\text{at}}} \sum_{\pi} |n - N_{\text{at}} + n|^2 \quad (3.46b)$$

$$= \frac{1}{2^{N_{\text{at}}}} \frac{1}{N_{\text{at}}} \binom{N_{\text{at}}}{n} (2n - N_{\text{at}})^2. \quad (3.46c)$$

Using the same arguments as for the CSS (approximating the binomial by a Gaussian and then changing its domain) we find

$$p_1(\Delta N) = \frac{1}{\sqrt{2\pi N_{\text{at}}}} \exp\left(-\frac{\Delta N^2}{2N_{\text{at}}}\right) \frac{\Delta N^2}{N_{\text{at}}}, \quad (3.47)$$

which is plotted in fig. 3.6. Calculating the variance of $p_1(\Delta N)$ we find $3N_{\text{at}}$, in agreement with eq. (3.34). Moreover $p_1(\Delta N)$ is a non-Gaussian function.

A different derivation of the results for \tilde{p}_0 and \tilde{p}_1 could be made in the following way. Taking the energy of the lower state to be zero, we find that the system is described by the harmonic-oscillator Hamiltonian

$$\hat{\mathcal{H}}_{\text{atom}} = \hbar\omega_0 \left(\hat{J}_z + \frac{1}{2}N_{\text{at}} \right). \quad (3.48)$$

The AFS therefore have harmonic-oscillator wave-functions, which if squared gives the measurement outcomes, i.e., \tilde{p}_0 and \tilde{p}_1 .

3.7 SUMMARY

Starting from a presentation of the complex multilevel structure of Cs atoms focusing on two hyperfine ground states allowed us to treat the ensemble as being composed of spin-1/2 particles. We introduced angular-momentum operators and considered several states of interest. Starting from the CSS, we considered SSS and AFS. All of these are states that we will be dealing with extensively in the remaining parts of this thesis. We introduced a projector allowing us to calculate the expected probability density for measurement outcomes of the population difference, ΔN . It was shown that the collective single excitation state, $|1\rangle_A$, has a *fundamentally* different distribution in comparison to the squeezed and coherent state. We have throughout this chapter emphasized the connection between the description of light and atoms. In the limit of large ensembles, $N_{\text{at}} \gg 1$, where the Holstein-Primakoff approximation is valid, the two descriptions become identical. The reason for this is that the Holstein-Primakoff approximation allows us to treat only the tangential plane of the Bloch sphere, neglecting the curvature.

LIGHT-ATOM INTERACTION

Having described both the light and atomic system we are finally ready to consider one of the central parts of this thesis, their interactions. We will focus on two things: first, how the interaction gives rise to an attenuation and a phase shift of the light field and especially how this can be used to measure the atomic population difference. Second, we recast the interaction in terms of the pseudo-spin operators for light and atoms, connecting it to the description of the individual systems in chap. 2 and 3. We proceed as follows. Starting from the dipole interaction, we derive Maxwell-Bloch equations for the time evolution of the atomic and light operators. This leads to a reformulation of the interaction Hamiltonian in terms of atomic populations and photon numbers, both directly measurable quantities. We then consider the evolution of the light field in more detail and find expressions for the absorption and phase shift it experiences doing the interaction. All results are then generalized to the case of an atomic ensemble and the multilevel structure of Cs. This allows us to recast the effective Hamiltonian in terms of the pseudo-spin operators for light and atoms, a result that in sec. 5.1 will be used to show the QND character of the interaction.

4.1 MAXWELL-BLOCH EQUATIONS

We consider the interaction between a light field \hat{a}_L and an atomic ensemble. Taking the field to be uniform, it interacts with all atoms in the same manner. We can therefore consider the interaction between the field and a single atom, from which the total interaction can be found by summing up each independent contribution (fig. 4.1(a)). We describe a three-level atom with two long lived ground states $|\uparrow\rangle$ and $|\downarrow\rangle$ interacting with a single mode electromagnetic field \hat{a}_L (fig. 4.1(b)). The total Hamiltonian describing the combined system is

$$\hat{\mathcal{H}} = \hat{\mathcal{H}}_{\text{light}} + \hat{\mathcal{H}}_{\text{atom}} + \hat{\mathcal{H}}_{\text{int}}. \quad (4.1)$$

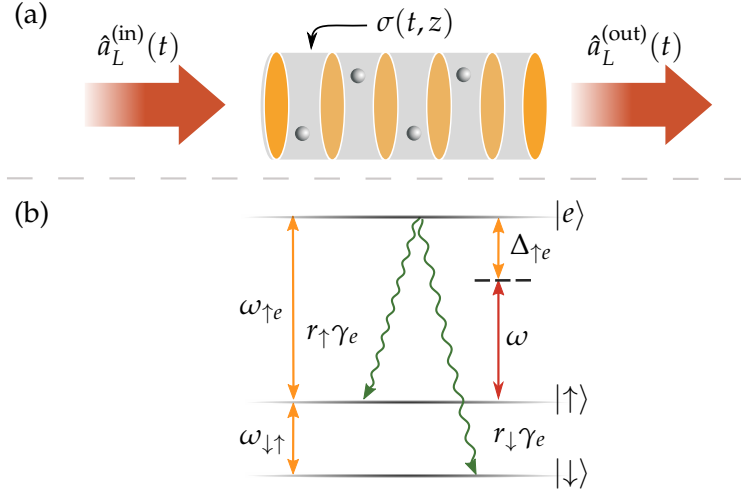


Figure 4.1.: Light-atom interaction: (a) Interaction between a light field \hat{a}_L and an ensemble of three-level atoms. Considering a uniform light field, we split the ensemble up into cross-sections $\sigma(z, t)$ for which we derive equations for the output field. The full interaction can then be found by summing up the individual contributions. (b) A single three-level atom with an excited state $|e\rangle$ which can decay to the long lived ground states with branching ratios r_{\uparrow} and r_{\downarrow} .

We consider a dipole interaction, make the dipole¹ and rotating-wave² approximations and set the energy zero point at the lower state, leading to

$$\hat{\mathcal{H}}_{\text{light}} = \hbar \omega \hat{a}_L^\dagger \hat{a}_L, \quad (4.2a)$$

$$\hat{\mathcal{H}}_{\text{atom}} = \hbar (\omega_{\uparrow} \hat{\sigma}_{\uparrow\uparrow} + \omega_e \hat{\sigma}_{ee}), \quad (4.2b)$$

$$\hat{\mathcal{H}}_{\text{int}} = \hbar (g_{\uparrow e}^* \hat{a}_L^\dagger \hat{\sigma}_{\uparrow e} + g_{\uparrow e} \hat{a}_L \hat{\sigma}_{e\uparrow}). \quad (4.2c)$$

¹ This means we neglect the spatial dependence of the oscillating field over the size of an atom. This is valid since the oscillating light field only changes on a length scale ~ 500 nm, much larger than the size of an atom ~ 0.1 nm.

² We only consider energy-preserving terms.

Here $\hat{\sigma}_{ij} \equiv |i\rangle\langle j|$ and the allowed values of i and j are \uparrow, \downarrow and e . The transition frequency to the excited state is $\omega_e \equiv \omega_{\downarrow\uparrow} + \omega_{\uparrow e}$, and g_{ij} is the coupling between light and the levels $|i\rangle$ and $|j\rangle$, given by

$$g_{ij} = i \frac{\omega_{ij}}{\sqrt{2\hbar V \omega \epsilon_0}} \boldsymbol{\epsilon} \cdot \hat{\mathbf{d}}_{ij} \quad (4.3)$$

in units of frequency. To calculate g_{ij} we therefore need the coupling dipole matrix-elements for a multilevel atom. Writing out these in terms of reduced dipole-matrix elements takes a fair amount of algebra and familiarity with addition of angular momenta,³ which we will refrain from here. A derivation can be found in for example [Loudon 2000; Sobelman 2006].

To derive Maxwell-Bloch equations we first use the Heisenberg equation of motion, giving the time derivative of an operator \hat{o} as

$$\dot{\hat{o}} \equiv \frac{d\hat{o}}{dt} = -\frac{i}{\hbar} [\hat{o}, \hat{\mathcal{H}}]. \quad (4.4)$$

From this we find the following set of equations:

$$\langle \hat{a}_L^{(\text{out})} \rangle = -i\omega \langle \hat{a}_L^{(\text{out})} \rangle - ig_{\uparrow e}^* \langle \hat{\sigma}_{\uparrow e} \rangle, \quad (4.5a)$$

$$\langle \hat{\sigma}_{\downarrow\downarrow} \rangle = r_{\downarrow} \gamma_e \langle \hat{\sigma}_{ee} \rangle, \quad (4.5b)$$

$$\langle \hat{\sigma}_{\uparrow\uparrow} \rangle = r_{\uparrow} \gamma_e \langle \hat{\sigma}_{ee} \rangle + ig_{\uparrow e} \langle \hat{a}_L \rangle \langle \hat{\sigma}_{e\uparrow} \rangle - ig_{\uparrow e}^* \langle \hat{a}_L^\dagger \rangle \langle \hat{\sigma}_{\uparrow e} \rangle, \quad (4.5c)$$

$$\langle \hat{\sigma}_{ee} \rangle = ig_{\uparrow e}^* \langle \hat{a}_L^\dagger \rangle \langle \hat{\sigma}_{\uparrow e} \rangle - ig_{\uparrow e} \langle \hat{a}_L \rangle \langle \hat{\sigma}_{e\uparrow} \rangle - \gamma_e \langle \hat{\sigma}_{ee} \rangle, \quad (4.5d)$$

$$\langle \hat{\sigma}_{\uparrow e} \rangle = -\gamma_e/2 \langle \hat{\sigma}_{\uparrow e} \rangle - i\omega_{\uparrow e} \langle \hat{\sigma}_{\uparrow e} \rangle - ig_{\uparrow e} \langle \hat{a}_L \rangle (\langle \hat{\sigma}_{\uparrow\uparrow} \rangle - \langle \hat{\sigma}_{ee} \rangle). \quad (4.5e)$$

Here we have introduced the inverse lifetime of the excited state γ_e and the branching ratios r_{\uparrow} and r_{\downarrow} , with $r_{\uparrow} + r_{\downarrow} = 1$. The decay between the two ground states have been neglected since it is slow compared to all other time scales in the problem. The excited state decay terms in red have been added by physical considerations. Formally this leads to eq. (4.5) only being valid for the mean values of the operators, which besides explaining the cumbersome notation means we cannot calculate correlations such as $\langle \hat{a}_L(t) \hat{a}_L(t + \tau) \rangle$ from eq. (4.5). This would require a derivation in terms of master equations and jump operators, which we withhold from here as the considered model will contain the relevant physics. For notional simplicity we will suppress the expectation values, as well as the explicit reference to the input or output part

³ The problem arises due to the fact that the “good” quantum number is given by the sum of electron spin, orbital angular momentum, and nuclear spin.

of the light field which should be clear from the context. We simplify the description by introducing *slowly* varying operators

$$\tilde{a}_L = \hat{a}_L e^{i\omega t}, \quad (4.6a)$$

$$\tilde{\sigma}_{\uparrow e} = \hat{\sigma}_{\uparrow e} e^{i\omega t}, \quad (4.6b)$$

corresponding to a coordinate frame rotating at the laser frequency ω .

Taking the time derivatives of the slowly varying operators and using eq. (4.5) we get a set of coupled differential equations

$$\dot{\tilde{a}}_L = -i g_{\uparrow e}^* \tilde{\sigma}_{\uparrow e}, \quad (4.7a)$$

$$\dot{\tilde{\sigma}}_{\uparrow e} = -(\gamma_e/2 - i\Delta_{\uparrow e}) \tilde{\sigma}_{\uparrow e} - i g_{\uparrow e} (\hat{\sigma}_{\uparrow\uparrow} - \hat{\sigma}_{ee}) \tilde{a}_L. \quad (4.7b)$$

Here $\Delta_{\uparrow e} \equiv \omega - \omega_{\uparrow e}$ is the detuning. Solving for the steady-state case, $\dot{\tilde{\sigma}}_{\uparrow e} = 0$, and assuming that $\hat{\sigma}_{ee} \ll 1$, we get

$$\tilde{\sigma}_{\uparrow e} = \frac{g_{\uparrow e} \tilde{a}_L}{\Delta_{\uparrow e} + i\gamma_e/2} (\hat{\sigma}_{\uparrow\uparrow} - \hat{\sigma}_{ee}). \quad (4.8)$$

Inserting this back into eq. (4.2c) allows us to rewrite $\hat{\mathcal{H}}_{\text{int}}$ as an effective Hamiltonian

$$\hat{\mathcal{H}}_{\text{eff}} = 2\hbar \frac{\hat{a}_L^\dagger \hat{a}_L |g_{\uparrow e}|^2 \Delta_{\uparrow e}}{\Delta_{\uparrow e}^2 + (\gamma_e/2)^2} (\hat{\sigma}_{\uparrow\uparrow} - \hat{\sigma}_{ee}). \quad (4.9)$$

The term originating from the commutator of \hat{a}_L and \hat{a}_L^\dagger has been neglected, since it is small compared to the photon number $\hat{a}_L^\dagger \hat{a}_L \gg 1$. The effective Hamiltonian (eq. (4.9)), only depends on the photon number and the population difference, both quantities that can be directly measured. Furthermore, the effective Hamiltonian only contains the light intensity $\hat{a}_L^\dagger \hat{a}_L$ and not the fields, which leads to two things. First, only the scalar polarizability is considered. Second, as the light polarization does not change the model does not include coherent transfer between different m_F states. With the effective description of the light atom interaction at our disposal, we now consider how the light field evolves as it passes through the atomic cloud.

4.1.1 Absorption and phase shift

We expect that the ensemble will act like a “piece of glass”, i.e., it will attenuate (absorb) and imprint a phase shift on the light. To derive the

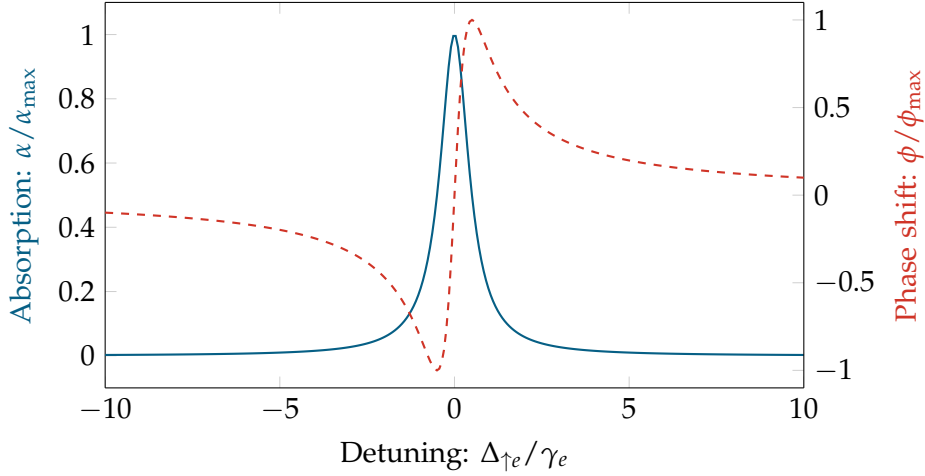


Figure 4.2.: As the light interacts with an atom, it is absorbed and shifted in phase. Both the absorption (blue) and phase shift (red) is plotted as a function of detuning. The absorption falls off as Δ^{-2} while as the phase shift goes as Δ^{-1} .

corresponding equations we insert eq. (4.8) into eq. (4.7a), which gives the differential equation

$$\dot{\tilde{a}}_L = -i \frac{|g_{\uparrow e}|^2 (\hat{\sigma}_{\uparrow\uparrow} - \hat{\sigma}_{ee})}{\Delta_{\uparrow e} + i\gamma_e/2} \tilde{a}_L. \quad (4.10)$$

Taking the population difference to be constant, we find

$$\hat{a}_L^{(\text{out})}(t) = \hat{a}_L^{(\text{in})}(t) \exp \left[-i |g_{\uparrow e}|^2 \frac{\Delta_{\uparrow e} - i\gamma_e/2}{\Delta_{\uparrow e}^2 + (\gamma_e/2)^2} (\hat{\sigma}_{\uparrow\uparrow} - \hat{\sigma}_{ee}) \frac{l_a}{c} \right], \quad (4.11a)$$

$$= \hat{a}_L^{(\text{in})}(t) \exp[-i\phi - \tilde{\alpha}], \quad (4.11b)$$

Here we have split the exponential into a real and imaginary part and introduced

$$\phi \equiv |g_{\uparrow e}|^2 \frac{\Delta_{\uparrow e}}{\Delta_{\uparrow e}^2 + (\gamma_e/2)^2} (\hat{\sigma}_{\uparrow\uparrow} - \hat{\sigma}_{ee}) \frac{l_a}{c}, \quad (4.12a)$$

$$\tilde{\alpha} \equiv |g_{\uparrow e}|^2 \frac{\gamma_e/2}{\Delta_{\uparrow e}^2 + (\gamma_e/2)^2} (\hat{\sigma}_{\uparrow\uparrow} - \hat{\sigma}_{ee}) \frac{l_a}{c}, \quad (4.12b)$$

together with the propagation time l_a/c . The interpretation of eq. (4.11) is as expected; light passes through the atomic cloud and experiences a phase shift of ϕ , while its intensity is decreased by $e^{-\alpha} = e^{-2\tilde{\alpha}}$. Both absorption and phase shift is dependent on the atomic populations. In the limit of large detuning the absorption falls off with Δ^{-2} , whereas the phase shift falls off with Δ^{-1} (fig. 4.2). The main insight of this is as follows. Consider the experimental relevant case where the total number of scattering events (Ramsey fringe reduction) is fixed. By detuning twice as much we can invest four times as many photons allowing to resolve phase shifts that are half as big ($\delta\phi \propto N_{\text{ph}}^{-1/2}$). As the phase shift imprinted by the atoms also drops by a factor of two no gain or loss in SNR is achieved. This shows that we can always detune our probe further and make the ensemble transparent such that the light will interact homogeneously with the atoms without loss of SNR.

4.2 STATE CHARACTERIZATION

Having described the interaction between light and a single atom, we consider how the effective Hamiltonian in eq. (4.9) can be used to characterize the spin state of an atomic ensemble. To stay close to the experimental setting, three complications needs to be taken into account. First, the full level structure of the Cs atoms should be considered. Second, we need to extend the description from a single atom to the whole ensemble. Third, we want to describe the interaction in terms of the pseudo-spin operators for light and atoms.

To extend the description to the multilevel structure of Cs, we note that which ground state the probe interacts with depends on the detuning Δ . Including interactions with the $|\downarrow\rangle$ state can then be done by adding an extra term to the Hamiltonian with the detuning $\Delta_{\downarrow e}$. Furthermore, there are many excited states, which we include by an appropriate summation. This leads to

$$\hat{\mathcal{H}}_{\text{eff}} = -\hbar \sum_{g=\uparrow e=2}^{\downarrow} \sum_{\ell=2}^5 \hat{a}_L^\dagger \hat{a}_L \mathcal{K}_{ge} (\hat{\sigma}_{gg} - \hat{\sigma}_{ee}), \quad (4.13a)$$

where we have introduced the state-dependent coupling

$$\mathcal{K}_{ge} = 2 |g_{ge}|^2 \frac{\Delta_{ge}}{\Delta_{ge}^2 + (\gamma_e/2)^2}. \quad (4.13b)$$

Having addressed the multilevel structure of the atom, we now expand the description to the whole ensemble. Taking the case of no atom-atom interactions and assuming that all atoms couple equally to the uniform light mode, corresponding to $\tilde{\alpha} \ll 1$, we can simply sum up the single atom contributions, which gives

$$\hat{\mathcal{H}}_{\text{eff}} = -\hbar \sum_{l=1}^{N_{\text{at}}} \sum_{g=\uparrow}^{\downarrow} \sum_{e=2}^5 \hat{a}_L^\dagger \hat{a}_L \mathcal{K}_{ge} \left(\hat{\sigma}_{gg}^{(l)} - \hat{\sigma}_{ee}^{(l)} \right). \quad (4.14)$$

The first summation is over the number of atoms, second over the two ground levels (for Cs $F = 3, 4$), and the third over all excited states. Generalizing the analysis in sec. 4.1.1 to take into account the multi-level structure and the whole ensemble we find the absorption and phase shift

$$\phi = \sum_{l=1}^{N_{\text{at}}} \sum_{g=\uparrow}^{\downarrow} \sum_{e=2}^5 |g_{ge}|^2 \frac{\Delta_{ge}}{\Delta_{ge}^2 + (\gamma_e/2)^2} \left(\sigma_{gg}^{(l)} - \sigma_{ee}^{(l)} \right) \frac{l_a}{c}, \quad (4.15a)$$

$$\tilde{\alpha} = \sum_{l=1}^{N_{\text{at}}} \sum_{g=\uparrow}^{\downarrow} \sum_{e=2}^5 |g_{ge}|^2 \frac{\gamma_e/2}{\Delta_{ge}^2 + (\gamma_e/2)^2} \left(\sigma_{gg}^{(l)} - \sigma_{ee}^{(l)} \right) \frac{l_a}{c}. \quad (4.15b)$$

To connect the interaction Hamiltonian to the pseudo-spin operators, we introduce an extra optical mode \hat{b}_L carrying half of the probe photons. From eqs. (2.23) and (3.3) we get the relations

$$\sum_{l=1}^{N_{\text{at}}} \hat{\sigma}_{\uparrow\uparrow}^{(l)} = \frac{\hat{N}_{\text{at}}}{2} + \hat{J}_z, \quad (4.16a)$$

$$\sum_{l=1}^{N_{\text{at}}} \hat{\sigma}_{\downarrow\downarrow}^{(l)} = \frac{\hat{N}_{\text{at}}}{2} - \hat{J}_z, \quad (4.16b)$$

$$\hat{a}_L^\dagger \hat{a}_L = \frac{\hat{N}_{\text{ph,tot}}}{2} + \hat{S}_z, \quad (4.16c)$$

where

$$\hat{N}_{\text{ph,tot}} \equiv \hat{N}_{\text{ph},a} + \hat{N}_{\text{ph},b} \quad (4.16d)$$

$$\hat{N}_{\text{at}} \equiv \hat{N}_{\text{at},\downarrow} + \hat{N}_{\text{at},\uparrow} \quad (4.16e)$$

is the total photon and atom number operators. Inserting this in eq. (4.14) and writing out the summation over the ground states we get

$$\hat{\mathcal{H}}_{\text{eff}} = -\hbar \left(\frac{\hat{N}_{\text{ph,tot}}}{2} + \hat{S}_z \right) \sum_{e=2}^5 \left[\mathcal{K}_{\downarrow e} \left(\frac{\hat{N}_{\text{at}_e}}{2} - \hat{J}_z \right) + \mathcal{K}_{\uparrow e} \left(\frac{\hat{N}_{\text{at}_e}}{2} + \hat{J}_z \right) \right]. \quad (4.17)$$

Here we have neglected the excited state population ($\hat{\sigma}_{ee} \approx 0$), which we had already assumed to be small. This corresponds to the experimentally relevant regime of large detunings where the saturation parameter $s = I/I_{\text{sat}}(\Delta) \ll 1$. The effective interaction has now been cast in a form depending on the number of photons, the number of atoms, and the z-component of the pseudo-spin vectors for light and atoms. As described in detail in chap. 3, the state of the atomic ensemble can be characterized by measuring \hat{J}_z or equivalently ΔN . Furthermore, we can measure \hat{S}_z using the MZI described in sec. 2.3. We can thus use the described light-atom interaction to infer the state of the atomic ensemble. Having a method to characterize the state of the atomic ensemble we now consider its interaction with a microwave source allowing for direct coherent manipulations of the pseudo-spin vector.

4.3 MICROWAVE INTERACTION

To directly address our two-level system of interest we use a microwave source, allowing us to perform arbitrary rotations of the Bloch vector $\hat{\mathbf{J}}$. The coherent interaction between the atoms and an oscillating magnetic field \mathbf{B} is given by

$$\hat{\mathcal{H}}_{\text{int}} = -\hat{\boldsymbol{\mu}} \cdot \hat{\mathbf{B}}, \quad (4.18)$$

where $\hat{\boldsymbol{\mu}}$ describes the magnetic dipole moment. To derive appropriate equations of motion one could perform a calculation similar to sec. 4.1. Instead of this, we start by simplifying the description substantially. The used microwave source has an output power on the order of 10 W and a frequency of $\omega_{\mu W} \approx \omega_{\text{clock}} \approx 9 \text{ GHz}$. We can thus neglect all its quantum features and treat it as a completely classical quantity. Furthermore, we apply a static magnetic field along the z-axis and choose this as the quantization axis. Taking a linearly polarized microwave

field⁴ the interaction becomes $-\mu_0 B_0$ and, as expected, we only drive $\Delta m_F = 0$ transitions. Solving for the time evolution of the pseudo-spin vector we find [Mandel et al. 1995, sec. 15.3]

$$\frac{d}{dt} \hat{\mathbf{J}} = \hat{\mathbf{J}} \times \boldsymbol{\Omega}, \quad (4.19a)$$

where

$$\boldsymbol{\Omega} = \begin{pmatrix} \text{Re}(\Omega_R) \\ \text{Im}(\Omega_R) \\ \Delta \end{pmatrix}. \quad (4.19b)$$

The Rabi frequency is given by $\Omega_R = 2 \langle \mu_0 B_0 \rangle / \hbar$ and Δ is the detuning. The interaction therefore leads to a rotation of the pseudo-spin vector, which we can be described by a rotation matrix $M_{\mu W}(\Omega t, \vartheta_R)$. The axis of rotation is defined by the phase between the microwave and the atoms, ϑ_R . The angle of rotation is set by the product of the interaction time t and the magnitude of the generalized Rabi frequency

$$\Omega = |\Omega| = \sqrt{\Delta^2 + |\Omega_R|^2}. \quad (4.20)$$

As the phase and duration of the applied field are easy to tune⁵ we can perform arbitrary rotations of $\hat{\mathbf{J}}$, giving the concept of π and $\pi/2$ pulses. To show the usefulness of this we consider the example of Ramsey spectroscopy.

The standard Ramsey sequence and corresponding Bloch spheres are shown in fig. 4.3. Starting with $\hat{\mathbf{J}}$ pointing towards the south pole of the Bloch sphere a $\pi/2$ pulse rotates $\hat{\mathbf{J}}$ into the equatorial plane, such that it points along the y -axis. We then let the atoms evolve for a time τ during which $\hat{\mathbf{J}}$ is rotated by an angle $\phi = \Delta\tau$. Since the rotation angle directly dependent on the detuning, it can be used to measure the atomic-transition frequency. To convert it into the measurable population difference, a second $\pi/2$ pulse rotates $\hat{\mathbf{J}}$ around the x -axis. Going through the relevant equations for the rotations we find⁶ that $\langle \hat{J}_z \rangle \propto \cos(\Delta\tau)$. In the experiment we will often use a slightly different sequence, which gives the same information. Starting with the Bloch

⁴ In the experiment we do not control the microwave polarization.

⁵ The main challenge is to make these pulses as reproducible and low-noise as possible, such that they do not wash away the atomic projection noise.

⁶ We have neglected the reduction of $|\hat{\mathbf{J}}|$ due to dephasing, which could simply be incorporated as $\exp(-\tau/T_2)$ where T_2 is the relevant dephasing time.

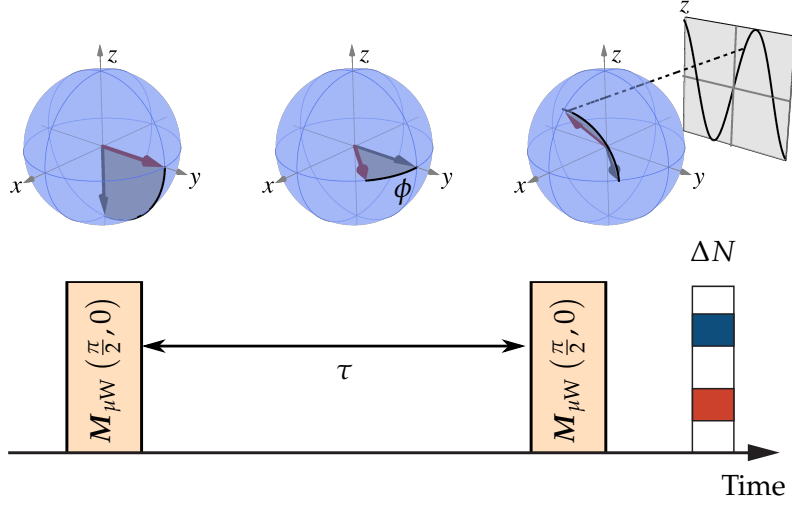


Figure 4.3.: Ramsey-spectroscopy sequence. A $\pi/2$ pulse rotates $\hat{\mathbf{J}}$ into the equatorial plane. Letting the system evolve freely the Bloch vector precesses and rotates by an angle $\phi = \tau\Delta$. To measure this rotation angle, a second $\pi/2$ pulse is made and a measurement of $\hat{J}_z \propto \Delta N$ is performed. Inset: population difference as a function of waiting time τ .

vector $\hat{\mathbf{J}}^{(\text{in})}$ aligned along the south pole the following pulse sequence is used

$$\hat{\mathbf{J}}^{(\text{out})} = M_{\mu W} \left(\frac{\pi}{2}, \vartheta_R \right) M_{\mu W} (0, \vartheta) M_{\mu W} \left(\frac{\pi}{2}, 0 \right) \hat{\mathbf{J}}^{(\text{in})}, \quad (4.21)$$

where $M_{\mu W} (0, \vartheta)$ corresponds to a free evolution. Comparing the measurement of $\hat{J}_z^{(\text{out})}$ for $\vartheta_R = \pi/2$ and $\vartheta_R = 3\pi/2$ we should for $\Delta = 0$ have as many atoms in the upper as the lower state, i.e., $\hat{J}_z^{(\text{out})} = 0$. In this way we can optimize the detuning, and from this find the transition frequency. The Ramsey sequence underpins almost all precision measurement made with atomic ensembles and has resulted in the most precise measurements ever made [Hinkley et al. 2013], but will in this work mainly be used for calibration purposes.

4.4 SUMMARY

Starting from the interaction of a single atom with an optical field, we derived Maxwell-Bloch equations for the light and atomic operators. This led to a description of the interactions in terms of an effective Hamiltonian only dependent on measurable quantities. Taking the field to interact uniformly with all atoms, the description could be extended to the whole ensemble by summing up the single-atom contributions. This allowed us to cast the interaction in terms of pseudo-spin operators. From the explicit coupling between the z-components of these we discussed how the interaction allows for the characterization of atomic spin states (sec. 3.6). Last, we introduced a method to directly manipulate the atoms within the two hyperfine ground states, using a microwave source.

EXPERIMENTAL CONSIDERATIONS

In the last chapters we studied light, atoms and their interactions. With \hat{J}_z entering directly in the effective Hamiltonian, we showed how the interaction allows for the characterization of atomic states by measuring the population difference. In this chapter we take the description one step further and consider how interactions between the systems allow us to *create* the atomic states discussed in chap. 3. We first consider the measurement-based generation of a [SSS](#). Using input-output relations we show that a [QND](#) interaction leads to a conditioned noise reduction, i.e., squeezing. To relate this to the experiment, we find that with a carefully chosen set of parameters we realize such a [QND](#) interaction. After this we consider the other state of interest, the collective-single-excitation state. Using the first step of the [DLCZ](#) protocol [Duan et al. 2001] this state can be probabilistically generated through the detection of a heralding photon. To show this we introduce the parametric-gain Hamiltonian and consider several of its key properties.

5.1 SPIN-SQUEEZED STATE

The [SSS](#) are defined as states with a variance below the [SQL](#) in a direction orthogonal to the mean spin direction (sec. 3.4). In the original proposal by Kitagawa et al. [1993] these states were generated through nonlinear interaction of the form $\hat{\mathcal{H}}_{\text{int}} \propto \hat{J}_z^2$. We will take a different approach based on a [QND](#) measurement. The idea is simple: if we perform a measurement on a system, *without* destroying it, we can predict the outcome of a subsequent measurement with improved precision. To understand how this works we first need to grasp the concept and idea behind [QND](#) measurements.

5.1.1 *Quantum-nondemolition measurement*

We start by considering a general description of a quantum mechanical measurement. In a measurement a system, \mathcal{S} , and a meter, \mathcal{M} , interact

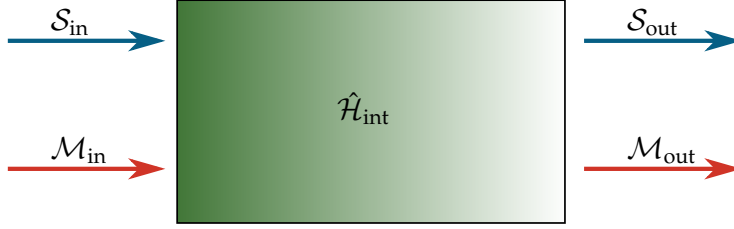


Figure 5.1.: A quantum measurement can be described by a system, \mathcal{S} , and a meter, \mathcal{M} , interaction through $\hat{\mathcal{H}}_{\text{int}}$. During the interaction they become entangled, and by projective measurement of the meter we obtain information about the system.

via $\hat{\mathcal{H}}_{\text{int}}$ and become entangled (fig. 5.1). A projective measurement on the meter then gives information about the state of the system. In general such an interaction changes the system. As the name suggests a **QND** measurement is the opposite: if an observable \hat{o} is measured at times t and t' and the outcomes are identical, \hat{o} is a **QND** observable. The simplest example of such an observable is a constant of motion

$$\frac{d}{dt}\hat{o}(t) = -\frac{i}{\hbar} [\hat{o}(t), \hat{\mathcal{H}}(t)] = 0. \quad (5.1)$$

This condition can be relaxed [Poizat et al. 1994] to be

$$[\hat{o}(t), \hat{\mathcal{H}}_{\text{int}}(t)] = 0. \quad (5.2)$$

Having determined if an observable is of the **QND** type or not, we now consider how a corresponding measurement can be quantified. Following [Walls et al. 2008, chap. 14] we introduce three measures:¹

EFFICIENCY: Correlation between the meter after the interaction (\mathcal{M}_{out}) and system before the interaction (\mathcal{S}_{in}). This criterion gives the measurement efficiency, and is directly related to the state characterization as described in sec. 4.2.

NON-DESTRUCTION: Correlations between the system before (\mathcal{S}_{in}) and after (\mathcal{S}_{out}) the interaction. It is related to the commutator in eq. (5.2). For the **SSS** this loss of correlation, corresponds to a reduction of the Bloch-vector length (loss of Ramsey fringe contrast) due to the interaction.

¹ A comparable description of quantum measurements of spin systems based on the concept of transfer coefficients can be found in [Mitchell et al. 2012; Sewell et al. 2013].

STATE PREPARATION: Correlations between meter (\mathcal{M}_{out}) and system *after* the interaction (\mathcal{S}_{out}). This is the central criterion for squeezing as it is directly linked to the conditioned noise reduction (information gain), and thus the amount of squeezing.

Considering the case of spectroscopically relevant squeezing, a combination of the last two criteria sets the limit on the amount of squeezing. A large noise reduction requires a high degree of state preparation, i.e., a strong measurement. On the other hand, using a strong measurement leads to a large degree of state destruction. Therefore, a trade-off will have to be made between the information gain and the state destruction. This is the essence of measurement-based squeezing and to quantify it we start by considering a generic QND interaction.

5.1.2 QND measurements and squeezing

To show how QND measurements allow for the creation of SSSs we consider the canonical QND interaction Hamiltonian

$$\hat{\mathcal{H}}_{\text{QND}} = \hbar \mathcal{K} \hat{S}_z \hat{J}_z, \quad (5.3)$$

where \mathcal{K} denotes the coupling between the two systems. Using Heisenberg's equation of motion — see eq. (4.4) — we construct input-output relations for the light and atomic pseudo-spin vectors:

$$\hat{S}_x^{(\text{out})} = \hat{S}_x^{(\text{in})} - \mathcal{K} \hat{S}_y^{(\text{in})} \hat{J}_z^{(\text{in})}, \quad \hat{J}_x^{(\text{out})} = \hat{J}_x^{(\text{in})} - \mathcal{K} \hat{J}_y^{(\text{in})} \hat{S}_z^{(\text{in})}, \quad (5.4a)$$

$$\hat{S}_y^{(\text{out})} = \hat{S}_y^{(\text{in})} + \mathcal{K} \hat{S}_x^{(\text{in})} \hat{J}_z^{(\text{in})}, \quad \hat{J}_y^{(\text{out})} = \hat{J}_y^{(\text{in})} + \mathcal{K} \hat{J}_x^{(\text{in})} \hat{S}_z^{(\text{in})}, \quad (5.4b)$$

$$\hat{S}_z^{(\text{out})} = \hat{S}_z^{(\text{in})}, \quad \hat{J}_z^{(\text{out})} = \hat{J}_z^{(\text{in})}. \quad (5.4c)$$

As expected, since $[\hat{J}_z, \hat{\mathcal{H}}_{\text{QND}}] = [\hat{S}_z, \hat{\mathcal{H}}_{\text{QND}}] = 0$, the two z -components are not changed by the interaction — they are QND observables. Taking the atomic and light pseudo-spin vectors to be aligned along the x -axis, we consider the fluctuations in the two orthogonal directions. To gain

information about the atomic system we measure² $\langle \hat{S}_y^{(\text{out})} \rangle = y_s$, and *conditioned* on this outcome we get [Hammerer et al. 2010, sec. IV. A.]

$$\langle \hat{J}_z^{(\text{out})} \rangle \Big|_{y_s} = \langle \hat{J}_z^{(\text{out})} \rangle - \frac{\langle \hat{J}_z^{(\text{out})} \hat{S}_y^{(\text{out})} \rangle}{\langle (\hat{S}_y^{(\text{out})})^2 \rangle} y_s, \quad (5.5a)$$

$$\text{var} \left(\hat{J}_z^{(\text{out})} \right) \Big|_{y_s} = \text{var} \left(\hat{J}_z^{(\text{out})} \right) - \frac{\langle \hat{J}_z^{(\text{out})} \hat{S}_y^{(\text{out})} \rangle^2}{\langle (\hat{S}_y^{(\text{out})})^2 \rangle}. \quad (5.5b)$$

Here we have taken \hat{J}_z and \hat{S}_y to be Gaussian-distributed random variables. This is valid as $\hat{S}_y^{(\text{in})}$ and $\hat{J}_z^{(\text{in})}$ are both Gaussian noise processes (shot noise and projection noise), and that $\hat{\mathcal{H}}_{\text{int}}$ is linear. Taking the limit where $\hat{J}_y^{(\text{out})}$ and $\hat{S}_y^{(\text{out})}$ are uncorrelated we see that a measurement of $\hat{S}_y^{(\text{out})}$ do not affect $\hat{J}_y^{(\text{out})}$, as expected from eq. (5.4b). From eqs. (2.23) and (5.4) we find that

$$\langle (\hat{S}_y^{(\text{out})})^2 \rangle = (1 + \kappa^2) \frac{N_{\text{ph}}}{4}, \quad (5.6)$$

where $\kappa^2 = \mathcal{K}^2 N_{\text{ph}} N_{\text{at}} / 4$. Inserting this back into eq. (5.5) gives

$$\langle \hat{J}_z^{(\text{out})} \rangle \Big|_{y_s} = \langle \hat{J}_z^{(\text{in})} \rangle - \frac{\kappa}{1 + \kappa^2} \sqrt{\frac{N_{\text{at}}}{N_{\text{ph}}}} y_s \quad (5.7a)$$

$$\text{var} \left(\hat{J}_z^{(\text{out})} \right) \Big|_{y_s} = \frac{1}{1 + \kappa^2} \text{var} \left(\hat{J}_z^{(\text{in})} \right). \quad (5.7b)$$

This eq. shows that the noise of \hat{J}_z has been reduced by a factor $(1 + \kappa^2)^{-1}$. As we are starting from a **CSS** which minimizes Heisenbergs uncertainty relation the variance $\text{var} \left(\hat{J}_z^{(\text{out})} \right)$ is reduced below the **SQL**, i.e., the ensemble is in a **SSS**.

To quantify the amount of squeezing, we relate the coupling constant \mathcal{K} to the resonant optical depth and use the Wineland criterion (eq. (3.20a)) and find

$$\xi_{\text{Wineland}} = \frac{1}{\exp(-\eta N_{\text{ph}})} \frac{1}{1 + \alpha_0 \eta N_{\text{ph}} / 4}, \quad (5.8)$$

² Recall that the last beam-splitter in the **MZI** maps the phase in the equatorial plane (\hat{S}_y) onto \hat{S}_z (sec. 2.3).

see app. E.2 for the full derivation. Here α_0 is the on-resonant optical depth, and η is the number of scattering events per photon, such that $\exp(-\eta N_{\text{ph}})$ gives the coherence. From eq. (5.8) it is clear that it is desirable to have a high optical depth and at the same time a low decoherence η . The photon number enters both in the loss of coherence (the more photons the worse) and in the noise reduction (the more photons the better). Therefore, the used photon number has to be carefully chosen to give enough information while at the same time not destroying the coherence.

Having seen that a QND measurement allows for the creation of SSSs we now want to relate the studied $\hat{\mathcal{H}}_{\text{QND}}$ to the interactions described in sec. 4.2. Recalling the effective Hamiltonian given in eq. (4.17), we modify it to take into account the free propagation in the MZI (sec. 2.3) and find

$$\hat{\mathcal{H}}_{\text{eff}} = -\hbar \left(\frac{\hat{N}_{\text{ph}}}{2} + \hat{S}_z e^{ik\Delta l} \right) \sum_{e=2}^5 \left[\mathcal{K}_{\downarrow e} \left(\frac{\hat{N}_{\text{at}}}{2} - \hat{J}_z \right) + \mathcal{K}_{\uparrow e} \left(\frac{\hat{N}_{\text{at}}}{2} + \hat{J}_z \right) \right]. \quad (5.9)$$

In the experiment we will use two lasers, one probing atoms in $|\uparrow\rangle$ and one probing atoms in $|\downarrow\rangle$ (referred to as the orange and purple probes respectively). The frequency difference of the lasers is on the order of the hyperfine splitting and therefore each probe only interacts with atoms in one of the two states leading to

$$\hat{\mathcal{H}}^{(o)} = -\hbar \mathcal{K}_{\uparrow e} \left(\frac{\hat{N}_{\text{ph}}^{(o)}}{2} + \hat{S}_z^{(o)} e^{ik_o \Delta l} \right) \left(\frac{\hat{N}_{\text{at}}}{2} + \hat{J}_z \right), \quad (5.10a)$$

$$\hat{\mathcal{H}}^{(p)} = -\hbar \mathcal{K}_{\downarrow e} \left(\frac{\hat{N}_{\text{ph}}^{(p)}}{2} + \hat{S}_z^{(p)} e^{ik_p \Delta l} \right) \left(\frac{\hat{N}_{\text{at}}}{2} - \hat{J}_z \right). \quad (5.10b)$$

Choosing the detuning such that the coupling constants are identical, $\mathcal{K} = \mathcal{K}_{\uparrow e} = \mathcal{K}_{\downarrow e}$, and the path-length difference such that the probes are out of phase, $\Delta l = \pi / (k_o - k_p)$, we find the total Hamiltonian

$$\begin{aligned} \hat{\mathcal{H}} = -\hbar \mathcal{K} \left[\hat{J}_z \left(\hat{S}_z^{(o)} + \hat{S}_z^{(p)} \right) + \hat{J}_z \left(\hat{N}_{\text{ph}}^{(o)} - \hat{N}_{\text{ph}}^{(p)} \right) \right. \\ \left. + \frac{\hat{N}_{\text{at}}}{2} \left(\hat{S}_z^{(o)} - \hat{S}_z^{(p)} \right) + \frac{\hat{N}_{\text{at}}}{4} \left(\hat{N}_{\text{ph}}^{(p)} + \hat{N}_{\text{ph}}^{(o)} \right) \right]. \quad (5.11) \end{aligned}$$

We identify the first term with the desired QND interaction, coupling \hat{J}_z to the total light operator $\hat{S}_z^{(\text{tot})} = \hat{S}_z^{(o)} + \hat{S}_z^{(p)}$. The second term is the probe-induced ac Stark shift, corresponding to the “back-action” of light on the atomic system. Taking the probe powers to be equal, this is on average zero, but will however have non-zero fluctuations due to the shot noise of the probes. The third term is the mean phase shift experienced by the probes due to the interaction with half of the atoms in the ensemble. Considering a CSS in the equatorial plane the average of this term is zero. The fourth, and last term, is the common-mode light shift which simply gives an energy offset that does not affect the dynamics. This leaves us with an interaction Hamiltonian

$$\hat{\mathcal{H}}_{\text{int}} = -\hbar\mathcal{K}\hat{J}_z\hat{S}_z^{(\text{tot})} \quad (5.12)$$

which is in the form of the canonical QND Hamiltonian (eq. (5.3)). Thus, with appropriate choices of probe powers and alignment of the MZI the considered interaction is of the QND type, which should allow for the creation of SSS. To actually observe a SSS we require a few more things. First, we should be able to resolve the atomic projection noise which is on the order of $1/\sqrt{N_{\text{at}}} \sim 1 \text{ mrad}$ for $N_{\text{at}} \sim 10^5$. Second, as we are dealing with variances, a large amount of realizations are required, meaning that a high degree of experimental stability and repeatability is needed.

5.2 COLLECTIVE-SINGLE-EXCITATION STATE

To create the collective-single-excitation state, introduced in sec. 3.5 we follow the first part of the DLCZ protocol [Duan et al. 2001], schematically shown in fig. 5.2. Neglecting the ac Stark shift of the ground state, the Hamiltonian describing the interaction is [Hammerer et al. 2010, eq. (33)]

$$\hat{\mathcal{H}}_G = \chi^* \hat{a}_A^\dagger \hat{a}_L^\dagger + \chi \hat{a}_A \hat{a}_L, \quad (5.13a)$$

where

$$\chi \equiv \frac{g(N_{\text{at}})\Omega_R}{2\Delta}. \quad (5.13b)$$

Here Δ denotes the detuning, Ω_R the Rabi frequency, and $g(N_{\text{at}}) = \sqrt{2\pi\omega N_{\text{at}}/c\epsilon} \cdot \mathbf{d}$ the light-atom coupling. This Hamiltonian is known

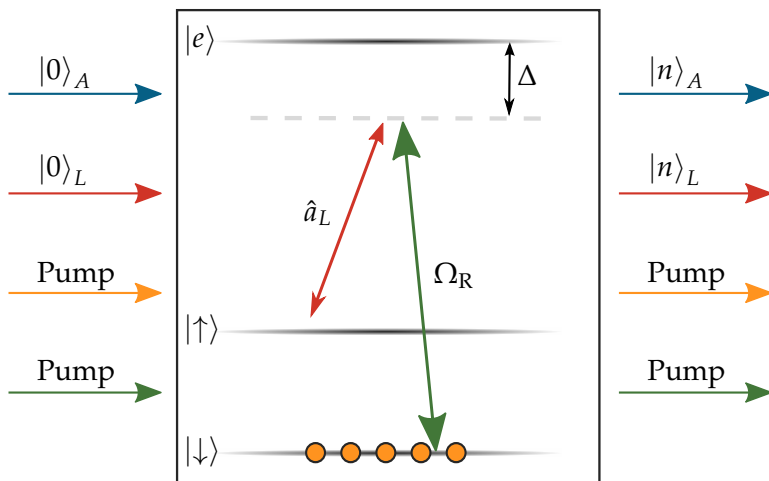


Figure 5.2.: The driven Raman transition can be described by the two-mode squeezing Hamiltonian in eq. (5.13a) and is therefore equivalent to a parametric amplifier. The presence of a single photon in the mode \hat{a}_L signals that a single *unknown* atom has been transferred to the state $|\uparrow\rangle$.

as the parametric-gain³ or two-mode-squeezing Hamiltonian. The light and atomic operators enter *symmetrically* in the Hamiltonian, which means that excitations will be created in pairs. To show this we consider the unitary time evolution of this system,

$$\hat{S}_G(\zeta) = \exp\left(\zeta^* \hat{a}_L^\dagger \hat{a}_A^\dagger + \zeta \hat{a}_L \hat{a}_A\right), \quad (5.14a)$$

where

$$\zeta = -\frac{i\chi}{\hbar} t. \quad (5.14b)$$

After the interaction the state is

$$|\zeta\rangle = \hat{S}_G(\zeta) |0, 0\rangle \quad (5.15)$$

where the first entry of the ket describes the light mode and the second the atomic mode. Expanding $|\zeta\rangle$ onto the Fock basis and using the transformation rule in eq. (A.3) we find

$$|\zeta\rangle = \frac{1}{\cosh(\zeta)} \sum_n (-\tanh(\zeta))^n |n, n\rangle, \quad (5.16)$$

³ Getting its name from the process of spontaneous parametric down conversion.

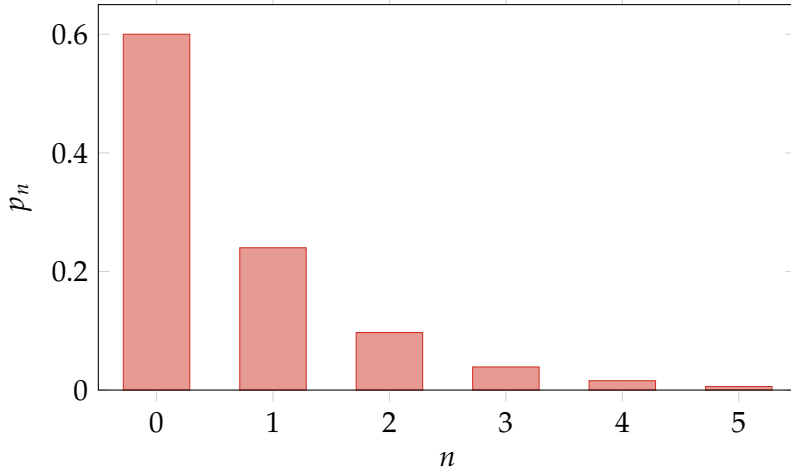


Figure 5.3.: The probability p_n to have n collective excitations in the ensemble for $\zeta = 0.75$, corresponding to a mean excitation number of 0.68.

with the detailed derivation given in app. A.1.1 or [Gerry et al. 2005, sec. 7.7]. This directly shows that only pair creation is allowed — a single photon in the mode \hat{a}_L signals that the ensemble carries a collective spin excitation. To find the probability of having a single atomic excitation we trace out the light system and obtain the reduced density matrix

$$\hat{\rho}_A = \sum_{n=0}^{\infty} p_n |n\rangle\langle n|, \quad (5.17a)$$

where

$$p_n = \frac{\tanh^{2n}(\zeta)}{\cosh^2(\zeta)} \quad (5.17b)$$

is a thermal distribution (fig. 5.3).

We now consider the conditioned generation using a single-photon-counting module (SPCM). Due to dead time after a click an SPCM can not distinguish if we detected one or two photons. It is therefore desirable to have the excitation probability, ζ small to avoid contributions from higher order excitations. On the other hand, this gives a low generation rate. In the experiment we therefore have to make a trade-off between high purity and high generation rate. Furthermore, considering the full level structure the excited atom can decay through many

different channels. As it is only one particular photon that generates the desired state, we must filter out photons from other decays. Last, for the excitation to be collective all atoms should interact equally with the light. We therefore want the optical depth on the excitation transition to be smaller than one.

5.3 SUMMARY

In this chapter we have outlined how the *SSS* and the collective-single-excitation state can be generated. We first considered a generic *QND* Hamiltonian and described how this allow for measurement based squeezing. To link this to the experiment we showed that for a careful choice of parameters, the light-atom interaction reduces to the *QND* Hamiltonian. Most notably, by balancing the probe powers we are first order insensitive to the ac Stark shift corresponding to the measurement back-action. To generate the collective single excitation state, we considered the parametric-gain Hamiltonian. We showed how this leads to the *pairwise* generation of excitations and heralding photons. This means that the detection of a single photon signals that the ensemble carries the desired collective excitation.

Part II

EXPERIMENT

In this part we start by considering the experimental implementation of the theoretical ideas presented in the last part. This is followed by a presentation of the three main results of the thesis. First, the creation of a spin-squeezed state (SSS) with a spectroscopically relevant noise reduction of -1.7 dB. Second, we show the generation of a collective-single-excitation state characterized using atomic homodyne tomography. Third, we consider the nanofiber based light-atom interface and show the detection and creation of an ensemble with a sub-Poissonian atom distribution.

EXPERIMENTAL TECHNIQUES

Due to large efforts of the previous generation of experimentalists, I was fortunate enough to arrive at a (somewhat) working setup. This means that there, naturally, will be some overlap in this chapter with [Windpassinger 2008, chap. 3; Oblak 2010, chap. 8 and 9]. However, having worked with the main experiment for the last four years — every optical component has been touched, sometimes for the better and sometimes for the worse, circuits designed, and control systems optimized to accommodate the constantly changing experimental demands. The experimental setup, and the structure of this chapter, can be divided into four sections; atom trapping, state preparation, state characterization, and the control and acquisition system making everything work together. Starting by loading atoms into a MOT they are transferred into a FORT where the experiments take place. Using optical pumping, microwave, and purification pulses we create a pure ensemble with all atoms in the $|\downarrow\rangle \equiv |F = 3, m_F = 0\rangle$ state. We then (try to) create and characterize the quantum states of interest — the spin-squeezed state (SSS) (chap. 7) and collective-single-excitation state (chap. 8). This brings us to the central part of the chapter and experiment — the measurement of the atomic population difference ΔN . The implementation of the two-color probing method (sec. 5.1) is described and a suppression of classical noise of tens of dB is shown. Finally, the experimental control and data acquisition are discussed.

6.1 ATOM TRAPPING

It is clear that before any meaningful interaction or measurement of the ensemble can be made the atoms needs to be localized in space.¹ The methods for atom trapping and cooling described in this section are standard techniques and implementations can be found in countless cold atom laboratories. We will therefore try and keep it short and skip

¹ The situation is much the same as if you are to measure the height of a person. Imagine the trouble it would be if the person were running around all over the place.

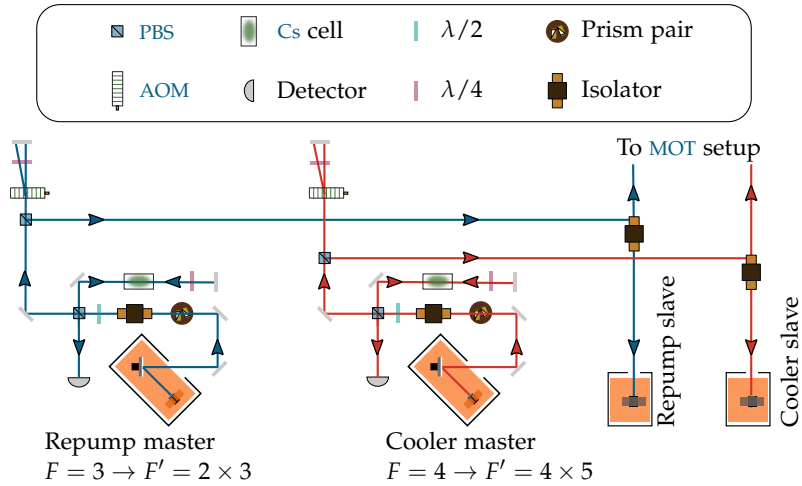


Figure 6.1.: Optical layout to lock the master and slave for the MOT repumper (blue) and cooler (red). The master lasers are locked via absorption spectroscopy and the slaves via injection locking.

some of the underlying ideas and focus on how they are implemented in our laboratory.

6.1.1 Magneto-optical trap

The atoms are situated inside a glass cell² connected to a vacuum system, where an ion pump keeps a pressure of $\approx 10^{-9}$ mbar. The only requirement is that we can create a MOT and the precise pressure is therefore not important.³ For this we use a standard six beam configuration together with a set of anti-Helmholtz coils.⁴ Three sets of compensation coils allow to nullify any static background magnetic field. To generate the cooling ($F = 4 \rightarrow F' = 4$) and re-pumping

² Starna cell of dimensions 120 mm \times 48 mm \times 48 mm, with anti-reflection coating on the outside.

³ The higher the pressure, the more likely trapped atoms are to collide with other atoms, therefore this could limit the coherence times of the trapped ensemble. Furthermore, it could give rise to pressure shifts of the atomic lines. Both effects only play a negligible role in this work.

⁴ Radius of 5 cm and 38 windings.

($F = 3 \rightarrow F' = 4$) light we use two separate laser systems in a master-slave configuration.

The two master lasers are home-built external cavity diode lasers (ECDLs) in a Littrow configuration (see fig. 6.1). We use 100 mW diodes from Axcel photonics⁵ and operate with about 20 mW of output power, and a linewidth of 500 kHz, measured over a few seconds [Windpassinger 2008, sec. 3.1]. To stabilize the laser frequency to the atomic line we use a Doppler free absorption spectroscopy setup combined with a Pound–Drever–Hall (PDH)-like method. By directly modulating the laser current we create sidebands⁶ on the light. After passing through the spectroscopy setup the light is detected and demodulated at the side-band frequency to obtain the required error-signal. The cooler is locked to the $F = 4 \rightarrow F' = 3 \times 4$ crossover and the repumper to the $F = 3 \rightarrow F' = 2 \times 3$ crossover. A double pass acousto optical modulator (AOM) setup allows us to tune the frequency of the master lasers before they are injected into the slaves (see fig. 6.1).

The slave lasers are home-built free running diode⁷ lasers, with an output of ≈ 100 mW stabilized via injection locking (see fig. 6.1).⁸ To have power and switching control we use a single pass AOM in each beam. The two laser beams are then combined on a polarizing beam-splitter (PBS) before they are split and coupled into six fibers which take them to the vacuum setup. The full optical layout is shown in fig. B.1. At the fiber outputs the beams are expanded to a diameter of ≈ 3 mm and a PBS and a $\lambda/4$ waveplate ensures that they are circularly polarized before they are overlapped with the magnetic gradient field (see fig. 6.6). To load atoms into the MOT from the vapor pressure, made by a set of SAES getter sources,⁹ the cooler and repumper are detuned by $\approx -2\gamma_e$ from their respective transitions and a gradient field of $\approx 12 \text{ G cm}^{-1}$ is applied. Atoms are loaded for ≈ 2000 ms which is followed by a phase of sub-Doppler cooling lasting ≈ 200 ms. This is done by further detuning the repumping and cooling lasers, while their powers are decreased. In this way we create an atomic cloud of

⁵ Type: M9-852-0100-S30.

⁶ Cooler at 20 MHz and repumper at 4 MHz .

⁷ Type: Eagleyard EYP-RWE-0850.

⁸ The slaves stay injected for a scan range of $\pm 6\gamma_e$ of the master lasers.

⁹ Since [Windpassinger 2008; Oblak 2010] a new pair of getters have been installed as we anyway had to break the vacuum, due to a power failure at the institute.

about 10^8 atoms with a diameter of a few mm and a temperature¹⁰ of hundreds of μK . From this dense, cold, and spatially concentrated cloud we can load the far-off-resonant dipole trap (FORT).

6.1.2 Far-off-resonant trap

A FORT is based on the ac Stark shift atoms experience in a light field. For a red-detuned trapping beam the ground state is shifted down in energy by an amount proportional to the light intensity.¹¹ Due to the Gaussian intensity profile of the beam, atoms are trapped at the beam center. A detailed description of the theory and experimental considerations can be found in [Grimm et al. 2000]. During the MOT loading the strong FORT laser is on, such that when the sub-Doppler cooling is over and the MOT beams are turned off, the remaining atoms are trapped in the conservative potential of the FORT.

Since the work of [Windpassinger 2008; Oblak 2010] and half a year before my arrival, the trap laser was changed from a troublesome Veradisk laser [Oblak 2010, sec. 9.1.2]. We now use a $\lambda_{\text{trap}} = 1064\text{ nm}$ fiber-coupled butterfly diode from EM4¹² outputting 200 mW which is sent to a Nufern fiber amplifier¹³ with 10 W of output power. The beam passes through an AOM for on/off switching and is overlapped with the probe using dichroic mirrors before it is focused down to a waist of $w_0^{\text{trap}} \approx 40\ \mu\text{m}$ (see fig. 6.6). The dipole trap half-lifetime is estimated daily and found to be $\tau_{1/2} \approx 250\text{ ms}$, comparable to the results in [Oblak 2010, sec. 9.2.1]. The calculated trap depth is 280 μK and the corresponding trap frequencies are $\omega_{\perp} \approx 2\pi \times 800\text{ Hz}$ in the transverse beam direction and $\omega_{\parallel} \approx 2 \times 5\text{ Hz}$ in the axial direction. As we were able to observe projection noise limited operation of the whole setup with the new laser; a systematic investigation of the trapped sample where not performed. We do, however, consider the two most used diagnostic tools to characterize the atomic sample.

¹⁰ We do not know the exact temperature of either the MOT, molasses or the FORT trapped atomic ensemble.

¹¹ Following chap. 4 this could be derived by diagonalizing the effective interaction Hamiltonian, finding the new energy eigenstates of the combined light-atom system. The reason it all works is again that the number of scattering events falls off with Δ^{-2} whereas the energy shifts scales as Δ^{-1} .

¹² Part number: EM509.

¹³ Part number: PSFA-1064-50-10W. The amplifier broke in the summer of 2011, only a few weeks after the warranty ran out, giving a few months of experimental downtime.

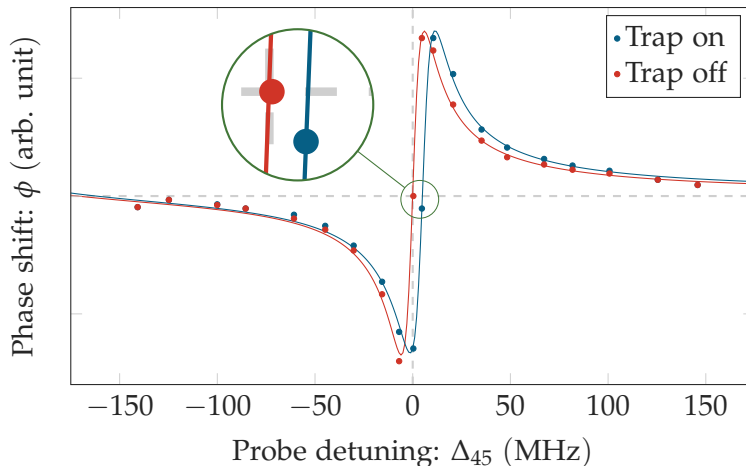


Figure 6.2.: Measured atomic-induced phase shift as a function of detuning from the $F = 4 \rightarrow F' = 5$ transition, Δ_{45} , with and without the FORT. To fit the data, a model taking into account the full atomic level structure, is used. A shift of 5 MHz is observed when the trap is turned on.

TRAP LIGHT SHIFT To estimate the light shift from the FORT, we measure the atomic induced phase shift, with and without the FORT, using a single-color probe on the $F = 4 \rightarrow F' = 5$ transition. Starting with all atoms isotropically distributed in the $F = 4$ hyperfine manifold the phase shift is measured¹⁴ as a function of probe detuning Δ_{45} (see fig. 6.2). To model the data we take the full atomic level structure into account (see eq. (4.15a)), with an initial population distributed evenly in the $F = 4$ manifold.¹⁵ We find that the shift of the transition due to the dipole trap is 5 MHz.

OTHER SHIFTS The other characterization experiment is a measurement of the transition frequency between $|\downarrow\rangle \rightarrow |\uparrow\rangle$ as a function of the trapping power P_{trap} . This is done using Ramsey spectroscopy (sec. 4.3 and inset fig. 6.3). The data are presented in fig. 6.3 and the expected

¹⁴ For now please just accept it as a fact that we can measure this phase shift, a description of *how* is to come.

¹⁵ To understand why this is important consider an ensemble pumped into the $|\uparrow\rangle$ state. As the transition $|\uparrow\rangle \rightarrow |F' = 4\rangle$ is forbidden (we use π polarization) light does not experience the associated dispersion curve which would be pulling the curve up for negative detunings, as is the case for an ensemble with isotropic populations in $F = 4$.

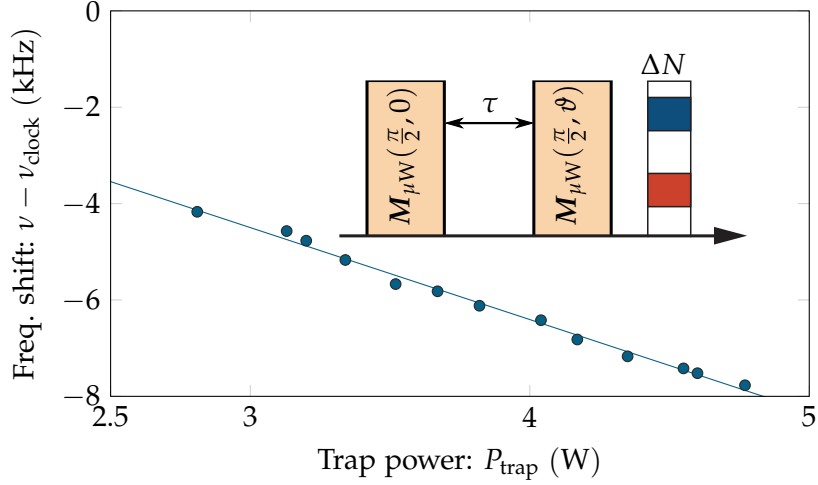


Figure 6.3.: Measured hyperfine transition frequency (using Ramsey spectroscopy, see inset) as a function of FORT power. For $P_{\text{trap}} \lesssim 2.5\text{W}$ we do not trap enough atoms to make a proper measurement of the transition frequency. Extrapolation allows us to infer the magnitude of non-trap induced shifts to be of 1.2 kHz.

linear dependence is observed. Extrapolating to zero, allows us to infer any shifts not originating from the FORT. These amount to 1.2 kHz, and could be due to inhomogeneous magnetic fields or density shifts. Such shifts would be a major concern if we were to run a state of the art atomic clock — whereas for the purpose here they do not constitute a major problem. With the atoms trapped, the next step before the actual experiments is to prepare them in a pure coherent spin state (CSS).

6.2 STATE PREPARATION

Having loaded atoms into the FORT, they are distributed in the $F = 3$ and $F = 4$ ground states¹⁶ (fig. 6.4a). In all our experiments we start by pumping as many atoms as possible into the $|\downarrow\rangle$ state, creating the ensemble ground state $|0\rangle_A \equiv |\theta = \pi, \phi\rangle_A$. Using the compensation coils a magnetic bias field of $|\mathbf{B}| = 1.5\text{G}$ is applied along the z -axis

¹⁶ We expect a larger population in the $F = 3$, state as the re-pumping efficiency is decreasing doing the sub-Doppler cooling.

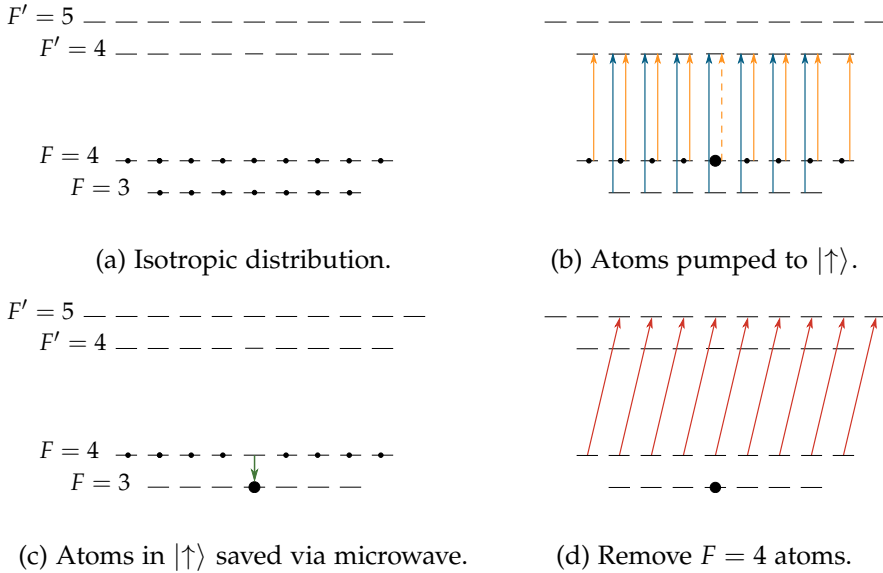


Figure 6.4.: The optical pumping method allows us to prepare a pure state of the ensemble. We transfer around 75 % of the initially trapped atoms into the $|\downarrow\rangle$ state. Atoms in other hyperfine states are removed via an on-resonant blow-away pulse, leaving us with about 1 % of the atoms in other hyperfine states.

(fig. 6.6). This lifts the degeneracy of the m_F states and sets a natural choice of quantization axes. The optical pumping beam is picked off from the MOT cooler. It is shifted down in frequency by a double-pass AOM, such that it is resonant with the $F = 4 \rightarrow F' = 4$ transition — its frequency can be tuned via the MOT cooler master. We carefully align its polarization to be π at the position of the atoms (fig. 6.6). Using this and the re-pumping beam ($F = 3 \rightarrow F' = 4$), atoms accumulate in the $|\uparrow\rangle$ state since the $|\uparrow\rangle \rightarrow |F' = 4, m_{F'} = 0\rangle$ transition is forbidden¹⁷ (fig. 6.4b). After $\approx 1500 \mu\text{s}$ around 75 % of the atoms are in the $|\uparrow\rangle$ state and then transferred to the $|\downarrow\rangle$ state via a microwave π pulse (fig. 6.4c).

To remove remaining atoms in the $F = 4$ state we use the MOT beam propagating along the gravitational axes, the weakest trap axis. It is tuned to be resonant with the $F = 4 \rightarrow F' = 5$ cycling transition (fig. 6.4d) and removes atoms from the trap by a combination of heating and pushing. A π pulse then brings the atoms in $|\downarrow\rangle$ to the $|\uparrow\rangle$ state

¹⁷ This is a $\Delta F = 0$ and $\Delta m_F = 0$ transition.

and the sequence is repeated. This leaves less than 1% of the atoms in other hyperfine ground states — we have created the desired pure ensemble. Having described how we can initially prepare the atomic ensemble in a given m_F state, we now consider how we can measure the quantity of interest, namely the desired population difference.

6.3 POPULATION-DIFFERENCE MEASUREMENT

In our theoretical discussion of both the atomic states (sec. 3.6) and the state characterization method (sec. 4.2) the parameter of interest was the population difference $\Delta N = N_{\uparrow} - N_{\downarrow} = 2 \langle \hat{J}_z \rangle$ and especially its fluctuations. We use a dual-color probing method (sec. 5.1) with several key advantages in comparison to a “standard” single-color measurement [Saffman et al. 2009]:

AC STARK: With the freedom to *independently* tune the frequency of each laser we cancel the probe induced differential ac Stark shift while having identical probing strengths for atoms in each level (sec. 5.1).

ACOUSTIC NOISE: The dual-color probing gives several tens of dB noise suppression for low frequency (up to a few kHz) acoustic noise (sec. 6.3.3).

CROSS PUMPING: Probing on the closed $F = 3 \rightarrow F' = 2$ and $F = 4 \rightarrow F' = 5$ transitions, we do not have cross pumping between the two ground states.

Having outlined the key advantages we now describe the actual implementation.

6.3.1 Probes

We use two home build **ECDLs**. One to probe atoms in the $|\uparrow\rangle$ state ($F = 4 \rightarrow F' = 5$ referred to as the orange probe) and one to probe atoms in the $|\downarrow\rangle$ state ($F = 3 \rightarrow F' = 2$ referred to as the purple probe). The optical layout is shown in fig. 6.5 and a detailed description of its operation can be found in [Oblak 2010, sec. 8.1] and will here only be outlined. The central feature is a digital beat-note lock described in [Appel, MacRae, et al. 2009] — it changes the frequency (via the

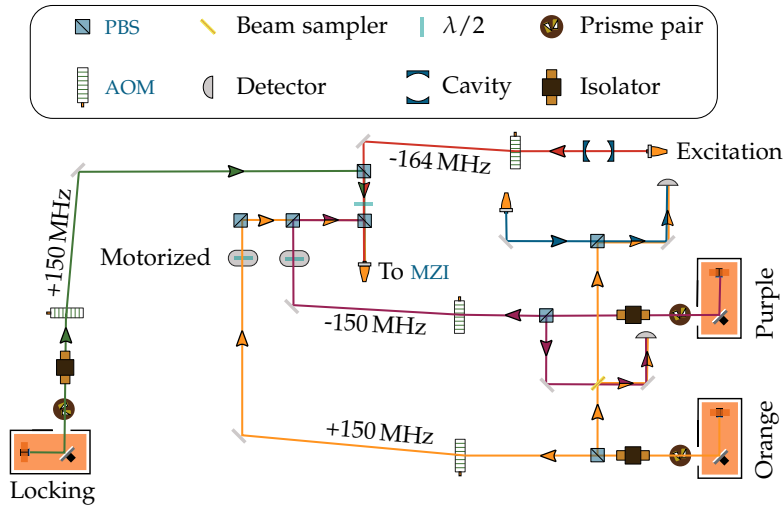


Figure 6.5.: Optical layout of the probes (orange and purple), locking (green) and excitation (red) lasers. All lasers are coupled into the same single mode fiber, taking them to the *MZI* setup. The orange probe is locked to the repumper master (blue), and the orange purple probe is locked to the orange.

current and piezo) of a slave laser such that its beat-note with a master laser matches an external reference frequency. First the orange probe is locked to the repump master, stabilizing its frequency and obtaining an absolute frequency reference.¹⁸ The purple probe is then locked to the orange probe. There are two important features of this locking chain.

First if the repump master drifts it does not change the frequency difference of the two probes. Second, the whole system is widely tunable, allowing to carefully set the light-atom coupling (eq. (5.10)), by changing the laser detunings. Having the lasers locked they are sent through an AOM used to create probe pulses (fig. 6.5). Each probe passes through a $\lambda/2$ waveplate on a motorized mount, which together with a PBS, allows setting the probe powers. After this, the beams are overlapped and coupled into a single-mode fiber taking them to the *MZI*.

¹⁸ How good this frequency references is depends on the saturation lock for the repumper. If there are any pressure shifts etc. in the vapor cell used for locking this would carry over as a frequency offset.

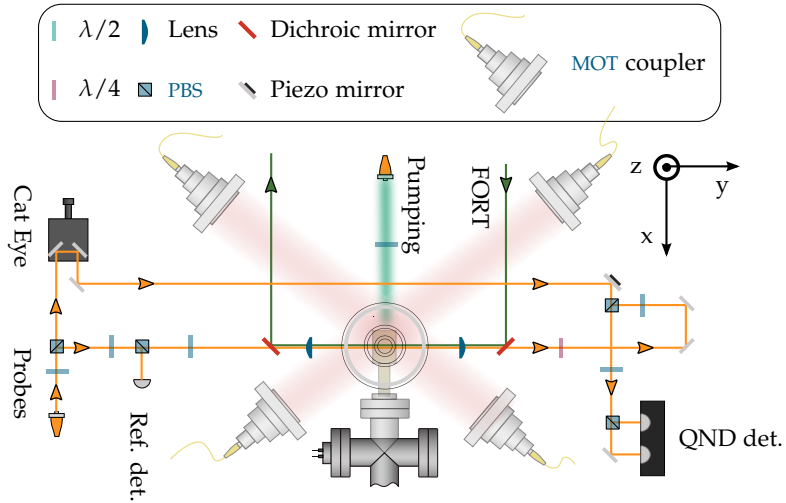


Figure 6.6.: Detailed optical layout of the MZI. The probes are split into the probe and reference arm with a ratio of 1 : 10. In the probe arm the FORT laser and the probes are overlapped using dichroic mirrors and are then focused down to tens of μm . After interacting with the atoms the probes are overlapped with the reference arm and a balanced homodyne detection of the MZI signal is performed.

6.3.2 Mach-Zehnder interferometer

As discussed in sec. 2.3 we use a MZI to measure the atomic induced phase shift, and thus the atomic populations — the setup is shown in fig. 6.6. The probes arrive at the MZI through the same single-mode fiber, making them perfectly mode-matched. After this they pass through a PBS splitting them into the two arms of the MZI. The splitting ratio is 90:10, and the reference arm will therefore act as a strong local oscillator (LO). In the reference arm of the MZI we have installed a cat-eye (retro-reflector). Together with a piezo mounted mirror, it is used to set the path-length difference Δl between the two arms. In the probe arm we first split off light for a power reference measurement after which a $\lambda/2$ wave plate allows us to set the polarization of the light interacting with the atomic ensemble. Choosing the quantization axes in the z -direction and with the light propagating in the y -direction we can address π and $x = (\sigma^+ + \sigma^-)/\sqrt{2}$ polarized light

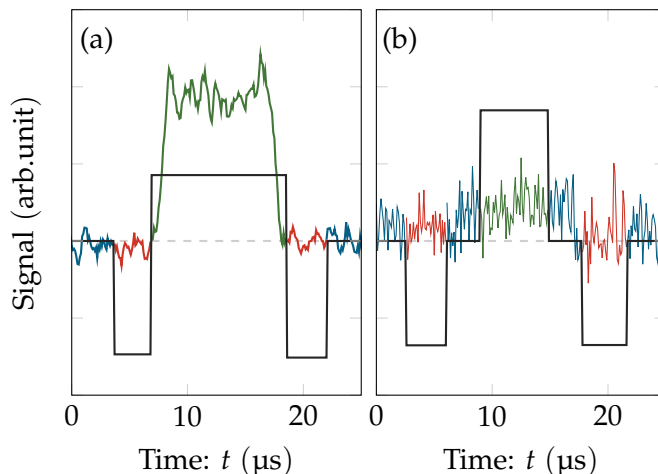


Figure 6.7.: The raw scope traces for a single probe pulse as seen on the [QND](#) (left) and reference detector (right), with the according integration matrix (black). Using the background (red) we can correct the pulse value (green) for any offsets. Note that the full pulse is included in the [QND](#) integration whereas for the power reference it is only the center value which is used.

and mixtures of the two. The probe beam is then focused down to a size of $w_0^{\text{probe}} \approx 30 \mu\text{m}$.¹⁹ To obtain the highest coupling between light and atoms, we then carefully align the [FORT](#) to obtain as high as signal as possible. This is a central point in the experiment as the light-atom coupling strength is directly dependent on this overlap (see eq. (4.3)). Having passed through the atomic sample the beam is re-collimated and mode-matched with the other arm of the [MZI](#). With the beams from the two arms overlapped, we perform a balanced homodyne measurement of the [MZI](#) output (\hat{S}_z). As described in sec. 2.3.1 this corresponds to a measurement of the optical phase shift from which we can deduce the population-difference and therefore the atomic state.

To measure the [MZI](#) signal we use a home-built pulsed differential detector described in [Windpassinger et al. 2009; Windpassinger 2008, chap. 4]. The main feature of this detector is the low photon number required for the light noise to exceed the electronic noise. These two

¹⁹ The probe beam is therefore smaller than the atomic sample.

are in a one to one ratio for $N_{\text{ph},3\text{dB}} = 8 \times 10^4$ corresponding to a power of $0.02 \mu\text{W}$ at 852 nm [Windpassinger et al. 2009]. The detector signal is sent to a digital oscilloscope operated in a “segmented” mode. It stores a predefined number of traces to its memory, each triggered by an external source. When the last trace is over, a binary file is saved for further processing. Given the time traces (fig. 6.7) we want to find the average signal value for each pulse. Considering the signal from the QND detector (fig. 6.7(a)) we make sure that the whole pulse (green) is used and we subtract the background (red) to avoid detector offsets. In contrast for the power reference detector (fig. 6.7(b)) we make the integration window such that we only get the central pulse value to avoid transient effects.

6.3.3 Noise sensitivity

To compare the states of interest we not only consider the mean value of ΔN but also its fluctuations (sec. 3.6). For the experiment to resolve such fluctuations it is crucial that we understand how different effects perturbs the detected photocurrent. A detailed discussion is presented in [Christensen 2012, sec. 6.2.2; Oblak 2010, chap. 6] and we will here simply outline the general framework used together with the key points obtained by the full analysis, summarized in table 6.1.

The photocurrent is linearised around its mean value²⁰ writing $i_- = \langle i_- \rangle + \delta i_-(t)$, where by definition $\langle \delta i_- \rangle = 0$. It is helpful to write this in terms of its Fourier components

$$\delta i_-(t) = \frac{1}{2\pi} \int_{-\infty}^{\infty} \delta i_-(\omega) e^{i\omega t} d\omega. \quad (6.1)$$

The variance of the photocurrent can be measured via the spectral density

$$\text{var}(i_-(t)) = \int_{-\infty}^{\infty} W_{i_-}(\omega) d\omega. \quad (6.2a)$$

where

$$W_{i_-}(\omega) = \frac{1}{2\pi} \langle |\delta i_-(\omega)|^2 \rangle \quad (6.2b)$$

²⁰ Defined classically as $\int_0^t i_-(t') dt'$ and quantum mechanically as the expectation value, $\langle \hat{i}_- \rangle$.

With no detection system being able to measure the whole frequency range we introduce the frequency response²¹ $g(\omega)$ which modifies the above to

$$\text{var}(i_-(t)) = \int_{-\infty}^{\infty} |g(\omega)|^2 W_{i_-}(\omega) d\omega. \quad (6.3)$$

As an example of how this framework is used we consider our most dreaded enemy, acoustic noise.

ACOUSTIC NOISE: The term acoustic noise will be used for any effect that change the path-length difference Δl of the **MZI**, i.e., mirror vibrations, people talking and moving in the lab or air flows just to name a few. The classical photocurrent output from the **MZI** was in sec. 2.3 found to be

$$i_- = -2\epsilon\mathcal{T}^2\tau \cos(\phi) \frac{N_{\text{ph}}}{t_p}. \quad (6.4)$$

Here \mathcal{T} was the field overlap, ϵ a conversion factor from photon number to photo-electrons, t_p the probe duration and τ is the probe arm transmission. To model the acoustic noise we split the phase shift, ϕ into its mean value, $\langle\phi\rangle$ and a fluctuating part $\delta\phi$. With $\langle\delta\phi\rangle = 0$ we can write

$$\phi = \langle\phi\rangle + \delta\phi, \quad (6.5a)$$

$$= \frac{\omega}{c} \langle\Delta l\rangle + \frac{\omega}{c} \delta(\Delta l), \quad (6.5b)$$

where we have assumed that the laser frequency ω does not fluctuate. Inserting this into eq. (6.4) and then in eq. (6.3) we get

$$\text{var}(i_-)_{\text{aco}} = \left(2\epsilon\mathcal{T}^2\tau\omega \frac{N_{\text{ph}}}{t_p} \sin(\langle\phi\rangle)\right)^2 \int_{-\infty}^{\infty} |g(\omega)|^2 W_{\delta(\Delta l)}(\omega) d\omega, \quad (6.6)$$

where we have expanded the cosine to first order. This depends quadratically on the probe photon number N_{ph} , in comparison to the shot noise which scales with N_{ph} (sec. 2.2). This difference in scaling allows us to distinguish the shot noise and acoustic noise in the detected signal. For

²¹ From which the detector bandwidth can be found.

many noise sources we would at this point be able to find a certain parameter that can be tweaked and tuned to suppress the fluctuations.²² The somewhat disappointing insight is that there is no direct way to suppress this type of noise for a single-color measurement.

Expanding the description to the used dual-color probing we note that any changes to Δl affect each probe identically — the fluctuations are common mode. This means that if we can detect the phase shift difference of the probes, these fluctuations would cancel out. In the experiment this is achieved by aligning the MZI such that $\Delta l \approx \omega_{\text{clock}}/2c = 17 \text{ mm}$ in the absence of atoms. To experimentally test that the described noise reduction works we measure the empty MZI noise spectrum with a single and dual-color probe (fig. 6.8). A noise reduction of 10 dB to 30 dB for frequencies up to 1.5 kHz is observed. This reduction of acoustic noise is instrumental for us to resolve the atomic projection noise. Furthermore, it was the same demand that was required in sec. 5.1 to reach the desired QND Hamiltonian. The deliberate misalignment of the path-length difference comes at a price — the MZI is *not* operated in the white-light position $\Delta l = 0$. Here the signal would be insensitive to frequency noise of the lasers. This suppression of frequency noise scales with $\Delta l/c$ (table 6.1), meaning that we still take advantages of it as we are only a “single beat” away from the optimal position.

OTHER NOISE SOURCES: As one can imagine the number of things that make the MZI signal fluctuate is endless. An overview of how some of these affect the photocurrent and how they can be suppressed is given in table 6.1. To understand each one a similar noise analysis to above can be performed [Oblak 2010, chap. 6], from which we get three key insights. First, we see if and how a given noise source can be suppressed by a careful choice of experimental parameters. Second, classical noise on the MZI signal will scale with N_{ph}^2 , allowing us to distinguish these from the light shot noise scaling as N_{ph} . Third, fluctuations in the atomic state measurement, i.e., loading noise and fluctuations in the light atom coupling constant, will scale with N_{at}^2 allowing us to distinguish these from the atomic projection noise scaling as N_{at} . These seemingly simple facts allow us to distinguish differ-

²² A well-known example is that frequency noise can be suppressed by having $\Delta l = 0$, the “white-light” alignment.

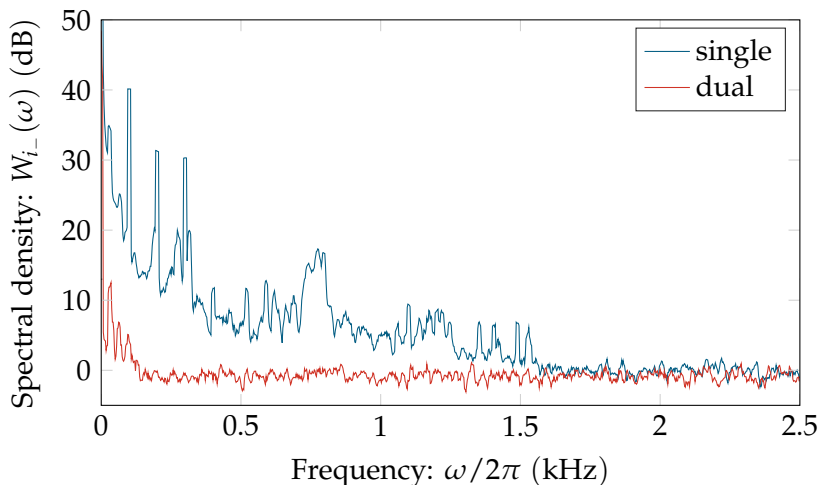


Figure 6.8.: A comparison of the empty MZI power spectral density for a single and dual-color probe (identical powers). A noise reduction of up to 30 dB is observed. Note that the curves have been shifted vertically such that the single-color measurement is zero at 2.5 kHz.

ent noise sources from one another and unambiguously show that the apparatus can resolve the atomic projection noise (sec. 7.3.1 and 8.3.1).

6.3.4 Locking

From table 6.1 it is clear that, to ensure optimal operation of the experiment, several parameters require active stabilization. In the following we consider the two most crucial feedback loops:

PATH-LENGTH: We actively stabilize the path-length difference of the MZI using a lock-in detection method. For this we use an auxiliary laser, again an ECDL, with a wavelength of $\lambda_{\text{lock}} = 830 \text{ nm}$. This is far detuned from any atomic resonance and therefore does not interact with the atoms. The lock laser is amplitude modulated with 100 kHz by using a single pass AOM. The modulation depth is 100% such that the laser is effectively turned on and off. It is then coupled into the same fiber that takes the probes to the MZI (fig. 6.5). The advantages of this setup is that the lock laser traces out the exact path we want to lock — that of

Table 6.1.: The scaling of the photocurrent variance, $\text{var}(i_-)$, from different noise sources and how it can be suppressed.

SOURCE	SCALING N_{ph}	SCALING N_{at}	SUPPRESSION
Light shot noise	N_{ph}	n/a	n/a
Laser intensity	N_{ph}^2	n/a	Balanced detection: $\langle i_-^{(1)} \rangle = \langle i_-^{(2)} \rangle$
Laser freq. or phase	N_{ph}^2	n/a	White light alignment: $\Delta l \ll \omega_{\text{clock}}/c$
Acoustic	N_{ph}^2	n/a	Dual-color probing: $\Delta l = \omega_{\text{clock}}/c$ $N_{\text{ph}}^{(o)} = N_{\text{ph}}^{(p)}$
Atomic projection noise	n/a	N_{at}	n/a
Atom number	n/a	N_{at}^2	Balanced atom number $N_{\uparrow} = N_{\downarrow}$
Coupling strength	n/a	N_{at}^2	Balanced atom number $N_{\uparrow} = N_{\downarrow}$

the probes. Demodulating the interferometer output signal at 100 kHz we directly measure the lock laser interference fringe, which is used as an error signal. As we want to lock the path-length to $\Delta l = \omega_{\text{clock}}/(2c)$ the PI lock drives the error signal to an offset value. This, together with the flexibility to change λ_{lock} , allows us to choose a setting where we sit at a zero-crossing (highest sensitivity $\phi_0 = \pi/2$), and at the same time have the two probes out of phase. To avoid any influence of the lock laser on the phase shift measurements the lock is frozen around the trains of probe pulses.

PROBE POWERS: To suppress the acoustic noise (sec. 6.3.3) and the probe induced differential ac Stark shift (sec. 5.1) the two probes should have identical powers. After each experimental run, when the atoms have been removed, the path-length lock is switched off. The piezo mirror is “wiggled” while a train of dual-color probe pulses is sent. If the probe powers (or more precisely their fringe amplitudes) are equal, the detected signal should *not* change during the wiggling. We can therefore directly use this as an error

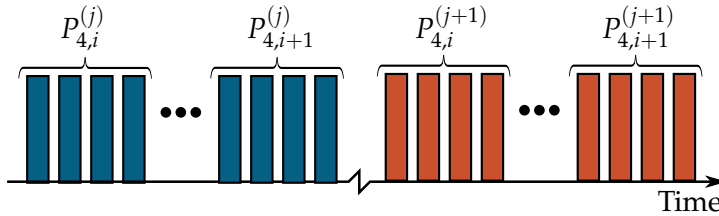


Figure 6.9.: The measurement sequence used to show the shot noise limited operation. Two pulse trains j and $j + 1$ spaced by ≈ 100 ms each with 20 pulses is sent. The pulses are then combined (above showing the case of 4 pulses). The light noise is now found by taking the variance over the many realizations.

signal that we feed back to the motorized wave plates changing the probe powers (fig. 6.5).

These servo loops are combined in one circuit and a detailed description can be found in [Oblak 2010, sec. 8.6]. Having described the [MZI](#), its operation and its noise sensitivity, the outstanding question is whether after all the trouble we are limited by some classical noise source or if we actually resolve the shot noise of light.

6.3.5 Shot noise limited operation

For the atomic state characterization the noise floor will be set by the inherent noise of the [MZI](#) which ideally should be the light shot noise. To show that this is the case we measure the [MZI](#) noise as a function of photons in the probe arm of the [MZI](#).²³ Two pulse-trains separated by ≈ 100 ms each with 20 probe pulses and a repetition rate of $20 \mu\text{s}$ (see fig. 6.9) is sent and we measure the [MZI](#) output. Repeating this experiment several times allows us to find the light noise in the following way; Each pulse is integrated to yield a single value (fig. 6.7) which is converted into a phase using the fringe calibration measurement. The light noise is then found as the variance over the many realizations.

To vary the photon number we either combine probe pulses within a single pulse train or between different pulse trains (fig. 6.7). First,

²³ The data is actually extracted from the reference measurement in the experiment regarding the creation and characterization of the [SSS](#), see chap. 7.

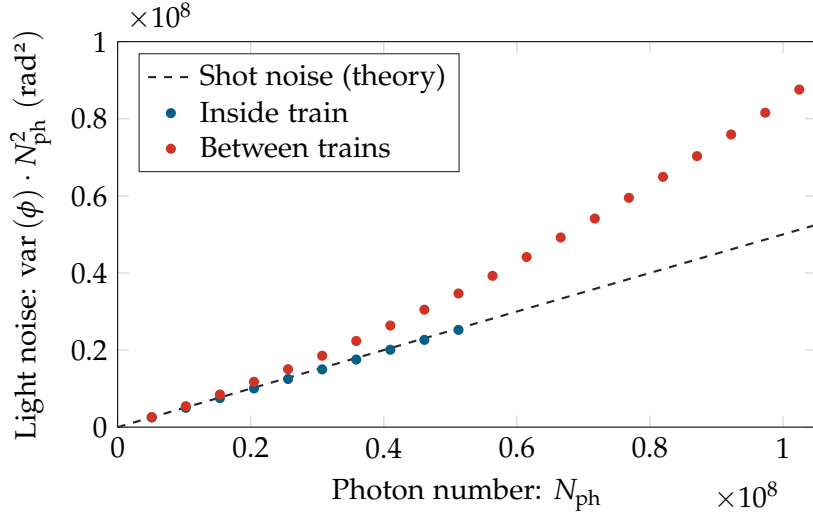


Figure 6.10.: Light noise as a function of probe photon number. Blue points show pulses combined within a train and red points shows pulses combined between subsequent trains. The full line shows the expected theory prediction, in good agreement with the data from within a single train (blue).

looking at the case where we combine pulses within a train we see a clear linear scaling (blue points fig. 6.10) meaning that the noise within a train is uncorrelated. Furthermore, we see that the linear scaling fits the expected shot noise scaling (dashed black fig. 6.10) from which we conclude that the empty MZI is shot noise limited. Turning to the case where we combine pulses between subsequent segments, we observe a quadratic component, a signature of correlated noise. There are two reasons for this. First, we consider higher probe photon numbers.²⁴ Second, looking on a longer time scale we are more sensitive to other noise effects, such as acoustic noise.

6.4 ACQUISITION AND CONTROL

Any experiment should be reproducible and easy to operate. To achieve at least the first the whole setup is computer controlled. The con-

²⁴ We can combine 20 pulses compared to the 10 pulses if we stay within one pulse train.

trol and acquisition system consists of two computers, Hedorah²⁵ and Gamera and a digital oscilloscope, already discussed. Hedorah is running the two main programs Carlos MOT controller (**CAMOT**) and DIO64 pulsing unit (**DIO**):

CAMOT: Controls three synchronized National Instruments (**NI**) cards with analog outputs and a timing resolution of ≈ 1 ms. The analog outputs set magnetic fields, power and frequency of the **MOT** lasers. Due to an update to Windows 7 and incompatibility with old drivers this program was completely rewritten since [Windpassinger 2008; Oblak 2010].

DIO: Controls a DIO64 card from Viewpoint systems, with 64 digital outputs and a timing resolution down to 50 ns. The digital outputs are connected to the probe **AOMs**, oscilloscope and everything else requiring precise timing. Before each run the timing sequence is uploaded to the buffer of the DIO64. The buffer is played when an external trigger from **CAMOT** is received.

In support of the two main programs, a long list of auxiliary programs are run from Gamera:

PLL: Sets the frequency of the two probe lasers, via the beat-note lock.

POWER BALANCER: Controls and feeds back to the two motorized waveplates, allowing to balance the probe powers (see sec. 6.3.4).

AD9910DDS: Controls the AD9910DDS chip, which is the central part of the home-built microwave source [Oblak 2010, sec. 10.2]. Not only does it allow to set the frequency, amplitude, and phase of the microwave pulses, it can play a programmed pulse sequences for use in for example Ramsey and echo experiments.

FILTER CAVITY: This program controls the filter cavities and the **SPCM**, used for the creation of the collective-single-excitation state (see chap. 8). The cavities are locked doing the **MOT** loading by a digital dither lock (see [Christensen 2012, sec. 9.3] and sec. 8.1.2).

SCOPE PROGRAM: Used to control and acquire data from the Agilent Infiniium 54832D digital oscilloscope. It also sets the lock point of the **MZI** such that both in the presence and absence of atoms,

²⁵ The computer formerly known as Godzilla.

the individual probes are balanced. Furthermore, the program also performs an initial analysis of the data, mainly used for debugging purposes.

With the control and acquisition system spread over several computers it is clear that synchronization is required. The program controlling all of this is the scope program. Before it allows a new experimental sequence (MOT loading) to start, it queries all other programs to make sure they are ready. If all programs are “good to go” a new run is started. The full outline of connections and dependencies is shown in fig. B.2.

6.5 SUMMARY

In this chapter we have described the main experimental techniques and their implementation. Starting from a description of the atom trapping and optical pumping we turned to the main topic of the chapter — the dual-color probing method. Special attention was given to how the dual-color measurement with appropriate alignment of the MZI allow for the suppression of acoustic noise, and we showed a reduction of a few tens of dB. Furthermore, we found that quantum fluctuations could be distinguished from their classical counterpart by their scaling with either the atom or photon number. To make the experiment as robust as possible to external fluctuations, the path-length difference and the probe powers are actively stabilized. Having described the operation of the setup we then showed that the MZI resolves the shot noise of light. This sets the noise floor for the atomic state measurements discussed in the next chapters.

SPIN SQUEEZING

In this chapter we present results showing the creation and characterization of a spin-squeezed state (SSS) and its nonclassical properties. To put the work into context we note that the setup was capable of producing a SSS before I joined the group in 2010, see [Appel, Windpassinger, et al. 2009; Louchet-Chauvet et al. 2010; Windpassinger 2008; Oblak 2010]. My contribution to the presented results has mainly been operating and optimizing the apparatus and the data analysis. Most notably is the observation of squeezing without correcting for the mean drifts of the experiment.¹ The analysis showing nonclassical features of the created state was done in collaboration with Prof. W. Vogel and Dr. T. Kiesel.

The chapter is structured as follows. We start by describing the experimental procedure, highlighting the key points, drawing especially on the insights of sec. 6.3.3. We then consider the main calibration experiment. By measuring the reduction of Ramsey fringe contrast due to a probe pulse, we infer the probe induced decoherence. After this the main experiment is discussed. Results showing a spectroscopically relevant squeezing of -1.7 dB of the single point variance is presented. Finally the nonclassical properties of the created state is verified, through atomic quadrature quasi-probability (AQQP) distributions. The chapter is based on [Kiesel et al. 2012; Christensen 2012].

7.1 EXPERIMENTAL PROCEDURE

Before embarking on a long experimental run, we want to make sure that everything works as expected. We therefore follow this “check list”:

VISIBILITY: The visibility of the MZI is optimized to be $\mathcal{T}^2 \geq 0.95$, a high visibility is crucial as it directly relates to the SNR of the phase detection (eq. (2.39)).

¹ This corresponds to the single- and two-point pulses, which we discuss in a bit.

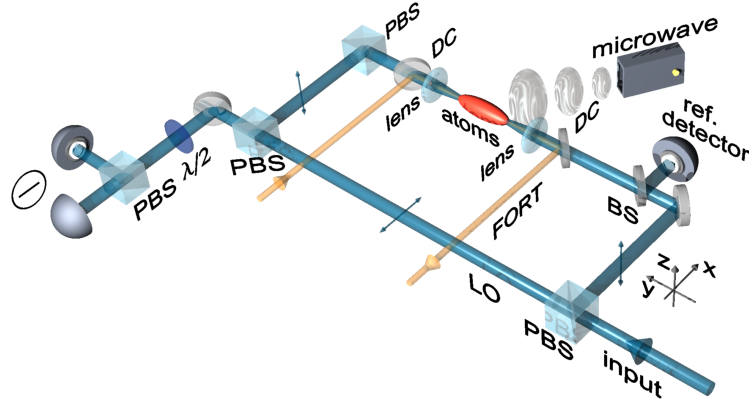


Figure 7.1.: The setup used to generate and characterize the SSS. Both probes arrive at the MZI through the same single mode fiber. The probes are focused down and overlapped with the atomic ensemble trapped in the FORT. It is then recollimated and overlapped with the LO and a balanced homodyne detection of the interference fringe is made.

FRINGE CALIBRATION: To establish a conversion between the fringe amplitude and the power reference measurement, we perform a “fringe calibration”. By scanning the piezo, we measure the fringe amplitude on the QND detector for a given signal on the reference detector (fig. 7.1) [Oblak 2010, sec. 8.6]. Besides calibration this also shows how well the two probes are out of phase, as required for the rejection of acoustic noise (sec. 6.3.3).

FORT LOADING: Using a single-color probe we measure the phase shift from atoms trapped in the FORT. This allows us to optimize the parameters (laser power, detuning, and spatial overlap) of the MOT loading and subsequent transfer to the FORT.

STATE PREPARATION: The pumping sequence (sec. 6.2) is fine tuned (duration and detuning of pumping and blow away pulses). The goal is to transfer as many atoms as possible into the $|\downarrow\rangle$ state while atoms in all other states are removed from the trap.

POWER BALANCING: We balance the output of the homodyne detection for both probes individually. This allows us to suppress intensity noise of the lasers (sec. 6.3.3).

LOCK MZI: The path-length difference of the interferometer is locked. An appropriate offset is chosen such that, in the absence of atoms, the individual probes do not experience a phase shift. This corresponds to being at a zero-crossing of the corresponding fringe.

$\pi/2$ **DURATION:** We optimize the duration of the $\pi/2$ pulse by comparing the population difference for this and a $3\pi/2$ pulse [Christensen 2012, sec. 7.2]. Typical durations are on the order of $5\ \mu\text{s}$, corresponding to a Rabi frequency of $\Omega_R \approx 2\pi \times 50\ \text{kHz}$.

MICROWAVE FREQUENCY: Using Ramsey spectroscopy (sec. 4.3) we optimize the microwave frequency to match that of the $|\downarrow\rangle \leftrightarrow |\uparrow\rangle$ transition.

AC STARK SHIFT: The detuning of the probes are optimized such that the differential ac Stark shift of the clock levels are minimized — again using a Ramsey spectroscopy. This means that the light-atom coupling strength is similar for the two probes. The optimal probe detunings found for the data presented in this chapter are $\Delta_{32} = -96\ \text{MHz}$ and $\Delta_{45} = -91\ \text{MHz}$.

REOPTIMIZE: As the parameters optimized above are not independent we redo the last four steps in an iterative fashion.

With the above checklist we are now ready to consider the decoherence and squeezing experiments in more detail.

7.2 DECOHERENCE

To completely characterize the created [SSS](#) it is crucial to know the destructiveness introduced by the dual-color probe pulse (sec. 3.4). To be more specific, given an ensemble of \tilde{N}_{at} *coherent* atoms subject to a probe pulse how many atoms will remain coherent after the interaction? This loss of coherence is due to scattering events² and described by

$$N_{\text{at}} = \tilde{N}_{\text{at}} e^{-\eta N_{\text{ph}}}, \quad (7.1)$$

which corresponds to the loss of Ramsey fringe contrast. Here η is the decoherence parameter, which is the number of scattering events

² Both Raman and Rayleigh scattering events.

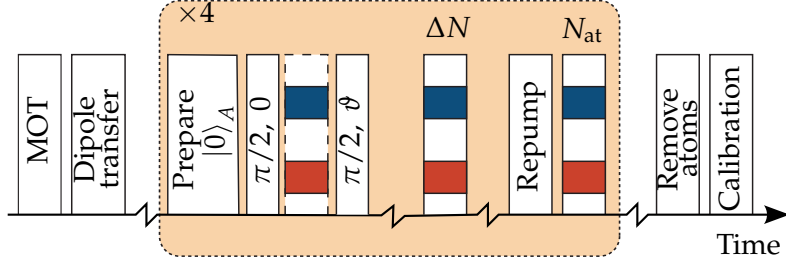


Figure 7.2.: To measure the probe induced decoherence a Ramsey experiment is performed. Starting with the ensemble in the state $|0\rangle_A$, we use a $\pi/2$ pulse followed by an *optional* probe pulse and a second $\pi/2$ pulse with a phase ϑ . Finally, we measure the population difference ΔN and perform calibration measurements.

per probe photon. To measure the decoherence we use the Ramsey like sequence shown in fig. 7.2. All atoms are pumped to the $|\downarrow\rangle$ state and a $\pi/2$ pulse rotates them into the equatorial plane such that the Bloch vector is pointing along the x -axis. The ensemble is in the CSS $|\theta = \pi/2, \phi = 0\rangle_A$. An *optional* dual-color probe pulse is sent, followed by a $\pi/2$ pulse with a phase $\vartheta \in [0 : 2\pi]$ and the population difference ΔN is measured. This is followed by a repumping pulse transferring all atoms to $F = 4$ and a measurement of the total atom number N_{at} is made. This is repeated four times before the atoms are removed from the trap and calibration measurements are performed. The normalized Ramsey fringe is given by $\Delta N/N_{at}$ and is shown in fig. 7.3. Knowing the number of photons in the probe pulse $N_{ph} = 5.25 \times 10^6$, from the power reference detector and the fringe reduction we find $\eta = 1 \times 10^{-8}$. Furthermore, as there is no phase shift between the probe on and probe off (fig. 7.3) the differential ac Stark shift cancellation works.

As an experimental detail this also allows us to measure the number of atoms lost between the measurement of ΔN and N_{at} . In the case where the phase of the second microwave pulse is $\vartheta = 0$, the measurement of ΔN and N_{at} should be identical³ in the absence of atom loss. As this is not the case, we find this difference and use it to relate the measured N_{at} to the actual atom number at the time the measure-

³ Up to the small error of atoms in different m_F states coupling different to the π polarized probe.

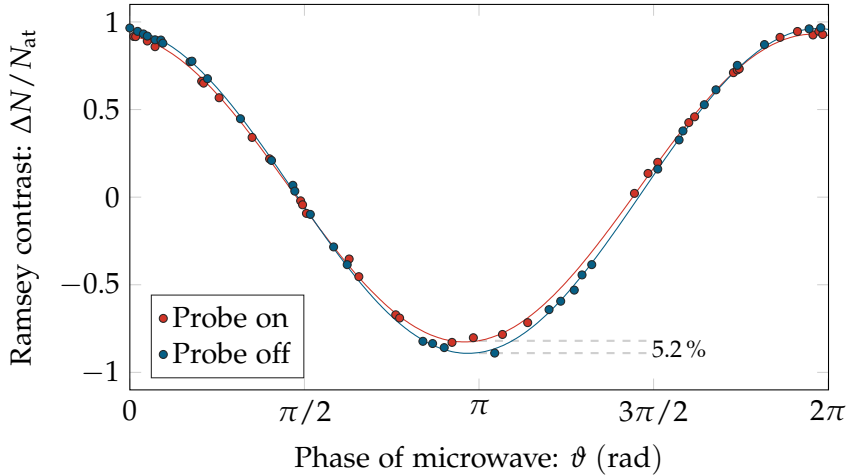


Figure 7.3.: Ramsey fringe contrast with and without the probe pulse, error bars are the size of the points. We observe a decrease in contrast of 5.2%, corresponding to a decoherence parameter of $\eta = 1.0 \times 10^{-8}$.

ment of ΔN is made. The importance of this is clear, when considering Wineland's squeezing criteria (sec. 3.4) where the measured atomic noise should be related to the noise of a CSS with a corresponding number of coherent atoms.

7.3 SQUEEZING

Knowing how a dual-color probe pulse affects the ensemble, we proceed with the main experiment. The experimental sequence is shown in fig. 7.4. Starting with all atoms in $|\downarrow\rangle$, a $\pi/2$ pulse prepares the ensemble in the CSS $|\theta = \pi/2, \phi = 0\rangle_{A'}$, corresponding to the pseudo-spin vector pointing along the x -axis. A sequence of 20 dual-color π -polarized probe pulses with a duration of $10 \mu\text{s}$ each containing $N_{\text{ph}} = 5.1 \times 10^6$, and a repetition rate of $20 \mu\text{s}$ is sent. Afterwards a repumping beam transfers the atoms to the $F = 4$ hyperfine manifold and a second sequence of probe pulses measures the atom number N_{at} . To avoid saturation of the detector the photons per pulse is decreased for the atom number measurement.⁴ To vary the number of atoms,

⁴ All atoms are in the $|\uparrow\rangle$ and we therefore expect the light to experience a large phase shift, meaning a large fringe amplitude, thus a high voltage that will saturate our

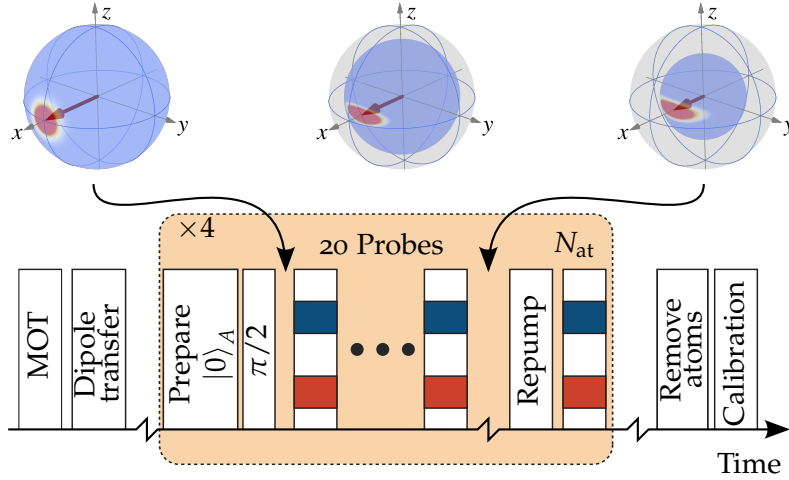


Figure 7.4.: Experimental sequence and Bloch spheres at corresponding points. The sequence is as follows; Starting with all atoms in $|\downarrow\rangle$, i.e., the ensemble is in the CSS $|0\rangle_A$ a $\pi/2$ pulse rotates the Bloch vector into the equatorial plane. We then use a train of 20 dual-color probe pulses to measure ΔN . The atoms are then re-pumped to the $F = 4$ manifold and we measure the total number of atoms N_{at} , this is repeated four times. We then use on-resonant light to remove all atoms and perform calibration measurements.

each FORT loading is reused four times. The atoms are then removed using light resonant with the $F = 4 \rightarrow F' = 5$ transition and calibration measurements of the empty MZI are made.⁵

To acquire enough files for the analysis, the experiment is kept running for as long as possible, in this case four days. With this we acquire $N_{\text{sam}} = 44\,988$ files each with four measurements of ΔN for varying N_{at} . For each realization, $i = 1, 2, \dots, N_{\text{sam}}$ we get a series of segments containing $\{t, V_{\text{QND}}, V_{\text{ref}}\}_i$, which should be analyzed. The main steps of this is outlined below, and a detailed description is given in [Oblak 2010, sec. 12.2]:

detector. In practice this is done by changing the amplitude of the radio frequency (RF) signal sent to the probe AOM.

⁵ These include MZI baseline, probe powers, and we also re-balance the used probe powers for the next experimental run.

INTEGRATION: The raw scope traces are integrated to yield a single point per pulse (sec. 6.3.1).

TWO-POINT PULSES: To compensate for long term drifts of mean values,⁶ pulses from different MOT cycles are subtracted giving us what we term “two-point pulses”. This allows to cancel drifts on a time scale between different realizations (≈ 5 s). Note that this is done for *calibration* purpose only. For the final data, showing reduced noise and nonclassical features, the single point pulses are used.

BASELINE: We subtract the signal measured in the absence of atoms, i.e., the baseline of the MZI. This again corrects for drifts of the MZI, now on a time scale within a realization, which is ≈ 100 ms.

FILTERING: Using *independently* measured quantities, probe powers, locking signals etc. we discard data showing a “non-normal” behavior and are left with 33 741 files. Files are rejected if they deviate by more than five standard deviations from their local mean. We dump about 25% of the data, a large amount but the experiment is at times (to allow the experimentalist to sleep) running unsupervised, i.e., if a laser falls out of lock we will acquire bad files until the problem is fixed in the morning.⁷

META PULSES: The 20 probe pulses are combined into two meta pulses — two successive QND measurements of the optical phase shift. We use 8 pulses for the first measurement ϕ_1 and 10 pulses for the second measurement ϕ_2 . The conversion from photocurrent to phase, is done by the fringe calibration measurement. We will refer to the corresponding phase shifts from the two-point pulses as

$$\varphi_j^{(i)} = \frac{1}{\sqrt{2}} \left(\phi_j^{(i)} - \phi_j^{(i+1)} \right), \quad (7.2)$$

where i denotes the sample number and $j = 1$ or 2 .

We are thus left with a data set $\{\phi_{\text{at}}, \phi_1, \phi_2\}_i$. The first question one might ask is how ϕ_{at} can be converted into an actual atom number.

⁶ Atom number loading, MZI offsets, power drifts etc.

⁷ This could be fixed by introducing digital locks, but with an already complicated and hard to use control system this was not investigated.

Since all atoms are in the same hyperfine level we can directly use the relation between the phase shift and the population difference (eq. (4.15a)). With this we present a simple model in agreement with the data, allowing us to show that the apparatus resolves the atomic projection noise and that we have created a *SSS*.

7.3.1 Projection noise

The measured optical phase shift can be split into three different components originating from light, atoms and other sources. Following [Louchet-Chauvet et al. 2010] we take the coupling between light and atoms to be identical⁸ for atoms in $|\uparrow\rangle$ and $|\downarrow\rangle$ and write the optical phase shift as

$$\phi = \sqrt{\frac{1}{2} + \frac{1}{2\beta^2} \frac{\delta N_{\text{ph}}}{N_{\text{ph}}}} + \mathcal{K}\Delta N + \delta\mathcal{K}N_{\text{at}}. \quad (7.3)$$

Here N_{ph} is the dual-color photon number (both colors) in the probe arm and $\delta N_{\text{ph,tot}}$ the corresponding shot noise contribution, $\beta = \sqrt{10}$ is the power ratio between the two arms⁹ of the *MZI*, \mathcal{K} is the coupling constant (see app. C.1) and $\delta\mathcal{K}$ denotes its fluctuations due to balancing errors etc. (table 6.1). As we are interested in the atomic projection noise, we consider the fluctuations of ϕ . We note that for the *CSS* $|\theta = \pi/2, \phi = 0\rangle_A$ we have $\langle \Delta N \rangle = 0$ and $\text{var}(\Delta N) = N_{\text{at}}$ (sec. 3.3) allowing us to write

$$\text{var}(\phi) = \underbrace{\left(\frac{1}{2} + \frac{1}{2\beta^2}\right) \frac{1}{N_{\text{ph}}}}_{\text{light}} + \underbrace{\mathcal{K}^2 N_{\text{at}}}_{\text{atom}} + \underbrace{\text{var}(\delta\mathcal{K}) N_{\text{at}}^2}_{\text{technical}}. \quad (7.4)$$

As in sec. 6.3.3 we see that the shot noise of light is independent of the atom number, the atomic projection noise depends linearly on the number of atoms and the technical (classical) noise scales quadratically with the number of atoms. In this way we can distinguish different contributions from each other.

⁸ Due to the fact that we can tune each probe independently this is an excellent approximation.

⁹ Corresponding to an angle of rotation of the pseudo-spin vector of 0.2π (eq. (2.29)).

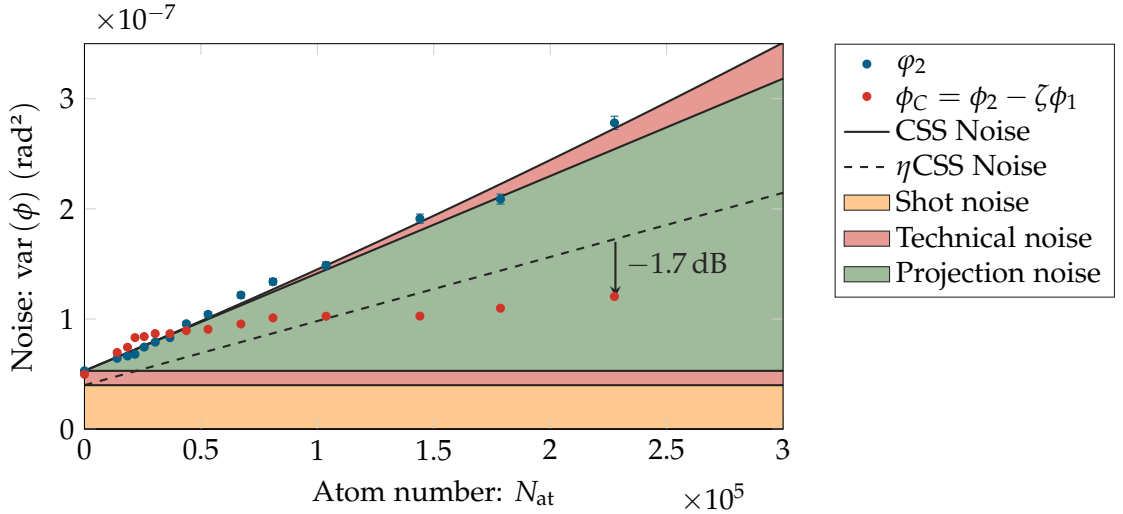


Figure 7.5.: Variance of the optical phase shift, as a function of atom number, N_{at} . The predominant linear scaling of $\text{var}(\varphi_2)$ is a clear sign that we resolve the atomic projection noise of the CSS. We see that $\text{var}(\varphi_C)$ has a reduced noise compared to a corresponding CSS, dashed black line. We have thus created and characterized a SSS with a noise reduction of $\zeta_{\text{Wineland}} = -1.7 \text{ dB}$. Note that the (statistical) error bars are comparable to the size of the data points.

In fig. 7.5 we plot $\text{var}(\varphi_2)$ as a function of N_{at} (blue points), and make a parabolic fit to the data.¹⁰ We observe a predominantly linear scaling (full black line), a clear signature of projection noise limited sensitivity (eq. (7.4)). As the projection noise is on the order of $1/\sqrt{N_{\text{at}}} \sim \text{mrad}$ for $N_{\text{at}} \sim 1 \times 10^5$, this is not a trivial task. It means that nothing in the experiment, lasers, magnetic fields etc. gives rise to fluctuations of the atomic phase¹¹ larger than this on the timescale of a experimental run $\approx 5 \text{ s}$. The above analysis to estimate the projection noise level is done using the two-points pulses, where drifts

¹⁰ To fit the data we actually do a combined fit to the variances of the first and second pulse as well as their covariance as a function of N_{at} , see [Oblak 2010, eqs. 12.8]. For the data presented in fig. 7.5 it might seem that a linear fit could do as good, but in the case of more technical noise it is clear that the data follows a quadratic dependence (see fig. 8.8).

¹¹ Angle ϕ of the Bloch vector in the equatorial plane.

of mean values are suppressed. Had the analysis been made on the single-point pulses, we would have seen a quadratic scaling due to the classical noise introduced by the experimental drifts over the run time of 4 days.

Before we consider the *SSS*, a small digression regarding the atom number is in order. From eq. (4.15a) we know that the measured phase shift is $\phi = \mathcal{K}\Delta N$. In the experimental sequence we measure the phase shift from the *CSS* $|\theta = \pi/2, \phi = 0\rangle_A$ denoted by ϕ_2 and with all atoms in $F = 4$, denoted by ϕ_{at} . From this we can determine the proportionality constant \mathcal{K} as follows

$$\frac{d}{d\phi_{\text{at}}}\text{var}(\phi_2) = \mathcal{K} \frac{d}{dN_{\text{at}}}\text{var}(\Delta N) \quad (7.5a)$$

$$= \mathcal{K}. \quad (7.5b)$$

We can therefore find \mathcal{K} and thus the atom number, from the slope of the projection noise scaling. This method is used to give the x -axis on fig. 7.5.

7.3.2 Noise reduction

Being able to observe the projection noise of a *CSS* we now turn the attention to the creation of a *SSS*. Following the procedure outlined in sec. 5.1 we consider two subsequent measurements each with a variance

$$\text{var}(\phi_1) = \left(\frac{1}{2} + \frac{1}{2\beta^2}\right) \frac{1}{N_{\text{ph},1}} + \mathcal{K}^2 N_{\text{at}}, \quad (7.6a)$$

$$\text{var}(\phi_2) = \left(\frac{1}{2} + \frac{1}{2\beta^2}\right) \frac{1}{N_{\text{ph},2}} + \mathcal{K}^2 N_{\text{at}}. \quad (7.6b)$$

Here we have assumed that the classical noise is negligible¹² in agreement with the data (fig. 7.5). The main thing to note is that the atomic contribution to the two measurements are equal due to the *QND* nature of the measurement — it is exactly this which gives rise to the noise reduction. The number of photons used for the first “squeezing” measurement is $N_{\text{ph},1} = 4.10 \times 10^7$ and the second characterization measurement contains $N_{\text{ph},2} = 5.12 \times 10^7$.

¹² It could be included and would give a term scaling with N_{at}^2 . As this term is uncorrelated it should cancel out in the variance of the combined measurement.

To use the first measurement to predict the outcome of the second measurement we consider

$$\phi_C \equiv \phi_2 - \zeta\phi_1, \quad (7.7a)$$

where

$$\zeta \equiv \frac{\text{cov}(\phi_1, \phi_2)}{\text{var}(\phi_1)} \quad (7.7b)$$

$$= \frac{\kappa^2}{1 + \kappa^2} \quad (7.7c)$$

is the optimal amount of information to use in the absence of any technical noise¹³ and $\kappa^2 = N_{\text{ph},1}\mathcal{K}^2N_{\text{at}}$. Note that the measurements used above are the single-point pulses, i.e., where we have not subtracted data from subsequent MOT cycles. Calculating the variance of the combined measurement we find

$$\text{var}(\phi_C) = \frac{\beta^2 + 1}{2\beta^2} \frac{1}{N_{\text{ph},2}} + \frac{1}{1 + \kappa^2} \mathcal{K}^2 N_{\text{at}}. \quad (7.8)$$

As expected this has a reduced noise in comparison to the individual measurements. With the initial state being a CSS, which is a minimum uncertainty state, the model predicts a SSS — in agreement with sec. 5.1. Considering $\text{var}(\phi_C)$ as a function of N_{at} , (fig. 7.5 red points) we observe a reduced variance in comparison to $\text{var}(\phi_2)$. To correct the projection noise level for the probe induced decoherence we use the decoherence measurement. Together with eq. (7.1) this gives the dashed line in fig. 7.5. The amount of squeezing can now be quantified using the criterion of Wineland and we find

$$\zeta_{\text{Wineland}} = -1.7 \text{ dB}. \quad (7.9)$$

This noise reduction is far from the record values reported in [Bohnet et al. 2014; Lücke et al. 2014]. Here a squeezing of ≈ -10 dB for ensembles of comparable size is shown. The main reason that we compare so poorly is that the presented data have been optimized for the detection of nonclassical features, the topic of the following section.¹⁴

¹³ It is clear that there must be a trade-off between the information gained and the probe induced decoherence. This is directly related to the correlation coefficient between the two measurements.

¹⁴ The change comes from using the single or two-point pulses — using the latter the squeezing becomes on the order of -3.5 dB comparable to the previous results obtained in our group [Appel, Windpassinger, et al. 2009].

With the above analysis being rather complicated, it is worth doing a few consistency checks outlined in app. C.1.1. From the waist of the probe beams, probe detunings and the maximum detected phase shift we can compute the expected maximum atom number to be 215×10^3 . This is in good agreement with fig. 7.5, where the atom number is deduced from the projection noise scaling. Furthermore, one can estimate the expected coherence left after the first measurement to be 77%. This is comparable with the measured value of $\exp(-\eta N_{\text{ph},1}) = 66\%$ — especially considering that we have not taken into account the photon losses through the glass cell or the spatial profile of the atoms. With this agreement we concluded that we have created and characterized a SSS. As the created state is squeezed even by the most stringent requirement by Wineland et al. [1994] it can directly improve¹⁵ the sensitivity of a phase estimate, as done in [Louchet-Chauvet et al. 2010].

7.4 NONCLASSICALITY

With the atomic ensemble in an entangled state we consider how associated nonclassical features may be inferred. It should be noted that there are several ways of defining a nonclassical state. We will use the definition and methods introduced in [Vogel 2000]. The idea behind this criterion is to compare the created state to the most classical states — the CSSs.

We expand the density operator describing a spin state in the basis of the CSSs [Kiesel et al. 2012, eq. (5)]

$$\hat{\rho} = \frac{2J+1}{4\pi} \int_0^\pi \sin(\theta) \int_0^{2\pi} P(\theta, \phi) |\theta, \phi\rangle_A \langle\theta, \phi| d\phi d\theta. \quad (7.10)$$

Here J is the magnitude of the pseudo-spin vector. This expansion is equivalent to the case of photonic systems and we identify $P(\theta, \phi)$, as the atomic equivalent to the Glauber-Sudarshan P -function $W(s = 1; X_L, P_L)$ (sec. 2.2.1).¹⁶ The term nonclassical is used if the expansion coefficients $P(\theta, \phi)$ can *not* be interpreted as a classical well-behaved probability distribution¹⁷ [Titulaer et al. 1965; Mandel 1986]. For a

¹⁵ In practice we also need the extra steps (microwave pulses) for a Ramsey sequence to not add noise to the state.

¹⁶ Recalling that both the coherent states of light and atoms (in the Holstein-Primakoff approximation) are harmonic oscillator states, this connection is not surprising.

¹⁷ That $P(\theta, \phi)$ must be ill-behaved for certain state can be understood in the following way. Since the CSS are the most classical states, the fact that any quantum state can be

nonclassical state, $P(\theta, \phi)$ therefore either takes on negative values or is more singular than the delta-function [Mandel et al. 1995, sec. 11.8]. A test for nonclassicality therefore seems straight forward — using quantum-state tomography [Leonhardt 1997, chap. 5; Lvovsky et al. 2009], we reconstruct the P -function from our data. However, as noted in sec. 2.2.1 due to the highly singular nature of the P -function this is a practically impossible task. Instead we use the methods of atomic quadrature quasi-probability (AQQP) distributions [Kiesel et al. 2012].

The idea is to recast the nonclassicality criterion in terms of characteristic functions of $P(\theta, \phi)$, and then use appropriate filter functions to search for nonclassical effects. The reasoning behind this procedure is that the characteristic functions can be estimated directly from the measurements of the atomic quadratures, $\langle \hat{P}_A \rangle \propto \langle \hat{J}_z \rangle \propto \Delta N$ which is exactly what we measure [Vogel 2000].

The characteristic function of $P(\theta, \phi)$ is given by the Fourier transform (eq. (2.21)) and is

$$\Phi(\xi) \equiv \left\langle \exp \left(\xi \hat{a}_A^\dagger - \xi^* \hat{a}_A \right) \right\rangle e^{|\xi|^2/2}. \quad (7.11)$$

To search for nonclassical effects, this is multiplied by a suitable filter function parameterized by a width w

$$\Phi_\Omega(\xi) \equiv \Omega_w(\xi) \Phi(\xi). \quad (7.12)$$

This allows us to introduce the nonclassicality quasi-probability as

$$P_\Omega(J_x, J_z) \equiv \frac{1}{\pi^2} \int_{\mathbb{C}} e^{i(J_z \xi_r - J_y \xi_i)} \Phi_\Omega(\xi) d^2 \xi. \quad (7.13)$$

Here J_y and J_z are the expectation values of the respective operators, and we have rewritten $\xi \equiv \xi_r + i\xi_i$. The AQQP distribution is the marginal of P_Ω along an angle θ

$$p_\Omega(J_\theta) \equiv \frac{1}{2\pi} \int_{-\infty}^{\infty} d\lambda \Phi(\lambda e^{i\theta}) \Omega_w(\lambda) e^{i\lambda J_\theta}. \quad (7.14)$$

Here \hat{J}_θ is the generalized quadrature operator (see eq. (2.10)). For this to be useful the filter function $\Omega_w(\xi)$ should give a regular $p_\Omega(J_\theta)$ for all states and it should not introduce any negativities in $p_\Omega(J_\theta)$. If this

expanded into this basis seems misleading. The crux is that the nonclassical features of a state $\hat{\rho}$ is “hidden” in the P -function. A beautiful and insightful description (as with everything else in the book) is given in [Leonhardt 1997].

is fulfilled the criterion has been recast into finding negativities of the [AQQP](#) instead of the P -function [Vogel 2000]. The last thing is to relate the [AQQP](#) distribution to the actual measurements.

The [AQQP](#) can be directly estimated from a data set, $\{\tilde{J}\}_i$ as the empirical mean [Kiesel et al. 2011]

$$p_{\Omega}(z) = \frac{1}{N_{\text{sam}}} \sum_{i=1}^{N_{\text{sam}}} f_{\Omega}(\tilde{J}_i; J_z, w). \quad (7.15)$$

Here f_{Ω} is a ‘‘pattern function’’ given by

$$f_{\Omega}(\tilde{J}; J_{\theta}, w) = \frac{1}{2\pi} \int_{-\infty}^{\infty} e^{k^2/2} e^{ik(\tilde{J}-J_{\theta})} \Omega_w(k) dk. \quad (7.16)$$

The task is now clear — given the i^{th} measurement $\{\phi_C, N_{\text{at}}\}_i$ we convert it into an atomic quadrature sample as

$$\tilde{J}_i = \frac{\phi_C^{(i)}}{\sqrt{h(\eta N_{\text{at}}^{(i)})}}, \quad (7.17)$$

where $h(N_{\text{at}})$ is the fitted function corrected for the decoherence (see the dashed black line in fig. 7.5). From this we can estimate the corresponding pattern function (eq. (7.15)), for a suitable filter function Ω_w .

The main problem with this conversion is that the optical phase shift contains light, technical and atomic noise where we are only interested in the last. As the added shot noise and technical noise are independent and Gaussian, this corresponds to a decrease in the quantum efficiency, $\varepsilon_{\text{noise}}$ of our detection¹⁸ [Appel et al. 2007]

$$\varepsilon_{\text{noise}} = \frac{h(N_{\text{at}}) - h(0)}{h(N_{\text{at}})}. \quad (7.18)$$

This is the ratio of atomic noise to other noise. In the following we only consider experiments where $\varepsilon_{\text{noise}} \geq 77\%$, leaving us with $N_{\text{sam}} = 4841$ for the following analysis.¹⁹ As the filter function we use a one-dimensional auto-correlation filter²⁰

$$\Omega_w(k) = \frac{1}{N} \int f(k') f(k' + k/w) dk \quad (7.19a)$$

¹⁸ We neglect the small amount of classical noise, scaling quadratically with N_{at} (see fig. 7.5).

¹⁹ The selection of data is not done directly on the noise but on the atom number.

²⁰ Other filters might be more suitable for other types of states, we have analyzed the data using a triangular filter instead, and nonclassical effects are still uncovered.

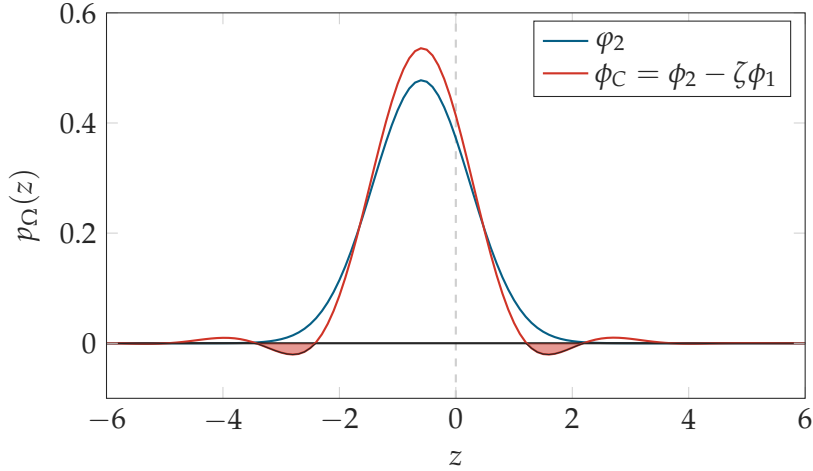


Figure 7.6.: Estimated AQQP (see eq. (7.15)), for a filter width of $w = 1.3$, note that the error is on the order of the linewidth. The AQQP for ϕ takes on negative values, a clear signature of nonclassical features. The shift of the mean from zero, is most likely due to a too short microwave $\pi/2$ time.

where

$$f(k) = e^{-k^4} \quad (7.19b)$$

and

$$\mathcal{N} = \int f(k)^2 dk \quad (7.19c)$$

is a normalization factor. We can now estimate the AQQP for a given filter width w , and an example is shown in fig. 7.6. We clearly observe that the AQQP takes statistical significant negative values — the created state is nonclassical.

Furthermore, we calculate the significance of the nonclassicality given by the negativity in units of standard deviation of the estimator

$$\Sigma(w) = \min \left(\frac{p_{\Omega}(z)}{\text{std}(p_{\Omega}(z))} \right) \quad (7.20)$$

as a function of the filter width w (see fig. 7.7). We see that the significance increases as the width goes to zero and observe a significance of up to 23 standard deviations. The method of inferring nonclassicality through the AQQP distributions where developed by Prof. W. Vogel and Dr. T. Kiesel.

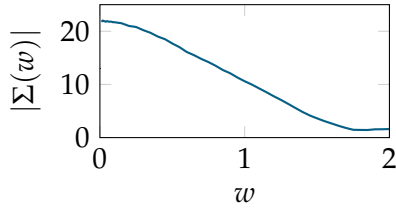


Figure 7.7.: Nonclassical features are observed with a significance of 23 standard deviations.

As it was hinted earlier there are several different definitions of nonclassical states. Most notably a more stringent requirement was put forth in [Kot et al. 2012]. In comparison to the criterion used here no explicit assumption of quantum mechanics is made. In the end the criterion by Kot et al. [2012] boils down to the following — if the Wigner function of the state takes negative values then the state is nonclassical.

negative values then the state is nonclassical.

7.5 SUMMARY

Starting by describing the measurement procedure and the central calibration measurement of the probe induced decoherence we turned our attention to the main experiment and presented three key results. First, we showed that the experimental apparatus resolves the atomic projection noise. Second, we created and characterized a SSS using atomic homodyne detection. The state had a spectroscopically relevant squeezing of -1.7 dB (in the single point measurements). From this we concluded that the atoms are in a many-body entangled state. Third, using the nonclassicality criterion of Vogel [2000], it was shown that the created state had nonclassical features with a statistical significance of up to 23 standard deviations.

COLLECTIVE-SINGLE EXCITATION

With the successful creation and characterization of a [SSS](#) and its non-classical properties we now turn our attention to the next state of interest — the collective-single-excitation state.¹ Compared to other implementations of this state [[Kuzmich et al. 2003](#); [MacRae et al. 2012](#); [Bimbard et al. 2014](#)] where the characterization is done by mapping the atomic excitation back into a photonic mode, we take a different approach. With a strong confidence in the atomic tomography methods used for the [SSS](#) we characterize the created state in a similar fashion.

The chapter is structured as follows. First we recap the general experimental ideas, based on the detection of a heralding photon (sec. [5.2](#)). We then consider the extra experimental “add-ons” required for this experiment and show that we still resolve the atomic projection noise. We then compare the measurement statistics for the case where a heralding click was observed or not. A statistically significant difference between the two cases is observed. This is followed by a model in excellent agreement with the observations. Together with an analysis of the excitation statistics conditioned on a detected photon this shows that we have created a (non-pure) collective-single-excitation state — the main result of the chapter. Using the insights gained from the model, we finish the chapter by considering several possible improvements. The chapter is based on [[Christensen et al. 2013](#); [Christensen et al. 2014](#)].

8.1 EXPERIMENTAL IMPLEMENTATION

To understand the extra requirements for the creation and characterization of the state we (once again) consider the generation procedure (sec. [5.2](#)) outlined in fig. [8.1](#). In the remaining parts of this chapter we take the ground state to be $|0\rangle_A \equiv |\theta = 0, \phi\rangle_A$. This is due to the fact

¹ This state is also known as the first Dicke state, first excited [AFS](#) or Werner state. In some ways this is the natural extension and follows the progress that was made in photonic systems where some of the first created nonclassical states were squeezed states, and afterwards the attention was turned to a single photon state.

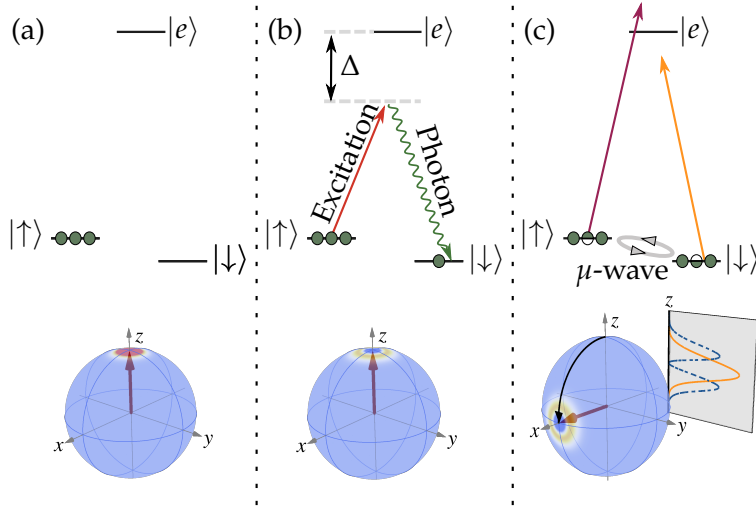


Figure 8.1.: Starting with all atoms in the upper state (a), a single unknown atom is flipped by the detection of a heralding anti-Stokes photon (b). The Bloch vector is then rotated into the equatorial plane via a $\pi/2$ pulse (c). The state is then characterized using the dual-color probing method (c). The inset in (c) shows the expected measurement outcomes for a CSS (orange) and the collective-single-excitation state (blue) as derived in sec. 3.6.

that the Clebsh-Gordon coefficients are more favorable for excitations from the $|\uparrow\rangle$ than the $|\downarrow\rangle$ state.² The method used to generate and characterize the collective-single-excitation state is as follows:

INITIAL STATE: Using the state creation method (sec. 6.2) a π pulse, and an optical purification pulse, the ensemble is prepared in the CSS (fig. 8.1(a))

$$|0\rangle_A \equiv |\theta = 0, \phi\rangle_A \quad (8.1a)$$

$$= |\uparrow\uparrow \dots \uparrow\rangle_A. \quad (8.1b)$$

The purification pulse is required to remove any remaining coherences (from the π pulse) between the two clock states.

² As the definition of the ground state in chap. 3 was rather arbitrary and the two states enter symmetric we can make this change without any changes to the theoretical part.

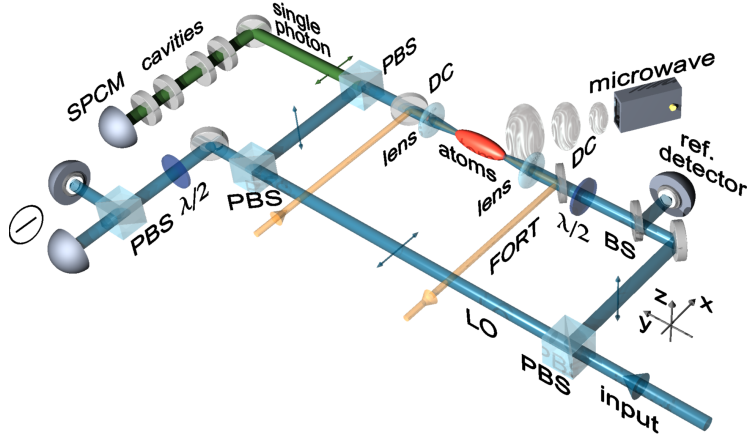


Figure 8.2.: Experimental setup used for the creation of the collective single-excitation state. The dual-color probe and excitation beams arrive at the MZI via one single mode fiber. The main changes from the setup used to create a SSS (fig. 7.1) is the addition of a $\lambda/2$ wave plate to set the polarization of the probe and excitation beams at the ensemble and polarization and frequency filtering in the single photon path (green).

SPIN FLIP: Following the DLCZ protocol (sec. 5.2) a single *unknown* atom is probabilistically transferred to the other spin state (fig. 8.1(b)). If the flip was unsuccessful the ensemble remains in

$$|0\rangle_A = |\uparrow\uparrow \dots \uparrow\rangle_A, \quad (8.2a)$$

and if the flip succeeded it becomes (sec. 5.2)

$$|1\rangle_A = \frac{1}{\sqrt{N_{\text{at}}}} \sum_{l=1}^{N_{\text{at}}} |\uparrow\uparrow \dots \uparrow \underbrace{\downarrow}_{l\text{th atom}} \dots \uparrow\rangle_A. \quad (8.2b)$$

ROTATION: The state is then rotated into the equatorial plane via a $\pi/2$ pulse. Leaving the ensemble in one of the states

$$|0'\rangle_A = |\leftarrow\leftarrow \dots \leftarrow\leftarrow\rangle_A, \quad (8.3a)$$

or

$$|1'\rangle_A = \frac{1}{\sqrt{N_{\text{at}}}} \sum_{l=1}^{N_{\text{at}}} |\leftarrow\leftarrow \dots \leftarrow \underbrace{\rightarrow}_{l\text{th atom}} \leftarrow \dots \leftarrow\leftarrow\rangle, \quad (8.3b)$$

depending on the success of the spin flip or not (fig. 8.1(c)).

DETECTION: A measurement of the population difference ΔN (fig. 8.1(c)) is made to characterize the state, and we compare the cases with and without an observed click.

As shown in sec. 3.6 we expect significantly different statistics of ΔN for the states $|0'\rangle_A$ and $|1'\rangle_A$ (inset in fig. 8.1(c)). Phrased differently, the detection of a *single photon* fundamentally changes the probability distribution of the atomic ensemble. These differences are due to the negative Wigner function and non-Gaussian marginal distribution of $|1'\rangle_A$. It can be understood as a quantum interference effect between the atoms. Before we describe the actual experiment we consider the required extra additions to the experiment — an excitation beam, single photon detection, polarization and frequency filtering, and a high magnetic bias field. The full setup is shown in fig. 8.2.

8.1.1 Excitation

The excitation laser is derived from the MOT cooler slave (fig. 6.5). To suppress the incoherent background of the diode we use a filtering cavity. Using a single-pass AOM setup we shift its frequency to be resonant with the $|F = 4\rangle \rightarrow |F' = 4\rangle$ transition. It is then coupled into the same single mode fiber taking the probe beams to the MZI (see fig. 6.5). Its frequency can be tuned by controlling the frequency of the cooler master. With the excitation and probe lasers arriving at the MZI via the same single mode fiber the optical excitation and probe modes are identical. This perfect spatial overlap comes at a price, the excitation and probe beams have similar polarizations at the atoms (fig. 8.2). This is a problem since the optimal polarization for state characterization is π as it allows to probe on a closed transition (see sec. 6.3). To excite the atoms on the desired $|\uparrow\rangle \rightarrow |F' = 4\rangle$ transition we require σ^+ or σ^- light.³

Due to the choice of quantization axis (again along the z -axes — see fig. 8.2) we can not address the circular polarizations exclusively but only a superposition of the two, i.e., $x = (\sigma^+ + \sigma^-)/\sqrt{2}$. We make a compromise by taking the beams to be 80% π -polarized and

³ Recall that the $|\uparrow\rangle \rightarrow |F' = 4, m_{F'} = 0\rangle$ transition is forbidden.

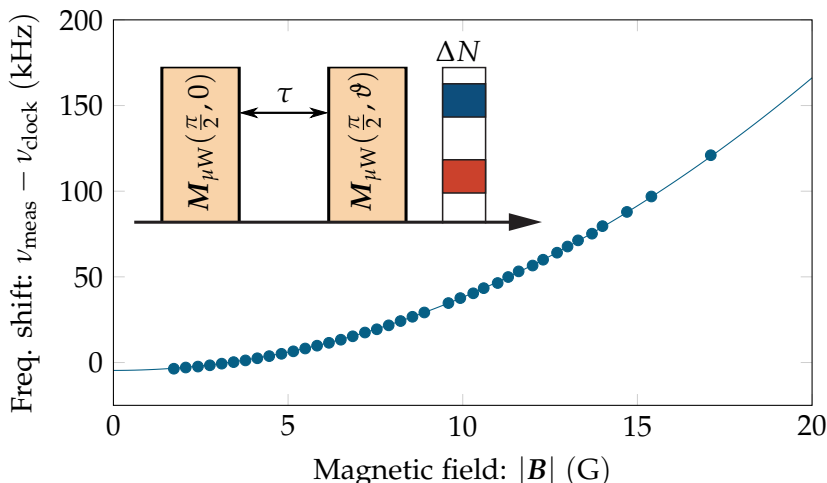


Figure 8.3.: The measured transition frequency between $|\downarrow\rangle \leftrightarrow |\uparrow\rangle$ as a function of applied magnetic field, $|B|$. We observe a clear quadratic dependence, in good agreement with the theoretical value of 427.45 Hz G^{-2} . Note that we have allowed for an offset in the theoretical curve to compensate for other shifts. Inset: The Ramsey sequence used to measure the transition frequency.

20% x -polarized.⁴ With the choice of polarization and quantization axis we will excite to an equal superposition of the $|F' = 4, m_{F'} = \pm 1\rangle$ states. As the Clebsh-Gordan coefficients describing the decay from $|F' = 4, m_{F'} = \pm 1\rangle$ to $|\downarrow\rangle$ have opposite phase, the photons emitted into our detection spatial mode — the forward direction — will interfere destructively.

To break the symmetry we take advantage of the optical Hanle effect (app. D.1) by applying a strong magnetic bias field $|B| \approx 20 \text{ G}$ along the quantization axis.⁵ This magnetic field is much higher than what the compensation coils can produce. We therefore switch the MOT coils from an anti-Helmholtz to a Helmholtz configuration and use these to

⁴ Instead of this one could consider a switchable polarization element. Wanting the experiment to be on the same time scale as for the SSS this requires switching times $\sim 10 \mu\text{s}$ which could be done by a Pockels cell. Due to technical limitations, and the fear of adding an extra potentially noisy element to the MZI this was not implemented.

⁵ From a different viewpoint this corresponds to shifting one of the states $|F = 4', m_{F'} = \pm 1\rangle$ out of resonance with the excitation beam.

create the field. To calibrate the applied field we run a Ramsey sequence (inset fig. 8.3), and measure the transition frequency between the $|\uparrow\rangle \leftrightarrow |\downarrow\rangle$ as a function of the applied magnetic field. We observe a clear quadratic scaling⁶ (fig. 8.3), in agreement with the theoretical value of 427 Hz G^{-2} , [Steck 2010]. Knowing how to drive the probabilistic spin flip we consider how to detect the heralding anti-Stokes photons.

8.1.2 Filtering

From the excited $|F' = 4\rangle$ state the atoms can decay through different channels as shown in fig. 8.4. As we are only interested in the decays to the $|\downarrow\rangle$ state, we need to filter out the other decay channels. Furthermore, the excitation beam (containing several thousands photons) is copropagating with the single photon and also needs to be rejected. The first filtering element is a PBS (fig. 8.2) allowing us to suppress π polarized photons from the excitation beam and decays to $|F, m_F = \pm 1\rangle$ states by 1 : 7000. The second filtering stage is done by two successive Fabry-Pérot cavities. Each with a finesse of $\mathcal{F} = 300$ and a linewidth of $\delta\nu_c = 25 \text{ MHz}$. They reject the excitation beam and decays to $|F = 4\rangle$ by a factor 1 : 2.7×10^8 and their design and operation is well described in [Christensen 2012]. The decay into the $|F = 3, m_F = \pm 2\rangle$ states can currently not be filtered out as the frequency difference to the heralding photon, even at the high magnetic field is on the order of the filter cavity linewidth. The cavities are locked to an auxiliary beam with a variable frequency, via a dither lock. The center frequency of the cavities can thus be set via the frequency of the auxiliary beam.

When tested, the filtering system initially did not perform according to its design specifications. The reason turned out to be the spontaneous emission background of the MOT cooler slave (from which the excitation beam is derived). This was solved by introducing a cleaning cavity (fig. 6.5) into the excitation beam.

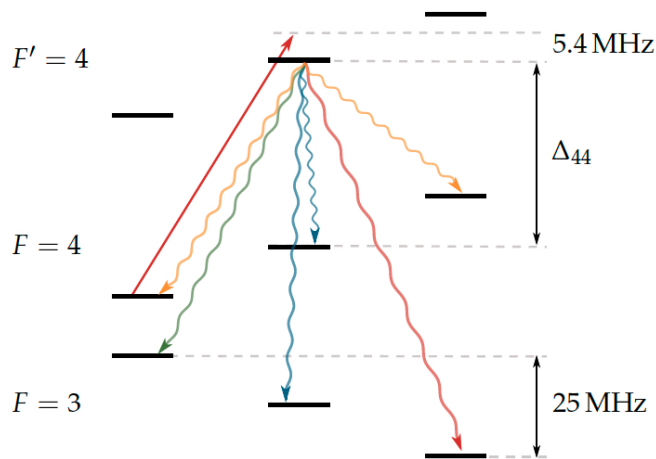


Figure 8.4.: Possible decay channels from the excited state. Considering only $m_F \geq 0$ we have six possible decays. To filter out decays to $m_F = 1$ (blue) we use a PBS. Decays to $F = 4$ (orange) are filtered out via two cavities. The decay to $|F = 3, m_F = 2\rangle$ (red) can not be filtered out as the frequency difference from the desired photons (green) is on the order of the filter cavity linewidth.

8.2 GAIN ESTIMATION

Before we proceed with the main experiment, we want to investigate the Raman scattering model introduced in sec. 5.2. This is done by considering the scaling of the number of emitted photons with the initial CSS amplitude. In app. A.1.2 we show that the expected scaling is

$$N_{\text{ph}} = (1 + N_{\text{at}} \sin^2(\theta)) \sinh^2(|\chi| t) \quad (8.4a)$$

$$\approx (1 + N_{\text{at}} \sin^2(\theta)) |\chi|^2 t^2, \quad (8.4b)$$

where we have assumed the input state

$$|\psi\rangle = |\theta, \phi\rangle_A |0\rangle_L \quad (8.4c)$$

⁶ To compensate for other shifts, from the dipole trap etc. of the transition frequency we allow for an offset in the theoretical curve.

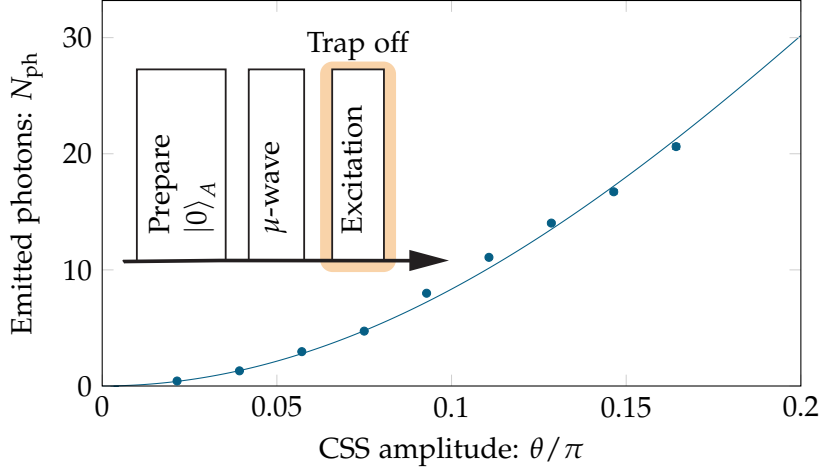


Figure 8.5.: The number of emitted photons as a function of the initial CSS amplitude. We observe the expected quadratic dependence, in agreement with the Raman scattering model presented in sec. 5.2.

and

$$\chi \propto \sqrt{N_{\text{at}}N_{\text{ph,ext}}}. \quad (8.4d)$$

To test this, we perform the experiment shown in the inset of fig. 8.5. After preparing all atoms in the $|\uparrow\rangle$ state we use a microwave pulse with a duration τ to perform a small rotation around the y -axis — creating the CSS, $|\theta, \phi = 0\rangle_A$. The FORT is switched off and an excitation beam with a total of $N_{\text{ph,ext}} = 1.4 \times 10^5$, detuned by $\Delta = 1.5\gamma_e \approx 8$ MHz from the $|\uparrow\rangle \rightarrow |F' = 4, m_F = 0\rangle$ transition and a duration of $10 \mu\text{s}$ is sent. The filter cavity lock is turned off and the SPCM is gated at the same time and will, due to the filtering, mainly count photons of the desired frequency. The data is shown in fig. 8.5 and we compare it to the parametric gain model (eq. (8.4a)). We clearly see the expected quadratic scaling with θ , and conclude that the model and data are in good agreement. Fitting the data to eq. (8.4a) with χ as the free parameter we find the probability to forward scatter a photon of the right frequency into our detection spatial mode for the unseeded process ($\theta = 0$) to be

$$p_{\text{forward}} = 1.4 \times 10^{-10} \frac{N_{\text{at}}N_{\text{ph,ext}}}{4\Delta^2}. \quad (8.5)$$

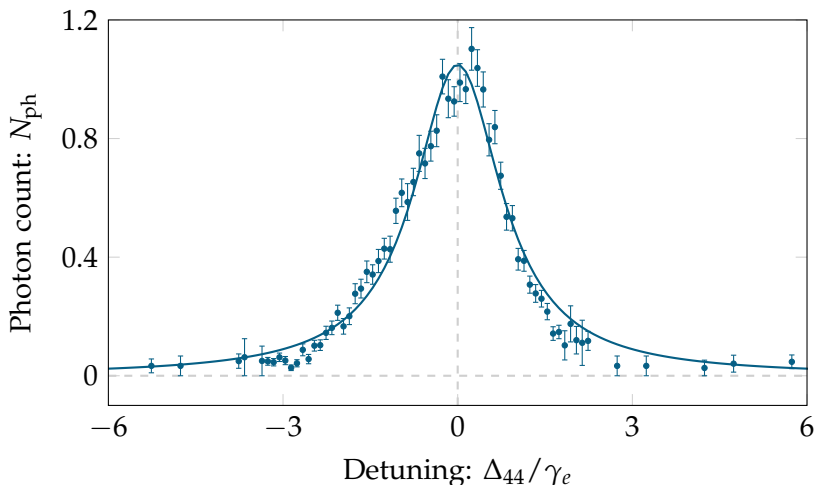


Figure 8.6.: Line Shape of the heralding photons. Fitting a Lorentzian function we find a linewidth of $1.8\gamma_e$. The broadening is ascribed to inhomogeneous shifts from the high magnetic field. We also see an asymmetry of the line shape — for $\Delta_{44} \geq 0$ we detect more photons. We believe this is due to a misalignment of the magnetic bias field and the polarization, meaning that we have more σ^+ than σ^- photons in the excitation beam. Note that the data has been shifted such that the peak is centered at $\Delta_{44} = 0$.

Given an atom number and a detuning we can estimate the number of excitation photons required to get a certain p_{forward} . Taking the experimental relevant numbers of $p_{\text{forward}} = 1\%$, $\Delta = 2\gamma_e$, and $N_{\text{at}} = 250 \times 10^3$ we find $N_{\text{ph,ext}} = 126 \times 10^3$.

We have also measured the line shape of the atomic transition by simply counting the number of emitted photons as a function of the detuning of the excitation beam. As we are driving a Raman transition, the frequency of the emitted photon depends on the frequency of the excitation laser. Therefore, the cavity lock position has to be changed accordingly as the excitation detuning is scanned. Due to human error this optimization was not done for the data presented in fig. 8.6. This will therefore be an underestimate of the actual linewidth. We fit a Lorentzian line shape, and deduce a width of $\gamma = 1.8\gamma_e$. The observed broadening is due to inhomogeneities in the applied magnetic field and the ac Stark shift introduced by the excitation beam. As we are

working in a configuration with a high magnetic bias field, $|\mathbf{B}| \approx 20 \text{ G}$, one would expect to resolve the different excited m_F states. The reason this is not the case is ascribed to inhomogeneous magnetic fields and the missing optimization of the filter cavity lock position. Although we are not able to resolve the excited m_F states, the symmetry has been broken, and due to the Hanle effect (app. D.1) we get the desired forward scattered signal photons.

8.3 SINGLE EXCITATION

At this point we are ready to turn the attention to the main experiment. We start by performing the same optimization procedure as for the SSS (sec. 7.1). The only modification is to set the number of excitation photons as well as optimizing the filter cavity lock position. With this, we proceed with the main experiment. Starting with all atoms in the $|\uparrow\rangle$ state. The FORT is switched off to avoid inhomogeneous effects and an excitation pulse containing $N_{\text{ph,ext}} = 8.9 \times 10^5$ photons⁷ with a duration of $\tau_{\text{exc}} = 2.5 \mu\text{s}$ is sent. A microwave $\pi/2$ pulse rotates the state into the equatorial plane and the FORT is switched back on. The population difference ΔN is measured using 18 dual-color probe pulses, each containing $N_{\text{ph}} = 8.9 \times 10^6$. The atoms are then pumped into $F = 4$, and we measure the total number of atoms N_{at} as for the SSS. This is done four times before the atoms are removed and calibration measurements of the empty MZI and filtering are performed. The filter cavity lock is switched off during the measurements and we rely on the passive stability of the cavities.

Using the calibration measurements we find the probability to scatter a photon of the correct frequency into our detection mode⁸ to be $p_{\text{forward}} = 1.43\%$. This is the ratio of experiments where a single photon was detected⁹ to the total number of runs. With the experiment running for almost three weeks we get $N_{\text{sam}} = 248\,326$ series of $\{t, V_{\text{QND}}, V_{\text{ref}}, N_{\text{ph,det}}\}_i$, each with four measurements for varying atom numbers. Before we compare the cases of when a heralding photon was detected and when it was not we show that even with the higher

⁷ This is the total photon number, i.e., in all polarizations.

⁸ Defined by the collecting single mode fiber.

⁹ This is the number of experiments where we observed a click corrected for dark counts and leakage photons etc.

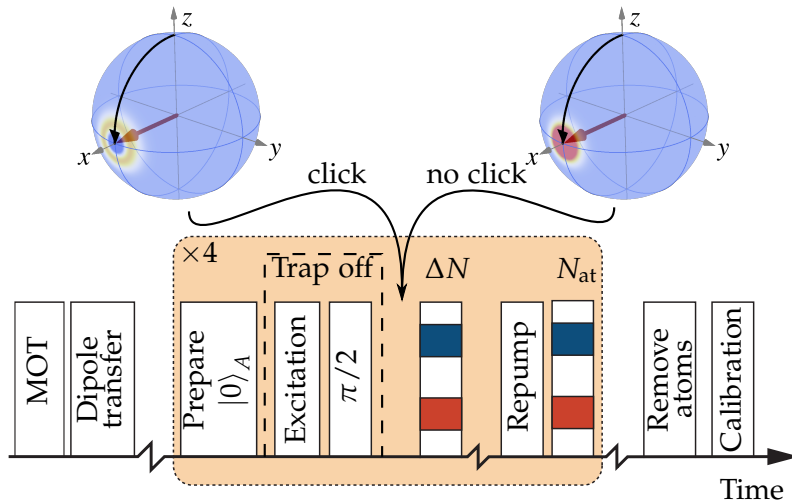


Figure 8.7.: Timing sequence for the single excitation experiment. Starting with all atoms in the state $|\uparrow\rangle$ we switch off the FORT to avoid any inhomogeneous shifts. We send the excitation pulse followed by a $\pi/2$ pulse before the FORT is again switched on. We then use 18 probe pulses to measure the population difference ΔN , before the atoms are repumped into $F = 4$ and the atom number N_{at} is measured. Finally, the atoms are removed from the trap, and we perform calibration measurements.

magnetic bias field and the excitation beam we still resolve the atomic projection noise.

8.3.1 Projection noise

To test if we resolve the projection noise we perform an almost identical analysis to the case of the SSS. The main difference is that to compensate for long term drifts of mean values, we use n -point pulses. This is simply the generalization of the two-point pulses. This is done for two reasons. First if a measurement of $|1'\rangle_A$ is subtracted from $|0'\rangle_A$, it will result in an incorrect estimation of the atomic projection noise. Second, using more files we hope to improve the cancellation of mean value drifts. We proceed in the following fashion:

INTEGRATION: The raw scope traces are integrated to yield a single point per pulse (sec. 6.3.2).

6-POINT PULSES: We find each file where a click was observed and mark the surrounding 12 files as reference measurements which we denote by ϕ . As the click probability is low these will contain purely measurements without a click.¹⁰ This leaves many files unused, for which the procedure is the same — we pick a file and mark the surrounding 12 samples as reference measurements. A crucial point is to make sure that there are no overlapping regions as this would introduce artificial correlations between our samples. From the uncorrected measurements $\tilde{\phi}$ we then get the decorrelated samples as

$$\phi_i = \tilde{\phi}_i - \sum_{\substack{j=-6 \\ j \neq 0}}^6 w_j \phi_i^j. \quad (8.6)$$

The weight factors, w_j are chosen such that $\text{var}(\{\phi_i\})$ is minimized (app. D.2). This leaves us with $N_{\text{sam}} = 20\,694$ for the analysis and have added an extra amount of shot and projection noise corresponding to $\sum w_j^2 = 0.09$ (app. D.2).

BASELINE: We subtract the baseline of the **MZI**, i.e., the signal measured in the absence of atoms. This corrects for any offsets of the **MZI**.

FILTERING: Using *independently* measured quantities, probe powers, locking signals etc., we discard data showing a “non-normal” behavior. With this we are left with $N_{\text{sam}} = 11\,589$. As it was the case for the **SSS**, a large amount of files have been discarded which is due to the experiment operating unsupervised at night.

PHASE SHIFT: We combine 10 pulses and use the power reference and fringe calibration measurement to convert into the corresponding phase shift measurement.

We are thus left with a data set $\{N_{\text{at}}, \phi, N_{\text{ph,det}}\}_i$ and can proceed in a similar fashion as for the **SSS** (sec. 7.3.1).

Without distinguishing between clicks and no-click events we consider $\text{var}(\phi)$ as a function of N_{at} . We perform a noise scaling analysis

¹⁰ To be sure our selection algorithm makes sure this does not happen.

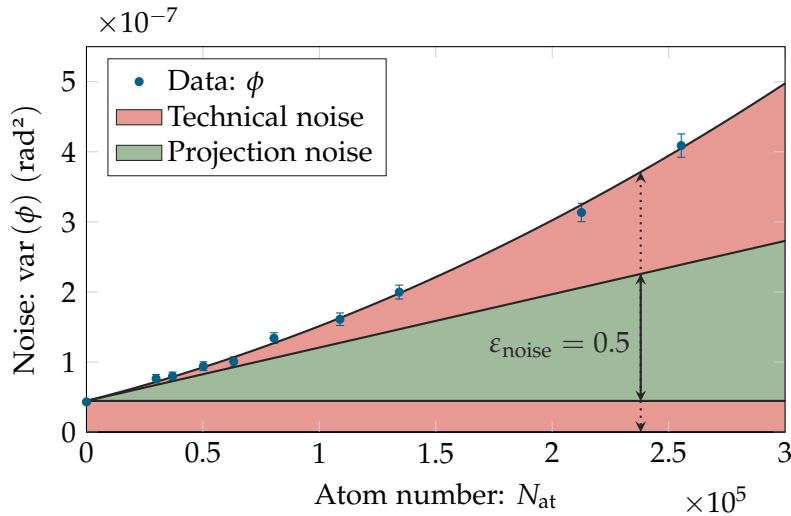


Figure 8.8.: Variance of the noise corrected optical phase shift ϕ , as a function of atom number N_{at} . A noise scaling analysis allows us to distinguish between technical noise (red) which is the shot noise (constant) and classical noise (scaling quadratically). The projection noise (green) scales linearly with the atom number. We deduce the quantum efficiency of the atomic tomography measurement as the amount of projection noise over the total noise to be $\epsilon_{\text{noise}} = 0.5$.

and present the results in fig. 8.8. A predominately linear scaling is observed. In comparison to the data for the SSS (fig. 7.5) extra classical noise, scaling quadratically with N_{at} is present. This is mainly due to the operation at the higher magnetic field where the clock transition $|\downarrow\rangle \rightarrow |\uparrow\rangle$ is magnetically sensitive (17.5 kHz G^{-1}). From the noise scaling we can also deduce the effective quantum efficiency of the atomic state detection, ϵ_{noise} . This is simply the amount of atomic projection noise to the total noise (see eq. (7.18)). For the highest atom number, this reaches values of 50%, and will become important when we model the observed data. In a similar fashion to the SSS (sec. 7.3.2 and app. C.1.1) we make a consistency check of the atom number and probe induced decoherence. We find a good agreement with the data presented in fig. 8.8.

From the measurement of the gain in sec. 8.2, we can also calculate the expected p_{forward} . Inserting the number of excitation photons and

the maximum atom number in eq. (8.5) we find $p_{\text{forward}} = 5\%$. Initially confused by the discrepancy with the measured 1.5%, we now believe that it is due to the multimode nature of the problem. In the seeding experiment the initial CSS makes it more favorable to scatter into our detection spatial mode in comparison to the single excitation experiment. We note that this discrepancy does not matter for the following analysis where we compare the cases with and without a click.

8.3.2 Variance increase

With a projection noise limited sensitivity, we should be able to distinguish the states $|0'\rangle_A$ and $|1'\rangle_A$ from each other. To do this we compare the variances of ϕ in the cases with and without a detected click. The analysis is as follows:

HIGH ATOM NUMBER: We only consider data with $N_{\text{at}} \geq 2 \times 10^5$. Here both the probability to detect a heralding photon and our detection efficiency, $\varepsilon_{\text{noise}}$ is the highest.

SAMPLE VARIANCE: For each measurement outcome we compute the variance of the $M = 200$ surrounding experiments

$$Y_i \equiv \text{var}(\{\phi_{i-M/2}, \dots, \phi_{i+M/2}\}). \quad (8.7)$$

Due to the low p_{forward} these data are mainly no-click¹¹ realizations corresponding to a measurement of $|0'\rangle_A$.

NORMALIZATION: To compensate for slow drifts in the light-atom coupling strength, resulting in a drifting projection noise level, (see eq. (7.4)), each measurement is normalized as

$$Z_i \equiv \frac{\phi_i}{\sqrt{Y_i}}. \quad (8.8)$$

This means that the no-click data ($|0'\rangle_A$) should have a variance of unity.

VARIANCE: The parameter of interest is the variance of this rescaled quantity

$$W_{\mathbf{L}} \equiv \text{var}(\{Z_i\}_{i \in \mathbf{L}}), \quad (8.9)$$

for the cases of $\mathbf{L} = \{i : \text{click}\}$ and $\mathbf{L} = \{i : \text{no click}\}$.

¹¹ On average there will be 3.6 click events in the 200 files.

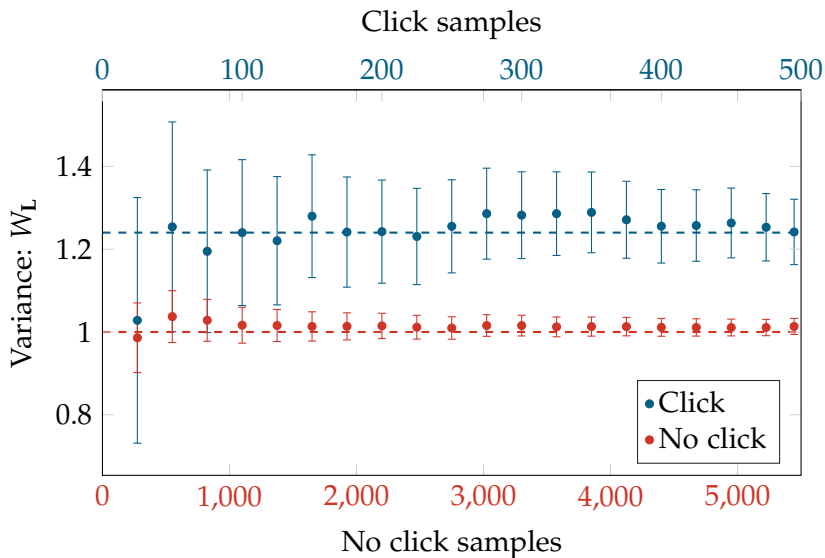


Figure 8.9.: Cumulative variance depending on a click (blue) or not (red). We see that the two cases are clearly distinguishable and a statistically significant increase in the variance is observed when a photon is detected.

The result of this analysis is presented in fig. 8.9, where we show W_L for an increasing number of samples for the click and no-click case. Using the full data set we find

$$W_{\text{no click}} = 1.02 \pm 0.02 \quad (8.10a)$$

$$W_{\text{click}} = 1.24 \pm 0.08. \quad (8.10b)$$

A statistical significant increase in the variance is observed if we condition on a detection click. This is a clear sign that if the photon is detected, the properties of the atomic ensemble has changed.

Due to our normalization procedure the Z_i are not independent. To minimize the effect of this we work in the range where $L \gg M \gg 1$ (app. D.3). The above error estimation is checked both by a bootstrapping method and by sub-dividing our data set (app. D.3). The somewhat disappointing news is that the above variance increase falls short of the expected factor of three, for the collective-single-excitation state (sec. 3.6.3).

8.4 VARIANCE MODEL

To understand quantitatively the observed increase in variance and why it does not reach its expected value — we present a model taking into account the effect of false positive events and the finite quantum efficiency of the tomography measurement. Both effects will result in a reduction of the expected variance increase.

8.4.1 False positives

The first and simplest to consider is the effect of false positive events, i.e., the detector clicked but it was not due to the heralding photon. Such clicks could be due to dark counts, leakage photons or the unfiltered decays to $|F = 3, m_F = \pm 1\rangle$. If this happens, we assign the created state to be $|1'\rangle_A$ but have actually created $|0'\rangle_A$. Conditioned on a click the state is therefore described as a statistical mixture

$$\hat{\rho} = p |1'\rangle_A \langle 1'| + (1 - p) |0'\rangle_A \langle 0'|. \quad (8.11)$$

Here p is the *classical* probability that the state $|1'\rangle_A$ is created conditioned on a click. The effect of the false positives is to decrease the variance as

$$W_{\hat{\rho}} = pW_{|1'\rangle_A} + (1 - p)W_{|0'\rangle_A}, \quad (8.12a)$$

$$= 2p + 1. \quad (8.12b)$$

We thus expect a variance increase of $2p$ for the state $\hat{\rho}$ as compared to $|0'\rangle_A$. From the reference measurements we find the probability for the different click origins (table 8.1) giving

$$p_{\text{state}} = 1 - p_{\text{dark}} - p_{\text{decay}} - p_{\text{ext}}, \quad (8.13a)$$

$$= 0.38. \quad (8.13b)$$

This is the purity of the state for which the expected variance increase is 76% still not in agreement with the observed 24%. The second thing to consider is the finite quantum efficiency of the atomic-state detection.

8.4.2 Finite efficiency

As it is the case for quantum state tomography of optical states, a finite quantum efficiency effectively decreases the quantum features of

Table 8.1.: Probability for clicks with different origins conditioned on the observation of a click.

ORIGIN	NOTATION	PROBABILITY (%)
Dark count	p_{dark}	13
Bad decay	p_{decay}	11
Excitation leakage	p_{exct}	38
Heralding photon	p_{state}	38

interest [Leonhardt 1997, sec. 5.3.1; Lvovsky et al. 2009]. This corresponds to a further reduction of p_{state} and therefore a decrease in the measured variance. We consider several effects reducing the quantum efficiency:

NOISE: The analysis is made on the optical phase shifts which contain both shot noise, atomic noise and classical noise. It is only the variance of the atomic part, that increases with the detection of a heralding photon. The light and classical noise therefore add an independent and Gaussian distributed contribution to the measurements. This will reduce the quantum efficiency [Appel et al. 2007] and from the noise scaling analysis, we find $\varepsilon_{\text{noise}} = 50\%$ (fig. 8.8).

MODE MATCHING: Non-perfect spatial overlap between the atomic excitation mode and the probe mode reduces the efficiency. This is in analogy to the overlap between the quantum field and LO (visibility) in optical homodyne detection, [Leonhardt 1997, sec. 4.2.3]. In our experiment this overlap corresponds to the coupling efficiency of the probe into the single mode fiber defining the excitation mode. In the absence of atoms this is measured to be $\varepsilon_{\text{mm}} = 75\%$.

SCATTERING: It is only coherent atoms in either $|\downarrow\rangle$ or $|\uparrow\rangle$ that are interfered by the microwave pulse. Atoms in other Zeeman states therefore do *not* contribute to the variance increase. To estimate this effect, a separate experiment (fig. 8.10) is performed. First we prepare all atoms in the state $|\uparrow\rangle$, we then switch off the

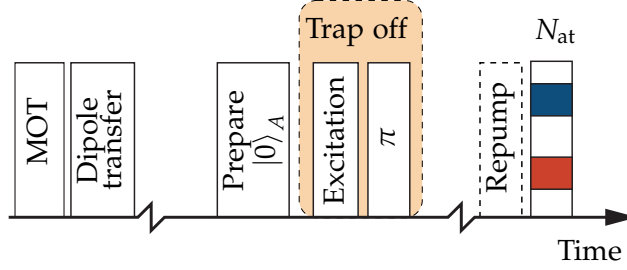


Figure 8.10.: To measure the number of atoms that scatter out of the two level system of interest we perform a separate experiment. Starting with all atoms in the upper state we switch off the FORT and an excitation pulse is sent followed by a microwave π -pulse. This is followed by an optional repumping pulse and a measurement of N_{\uparrow} . From this we find that 23% of the atoms are scattered into other hyperfine levels.

FORT and the excitation pulse¹² is sent followed by a π -pulse before the FORT is switched back on. An optional repumping pulse is sent and the number of atoms in the $|\uparrow\rangle$ state N_{\uparrow} is measured (single-color probe). In the absence of the repumper we measure all atoms that are initially in $|F = 4, m_F \neq 0\rangle$ and $|\downarrow\rangle$. When the repumping pulse is sent *all* atoms in the trap are measured, $N_{\uparrow} = N_{at}$. Comparing the measured N_{\uparrow} in the two cases and using the Clebsch–Gordan coefficients we deduce that $1 - \varepsilon_{scatter} = 23\%$ of the atoms undergo a scattering event.

PHASE SHIFT: Due to the initial atomic population in $|\uparrow\rangle$, the single photon ($|F' = 4\rangle \rightarrow |\downarrow\rangle$) and excitation beam ($|\uparrow\rangle \rightarrow |F' = 4\rangle$) experience different refractive indices as they propagate through the cloud. This results in a phase shift between the two, which effectively decreases the mode-overlap. Using a one-dimensional (1D) model, the phase shift is described by

$$\phi(y) = y\Delta k, \quad (8.14a)$$

$$\Delta k = k_{\mu\text{-wave}} + k_{\text{ext}} - k_{\text{photon}}. \quad (8.14b)$$

¹² With the same number of photons as in the single excitation experiment. We use this experiment to set $N_{\text{ph,ext}}$.

As no atoms are in the $|\downarrow\rangle$ state, the phase mismatch only comes from the excitation beam $\phi_{\text{exct}} = \phi(l_a)$, where l_a is the length of the atomic sample. Assuming that the atoms have a homogeneous distribution this decreases the mode-overlap by

$$\varepsilon_{\text{phase}} = \left| \frac{1}{l_a} \int_0^{l_a} e^{-i\phi(y)} dy \right|^2 \quad (8.15a)$$

$$= \text{sinc}^2(\phi_{\text{exct}}/2), \quad (8.15b)$$

as shown in app. D.4. We are thus interested in estimating the phase shift of the excitation beam ϕ_{exct} .

From Clebsh-Gordon coefficients we can relate this to the phase shift of the QND probing ϕ_{probe} in the following way. The resonant optical depth on a cyclic, $|F = 4, m_F = 4\rangle \rightarrow |F' = 5, m_{F'} = 5\rangle$ transition is denoted by α_0 . As derived in sec. 4.1.1 light propagating through a medium will experience a phase shift

$$\phi(\Delta, \alpha_0) = \frac{\alpha_0}{4} \sum_m \wp_m \frac{\Delta_m}{\Delta_m^2 + (\gamma_e/2)^2}, \quad (8.16)$$

where Δ , is the detuning and \wp_m is the strength of the m^{th} transition. From the atom number measurement, where all atoms are in $F = 4$, we measure an optical phase shift corresponding to an optical depth of $\alpha_0 = 31$. From this, using the above equations, we find $\phi_{\text{exct}} = 42^\circ$, giving $\varepsilon_{\text{phase}} = 95\%$. This is a small effect in comparison to the detection noise and mode-mismatch.

AC STARK SHIFT: The excitation beam induces a light shift on the $|\uparrow\rangle$ and the excited $F' = 4$ states as it propagates through the atomic cloud. This directly leads to a dephasing of the spin wave [Hammerer et al. 2010], reducing the expected variance increase. To model this we consider the spatially inhomogeneous shift of the $|\uparrow\rangle$ state. With the atomic cloud being short compared to the Rayleigh length of the probe beam we only consider transverse effects. From Hammerer et al. [2010] we have

$$\varepsilon_{\text{ac-Stark}} = \frac{\int_0^{\tau_{\text{exc}}} \left| \iint \varrho_{\text{at}}(x, z) I(x, z)^2 e^{-i\omega_{\text{LS}}(x, z)t} dx dz \right|^2 dt}{\tau_{\text{exc}} \left| \iint \varrho_{\text{at}}(x, z) I(x, z)^2 dx dz \right|^2}. \quad (8.17)$$

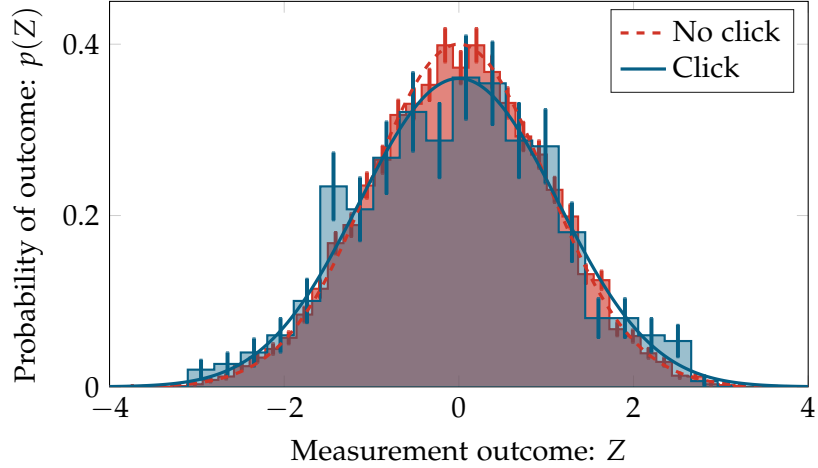


Figure 8.11.: Histograms of the measurement outcomes for click (blue) and no click (red) with the gray dark region as their overlap. The full lines are the expected probability distributions derived in sec. 3.6.1, taking into account that the single excitation state is non-pure according to the model explained in the text.

Here $I(x, z)$ is the transverse Gaussian intensity profile of the beam and $\varrho_{\text{at}}(x, z)$ is the atomic column density, and the integration over x and z is over all space. The relevant frequency shift is $\omega_{\text{LS}}(x, y) \propto I(x, z)$ and τ_{exc} is the pulse duration. The fourth power of the intensity comes from carrying a squared mode function from the classical and the quantum field [Hammerer et al. 2010]. Numerical evaluation yields $\varepsilon_{\text{ac-Stark}} = 97\%$, again a small contribution.

Combining all these inefficiencies we find a total detection efficiency of $\varepsilon = 27\%$. This non-perfect detection corresponds to an extra vacuum admixture [Appel et al. 2007], which effectively decreases the state purity

$$p_{\text{mod}} = p_{\text{state}}\varepsilon \quad (8.18a)$$

$$= 10\%. \quad (8.18b)$$

The corresponding variance of 20% (eq. (8.12)) is in good agreement with the measured $24 \pm 8\%$.

To compare the model and the data, a histogram of the measurement outcomes Z_i for the click and no-click case is shown in fig. 8.11. In the figure, we also plot the theoretical expected measurement outcomes. For the no-click case this is $p_0(\Delta N)$ (eq. (3.40)). Whereas for the click case this is

$$p_{\hat{\rho}}(\Delta N) = p_1(\Delta N)p_{\text{mod}} + p_0(\Delta N)(1 - p_{\text{mod}}), \quad (8.19)$$

where $p_1(\Delta N)$ is given in eq. (3.47). From fig. 8.11 two things can be seen. First, the measurement and theoretical predictions are in agreement. Second, comparing the case of a click and no-click we see a slight change in the distribution of measurement outcomes.

8.5 MULTIPLE EXCITATIONS

The observed variance increase could be due to higher order excitations or classical effects.¹³ To support our claim that the observed variance increase is due to the creation of a (non-pure) collective-single-excitation state we perform a careful analysis of the excitation statistics conditioned on a detected click.

The quantity of interest is the probability that the n^{th} AFS is created *conditioned* on the detection of a single click. Using Bayes formula we write this as

$$p(n|1\text{click}) = \frac{p(n)p(1\text{click}|n)}{p(1\text{click})}. \quad (8.20)$$

Here $p(n)$ is the probability to scatter n photons of the correct frequency into the desired detection mode. The probability to have n photons with a frequency corresponding to a decay into $|\downarrow\rangle$ follows a thermal distribution (eq. (5.17b))

$$p_{S0}(n) = (1 - p_0) p_0^n, \quad (8.21)$$

here p_0 is the probability to generate at least one of the desired photons, i.e., p_{forward} . Photons corresponding to the unfiltered decay into $|F = 4, m_F = \pm 2\rangle$ also follows a thermal distribution

$$p_{S2}(n) = (1 - p_2) p_2^n. \quad (8.22)$$

¹³ It does not require a vivid imagination to come up with effects that would make a minimum uncertainty state, more noisy.

Here p_2 is the probability to scatter at least one of these photons into our detection spatial mode.¹⁴ In contrary false positive events from dark counts and leakage¹⁵ are Poissionian distributed

$$p_{\text{DE}}(n) = \frac{p_{\text{f}}^n e^{-p_{\text{f}}}}{n!}, \quad (8.23)$$

where $(1 - p_{\text{f}})$ is the probability to get at least one false positive from either dark counts or leakage.

To calculate the probability to get false positive events from the decay into $|F = 4, m_F = \pm 2\rangle$, we introduce our detection probability $p_{\text{d}} = 0.8^2 \times 0.56 \times 0.5 = 0.18$. The factors are the transmission through the two filter cavities, other optical losses in the path and the quantum efficiency of the SPCM. If m photons are emitted the probability to detect n of these is given by the Binomial distribution

$$p_{\text{DS2}}(n) = \sum_{m=n}^{\infty} p_{\text{S2}}(m) \binom{m}{m-n} \tilde{p}_{\text{d}}^{m-n} p_{\text{d}}^n, \quad (8.24a)$$

$$= \frac{(1 - p_2) (p_2 p_{\text{d}})^n}{(1 - p_2 \tilde{p}_{\text{d}})^{n+1}}, \quad (8.24b)$$

where $\tilde{p}_{\text{d}} = 1 - p_{\text{d}}$. This allows us to find the probabilities to either have no or a single false positive event

$$p_{\text{F}}(0) = p_{\text{DE}}(0) p_{\text{DS2}}(0), \quad (8.25a)$$

$$p_{\text{F}}(1) = p_{\text{DE}}(1) p_{\text{DS2}}(0) + p_{\text{DE}}(0) p_{\text{DS2}}(1). \quad (8.25b)$$

The probability to detect a single click given n photons emitted into our desired mode is then

$$p(1\text{click}|n) = n p_{\text{d}} \tilde{p}_{\text{d}}^{n-1} p_{\text{F}}(0) + \tilde{p}_{\text{d}}^n p_{\text{F}}(1). \quad (8.26)$$

The first term is the probability that exactly one of the n photons gives a click while no false positive event happened. The second term is the probability that none of the n emitted photons gives a click while exactly one false positive event gives a click.

The remaning unknown in eq. (8.20) is $p(1\text{click})$, which can be found via the normalization condition $\sum_n p(n|1\text{click}) = 1$ giving

$$p(n|1\text{click}) = \frac{\tilde{p}_{\text{d}}^n p_0^n (1 - \tilde{p}_{\text{d}} p_0) \left(n \frac{p_{\text{d}}}{\tilde{p}_{\text{d}}} + p_{\text{f}} + \frac{p_{\text{d}} p_2}{1 - \tilde{p}_{\text{d}} p_2} \right)}{p_{\text{f}} + \frac{p_{\text{d}} p_2}{1 - \tilde{p}_{\text{d}} p_2} + \frac{p_{\text{d}} p_0}{1 - \tilde{p}_{\text{d}} p_0}}. \quad (8.27)$$

¹⁴ This can be found directly from the Clebsh-Gordon coefficients and p_{forward} .

¹⁵ Mainly from the excitation beam.

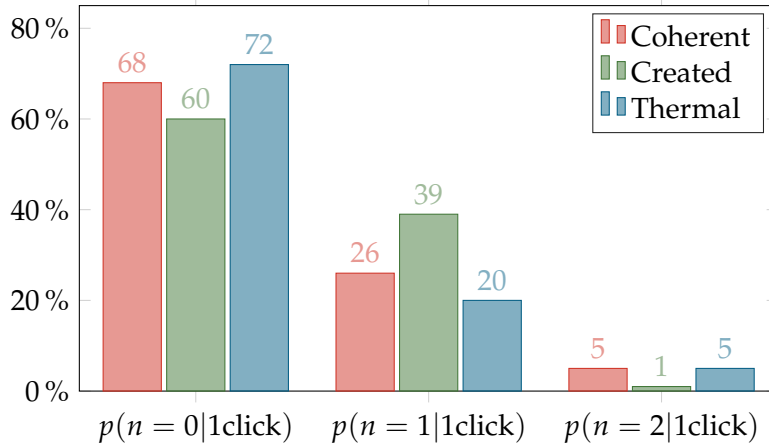


Figure 8.12.: Probability of having n excitations for the created state, a coherent state and thermal state with same mean photon number. We clearly see that the single excitation component of the created state is not compatible with neither the coherent nor thermal state. Note that the reason the thermal state does not add up to 100% is that we have not included $p(n \geq 3|1\text{click})$.

Evaluating for the first few values of n we find

$$p(n=0|1\text{click}) = 0.606 \pm 0.021, \quad (8.28a)$$

$$p(n=1|1\text{click}) = 0.385 \pm 0.021, \quad (8.28b)$$

$$p(n=2|1\text{click}) = 0.009 \pm 0.001. \quad (8.28c)$$

This is the conditioned excitation probability for the created mixture state $\hat{\rho}$. To benchmark these numbers we compare them to the expected distribution for a coherent and thermal state with an identical mean excitation number of 0.39 (see fig. 8.12). We see that $p(n=1|1\text{click})$ is significantly higher, and incompatible, with both the thermal and coherent state. The above error has been found through Gaussian error propagation of eq. (8.27) where the largest contribution comes from the measurement of the detection probability p_d .

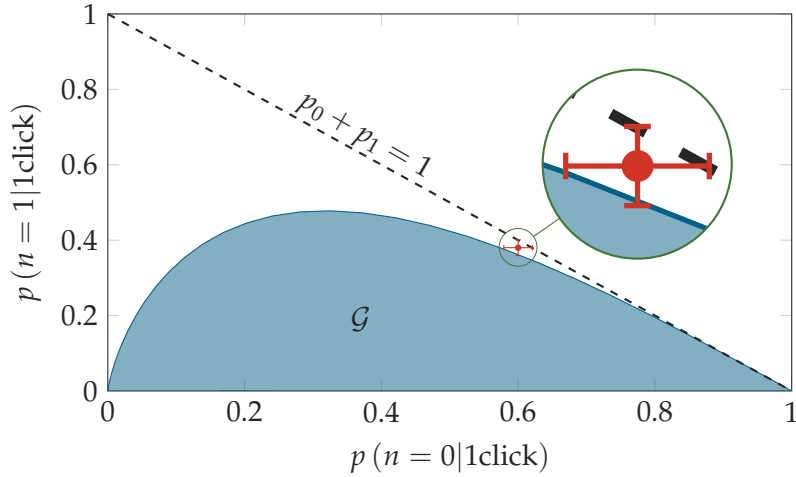


Figure 8.13.: Non-Gaussianity criteria. All Gaussian states lie in the blue region marked by \mathcal{G} . Using eq. (8.28) we find the red point.

8.6 NONCLASSICALITY AND NON-GAUSSIANITY

With the prospect of the collective-single-excitation being both nonclassical and non-Gaussian we consider if these features can be inferred from our data.

As described in sec. 2.2.1 and 7.4 a negativity of the Wigner function is a clear sign of a nonclassical state.¹⁶ The created state is a mixture of the collective-single-excitation and CSS (vacuum) state,

$$\hat{\rho} = p |1'\rangle_A \langle 1'| + (1-p) |0'\rangle_A \langle 0'|. \quad (8.29)$$

It can be shown that negative values of the Wigner function requires $p > 0.5$. As we have $p_{\text{mod}} = 10\%$, no negativity is expected.

The other possibility is to test for nonclassicality using the criterion by Vogel [2000] (sec. 7.4). Lvovsky et al. [2002] showed that no matter the amount of vacuum admixture to the single excitation state it is still nonclassical according to this criterion. Furthermore, the article considers the number of samples required to show this nonclassicality for a given vacuum admixture. From [Lvovsky et al. 2002, fig. 2] we see that for $p_{\text{mod}} = 10\%$ it would require $\sim 10^{10}$ samples. With only

¹⁶ This is no matter which definition of nonclassicality that is used.

495 samples it would be impossible to infer any nonclassicality of the created state using this method. The last predicted property of the state is the non-Gaussian distribution of the measurement outcomes (sec. 3.6.3). We test for this in two ways:

EXCITATION PROBABILITY: In [Filip et al. 2011; Ježek et al. 2011] a simple criterion to test non-Gaussianity based on excitation probabilities was derived. For the case of $p(n \geq 2 | \text{1click}) \ll 1$ an optimization over all Gaussian states was performed. It was found that all mixtures of Gaussian states lie in the blue region labeled \mathcal{G} in fig. 8.13. With the conditioned probabilities and their corresponding errors (eq. (8.28)) we can compare the created state (red point in fig. 8.13) to this criterion. We see that the mean of the point lies in the non-Gaussian region, but when the errors are taken into account the point overlaps with the Gaussian region. We can therefore not, with statistical significance, claim any non-Gaussian features of the created state.

CUMULANT: Dubost et al. [2012] described how cumulants can be used to test for non-Gaussianity. The idea is simply to consider the fourth cumulant

$$\kappa_4 = \mu_4 - 3\mu_2^2 \quad (8.30)$$

where μ_n denotes the n^{th} moment. As all Gaussian distributions have $\kappa_4 = 0$, a test for non-Gaussianity can be made by estimating κ_4 from the data — if $\kappa_{4,\text{est}} \neq 0$, the state is non-Gaussian.

We estimate the fourth cumulant and its error in three different ways. First, we use k -statistics which are the unbiased estimators of the cumulants. The relevant formulas to evaluate these and their variance can be found in [Kenney et al. 1951]. Second, we sub-divide our data set into five bins of equal size. We then find the fourth cumulant in each subset, together with the mean and standard deviation. Third, we use a bootstrapping method.

From table 8.2 we see that the three methods agree and that $\kappa_{4,\text{est}}^{(\text{click})} \neq 0$ with about one standard deviation of significance. We do however also see that $\kappa_{4,\text{est}}^{(\text{no click})} \neq 0$, making it incompatible with the expected Gaussian (eq. (3.40)). The reason for this is still not understood but could be related to the normalization procedure, outliers in the data, or

Table 8.2.: Estimated fourth cumulants and corresponding statistical error.

L	METHOD	$\kappa_{4,EST}$
Click	<i>k</i> -statistics	-0.4 ± 0.2
	Sub-divide	-0.5 ± 0.3
	Bootstrapping	-0.4 ± 0.2
No-click	<i>k</i> -statistics	-0.2 ± 0.1
	Sub-divide	-0.2 ± 0.1
	Bootstrapping	-0.2 ± 0.1

simply the coincidence¹⁷ that our experiment is a 2σ event. Assuming the latter is the case and using the fact that the cumulants are additive we can subtract $\kappa_{4,est}^{(no\ click)}$ from $\kappa_{4,est}^{(click)}$. Doing this the click data becomes compatible with a Gaussian — in agreement with the other criterion. With all of the used criteria for nonclassicality and non-Gaussianity being unsuccessful we now consider possible improvements.

8.7 IMPROVEMENTS

Having showed that the observed variance increase is due to the collective-single-excitation state, the natural question to ask is which improvements could lead to the detection of associated nonclassical and non-Gaussian features.

EXCITATION LEAKAGE: The biggest contribution in decreasing p_{state} is from leakage of the excitation beam (table 8.1). This could be addressed in two ways. Either we improve the filtering ratio of the two cavities, i.e., narrow their linewidth or we simply decrease the number of excitation photons used. The latter is not feasible as it would also decrease the probability of actually generating the heralding photon ($p_{forward}$) thus increasing the experimental run time.¹⁸ If however we could increase the collection efficiency we would, keeping the same $p_{forward}$, be able to use fewer ex-

¹⁷ Having numerically confirmed that $\kappa_{4,est}$ for normally distributed data is Gaussian distributed, a 2σ event should happen with a 5% chance.

¹⁸ Recall that for the presented data the experiment was kept running for three weeks.

citation photons.¹⁹ To improve the filtering we can increase the finesse of each of the cavities by using a new set of cavity mirrors with a higher reflection or increasing the cavity length.²⁰

BAD DECAY FILTERING: Another possible improvement would be the filtering of the photons originating from the decay to $|F = 3, m_F = \pm 2\rangle$. The simplest way to improve this would again be by decreasing the linewidth of the filter cavities by increasing their finesse or the cavity length.

DARK COUNT RATE: To decrease the number of dark counts two things can be done. Either we get a new **SPCM** with a lower dark count rate, ν_{dark} or we reduce the gating time τ_{exc} . The current detector has $\nu_{\text{dark}} \approx 250$ Hz using commercially available state of the art **SPCM**²¹ this can be improved to $\nu_{\text{dark}} \approx 25$ Hz without loss in quantum efficiency.

All of the above are “simple” technical improvements, which should increase the state purity to be $p_{\text{state}} \approx 70\%$, allowing for the observation of both non-Gaussianity as well as the negativity of the Wigner function. The state purity and characterization would be comparable to state of the art experiments where the excitation is mapped onto an optical state and then characterized [Bimbard et al. 2014].

8.8 SUMMARY

In this chapter we have presented the second experimental result of the thesis — the creation of a (low purity) collective-single-excitation state in an atomic ensemble. Starting by recapping the idea behind the state generation we discussed the extra experimental requirements — a high magnetic bias field and frequency and polarization filtering. After this a detailed description of how the experiment was performed and analyzed was presented. Two main results were obtained. First, it were shown that the experiment resolves the atomic projection noise. Second, comparing the variance of the measurement outcomes for the click and no click case a difference of 24% was observed — a clear

¹⁹ This possibility is discuss in sec. 9.5.

²⁰ For a different project in the group, we are currently developing stable filtering cavities with a linewidth of $\delta\nu_C \leq 100$ kHz.

²¹ This could for instance be a Perkin-Elmer SPCM-AQRH-16.

signature of the collective-single-excitation state. To quantitatively explain the variance increase a detailed model, considering false positive events and the finite quantum efficiency of our detection was introduced. The model and data were in excellent agreement. A careful investigation of the counting statistics was made, showing that the observed state is incompatible with both a coherent and thermal state. Finally a discussion of possible improvements which would allow for the detection of a non-Gaussian state with a negative Wigner function was presented.

NANOFIBER-TRAPPED ATOMIC ENSEMBLE

In the last chapters we described experiments using an atomic ensemble trapped in a [FORT](#). In this chapter we instead consider the newest experimental venture of our group — a nanofiber based light-atom interface. We start by addressing the question of why a new setup is required. This is followed by a short description of the used trapping and probing methods. We then consider two experiments. First, the atom number and the optical depth per atom is determined by measuring optical pumping transients. Second, we present an experiment showing the measurement and preparation of an ensemble with a sub-Poissonian atom number distribution. This leads to a feasibility study where we consider the performance of the setup for state tomography and generation. Much of the experimental work was done by Jean-Baptiste Béguin who was later joined by Eva Bookjans and my role has mainly been in the initial steps,¹ model development, and data analysis. The chapter is based on [Béguin et al. 2014].

9.1 WHY A NANOFIBER?

With the quantum noise limited performance and shown state preparation capability of the [MZI](#) setup a natural question to ask is — why are we building a new setup? To understand this we start by recapping the main insights gained in the previous chapters:

OPTICAL DEPTH: The central parameter for the squeezing experiment was the resonant optical depth α_0 (see eq. (5.8)) the higher α_0 the more squeezing. The optical depth is not only central for the creation of a [SSS](#) but for a large range of applications with light-atom interfaces [Hammerer et al. 2010]. The optical depth can be increased by either using more atoms or increasing the light-atom coupling strength.

¹ Transfer of the fiber to the vacuum setup, building [MOT](#) coils and optics for the [MOT](#) beams.

CLASSICAL NOISE: From the noise model presented in sec. 7.3.1 it is clear that one of the biggest enemies is the classical noise, scaling quadratically with the number of atoms. To minimize this it is desirable to have as few atoms as possible. It is therefore preferable to increase the optical depth through the light-atom coupling strength.

REPETITION RATE: Interested in the second and higher order moments of the measurement outcomes (sec. 8.6) we require a large amount of samples to infer these from experiments. Therefore, to lower the overall experimental time, a high repetition rate is desirable.

To build a light-atom interface with these properties we use a tapered nanofiber. This is a conventional step-index optical fiber where the diameter have been reduced to $\sim 1 \mu\text{m}$ over a few mm. As light can be effectively coupled in and out of the tapered section [Ding et al. 2010; Hoffman et al. 2014] and atoms can be trapped in the evanescent field, this system addresses all of the above criteria. The light-atom coupling is high due to the small quantization volume.² For a few thousand atoms we measure resonant optical depths of $\alpha_0 \approx 20$ comparable to the free space setup. With so few atoms, the classical noise is expected to be small compared to the atomic projection noise. This should give a high atomic tomography efficiency $\varepsilon_{\text{noise}}$ (eq. (7.18)). With the low atom number we also hope to push the trap loading time into the ms range, allowing for a similar increase of the repetition rate.

Besides the direct relation to the topics of the previous chapters this system also opens up for several other avenues:

SCALABILITY: Since the tapering from the conventional fiber to the nanofiber can be made almost lossless the trapped ensemble can be integrated as nodes in quantum networks [Kimble 2008]. A first step towards this would be the implementation of teleportation or memory protocols between two ensembles — inspired by the work of [Sherson et al. 2006; Jensen et al. 2010; Krauter et al. 2013].

FIBER-COUPLED ATOMS: With atoms trapped in the evanescent field of the fiber guided light, coupling atoms to other systems should be

² This is set by the size of the evanescent field which decays as $\exp(-r/\lambda)$ confining the light to a few μm , in comparison to the $\approx 30 \mu\text{m}$ in the free space setup.

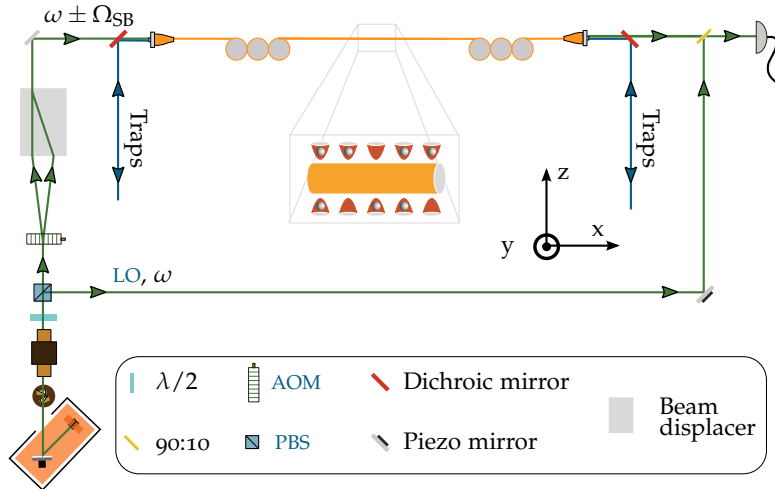


Figure 9.1.: Experimental setup. From a ECDL two sidebands are generated via a AOM. They are overlapped using a beam displacer and combined with the two trapping beams on a dichroic mirror after which they are coupled into the nanofiber. At the output the probe and traps are filtered out by a dichroic mirror. Afterwards the probe is overlapped with the LO and the beat-note is detected.

straight forward. The great prospect of this comes with the fact that systems ranging from mechanical [Aspelmeyer et al. 2013] to solid-state [Lodahl et al. 2013] have been coupled to light. To take the next step and couple such systems to a fiber-trapped ensemble, would “only” require to couple light into the nanofiber. This has given rise to the term “fiber-coupled atoms”.

9.2 EXPERIMENTAL SETUP

In this section we briefly outline the methods for atom trapping and probing. The main experimental work was done by Jean-Baptiste Béguin and will be part of his PhD thesis [Béguin n.d.]. We therefore keep it short and only give enough information to understand the two experiments we have conducted so far.

TRAPPING: Several different trapping configurations have been proposed [Sagué et al. 2008; Lacroûte et al. 2012]. We follow the original idea by Le Kien et al. [2004], which led to the first nanofiber trapped ensemble [Vetsch et al. 2010]. Using a combination of light fields the strong van der Waal force from the fiber can be overcome and at the same time stable trapping potentials for the atoms can be created. We use a blue-detuned trap $\lambda_{\text{blue}} = 780 \text{ nm}$ with a power of $P_{\text{blue}} = 10 \text{ mW}$ and a standing wave red-detuned trap $\lambda_{\text{red}} = 1057 \text{ nm}$ with a total power of $P_{\text{red}} = 2 \times 0.9 \text{ mW}$. The traps are overlapped with the probe beam using dichroic mirrors and coupled into a nanofiber with a diameter of 500 nm (fig. 9.1). The red and blue detuned traps have orthogonal polarizations in the fiber and form two standing wave potentials with local trapping minima $U_{\text{trap}} = -0.2 \text{ mK}$ at a distance $d_{\text{trap}} \approx 200 \text{ nm}$ above and below the fiber surface (fig. 9.2). The trap is expected to operate in the collisional blockage regime, where there is only a single atom per trapping site.³ Note that the trapping configuration is very sensitive to the power balancing of the two traps. If it is off by 10 % the trap is almost completely gone.

PROBING: To probe the atomic ensemble we measure atoms⁴ in $F = 4$ using a method closely related to the dual-color probing method used in the MZI setup (sec. 6.3). The setup is shown in fig. 9.1. Two sidebands detuned by $\Omega_{\text{SB}} = \pm 2\pi \times 62.5 \text{ MHz}$ from the $F = 4 \rightarrow F' = 5$ resonance are created by an AOM. They are then overlapped using a beam-displacer before they are coupled into the nanofiber. The atoms imprint a phase shift of ϕ with opposite sign on each sideband (chap. 4). The probes are then mixed with a *common* optical local oscillator (LO) and the beat-note signal is detected. Mixing the signal to a direct current (DC) with an I/Q mixer we detect both the phase shift and the combined absorption of the two sidebands.

The phase resolution is set by the shot noise of light and is [Béguin et al. 2014, eq. (S12)]

$$\delta\phi = \frac{1}{2\sqrt{\epsilon N_{\text{ph}}}}. \quad (9.1)$$

³ This has never been experimentally verified.

⁴ We have not (yet) introduced hyperfine pumping allowing us to distinguish different m_F states for this experiment.

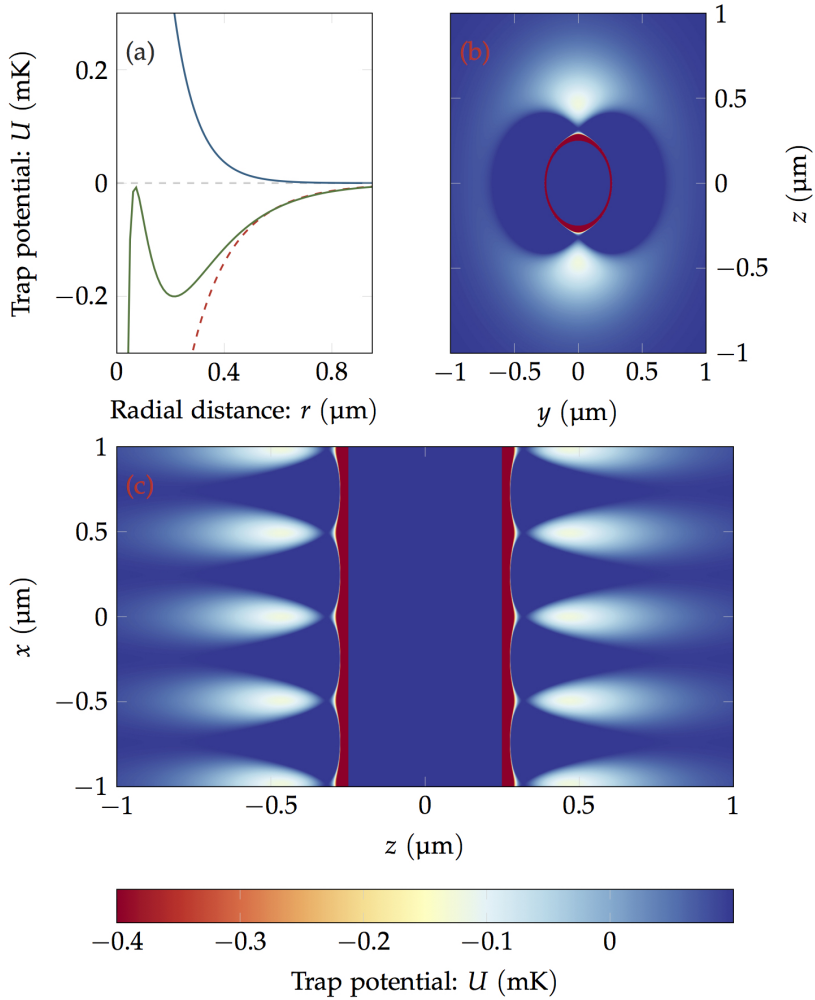


Figure 9.2.: Calculated trap potentials for a fiber of radius $a = 250$ nm and powers and wavelengths as given in the text. (a) Potentials as a function of the radial distance r , for $y = x = 0$. In red the red-detuned trap, blue the blue detuned trap, and green the combined potential taking into account the van der Waals potential from the fiber. (b) Potentials in the yz plane for $x = 0$. (c) Potentials in the xz plane for $y = 0$.

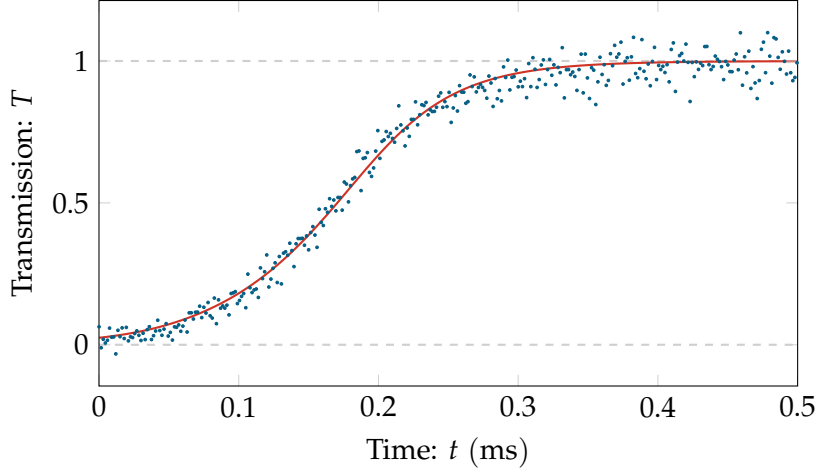


Figure 9.3.: Probe transmission as a function of time, blue points are the average over 179 experiments. The red line is the average of the individual fits to eq. (9.7) giving $N_{\text{at}} = 1605$. The data points have been decimated for the visual presentation.

Here N_{ph} denotes the *total* number of photons (in both sidebands) and ϵ is the effective quantum efficiency of the detection given by

$$\epsilon = \mathcal{T}^2 \epsilon_{\text{QE}} (1 - \tau) \epsilon_{\text{elec}} \quad (9.2a)$$

$$= 0.4. \quad (9.2b)$$

Here $\epsilon_{\text{QE}} = 0.89$ is the detector quantum efficiency, $\tau = 0.7$ is the losses from the fiber to the detector,⁵ $\epsilon_{\text{elec}} = 0.73$ is the ratio of electronic noises to shot noise, and $\mathcal{T}^2 = 0.89$ is the visibility. To stabilize the path-length difference between the LO and the probes a dither lock is implemented. The shot noise limited operation is shown by measuring the Allan variance and is in agreement with the predictions from eq. (9.1) [Béguin et al. 2014, fig. S1].

9.3 ATOM NUMBER

With the experimental setup limited by the shot noise of light we determine the atom number by measuring optical pumping transients.

⁵ Mainly from an optical isolator with a transmission of ≈ 0.8 inserted to prevent resonant back-scattering.

With all atoms in $F = 4$ we use a *single* sideband resonant with the $F = 4 \rightarrow F' = 4$ transition. An atom excited to $F' = 4$ can decay to both $F = 4$ and $F = 3$. The latter is far-detuned from our probe laser, and do therefore not interact with the light. The average number of photons it takes to pump an atom from $F = 4$ to $F = 3$ can be calculated from the branching ratios (sec. E.1). We therefore simply need to “count” the number of photons it takes to bleach the ensemble transparent from which the atom number can be determined.⁶ The experiment is made 10 ms after a sub-Doppler cooling phase and the data are shown in fig. 9.3. In agreement with the qualitative description above, the probe is initially fully absorbed and for long times (when all atoms are in $F = 3$) we observe a fully transparent ensemble.

To understand the experiment on a quantitative level we present a simple model describing the optical depth as a function of time. Considering a three level system (fig. 9.4) the number of atoms in $F = 4$ changes according to

$$\frac{dN_{\text{at},4}}{dt} = \frac{1}{q} (\Phi_{\text{in}}(t) - \Phi_{\text{out}}(t)). \quad (9.3)$$

Here $q = 2.4$ is the number of scattering events it on average takes to pump an atom from $F = 4$ to $F = 3$ (app. E.1) and Φ_{in} (Φ_{out}) is the input (output) photon flux. The change of photon flux follows Lambert-Beer’s law

$$\frac{d\Phi_{\text{out}}(t)}{dt} = \Phi_{\text{in}}(t) \exp[-N_{\text{at},4}(t)\alpha_{\text{at}}], \quad (9.4)$$

where α_{at} is the optical depth per atom. Combining eqs. (9.3) and (9.4) and taking a constant input flux we get

$$\frac{d\alpha(t)}{dt} = -\frac{\alpha_{\text{at}}}{q} \Phi_{\text{in}} [1 - \exp(-\alpha)], \quad (9.5)$$

with $\alpha = N_{\text{at},4}\alpha_{\text{at}}$. The solution to this differential equation is

$$\alpha(t) = \ln \left[1 + \left(e^{\alpha(t=0)} - 1 \right) \exp(-\alpha_{\text{at}}\Phi_{\text{in}}t/q) \right]. \quad (9.6)$$

From which we find the transmission using Lambert-Beer’s law

$$T(t) = \frac{1}{1 + [\exp(\alpha_{\text{at}}N_{\text{at},4}) - 1] \exp(-\alpha_{\text{at}}\Phi_{\text{in}}t/q)}. \quad (9.7)$$

⁶ A similar method has been used to count the number of Bragg excitations in a degenerate quantum gas [Pino et al. 2011].

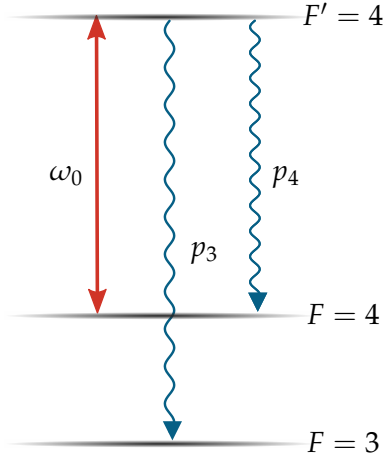


Figure 9.4.: Three level atom with a resonant probe on the $F = 4 \rightarrow F' = 4$ transition. An excited atom in the $F' = 4$ state can decay to either the $F = 4$ or $F = 3$ ground-state with the rates p_4 and p_3 .

The only free parameters in this expression is the optical depth per atom, and the number of atoms.

Using the measured power $P = 5.0$ pW we fit eq. (9.7) to each of the 200 realizations with $N_{\text{at},4} = N_{\text{at}}$ and α_{at} as the free parameters. In the following we only consider experiments where $N_{\text{at}} \geq 1000$ leaving us with 179 realizations. The average of the fitted traces are shown in fig. 9.3 and are in good agreement with the data. Taking the mean of the individual fit parameters we find the following estimates⁷

$$\langle N_{\text{at}} \rangle_{\text{est}} = 1605 \pm 4(\text{stat}) \pm 161(\text{sys}) \quad (9.8a)$$

$$\langle \alpha_{\text{at}} \rangle_{\text{est}} = 0.32\%. \quad (9.8b)$$

Here α_{at} is quoted for atoms isotropically distributed (an unpolarized ensemble) and probed on the $F = 4 \rightarrow F' = 4$ transition. For the atom number, we have given both a statistical and systematic uncertainty, which are discussed below. For the optical depth per atom the fitting procedure plays a central role. To show this the data have been fitted in three different ways. Either we fit the mean of the 200 traces, each trace

⁷ We will in the following make the explicit distinction between true values and our estimators.

Table 9.1.: A comparison of the three different methods used to fit the data. For the individual and common α_{at} fits we discard realizations where $N_{\text{at}} < 1000$.

Method	Traces	N_{at}	α_{at} (%)
Mean traces	200	1525	0.25
Individual traces	179	1605	0.32
Common α_{at}	177	1603	0.31

individually or make a combined fit with a common α_{at} for all traces and an independent atom number for each trace as the fit parameters. The outcomes of these fitting procedures are summarized in table 9.1. Most notably we see that fitting the mean traces gives a smaller α_{at} than the other methods. The reason for this is as follows; realizations with different atom numbers (loading noise) will start to bleach (increase in transmission, see fig. 9.5) at different times. When taking the mean over the different realizations this will reduce the slope of the pumping transient (see fig. 9.5), which determines α_{at} .

9.3.1 Error estimate

To quantify how precise the atom number estimate is we need to consider its associated error. This has been divided into a statistical and systematic contribution.

STATISTICAL: To estimate the statistical uncertainty of $\langle N_{\text{at}} \rangle_{\text{est}}$ we consider a single of the 179 experiments. The atom number is determined by fitting the transmission function (eq. (9.7)). This is equivalent to finding it from the number of scattered photons

$$N_{\text{at}} = \frac{N_{\text{ph,sc}}}{q}, \quad (9.9)$$

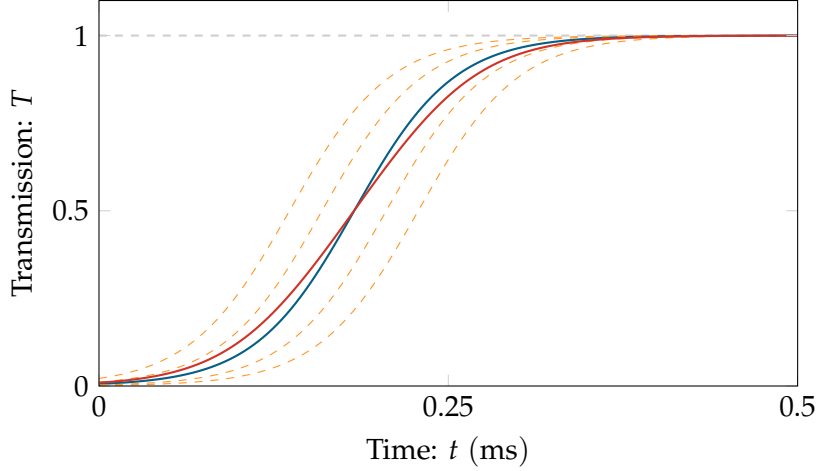


Figure 9.5.: Reduction of slope. The dashed orange lines show eq. (9.7) plotted for $N_{\text{at}} = 1200, 1400, 1800, 2000$ and a fixed optical depth per atom. In red is the mean of these traces, corresponding to an atom number of 1600. Compared to eq. (9.7) evaluated for $N_{\text{at}} = 1600$ which is shown in blue, we clearly see that the slope of the average trace is reduced.

where $N_{\text{ph,sc}} = N_{\text{ph,in}} - N_{\text{ph,out}}$. Using Gaussian error propagation we get⁸

$$\text{var}(N_{\text{at}})_{\text{est}} = \frac{\langle N_{\text{at}} \rangle_{\text{est}}^2 \text{var}(q)}{\langle q \rangle^2 \langle N_{\text{at}} \rangle_{\text{est}}} + \frac{\text{var}(N_{\text{ph,in}})_{\text{est}}}{\langle q \rangle^2} + \frac{\text{var}(N_{\text{ph,out}})_{\text{est}}}{\langle q \rangle^2}. \quad (9.10)$$

Using coherent light states⁹ and assuming the laser is shot noise limited we have $\text{var}(N_{\text{ph}}) = N_{\text{ph}}$. The number of input and output photons can be rewritten in terms of the corresponding fluxes and the measurement time, t_p , giving

$$\text{var}(N_{\text{at}})_{\text{est}} = \frac{\langle N_{\text{at}} \rangle_{\text{est}}^2 \text{var}(q)}{\langle q \rangle^2 \langle N_{\text{at}} \rangle_{\text{est}}} + \frac{t_p \langle \Phi_{\text{in}} \rangle_{\text{est}}}{\langle q \rangle^2} + \frac{\langle T(t) \rangle_{t_p} t_p \langle \Phi_{\text{in}} \rangle_{\text{est}}}{\langle q \rangle^2}. \quad (9.11)$$

⁸ The factor of $\langle N_{\text{at}} \rangle_{\text{est}}^{-1}$ in the first term is because we are interested in the variance of the *mean* of q and we perform the “experiment” for each atom.

⁹ Modeling each atom as a beam-splitter, the output is also in a coherent state.

Where the output flux has been written in terms of the average transmission during the measurement time $\langle T(t) \rangle_{t_p}$. Considering the specific case above and inserting the relevant numbers we get a statistical uncertainty for a single realization. Converting this to the standard deviation of the mean we find $\text{std}(N_{\text{at}})_{\text{est}} = 4$.

SYSTEMATIC: The systematic effects are much larger than the statistical, with the main contribution from ϵ . We ascribe a 10% fractional uncertainty to ϵ , coming from the measurement of the probe power, visibility and losses. This carries directly over to the atom number (eq. (9.2)). By technical improvements¹⁰ this could be reduced to be on the percent level. Other more physical, effects that could influence the estimation are radiation trapping, collective-back scattering and dark-state pumping. If significant radiation trapping is present, a single photon could pump multiple atoms. This would lead to an underestimate of the atom number. Collective back-scattering would also result in the estimated N_{at} being too low. As we would not “count” all the photons it took to bleach the ensemble. We note that both of these effects should be minimal in our experiment due to the 1D geometry. Special care should also be taken to make sure that no $F = 4$ dark-state exists. This can be done by an appropriate magnetic field¹¹ leading to a mixing of m_F states. Effects such as laser detuning, polarization, and inhomogeneous broadening do not affect the measurement [Chen et al. 2001].

9.4 NUMBER SQUEEZING

The second experiment performed shows the preparation and detection of an ensemble with a sub-Poissonian atom number distribution. The ensemble is measured 10 ms after the sub-Doppler cooling phase¹² using a dual-sideband continuous probe with a power of $P = 155$ pW. This is well below the expected saturation intensity and we record the phase shift (or equivalently the atom number) for 4 ms. To track and

¹⁰ To start with, a National Institute of Standards and Technology (NIST) calibrated power meter would help.

¹¹ This could be external or a fictitious magnetic field due to the strong trapping beams [Le Kien et al. 2013].

¹² This is to avoid any residual atoms from the molasses passing through the probe volume.

update the atom number distribution at each measurement we subdivide samples into evenly spaced time bins of length $\Delta t = 5 \mu\text{s}$, each containing $N_{\text{ph}} = 3.3 \times 10^3$. Using the method of Bayesian inference we estimate the atom number distribution conditioned on *all* previous measurement outcomes as

$$p(N_l|\phi_l) = \mathcal{N} p(\phi_l|N_l) p(N_l|\phi_{l-1}). \quad (9.12)$$

Here \mathcal{N} is a normalization factor.

We first consider $p(\phi_l|N_l)$ which is the most probable measurement outcome of the phase shift given a certain atom number N_l . We split ϕ_l into a mean and a fluctuating part and have

$$\phi_l = \phi_{\text{at}}N_l + \delta\phi. \quad (9.13)$$

Using the dual-sideband probing method we measure the total phase shift of the atomic ensemble which combined with an atom number measurement gives a phase shift per atom¹³ of $\phi_{\text{at}} = 0.2 \text{ mrad}/N_{\text{at}}$. The fluctuations $\delta\phi$ are due to light shot noise (eq. (9.1)) which is Gaussianly distributed such that

$$p(\phi_l|N_l) = \frac{1}{\sqrt{2\pi\text{var}(\delta\phi)}} \exp\left(-\frac{(\phi_l - \phi_{\text{at}}N_l)^2}{2\text{var}(\delta\phi)}\right). \quad (9.14)$$

The last factor in the Bayesian update rule (eq. (9.12)) is the probability to have N_l atoms, given all previous samples $p(N_l|\phi_{1\dots l-1})$. With the atom loss being a Markov process we can write this as

$$p(N_l|\phi_{1\dots l-1}) = \sum_{N_{l-1}=0}^{\infty} p(N_l|N_{l-1})p(N_{l-1}|\phi_{1\dots l-1}). \quad (9.15)$$

This is our “best prediction” for N_l given N_{l-1} atoms in the previous sample. To model this we consider the stochastic loss of atoms from the trap due to heating, pumping and other decays. In each time step there is a probability P that an atom is lost. Therefore, $p(N_l|N_{l-1})$ follows the binomial distribution

$$p(N_l|N_{l-1}) = \binom{N_{l-1}}{N_l} (1-P)^{N_l} P^{N_{l-1}-N_l}. \quad (9.16)$$

¹³ To calibrate this we probe the ensemble 40 ms after the sub-Doppler cooling and find $N_{\text{at}} = 416$ and a maximum phase shift of $\phi = 85 \text{ mrad}$ on the $F = 4 \rightarrow F' = 5$ transition.

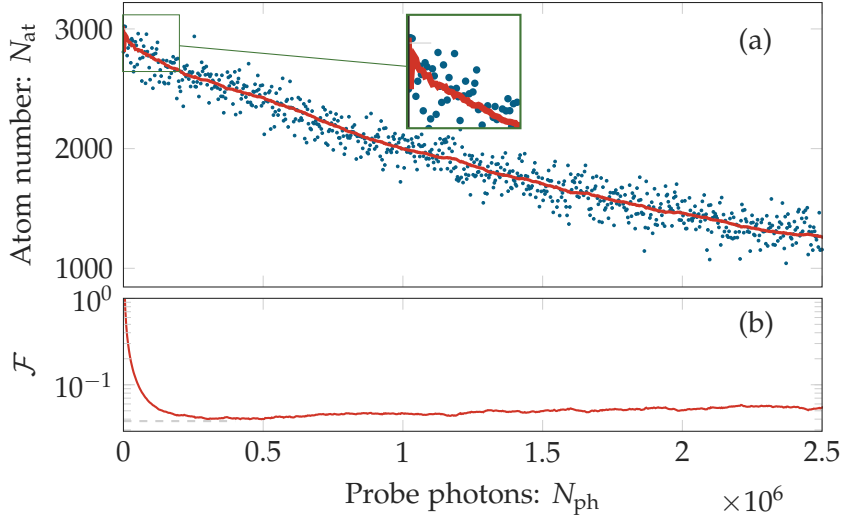


Figure 9.6.: Bayesian inference. (a) Measured atom number (blue points) as a function of probe photons together with the mean of $p(N_i|\phi_{1\dots l})$ (red). (b) Estimated Fano factors.

Since

$$\langle N_l \rangle = N_0 \exp(-lP) \quad (9.17a)$$

$$= N_0 \exp\left(-\frac{t}{\Delta t}P\right), \quad (9.17b)$$

we can find P from the decay rate (fig. 9.6(a)).

The only thing left is a starting point for the algorithm, $p(N_0)$. For this we take a uniform distribution for the atom number in the range $[0, 4400]$. Having all the ingredients for the Bayesian inference model (eq. (9.12)) we can estimate the probability distribution at each sample. The mean of the estimated distribution (red) and the data (blue points) are in good agreement already after the first few updates (see fig. 9.6(a)). With the knowledge of the full distribution and not only its mean we can also estimate the variance of N_{at} . From this we find the Fano factor $\mathcal{F} = \langle N_{\text{at}} \rangle / \text{var}(N_{\text{at}})$ — which if smaller than one corresponds to a sub-Poissonian atom number distribution also known as number squeezing. We find a minimum of $\mathcal{F} = -14$ dB (fig. 9.6(b)) after we have invested $N_{\text{ph}} = 4.9 \times 10^5$. This corresponds to a loss of 15% of the atoms. This clearly shows the capability of the apparatus to

create and measure an ensemble of $N_{\text{at}} \geq 1000$ with a sub-Poissonian atom number distribution.

9.4.1 Variance estimator model

To quantify the performance and the limits of the probing method, we consider a simple model for the atom number variance, inspired by [Zhang et al. 2012]. Two effects change the variance — the information gain due to measurements and the information loss due to atoms being removed from the trap.

Starting with the information gain, we consider the single atom phase shift (eq. (4.12a))

$$\phi_{\text{at}} = \alpha_{\text{at}} \frac{\Delta/(\gamma_e/2)}{(\gamma_e/2)^2 + \Delta^2} \quad (9.18a)$$

$$\approx \alpha_{\text{at}} \frac{1}{\Delta/(\gamma_e/2)}, \quad (9.18b)$$

where the approximation holds for $\Delta/(\gamma_e/2) \gg 1$. Furthermore, the number of scattered photons follows from eq. (4.12b)

$$N_{\text{ph,sc}} = \alpha_{\text{at}} \frac{1}{\Delta^2 + (\gamma_e/2)^2} N_{\text{ph,in}} \quad (9.19a)$$

$$\approx \alpha_{\text{at}} \frac{1}{\Delta^2} N_{\text{ph,in}}, \quad (9.19b)$$

where the approximation is again for large detunings. Combining eqs. (9.18) and (9.19) we can rewrite the single atom phase shift as

$$\phi_{\text{at}}^2 = \frac{\alpha_{\text{at}} N_{\text{ph,sc}}}{4 N_{\text{ph,in}}}. \quad (9.20)$$

Together with eq. (9.1) the variance of the atom number due to the shot noise of light is then

$$\text{var}(N_{\text{at}}) = \frac{1}{\epsilon \alpha_{\text{at}} N_{\text{ph,sc}}}. \quad (9.21)$$

This is independent of the total number of atoms and inverse proportional to the detection efficiency ϵ , the light-atom coupling α_{at} and the number of scattered photons $N_{\text{ph,sc}}$.

The second part of the model is the variance increase due to atoms being lost as we probe. To describe this we introduce n_{loss} as the number of scattering events it takes to lose an atom. Adding the different contributions up we get for the total variance [Zhang et al. 2012]

$$\text{var}(N_{\text{at}}) = \left(\frac{1}{\text{var}(N_{\text{at}})_{\text{prior}}} + \epsilon \alpha_{\text{at}} N_{\text{ph,sc}} \right)^{-1} + N_{\text{at}} \frac{N_{\text{ph,sc}}}{n_{\text{loss}}}, \quad (9.22)$$

where any prior information is contained in $\text{var}(N_{\text{at}})_{\text{prior}}$.

We neglect any prior information and minimize this expression with respect to $N_{\text{ph,sc}}$. In this way we find the optimal trade-off between the information gained due to probing and information lost due to loss of atoms (partition noise)

$$\min \{ \text{var}(N_{\text{at}}) \} = \left(\frac{4N_{\text{at}}}{n_{\text{loss}} \epsilon \alpha_{\text{at}}} \right)^{1/2}, \quad (9.23a)$$

$$\min \{ \mathcal{F} \} = \left(\frac{4}{N_{\text{at}} n_{\text{loss}} \epsilon \alpha_{\text{at}}} \right)^{1/2}, \quad (9.23b)$$

for

$$N_{\text{ph,sc}} = \left(\frac{n_{\text{loss}}}{N_{\text{at}} \epsilon \alpha_{\text{at}}} \right)^{1/2}. \quad (9.23c)$$

To consider the performance of the probing for different tasks we need the relevant loss rate, n_{loss} . Atoms can be “lost” either due to hyperfine pumping (n_{hf}) to $F = 3$, heating (n_{heat}) or trap decay in the absence of any probing. As the trap lifetime ($1/e$) is 20 ms we can neglect it on the 4 ms time scale we have in this experiment. From the measured decay time (fig. 9.6(a)) and theoretical calculation we find $n_{\text{heat}} = 56$ and $n_{\text{hf}} = 67$.

Considering preparation of number squeezed states, the limiting loss mechanism is atoms being removed from the trap, i.e., $n_{\text{loss}}^{\text{prep}} = n_{\text{heat}}$ from which we get a minimal Fano factor of

$$\min \{ \mathcal{F} \}_{\text{prep}} = -10.7 \text{ dB} \quad (9.24)$$

using $N_{\text{at}} = 2500$ and a conservative optical depth per atom of $\alpha_{\text{at}} = 1\%$. This is comparable to the observed -14 dB. The discrepancy comes since the model only makes a single update in comparison to the Bayesian inference model. The pseudo-continuous update formula

(eq. (9.12)) monitors and updates the atom loss whereas the single update formulation do not.

For state tomography the requirement is more stringent and noise is added if either an atom is lost *or* pumped to the other hyperfine level

$$n_{\text{loss}}^{\text{tomo}} = \frac{1}{n_{\text{heat}}^{-1} + n_{\text{hf}}^{-1}} \quad (9.25a)$$

$$= 31. \quad (9.25b)$$

A typical tomography experiment, as studied in depth in the previous chapters, are made on $|\theta = \pi/2, \phi\rangle_A$. The probe therefore, only interacts with half the atoms leading to $N_{\text{at}} = 1250$ which gives

$$\min \{\mathcal{F}\}_{\text{prep}} = -7.9 \text{ dB}. \quad (9.26)$$

Neglecting the influence of technical noise this should result in a high quantum state tomography efficiency, ϵ_{noise} (eq. (7.18)).

From eq. (9.23b) we also directly see how the probing can be improved, most notable is the dependence on the quantum efficiency. We are currently limited by the electronic noise entering through ϵ_{elec} . This could be improved by simply increasing the LO power or by making a balanced detection of both outputs of the beam splitter combining the probe and LO.

Related results with lower Fano factors were obtained in a cavity system [Zhang et al. 2012] and in a dedicated MOT [Hume et al. 2013].

9.5 PROJECTED SINGLE EXCITATION PURITY

With the biggest motivation of setting up the nanofiber experiment being the prospect of outperforming the free-space setup we want to estimate the expected purity of a collective-single-excitation state. Staying as close to the MZI experiment as possible we consider a similar experiment.¹⁴ A strong magnetic bias field is applied along the z-axis (fig. 9.1) and defines the quantization axes, and atoms are excited us-

¹⁴ We are currently considering if this is the optimal setting. We are mainly concerned with the polarizations in the nanofiber.

ing x -polarized light. The expected state purity can be found from eq. (8.27) which we reprint here

$$p(n|1\text{click}) = \frac{\tilde{p}_d^n p_0^n (1 - \tilde{p}_d p_0) \left(n \frac{p_d}{\tilde{p}_d} + p_f + \frac{p_d p_2}{1 - \tilde{p}_d p_2} \right)}{p_f + \frac{p_d p_2}{1 - \tilde{p}_d p_2} + \frac{p_d p_0}{1 - \tilde{p}_d p_0}}. \quad (9.27)$$

To evaluate this we need the probability to detect a photon emitted into our detection spatial mode p_d , the forward scattering probability of the heralding (p_0) and bad (p_2) photons, and the probability of false positives from dark counts or leakage photons, p_f . To estimate p_0 we first consider the collection efficiency, i.e., the probability that an emitted photon goes into the nanofiber mode. From this we can find the required number of excitation photons leading to a consideration of the required filtering efficiencies. In comparison to the MZI setup we need to take particular care with respect to filtering out the two trap beams, since they are propagating in our detection mode.

EXCITATION PHOTONS The nanofiber is a wave-guide and we therefore expect that the scattering into this mode is enhanced by the β -factor [Lodahl et al. 2013]. As we only collect photons emitted into one direction, the relevant quantity is the directional β -factor given by¹⁵ $\beta_{\text{dir}} = \beta/2$. From [Le Kien et al. 2005] we find the conservative estimate¹⁶ $\beta_{\text{dir}} = 0.01$. The probability of scattering a photon of the desired energy into the detection spatial mode, is then

$$p_{\text{forward}} = p_{|e\rangle \rightarrow |\downarrow\rangle} N_{\text{exc}} \beta_{\text{dir}}. \quad (9.28)$$

Here $p_{|e\rangle \rightarrow |\downarrow\rangle} = 0.15$ is the probability for an atom excited to the state $|F' = 4, m_{F'} = 1\rangle$ to decay into the state $|\downarrow\rangle$, and N_{exc} is the number of excited atoms.

To proceed with the calculation we fix the number of excited atoms, N_{exc} . To avoid state degradation due to atoms in other states (sec. 8.4) this should be much smaller than the total atom number. Taking $N_{\text{exc}} = 30$ the number of photons required follows from Lambert-Beer's law

$$N_{\text{ph,out}} = N_{\text{ph,in}} \exp(-N_{\text{at}} \alpha_{\text{at}}(\Delta)) \quad (9.29a)$$

¹⁵ Recent work [Mitsch et al. 2014; Petersen et al. 2014] have shown that the directionality of nanofiber systems can be greatly improved.

¹⁶ This should be compared to the collection efficiency of $1 : 40 \times 10^3$ in the MZI setup.

where

$$\alpha_{\text{at}}(\Delta) = \frac{\alpha_{0,\text{at}}}{1 + (\Delta/(\gamma_e/2))^2}. \quad (9.29\text{b})$$

and $\alpha_{0,\text{at}}$ is the resonant optical depth of a single atom. Using $N_{\text{exc}} = N_{\text{ph,in}} - N_{\text{ph,out}}$ we can write the number of excited atoms as

$$N_{\text{exc}} = N_{\text{ph,in}}(1 - \exp(-N_{\text{at}}\alpha_{\text{at}})). \quad (9.30)$$

To have an equal probability of interacting with each atom we want $\alpha(\Delta) \ll 1$. This can always be fulfilled by increasing Δ . As the detuning increases we require more input photons to get the desired N_{exc} , and thus require an improved filtering ratio. Taking $\alpha_0 = 10$ (on the $|F = 4, m_F = 4\rangle \rightarrow |F' = 5, m_{F'} = 5\rangle$ transition and $\Delta = 10\gamma_e$, the optical depth experienced by the excitation beam ($|\uparrow\rangle \rightarrow |F' = 4, m_{F'} = 1\rangle$) is $\alpha_{\text{exc}}(10\gamma_e) = 0.007$. Solving eq. (9.30) with these numbers we find the required number of input photons to be $N_{\text{ph,in}} = 4140$. With a rejection of $1 : 2.7 \times 10^8$ the current filtering cavities, should be able to filter these photons out completely.

FILTERING OF TRAPS To filter out the traps we use a dichroic mirror similar to those overlapping the trap and the probe (sec. 9.1) with a reflection coefficient of $r^2 > 99.9\%$ for our trap wavelengths. This is combined with two volume Bragg gratings with a rejection¹⁷ of the traps of $1 : 10^9$, for both wavelengths as measured by Kyung [2010]. This gives a rejection of $1 : 1 \times 10^{19}$ for the traps, which is more than enough to make these negligible.

OTHER IMPROVEMENTS As noted in sec. 8.7 we are limited by the decay into $|F = 3, m_F = 2\rangle$ and without further improvements the state purity will never exceed 70%. Increasing the reflection coefficient of the current cavity mirrors by 0.5% the cavity linewidth becomes $\delta\nu_c = 6.3$ MHz. Keeping all other cavity parameters fixed this should filter out the bad decay by a factor $1 : 33$, if a magnetic bias field of $|\mathbf{B}| = 20$ G is assumed. The last thing to consider is the used SPCM, for the best commercially¹⁸ available photon counters the dark count rate is as low as $\nu_{\text{dark}} \approx 25$ Hz

¹⁷ This rejection is so large that it might be compromised by dust particles and have to really be measure at the wavelengths of interest in the setup.

¹⁸ This could for instance be a Perkin-Elmer SPCM-AQRH-16.

With these improvements we find the following set of parameters¹⁹

$$p_0 = 0.045 \quad (9.31a)$$

$$p_2 = 4.0 \times 10^{-4} \quad (9.31b)$$

$$p_d = 0.16 \quad (9.31c)$$

$$p_f = 6.5 \times 10^{-5}. \quad (9.31d)$$

The state purity can then be found by evaluating eq. (8.27) which gives

$$p(n = 0|1\text{click}) = 0.016, \quad (9.32a)$$

$$p(n = 1|1\text{click}) = 0.911, \quad (9.32b)$$

$$p(n = 2|1\text{click}) = 0.068. \quad (9.32c)$$

This should be compared to the state purity of 0.38 attained in the free-spaces setup. In combination with the high detection efficiency $\varepsilon_{\text{noise}}$ the nanofiber setup offers an exciting prospect for “re-doing” the experiment regarding the collective-single-excitation state. We note that the main improvements comes from the reduced number of required excitation photons and the filtering of the bad decay channel.

9.6 SUMMARY

In this chapter we briefly decribed our newest setup — a light-atom interface based on a optical nanofiber. We discussed two different experiments. First, a fast and robust method to determine the atom number and the optical depth per atom. Second, we performed a dual-frequency dispersive measurement of the atomic induced phase shift. Using the method of Bayesian inference we estimated the Fano factor and found a minimum value of $\mathcal{F} = -14$ dB. This clearly shows the sub-Poissonian resolution and preparation capabilities of the experiment — the main result of the chapter. With this we estimated the feasibility for the setup to be used for quantum state tomography. We ended the chapter by considering the setup for the creation of a collective-single-excitation state and found that we should expect state purity of 90% or more.

¹⁹ To include the extra filtering of the bad decays we simply reduce the generation rate of these, i.e., p_2 .

Part III

CONCLUSION AND OUTLOOK

In this, the last, part of the thesis we summarize and conclude the work. This is followed by an outlook considering possible improvements and extensions of the work. Last, we present a short review of related work, regarding the creation and characterization of non-Gaussian and nonclassical states of atomic ensembles.

CONCLUSION

In this thesis we have dealt extensively with the generation and characterization of exotic quantum states within a cold atomic ensemble. We presented results showing the creation and characterization of a spin-squeezed state (SSS), a collective-single-excitation state as well as the preparation of ensembles with a sub-Poissonian atom number distribution coupled to a nanofiber.

To understand these results we started by introducing an elaborate framework of light, atoms and their interactions. We especially focused on the unified description of the two systems as harmonic oscillators and pseudo-spins. This allowed us to draw clear analogies between the well known states of light and the spin-states of the ensemble. With the description of the two independent systems we considered their interactions. We especially focused on the use of a dispersive dual-color measurement to characterize and prepare collective atomic states. The main feature of this method is the (to first order) cancellation of the ac Stark shift, which allows us to realize the desired QND Hamiltonian. With this background we then presented the three main results of the thesis.

First, the creation and characterization of a SSS and its associated nonclassical features. With the light-atom interaction being of the QND type it directly allows for measurement based squeezing. Using this we created a SSS with a spectroscopically relevant noise reduction of -1.7 dB. This noise reduction is due to nonclassical correlation — the ensemble is in a many-body entangled state. Furthermore using the concept of atomic quadrature quasi-probability (AQQP) distributions we demonstrated the nonclassical features of the state with up to 23 standard deviations of statistical significance. With this high significance even for this weakly squeezed state the usefulness and feasibility of the atomic homodyne tomography and AQQP method is evident.

Second, we used the atomic tomography method to characterize a collective-single-excitation state — the atomic equivalent of a single photon state. This state is probabilistically generated by the detection of a single photon which heralds the atomic state. To characterize

this state we compared the variance of the measured population difference in the cases with and without a heralding click. A variance increase of 24% was observed distinguishing the created collective-single-excitation state from the CSS by three standard deviations. To explain quantitatively the observed variance increase we presented a general model taking into account the effect of false positive events and the inefficient detection. This model is in excellent agreement with the observation. Furthermore, we analyzed the probability that we created the n^{th} collective-excitation state conditioned on detecting a heralding click. This shows a state purity (corrected for detection) of $p_{\text{state}} = 38\%$ — incompatible with both a CSS and a thermal state with the same mean excitation number. Several tests for nonclassicality and non-Gaussianity were made. Due to the limited number of samples, neither the nonclassicality or non-Gaussianity of the state could be inferred with statistical significance from the data. With the presented model we identified possible technical improvements which should allow to increase the state purity to $p_{\text{state}} \geq 70\%$. This should allow for the observation of non-Gaussian features and possibly a negative Wigner function. The presented experiment is, to the best of my knowledge, the first implementation of a hybrid discrete-continuous light-atom interface.

Third, with the insights gained from the creation of the SSS and collective-single-excitation state we set out to implement a light-atom interface based on a tapered optical nanofiber. We presented a fast and robust way of determining the atom number and single atom coupling strength based on optical pumping transients. In combination with a dispersive phase shift measurement this allows for a atom number resolution approaching the single atom level for ensembles of a few thousand atoms. Furthermore, using Bayesian inference we continuously track the full atom number distribution, showing Fano factors of $\mathcal{F} = -14\text{ dB}$. This is well below Poissonian noise, equivalent to number squeezing. This shows the capability to prepare and characterize an ensemble with sub-Poissonian atom number distribution.

OUTLOOK

The work presented here and in [Petrov 2006; Windpassinger 2008; Oblak 2010] gives an account of our groups contribution to the field of “quantum state engineering of cold atomic ensembles”. As part of the third generation of PhD students in our group I joined an experiment and field in rapid development. During my time a few problems both technical and more fundamental were solved allowing to take our experimental efforts to the next level. With this we (as always) hope to explore and observe new physics which is discussed in the following.

SINGLE EXCITATION STATE The obvious next steps would be to prepare higher purity collective-single-excitation states. These states could be created either in the [MZI](#) setup (sec. 8.7) or in the nanofiber setup (sec. 9.5). With a main goal being the direct observation of a negative Wigner function of the ensemble, a high detection efficiency is required. This makes the nanofiber setup an excellent platform for such an experiment. With only minor modification of the filter cavities needed and the theoretical framework presented here “only” two things are missing. First, hyperfine pumping and coherent manipulation of the atoms. For this we are currently setting up a laser to drive Raman transitions. With expected coherence times being on the order of 1 ms [Reitz et al. 2013] and the potential of high Rabi frequencies due to the highly focused light we expect fast manipulations of the atoms. Second, is the challenge of operating the setup at the projection noise level. There should be no fundamental problem in this and with the low atom number it could turn out to be easier than in the [MZI](#) setup.

OTHER STATES Combining the capabilities presented in this work should allow to create a wide range of atomic spin states. Most straightforward would be a squeezed single-excitation state. Making a non-destructive [QND](#) measurement of the collective-single-excitation state, such a state will be created.

OUTLOOK

More interesting would be the generation of a Schrödinger cat state within the ensemble. Several proposals [McConnell et al. 2013] for how this could be done exist, with that of Brask et al. [2010] being of particular relevance. Starting from a single excitation state the cat is generated by conditioning on the outcome of quadrature measurements. Besides the clear interest from a fundamental perspective a Schrödinger cat state would allow for the enhancement of measurement precision as well as the implementation of quantum information protocols. A consideration of the details regarding these topics is far beyond the scope of this work.

ATOMIC MIRROR By carefully spacing the fiber trapped atoms by $\lambda/2$, they fulfill the Bragg condition. This means that light scattered backwards (reflected) from each atom interferes constructively. In this way the atoms form a mirror with close to unity reflection [Chang et al. 2012]. Such a mirror would have a narrow bandwidth as only close to resonant light would interact with the atoms and hence be reflected. Furthermore, it should be switchable as the atoms could be pumped back and forth between dark and bright states.

With the help of our local theory collaborators Prof. Anders Sørensen and Ivan Yakoubov we have found that a “patterned optical pumping” technique should allow to prepare the evenly spaced ensemble — giving reflections on the order of 50% for current experimental parameters. The idea would be to pump all atoms into $F = 3$ and shine a standing wave repumping beam ($F = 3 \rightarrow F' = 4$) on for a time τ . Atoms at the anti-nodes (with $\lambda/2$ spacing) will have the largest chance of being transferred to $F = 4$, the bright state. With the theoretical support we are actively pursuing this and are in the process of setting up a detection channel for the reflected light, together with other minor modifications of the setup.

With this list of possible future topics, it is safe to say that the next generation of PhD students will have more than enough to do. It is therefore a pleasure to leave the experimental playground to them.

REVIEW OF RELATED WORK

The generation of non-Gaussian and nonclassical spin states is a vast and active research area. In this section we review some of the main results of this field. We focus on the implementation of non-Gaussian states, and refer the reader to [Ma et al. 2011] for a discussion of SSS.

[BIMBARD ET AL. 2014] The current state of the art implementation based on the DLCZ protocol has been made in the group of Prof. P. Grangier in Paris. This work is based on many years of improvements [Wal et al. 2003; Chou et al. 2005; Thompson et al. 2006; MacRae et al. 2012]. An ensemble of 10×10^3 rubidium (Rb) atoms is trapped and cooled inside a cavity of finesse $\mathcal{F} = 120$. Using the DLCZ protocol an atomic excitation is created and is retrieved with a maximal efficiency (corrected for detection imperfections) of 80%. Storing the atomic excitation in the ensemble for longer times decreases¹ the efficiency. For a storage time of $1 \mu\text{s}$ the efficiency is on the order of 50%. The retrieved excitation is characterized by both photon-correlation measurements and optical homodyne tomography.

For the short storage times ($< 1 \mu\text{s}$) reconstructed Wigner functions show negativities, even for the uncorrected data — a clear sign of non-classicality and non-Gaussianity. With the high conversion efficiencies presented, the method has the potential to be expanded to characterize more complex atomic states. Going to non-symmetric states will however require to actively stabilize and control the phase between the LO and the read-beam.

[McCONNELL ET AL. 2013] In the group of Prof. V. Vuletić at MIT work on creating collective-single-excitation states is ongoing. Their proposal is described in the article by McConnell et al. [2013]. The idea is, as they note, closely related to ours²

¹ Among other things this is due to the random motion of the atoms, which could be solved by more sophisticated trapping [Zhao et al. 2008].

² The citations have been cast into the format of this thesis.

The scheme proposed and investigated in Refs. [Christensen et al. 2013; Christensen et al. 2014] for Dickie-state preparation is similar to our scheme and should allow the same metrological gain.

However, with their ensemble being trapped inside a high finesse cavity ($\mathcal{F} \approx 5.5 \times 10^3$), a smaller atom number ($N_{\text{at}} \approx 2000$) and higher detection efficiency [Zhang et al. 2012] their implementation should allow for a higher state purity than the $p_{\text{state}} = 38\%$ presented in this work.

[HAAS ET AL. 2014] In the group of Prof. J. Reichel in Paris, Werner states — equivalent to the collective single-excitation-state — in an ensemble of $N_{\text{at}} = 41$ have been created. The ensemble is situated in a high finesse ($\mathcal{F} \approx 35 \times 10^3$) fiber based cavity. With all atoms in the ground state $|\downarrow\rangle$ the cavity is fully transmitting. If a single atom is in the $|\uparrow\rangle$ state the cavity is shifted out of resonance and reflects the input light. In this way the cavity allows for a binary readout of the atomic state [Volz et al. 2011] — if the cavity reflects *one or more* atoms are in $|\uparrow\rangle$ if it transmits all atoms are in $|\downarrow\rangle$. The desired state can then be created in the following way. Starting with all atoms in $|\downarrow\rangle$ a weak microwave pulse creates a CSS with a small amplitude. This is followed by the binary measurement. The measurement projects the CSS onto $|0\rangle_A$ or $|1\rangle_A$ depending on its outcome. To characterize the state measurements of the Q -function are made

$$Q(\theta, \phi) = \langle 0 | \mathbf{M}_{\mu W}^\dagger(\theta, \phi) \rho \mathbf{M}_{\mu W}(\theta, \phi) | 0 \rangle. \quad (12.1)$$

Several key results are obtained in the experiment. First the created collective-single-excitation state has a purity of $p_{\text{state}} = 0.42$. Second, the measured Q -function is clearly non-Gaussian, showing the characteristic dip of the single-excitation state.³ Third, a careful analysis shows that in the ensemble of $N_{\text{at}} = 41$ at least 13 of the atoms are entangled.

Several differences between this and our work should be noted. First and foremost, is the difference in the number of atoms. In the considered free-space setup we work with $N_{\text{at}} \approx 100 \times 10^3$ compared to the

³ This should be puzzling as a state $\hat{\rho} = p |1'\rangle_A \langle 1'| + (1-p) |0'\rangle_A \langle 0'|$ for $p = 0.42$ does not have a dip. The reason this is still observed is that their measurement is *only* sensitive to the symmetric sub-space $J = N_{\text{at}}/2$, where about 45% of the population remains.

$N_{\text{at}} = 40$ used in this work. Second, is the measurement method. In comparison to the continuous variable Gaussian measurement used in this work, that of Haas et al. [2014] is a non-Gaussian measurement.

[STROBEL ET AL. 2014] The recent work in the group of Prof. M. Oberthaler in Heidelberg shows the creation of a non-Gaussian state in a Bose–Einstein condensate (BEC) of $N_{\text{at}} \approx 400$. The state is created using a spin dependent nonlinear interactions between particles in the BEC. This realizes one-axis twisting dynamics $\hat{\mathcal{H}}_{\text{int}} \propto \chi \hat{J}_z^2 - \Omega \hat{J}_x$, where the \hat{J}_x term is due to Rabi coupling between the two states. Starting from a CSS aligned along the x -axis the evolution leads first to a SSS followed by a non-Gaussian “bend” state.

Loading a large BEC in a 1D optical lattice 35 separate condensates are formed. They now evolve for a time τ , and depending on this a SSS or bend non-Gaussian state is realized. A measurement of the population difference is done by site resolvable absorption measurements.

The created state is characterized in two ways. First a maximum-likelihood reconstruction of the density matrix is made. This allows for the calculation of the Q -function in good agreement with theoretical expectation. Second, in close connection to the use of the created state for quantum assisted metrology it is characterized through measurements of its Fisher information. This method for extraction of the Fisher information should be applicable for a wide variety of states. Furthermore, the non-squeezed but non-Gaussian state is used for sub-projection noise measurement.

Part IV

APPENDICES

EXPERIMENTAL CONSIDERATIONS

A.1 PARAMETRIC GAIN HAMILTONIAN

We consider the parametric gain Hamiltonian given in eq. (5.13a), which we reprint here

$$\hat{\mathcal{H}}_G = \chi^* \hat{a}_A^\dagger \hat{a}_L^\dagger + \chi \hat{a}_A \hat{a}_L, \quad (\text{A.1a})$$

where

$$\chi = \frac{g(N_{\text{at}})\Omega_R}{2\Delta}. \quad (\text{A.1b})$$

The unitary evolution of this operator is given as

$$\hat{S}_G(\zeta) = \exp(-i\hat{\mathcal{H}}_G t/\hbar) \quad (\text{A.2a})$$

$$= \exp\left(\zeta^* \hat{a}_L^\dagger \hat{a}_A^\dagger + \zeta \hat{a}_L \hat{a}_A\right), \quad (\text{A.2b})$$

where

$$\zeta = -\frac{i\chi}{\hbar} t. \quad (\text{A.2c})$$

This is the two-mode squeezing operator, leading to a Bogolibov transformation of the light and atomic operators as [Gerry et al. 2005, sec. 7.7]

$$\hat{a}_L \rightarrow \hat{a}_L \cosh(\zeta) - \hat{a}_A^\dagger \sinh(\zeta), \quad (\text{A.3a})$$

$$\hat{a}_A \rightarrow \hat{a}_A \cosh(\zeta) - \hat{a}_L^\dagger \sinh(\zeta), \quad (\text{A.3b})$$

$$\hat{a}_L^\dagger \rightarrow \hat{a}_L^\dagger \cosh(\zeta) - \hat{a}_A \sinh(\zeta), \quad (\text{A.3c})$$

$$\hat{a}_A^\dagger \rightarrow \hat{a}_A^\dagger \cosh(\zeta) - \hat{a}_L \sinh(\zeta). \quad (\text{A.3d})$$

From this we will calculate two things, first we show that excitations are created in pairs and secondly we show that the process, can be seeded.

A.1.1.1 *Excitation created in pairs*

Considering the ground state of the two modes, $|0,0\rangle$ where neither the atomic or photonic mode has excitations. Applying the two mode squeezing operator leads to

$$|\zeta\rangle = \hat{S}_G(\zeta) |0,0\rangle. \quad (\text{A.4})$$

Expanding this on the complete basis of Fock states we get

$$|\zeta\rangle = \sum_{n=0}^{\infty} \sum_{m=0}^{\infty} C_{n,m} |n,m\rangle, \quad (\text{A.5})$$

we are interested in deriving an expression for $C_{n,m}$ and show that this contains a delta function in n and m . To do this we consider the eigenvalue equation

$$\hat{a}_L |0,0\rangle = 0, \quad (\text{A.6})$$

we multiply by \hat{S}_G from the left and use that \hat{S}_G is unitary

$$\hat{S}_G(\zeta) \hat{a}_L \hat{S}_G(\zeta)^\dagger \hat{S}_G(\zeta) |0,0\rangle = 0, \quad (\text{A.7a})$$

$$\hat{S}_G(\zeta) \hat{a}_L \hat{S}_G(\zeta)^\dagger |\zeta\rangle = 0 \quad (\text{A.7b})$$

$$\left(\hat{a}_L \cosh(\zeta) + \hat{a}_A^\dagger \sinh(\zeta) \right) |\zeta\rangle = 0 \quad (\text{A.7c})$$

$$\sum_{n=0}^{\infty} \sum_{m=0}^{\infty} C_{n,m} \left(\sqrt{n} \cosh(\zeta) + \sqrt{m+1} \sinh(\zeta) \right) |n,m\rangle = 0 \quad (\text{A.7d})$$

By multiplying with $\langle n, m+1|$ from the left leads to the recursive definition

$$C_{n,m} = \delta_{n,m} (-1)^n \frac{\tanh(\zeta)^n}{\cosh(\zeta)} \quad (\text{A.8})$$

where $C_{0,0}$ is found via normalization.

 A.1.2 *Expected photon number*

We are interested in calculating the expected photon number in the detection mode described by \hat{a}_L and consider the time evolution of the

initial state $|\psi\rangle = |0, \alpha\rangle = |0\rangle_L |\theta, \phi\rangle_A$. The expected photon number is

$$N_{\text{ph}} = \langle \psi | \hat{a}_L^\dagger(t) \hat{a}_L(t) | \psi \rangle \quad (\text{A.9a})$$

$$= \langle \psi | \hat{U}^\dagger \hat{a}_L^\dagger \hat{U} \hat{U}^\dagger \hat{a}_L \hat{U} | \psi \rangle \quad (\text{A.9b})$$

$$= \left(\langle 0, \alpha | \hat{a}_A \hat{a}_A^\dagger | 0, \alpha \rangle \right) \sinh^2(\chi t) \quad (\text{A.9c})$$

$$= (1 + \alpha^2) \sinh^2(\chi t) \quad (\text{A.9d})$$

where α^2 is the amplitude of the CSS and from the second to third line we have used eq. (A.3). We are thus left with re-expressing α in terms of known quantities, it is simply the projection onto the z-axis allowing us to write

$$N_{\text{ph}} = (1 + N_{\text{at}} \sin^2(\theta)) \sinh^2(\chi t). \quad (\text{A.10})$$

EXPERIMENTAL TECHNIQUES

We present two additional drawings first of the optical setup used to create the MOT see fig. B.1 and second the acquisition and control system fig. B.2

EXPERIMENTAL TECHNIQUES

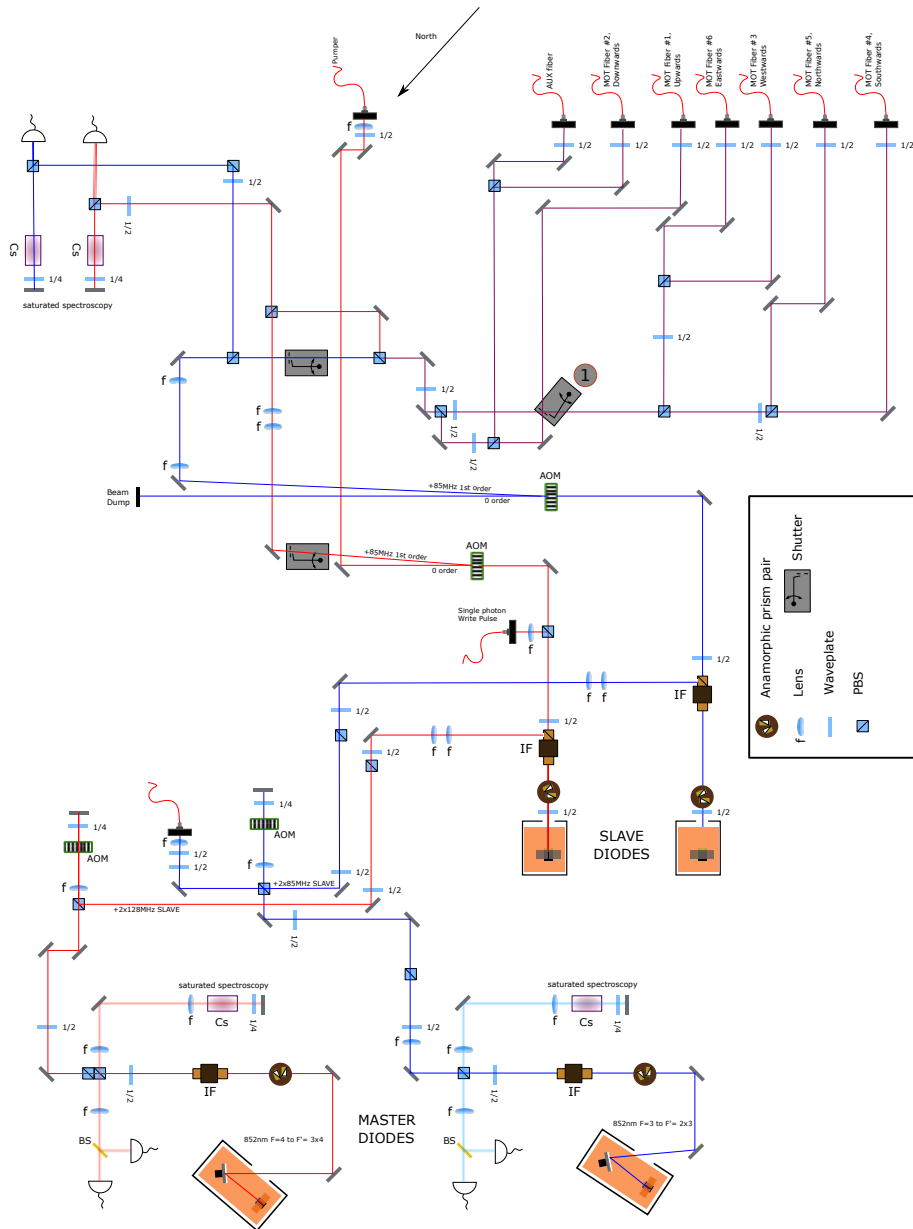


Figure B.1.: Setup used for generating the six beams for the MOT. As the setup was built around 10 years ago there is room for improvement, especially making it more compact. As the setup is in a working condition, there was no intention to change and modify it.

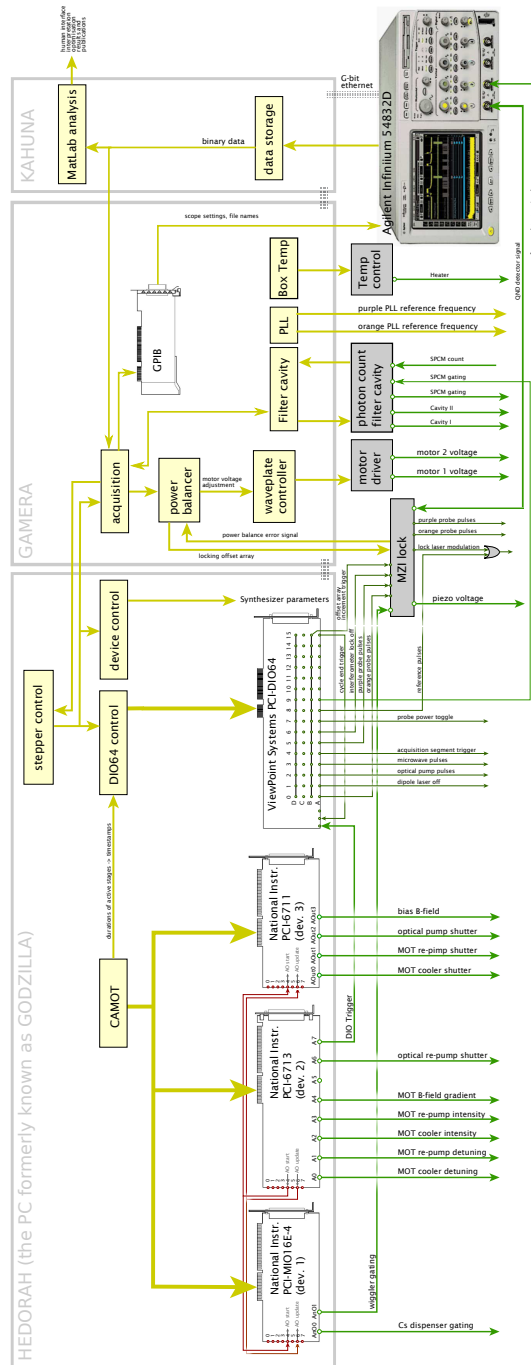


Figure B.2.: Outline of the acquisition and control system. Figure modified (with permission) from [Oblak 2010, fig. 7.2].

SPIN SQUEEZING

In this appendix we follow [Appel, Windpassinger, et al. 2009] and consider a different derivation of the detected signal and relate it the model used in sec. 7.3.1 and 7.3.2. We are especially interested in showing the relation $\phi = \mathcal{K}\Delta N$.

C.1 QND MASTER EQUATION

For a plane wave propagating along the y -direction through a medium with a refractive index n the field is

$$E(y, t) = E_0 \exp [i(ky - \omega t)] + \text{C.C.} \quad (\text{C.1})$$

$$= E_{\text{vac}}(y, t) \exp [i\phi(y)] \exp [-\alpha z/2] + \text{C.C.} \quad (\text{C.2})$$

where

$$\phi(y) = \frac{\pi}{\lambda} y \text{Re}(\chi) \quad (\text{C.3})$$

$$\alpha = \frac{2\pi}{\lambda} \text{Im}(\chi) \quad (\text{C.4})$$

$$E_{\text{vac}}(y, t) = E_0 \exp(i\omega(y/c - t)). \quad (\text{C.5})$$

These equations are similar to what is presented in sec. 4.1.1 but written in terms of the complex value susceptibility

$$\chi = \frac{\lambda}{2\pi} \frac{\varrho_{\text{at}}}{l_a} Q \quad (\text{C.6a})$$

where

$$Q = \sum_m \frac{\wp_m}{\Delta_m / \gamma_e + i/2}. \quad (\text{C.6b})$$

The atomic column density is ϱ_{at} and the summation is over the different levels. The susceptibility is related to the refractive index through

$$n = \sqrt{1 + \chi} \quad (\text{C.7a})$$

$$\stackrel{\chi \ll 1}{\approx} 1 + \frac{\chi}{2}. \quad (\text{C.7b})$$

With the two probes only interacting¹ with atoms in either of the states $|\uparrow\rangle$ or $|\downarrow\rangle$ we find

$$\phi_i = \frac{1}{2} q_i \text{Re}(Q_i) \quad (\text{C.8a})$$

$$\alpha_i = q_i \text{Im}(Q_i) \quad (\text{C.8b})$$

where $i = \uparrow, \downarrow$. The MZI is locked around a zero crossing of the two probes which are out of phase (sec. 5.1) the photon-number-difference of the two detectors are

$$N_{\text{ph},-} = \pm 2 \sin(\phi_{\uparrow} - \phi_{\downarrow}) \sqrt{t N_{\text{ph},i,R} N_{\text{ph},i,P}} \quad (\text{C.9a})$$

$$\stackrel{\phi \ll 1}{\approx} \pm 2(\phi_{\uparrow} - \phi_{\downarrow}) \sqrt{t N_{\text{ph},R} N_{\text{ph},P}}. \quad (\text{C.9b})$$

Here $N_{\text{ph},R}$ and $N_{\text{ph},P}$ is the photon numbers in the reference and probe arm and t the probe arm transmission. We have taken the phase-shift to be small, in agreement with the previous assumption of $\chi \ll 1$.

The detected phase shift ϕ_i is averaged over the transverse spatial profile of the probe

$$\phi_i = \frac{1}{2} \text{Re}(Q_i) \int_0^{2\pi} d\theta \int_0^{\infty} r dr I_P(r) q_i(\theta, r) \quad (\text{C.10})$$

with

$$I_P(r) = \frac{2}{\pi (w_0^{\text{probe}})^2} \exp\left(-2 \frac{r^2}{(w_0^{\text{probe}})^2}\right). \quad (\text{C.11})$$

As in sec. 5.1 we take

$$N_{\text{ph}} \equiv N_{\text{ph},\uparrow} = N_{\text{ph},\downarrow} \quad (\text{C.12})$$

$$Q \equiv Q_{\uparrow} = Q_{\downarrow}. \quad (\text{C.13})$$

With this the interference fringe amplitude becomes

$$\tilde{N}_{\text{ph}} = \sqrt{t N_{\text{ph},R} N_{\text{ph},P}} \quad (\text{C.14})$$

which gives a signal from the atoms as

$$N_{\text{ph},-} = \tilde{N}_{\text{ph}} \text{Re}(Q) \int_0^{2\pi} d\theta \int_0^{\infty} r dr I_P(r) (q_{\uparrow}(\theta, r) - q_{\downarrow}(\theta, r)). \quad (\text{C.15})$$

¹ They are far-detuned from the other transition.

Here q_\downarrow and q_\uparrow denotes the column density of atoms in the respective level and we have

$$q_{\text{at}} = q_\downarrow + q_\uparrow. \quad (\text{C.16})$$

For the atom number measurement we have all atoms in the upper state which means

$$N_{\text{ph},-}^\uparrow = q_\uparrow \tilde{N}_{\text{ph}} \text{Re}(Q), \quad (\text{C.17})$$

as $I_P(r)$ is normalized.

To relate this to the model used in the main text we define

$$N_{\text{at},i} \equiv \pi (w_0^{\text{probe}})^2 \int_0^{2\pi} d\theta \int_0^\infty r dr I_P(r) q_i \quad (\text{C.18})$$

$$\mathcal{K} \equiv \frac{\tilde{N}_{\text{ph}} \text{Re}(Q)}{N_{\text{ph,tot}} \pi (w_0^{\text{probe}})^2} \quad (\text{C.19})$$

$$N_{\text{ph,tot}} \equiv 2(N_{\text{ph},i,\text{R}} + t N_{\text{ph},i,\text{P}}) \quad (\text{C.20})$$

We can find the phase shift as

$$\phi = \frac{N_{\text{ph},-}}{N_{\text{ph,tot}}} \quad (\text{C.21a})$$

$$= \mathcal{K} \Delta N. \quad (\text{C.21b})$$

This is simply the atomic contribution in eq. (7.3). Furthermore we can calculate the variance of the CSS aligned along the x -axis of the Bloch sphere. For this state $q_\uparrow(\theta, r) = q_\downarrow(\theta, r)$ which means that $\langle N_{\text{ph},-}^{(\text{CSS})} \rangle = 0$ with a variance

$$\text{var} \left(N_{\text{ph},-}^{(\text{CSS})} \right) = \tilde{N}_{\text{ph}}^2 (\text{Re}(Q))^2 \int_0^{2\pi} d\theta \int_0^\infty r dr I_P^2(r) \text{var} (q_\uparrow(\theta, r) - q_\downarrow(\theta, r)) \quad (\text{C.22a})$$

$$= \tilde{N}_{\text{ph}}^2 (\text{Re}(Q))^2 \frac{q_{\text{at}}}{\pi (w_0^{\text{probe}})^2} \quad (\text{C.22b})$$

Considering the corresponding phase-shift we find $\text{var}(\phi) = \mathcal{K}^2 \text{var}(\Delta N)$, which is the atomic contribution in eq. (7.4).

C.1.1 Consistency check

From the phase shift measurement with all atoms in $|\uparrow\rangle$ we can determine the atom number as

$$N_{\text{at}} = \frac{\phi_{\text{at}}}{\mathcal{K}}. \quad (\text{C.23})$$

We therefore need to determine \mathcal{K} which can be done in two ways. First, from the projection noise scaling as shown in eq. (7.5). Second, it can be estimated directly from eq. (C.19) as

$$Q_{\uparrow} = -\frac{3\lambda^2}{4\pi}\gamma_e \left[\frac{5/9}{\Delta_{\uparrow} + i\gamma_e/2} + \frac{1/9}{\Delta_{\uparrow} + 452 \text{ MHz} + i\gamma_e/2} \right] \quad (\text{C.24})$$

where the first term is the coupling to $F' = 5$ and second term to $F' = 4$.

Furthermore, we also estimate the expected decoherence. For the probe interacting with an ensemble in the CSS aligned along the x -axis of the Bloch sphere the absorption coefficient is

$$\alpha^{(\text{CSS})} = \frac{\varrho_{\text{at}}}{4} (\text{Im}(Q_{\downarrow}) + \text{Im}(Q_{\uparrow})) \quad (\text{C.25})$$

With the total number of probe photons being $2N_{\text{ph}}$ this leads to $2\alpha^{(\text{CSS})}N_{\text{ph}}$ scattering events. With each single scattering event revealing the internal state of the atom this gives the amount of decoherence. Denoting the column density of atoms in the CSS by $\varrho_{\text{at}}^{(\text{CSS})}$ we have

$$\varrho_{\text{at}}^{(\text{CSS})} = \varrho_{\text{at}} \exp\left(-2\alpha^{(\text{CSS})}I_P(r)\frac{N_{\text{ph}}}{\varrho_{\text{at}}}\right). \quad (\text{C.26})$$

Considering the decoherence we find

$$\eta = 1 - \frac{N_{\text{at}}}{N_{\text{at}}^{(\text{CSS})}} \quad (\text{C.27a})$$

$$= 1 - \int_0^{2\pi} d\theta \int_0^{\infty} r dr I_P(r) \frac{\varrho_{\text{at}}^{(\text{CSS})}}{\varrho_{\text{at}}} \quad (\text{C.27b})$$

$$= 1 - \int_0^{2\pi} d\theta \int_0^{\infty} r dr I_P(r) \exp\left(-2\alpha^{(\text{CSS})}I_P(r)\frac{N_{\text{ph}}}{\varrho_{\text{at}}}\right). \quad (\text{C.27c})$$

As above this can directly be evaluated and compared to the measurements as done at the end of sec. 7.3.2.

SINGLE EXCITATION STATE

D.1 HANLE EFFECT

In the main text, sec. 8.1, we argued that heralding photons could scatter into our detection spatial mode due to the Hanle effect. Following [Demtröder 2008, sec. 7.1] we consider the V -system shown in fig. D.1(a). We take the light to propagate along y -direction, the excitation is made with x -polarized light (σ^+ and σ^-). A magnetic bias field \mathbf{B} is applied along the z -direction and we are interested in detecting x -polarized light emitted into the propagation directions, see fig. D.1(b). The x -polarized excitation light will create the excited state superposition

$$\psi_x = -\frac{1}{\sqrt{2}} (|F' = 4, m_F = 1\rangle + |F' = 4, m_F = -1\rangle). \quad (\text{D.1})$$

This state evolves according to

$$\psi_x(t) = e^{-\gamma_e t/2} \exp(-i\hat{\mathcal{H}}t/\hbar) \psi_x(0). \quad (\text{D.2})$$

Here the decay term has been added by hand and $\hat{\mathcal{H}}$ is the relevant Hamiltonian with eigenvalues $E_{m_F} = E_0 + \Delta\omega_{\text{Zeeman}}\hbar$, where $\Delta\omega_{\text{Zeeman}} = \mu_B g_F m_F |\mathbf{B}| / \hbar$, (eq. (3.1b)). This gives

$$\psi_x(t) = e^{-\gamma_e t/2} e^{-iE_0 t/\hbar} [\cos(\Delta\omega_{\text{Zeeman}} t) \psi_z + \sin(\Delta\omega_{\text{Zeeman}} t) \psi_x] \quad (\text{D.3a})$$

where

$$\psi_y = -\frac{i}{\sqrt{2}} (|F' = 4, m_F = 1\rangle - |F' = 4, m_F = -1\rangle). \quad (\text{D.3b})$$

For the detected intensity I_{fl} we will due to the polarization filter only see ψ_x which gives

$$I_{\text{fl}}(t) \propto e^{-\gamma_e t} \sin^2(\Delta\omega_{\text{Zeeman}} t). \quad (\text{D.4})$$

We see that $I_{\text{fl}}(t=0) = 0$, which as argued in the main text, is due to destructive interference. However for $\Delta\omega_{\text{Zeeman}} \gg \gamma_e$ the oscillating term averages out and $I_{\text{fl}} \neq 0$.

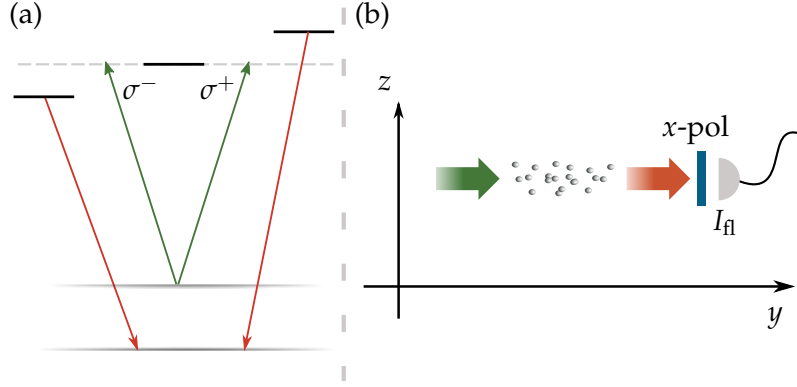


Figure D.1.: Hanle effect. (a) shows the atomic level structure for the considered case. (b) the spatial configuration considered.

D.2 n -POINT PULSES

To improve on the two-point pulses we have developed its generalization to n -point pulses.

Consider the general case of two measurements described by

$$\mathbf{a}_i = (a_{1,i}, a_{2,i}, \dots, a_{n,i}) \quad (\text{D.5})$$

$$\mathbf{b}_i = (b_{1,i}, b_{2,i}, \dots, b_{n,i}). \quad (\text{D.6})$$

We want to show that the quantity

$$\boldsymbol{\beta}_i = \mathbf{b}_i - K^T \mathbf{a}_i \quad (\text{D.7a})$$

is completely uncorrelated to \mathbf{a}_i , where

$$K = (C^{aa})^{-1} \cdot C^{ab}, \quad (\text{D.7b})$$

and

$$C \equiv \text{cov}(\mathbf{a}_i, \mathbf{b}_i) \quad (\text{D.7c})$$

$$= \begin{pmatrix} C^{aa} & C^{ab} \\ C^{ba} & C^{bb} \end{pmatrix}. \quad (\text{D.7d})$$

We start by defining the matrix

$$\tilde{K} \equiv \begin{pmatrix} 1 & -K \\ 0 & 1 \end{pmatrix}. \quad (\text{D.8})$$

We can now calculate the covariance matrix between \mathbf{a}_i and $\boldsymbol{\beta}_i$ as follows

$$\tilde{\mathbf{C}} \equiv \text{cov}(\mathbf{a}_i, \boldsymbol{\beta}_i) \quad (\text{D.9})$$

$$= \tilde{\mathbf{K}}^T \mathbf{C} \mathbf{K} \quad (\text{D.10})$$

$$= \begin{pmatrix} C^{aa} & C^{ab} - C^{aa} \mathbf{K}^T \\ C^{ba} - \mathbf{K}^T C^{aa} & C^{\beta\beta} \end{pmatrix} \quad (\text{D.11})$$

$$= \begin{pmatrix} C^{aa} & 0 \\ 0 & C^{\beta\beta} \end{pmatrix} \quad (\text{D.12})$$

where we in the last line have used the definition of \mathbf{K} . As the off-diagonal blocks are zero, we have shown that the measurements \mathbf{a}_i and $\boldsymbol{\beta}_i$ are now uncorrelated.

As an example we consider the 6-point pulses used in the analysis of the collective single excitation state in sec. 8.3.1 where the noise subtracted measurements are defined as eq. (8.6)

$$\phi_i = \tilde{\phi} - \sum_{\substack{j=-6 \\ j \neq 0}}^6 w_j \varphi_i^j. \quad (\text{D.13})$$

From eq. (D.7) we can now find the weight coefficients w_j (fig. D.2). Considering the variance of ϕ_i we have

$$\text{var}(\phi_i) = \text{var}(\tilde{\phi}) + \sum_{\substack{j=-6 \\ j \neq 0}}^6 w_j^2 \text{var}(\varphi_i^j). \quad (\text{D.14})$$

Taking the case where $\text{var}(\tilde{\phi}) = \text{var}(\varphi) = 1$, we see that the decorrelated measurements have an extra noise contribution of $\sum_j w_j^2 = 0.09$.

D.3 ERROR ESTIMATE

In this section we consider the statistical uncertainty on the quantity of interest (eqs. (8.7), (8.8) and (8.8))

$$W_{\mathbf{L}} \equiv \text{var}(\{Z_i\}_{i \in \mathbf{L}}) \quad (\text{D.15a})$$

where

$$Z_i \equiv \frac{\phi_i}{\sqrt{Y_i}} \quad (\text{D.15b})$$

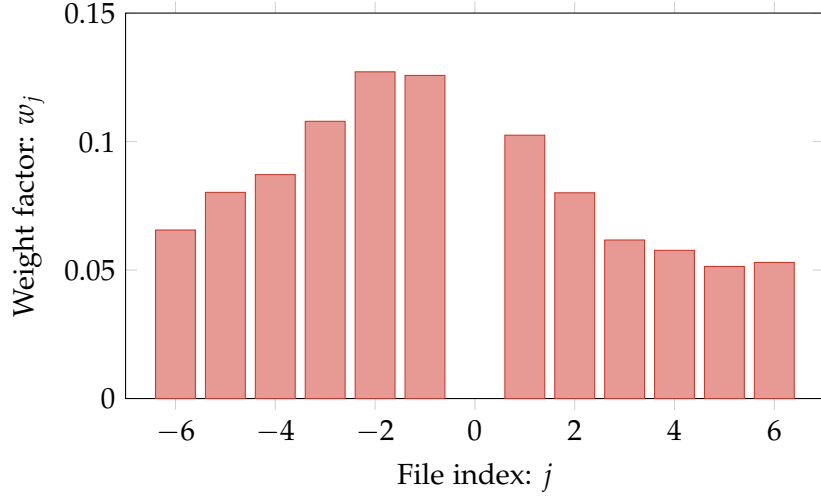


Figure D.2.: Weight factors used for the optimal noise subtraction.

and

$$Y_i \equiv \text{var}(\{\phi_{i-M/2}, \dots, \phi_{i+M/2}\}). \quad (\text{D.15c})$$

In calculating the W_L care needs to be taken.

The error in estimating Y_i is

$$\delta Y_i = \sqrt{\frac{2}{M-1}} Y_i, \quad (\text{D.16})$$

which, since all ϕ_i are independent and identical distributed just the mean squared error (MSE). The variance on Z_i can then be found via a Taylor expansion around the mean of Y_i

$$\text{var}(Z_i) = \left(1 + \frac{1}{4} \frac{2}{M+1}\right) \text{var}\left(\frac{\phi_i}{\langle Y_i \rangle}\right). \quad (\text{D.17})$$

From this we clearly see the effect of correlations between Z_i in a range M to make this negligible small we take $M \gg 1$. By taking $L \gg M$ we see that W_L is the unbiased estimator for the variance of Z_i . Its error is then simply the MSE given by

$$\delta W_L = \sqrt{\frac{2}{L-1}} W_L. \quad (\text{D.18})$$

This error-estimate have been tested both by a bootstrapping method [Efron et al. 1994] and by sub-dividing our data set, see table D.1.

Table D.1.: Error estimates using different methods.

METHOD	L	W_L	δW_L
MSE	Click	1.24	0.079
	No click	1.01	0.019
Sub-dividing	Click	1.25	0.076
	No click	1.01	0.020
Bootstrapping	Click	1.24	0.074
	No click	1.01	0.018

D.4 COLLECTIVE SINGLE EXCITATION STATE W. PHASE PROFILE

In this section we consider the single excitation state with a phase profile given as

$$|\tilde{1}'\rangle_A = \frac{1}{\sqrt{N_{\text{at}}}} \sum_{l=1}^{N_{\text{at}}} \exp(i\Delta k z_l) |\uparrow\uparrow \dots \uparrow\downarrow\uparrow \dots \uparrow\rangle. \quad (\text{D.19})$$

Using the the formalism introduced in chap. 3 and especially in sec. 3.6 we find

$$\tilde{p}_{\tilde{1}}(n) \equiv \langle \tilde{1}' | \hat{\mathcal{P}}(n) | \tilde{1}' \rangle \quad (\text{D.20a})$$

$$= \frac{1}{2^{N_{\text{at}}}} \frac{1}{N_{\text{at}}} \sum_{\pi} \left| \sum_{l=1}^{N_{\text{at}}} e^{i\phi_l} \left(\delta_{l\uparrow}^{\pi} - \delta_{l\downarrow}^{\pi} \right) \right|^2 \quad (\text{D.20b})$$

Where we have introduce two delta functions and the phase parameter $\phi_l = \Delta k z_l$. The simplest case is $\phi_l = 0 \forall l$, where the above becomes

$$\tilde{p}_{\tilde{1}}(n) = \frac{1}{2^{N_{\text{at}}}} \frac{1}{N_{\text{at}}} \binom{N_{\text{at}}}{n} (2n - N_{\text{at}})^2, \quad (\text{D.21})$$

in agreement with eq. (3.46). The main question is what happens when the phase $\phi_l \neq 0$. We assume that ϕ_l are uniformly distributed as

$$\phi_l \in \left[-\frac{\theta_M}{2}, \frac{\theta_M}{2} \right], \quad (\text{D.22})$$

This fits the experiment well. As the light travels through the atomic cloud each time it sees an atom it will get a phase shift — which can not depend on the atomic position in the regime of low optical depth.

The phasor sum can now be projected on to the real axes of the complex plane as

$$\operatorname{Re} \left(\sum_{l=1}^{N_{\text{at}}} e^{i\phi_l} \right) = \frac{1}{\theta_M} \int_{-\frac{\theta_M}{2}}^{+\frac{\theta_M}{2}} \cos(\phi) d\phi \quad (\text{D.23a})$$

$$= \operatorname{sinc}^2 \left(\frac{\theta_M}{2} \right). \quad (\text{D.23b})$$

This leaves us with the last demand which is to still have something that is normalized, which is done by “adding” a corresponding vacuum leading to the result

$$p_{\bar{1}}(\Delta N) = \operatorname{sinc}^2 \left(\frac{\theta_M}{2} \right) p_1(\Delta N) + \left[1 - \operatorname{sinc}^2 \left(\frac{\theta_M}{2} \right) \right] p_0(\Delta N). \quad (\text{D.24})$$

Which should be compared to eq. (3.47).

NANOFIBER EXPERIMENT

E.1 ATOM NUMBER

We consider the three level model showed in fig. 9.4 and are interested in how many photons it on average takes to move and atom to the $F = 3$ state, i.e., the parameter q . The probability to be in the $F = 3$ state after n scattering events is

$$p(1) = p_3 \tag{E.1a}$$

$$p(2) = p_3 p_4 \tag{E.1b}$$

$$p(3) = p_3 p_4^2 \tag{E.1c}$$

$$\vdots$$

$$p(n) = p_3 p_4^{n-1}. \tag{E.1d}$$

We easily find the mean value of n

$$\langle n \rangle = \sum_{n=1}^{\infty} n p(n) \tag{E.2a}$$

$$= 2.4 \tag{E.2b}$$

where we have used $p_4 = 7/12$ and $p_3 = 5/12$. More interesting is it to compute the variance

$$\text{var}(n) = \langle n^2 \rangle - \langle n \rangle^2 \tag{E.3a}$$

$$= 3.36. \tag{E.3b}$$

With $\text{var}(n) \geq \langle n \rangle$ this is a super-Poissonian process.

E.2 SQUEEZING ESTIMATION

We consider a two-level atom, which imprints a phase-shift on a light pulse given by

$$\phi = -\frac{1}{2}\mathcal{L}(\Delta)\frac{\Delta}{\gamma_e/2}N_{\text{at}} \quad (\text{E.4a})$$

$$\stackrel{\Delta \gg \gamma_e/2}{\approx} -\frac{1}{4}\frac{\gamma_e}{\Delta} \quad (\text{E.4b})$$

where

$$\mathcal{L}(\Delta) \equiv \alpha_{\text{at}} \frac{1}{1 + (\frac{\Delta}{\gamma_e/2})^2}. \quad (\text{E.4c})$$

This is a Lorentzian line-shape and α_{at} is the optical depth per atom. This gives a per atom phase-shift of

$$\phi_{\text{at}} = -\frac{1}{2}\mathcal{L}(\Delta)\frac{\Delta}{\gamma_e/2}. \quad (\text{E.5})$$

For a *homodyne* measurement using N_{ph} the minimum resolvable phase, limited by the shot noise of light, is

$$\delta\phi = \frac{1}{2\sqrt{\epsilon N_{\text{ph}}}} \quad (\text{E.6a})$$

with

$$\epsilon = \epsilon_{\text{vis}}\epsilon_{\text{elec}}\epsilon_{\text{loss}} \quad (\text{E.6b})$$

the total efficiency of the detection. Note that this is equivalent to our dual-sideband heterodyne measurement. This means that the number of atoms we can resolve is given by

$$\delta N_{\text{at}} = \frac{\delta\phi}{|\phi_{\text{at}}|} \quad (\text{E.7})$$

$$= \frac{1}{\sqrt{\epsilon N_{\text{ph}}}} \frac{1}{\mathcal{L}(\Delta)} \frac{\gamma_e/2}{\Delta} \quad (\text{E.8})$$

The variance then becomes

$$\text{var}(\delta N_{\text{at}}) = \frac{1}{\epsilon N_{\text{ph}} \mathcal{L}(\Delta)} \frac{1}{\mathcal{L}(\Delta)} \left(\frac{\gamma_e/2}{\Delta} \right)^2 \quad (\text{E.9})$$

$$= \frac{1}{\epsilon N_{\text{ph}} \mathcal{L}(\Delta)} \frac{1}{\alpha_{\text{at}}} \left[1 + \left(\frac{\Delta}{\gamma_e/2} \right)^2 \right] \left(\frac{\gamma_e/2}{\Delta} \right)^2 \quad (\text{E.10})$$

$$= \frac{1}{\epsilon N_{\text{ph}} \mathcal{L}(\Delta)} \frac{1}{\alpha_{\text{at}}} \left[1 + \left(\frac{\gamma_e/2}{\Delta} \right)^2 \right] \quad (\text{E.11})$$

$$\stackrel{\Delta \gg \gamma_e/2}{\approx} \frac{1}{\epsilon N_{\text{ph}} \mathcal{L}(\Delta) \alpha_{\text{at}}}. \quad (\text{E.12})$$

We now consider the disturbance of the measurement, on a CSS. The fraction of atoms that scatter is given as

$$\frac{N_{\text{ph,in}} - N_{\text{ph,out}}}{N_{\text{at}}} = \mathcal{L}(\Delta) N_{\text{ph,in}} \Rightarrow \quad (\text{E.13a})$$

$$\tilde{\eta} = \exp\left(-\frac{\mathcal{L}(\Delta) N_{\text{ph,in}}}{2}\right) \quad (\text{E.13b})$$

where $\tilde{\eta}$ is the *coherence*, and the factor of 2 in the exponential comes from the fact that only atoms in the upper state scatters. This leads to the natural definition of the decoherence parameter

$$\eta \equiv \frac{\mathcal{L}(\Delta)}{2}, \quad (\text{E.14})$$

which is simply the number of scattering events per photon.

We now consider the sequence where we have a total of N_{at} , make a $\pi/2$ pulse to create a equal superposition state and then measure N_{\uparrow} and have

$$\langle N_{\uparrow} \rangle = \frac{N_{\text{at}}}{2} \quad (\text{E.15a})$$

$$\text{var}(N_{\uparrow}) = \frac{N_{\text{at}}}{4}, \quad (\text{E.15b})$$

where $\text{var}(N_{\uparrow})$ is the projection noise. The signal to noise (atomic noise to shot noise) is given by

$$\kappa^2 = \frac{\text{var}(N_{\uparrow})}{\text{var}(\delta N_{\uparrow})^2} \quad (\text{E.16a})$$

$$= \frac{N_{\text{at}}}{4} \epsilon N_{\text{ph}} \mathcal{L}(\Delta) \alpha_{\text{at}} \quad (\text{E.16b})$$

$$= \alpha_{\text{eff}} \frac{N_{\text{ph}} L(\Delta)}{2} \quad (\text{E.16c})$$

where we have defined the *effective* optical depth as

$$\alpha_{\text{eff}} \equiv \frac{N_{\text{at}}}{2} \epsilon \alpha_{\text{at}} \quad (\text{E.17})$$

The amount of squeezing we can obtain is given by [Appel, Windpassinger, et al. 2009]

$$\zeta_{\text{Wineland}}^2 = \frac{1}{1 + \kappa^2} \frac{1}{\tilde{\eta}^2} \quad (\text{E.18a})$$

$$= \frac{1}{1 + \kappa^2} \frac{1}{\exp(-\mathcal{L}(\Delta) N_{\text{ph}})} \quad (\text{E.18b})$$

$$= \frac{1}{1 + \alpha_{\text{eff}} \frac{N_{\text{ph}} \mathcal{L}(\Delta)}{2}} \frac{1}{\exp(-\mathcal{L}(\Delta) N_{\text{ph}})}. \quad (\text{E.18c})$$

$$(\text{E.18d})$$

We minimize this and find

$$\min \{ \zeta_{\text{Wineland}}^2 \} = \frac{2}{\alpha_{\text{eff}}} \exp(1 - 2/\alpha_{\text{eff}}) \quad \text{for} \quad N_{\text{ph}} \mathcal{L}(\Delta) = \frac{\alpha_{\text{eff}} - 2}{\alpha_{\text{eff}}}. \quad (\text{E.19})$$

The requirement for obtaining spin squeezing is therefore

$$2 < \alpha_{\text{eff}} = \frac{N_{\text{at}}}{2} \epsilon \alpha_{\text{at}}. \quad (\text{E.20})$$

BIBLIOGRAPHY

- [Appel, Windpassinger, et al. 2009] J. Appel, P. J. Windpassinger, D. Oblak, U. B. Hoff, N. Kjærgaard, and E. S. Polzik (2009). „Mesoscopic atomic entanglement for precision measurements beyond the standard quantum limit.“ *Proceedings of the National Academy of Sciences* **106.27**, pp. 10960–10965. DOI: [10.1073/pnas.0901550106](https://doi.org/10.1073/pnas.0901550106) (cit. on pp. [2](#), [4](#), [85](#), [95](#), [169](#), [182](#)).
- [Appel et al. 2007] J. Appel, D. Hoffman, E. Figueroa, and A. I. Lvovsky (2007). „Electronic noise in optical homodyne tomography.“ *Physical Review A* **75.3**, p. 035802. DOI: [10.1103/PhysRevA.75.035802](https://doi.org/10.1103/PhysRevA.75.035802) (cit. on pp. [98](#), [117](#), [120](#)).
- [Appel, MacRae, et al. 2009] J. Appel, A. MacRae, and A. I. Lvovsky (2009). „A versatile digital GHz phase lock for external cavity diode lasers.“ *Measurement Science & Technology* **20.5**, p. 055302. DOI: [10.1088/0957-0233/20/5/055302](https://doi.org/10.1088/0957-0233/20/5/055302) (cit. on p. [72](#)).
- [Arecchi et al. 1972] F. T. Arecchi, H. Thomas, R. Gilmore, and E. Courtens (1972). „Atomic Coherent States in Quantum Optics.“ *Physical Review A* **6.6**, pp. 2211–2237. DOI: [10.1103/PhysRevA.6.2211](https://doi.org/10.1103/PhysRevA.6.2211) (cit. on p. [29](#)).
- [Aspelmeyer et al. 2013] M. Aspelmeyer, T. J. Kippenberg, and F. Marquardt (2013). „Cavity Optomechanics.“ arXiv: [1303.0733v1](https://arxiv.org/abs/1303.0733v1) (cit. on p. [131](#)).
- [Babichev et al. 2004] S. Babichev, J. Appel, and A. Lvovsky (2004). „Homodyne Tomography Characterization and Nonlocality of a Dual-Mode Optical Qubit.“ *Physical Review Letters* **92.19**, p. 193601. ISSN: 1079-7114. DOI: [10.1103/physrevlett.92.193601](https://doi.org/10.1103/physrevlett.92.193601) (cit. on p. [2](#)).
- [Béguin n.d.] J. B. Béguin. „A Novel Invisible Quantum Interface Between few Atoms and few Photons.“ To be published (cit. on pp. [6](#), [131](#)).
- [Béguin et al. 2014] J. B. Béguin, E. Bookjans, S. L. Christensen, H. L. Sørensen, J. H. Müller, J. Appel, and E. S. Polzik (2014). „Generation

Bibliography

- and detection of a sub-Poissonian atom number distribution in a one-dimensional optical lattice.” arXiv: [1408.1266v1](https://arxiv.org/abs/1408.1266v1) (cit. on pp. [6](#), [129](#), [132](#), [134](#)).
- [Bimbard et al. 2014] E. Bimbard, R. Boddeda, N. Vitrant, A. Grankin, V. Parigi, J. Stanojevic, A. Ourjoumtsev, and P. Grangier (2014). „Homodyne Tomography of a Single Photon Retrieved on Demand from a Cavity-Enhanced Cold Atom Memory.” *Physical Review Letters* **112.3**, p. 033601. DOI: [10.1103/PhysRevLett.112.033601](https://doi.org/10.1103/PhysRevLett.112.033601) (cit. on pp. [1](#), [101](#), [127](#), [155](#)).
- [Bizarro 1994] J. P. Bizarro (1994). „Weyl-Wigner formalism for rotation angle and angular-momentum variables in quantum mechanics.” *Physical Review A* **49** (5), pp. 3255–3276. DOI: [10.1103/PhysRevA.49.3255](https://doi.org/10.1103/PhysRevA.49.3255) (cit. on p. [28](#)).
- [Bohnet et al. 2014] J. G. Bohnet, K. C. Cox, M. A. Norcia, J. M. Weiner, Z. Chen, and J. K. Thompson (2014). „Reduced spin measurement back-action for a phase sensitivity ten times beyond the standard quantum limit.” *Nature Photonics*, pp. 1–4. DOI: [10.1038/nphoton.2014.151](https://doi.org/10.1038/nphoton.2014.151) (cit. on p. [95](#)).
- [Brask et al. 2010] J. B. Brask, I. Rigas, E. S. Polzik, U. L. Andersen, and A. S. Sørensen (2010). „Hybrid Long-Distance Entanglement Distribution Protocol.” *Physical Review Letters* **105.16**, [10.1103/PhysRevLett.105.160501](https://doi.org/10.1103/PhysRevLett.105.160501). ISSN: 1079-7114. DOI: [10.1103/physrevlett.105.160501](https://doi.org/10.1103/physrevlett.105.160501) (cit. on p. [154](#)).
- [Cahill et al. 1969] K. E. Cahill and R. J. Glauber (1969). „Density Operators and Quasiprobability Distributions.” *Physical Review* **177** (5), pp. 1882–1902. DOI: [10.1103/PhysRev.177.1882](https://doi.org/10.1103/PhysRev.177.1882) (cit. on p. [13](#)).
- [Chang et al. 2012] D. E. Chang, L. Jiang, A. V. Gorshkov, and H. J. Kimble (2012). „Cavity QED with atomic mirrors.” *New Journal of Physics* **14.6**, p. 063003. DOI: [10.1088/1367-2630/14/6/063003](https://doi.org/10.1088/1367-2630/14/6/063003) (cit. on p. [154](#)).
- [Chen et al. 2001] Y. C. Chen, Y. A. Liao, L. Hsu, and I. A. Yu (2001). „Simple technique for directly and accurately measuring the number of atoms in a magneto-optical trap.” *Physical Review A* **64.3**, p. 031401. DOI: [10.1103/PhysRevA.64.031401](https://doi.org/10.1103/PhysRevA.64.031401) (cit. on p. [139](#)).

- [Choi et al. 2008] K. S. Choi, H. Deng, J. Laurat, and H. J. Kimble (2008). „Mapping photonic entanglement into and out of a quantum memory.“ *Nature* **452.7183**, pp. 67–71. ISSN: 1476-4687. DOI: [10.1038/nature06670](https://doi.org/10.1038/nature06670) (cit. on p. 2).
- [Choi et al. 2010] K. S. Choi, A. Goban, S. B. Papp, S. J. van Enk, and H. J. Kimble (2010). „Entanglement of spin waves among four quantum memories.“ *Nature* **468.7322**, pp. 412–416. ISSN: 1476-4687. DOI: [10.1038/nature09568](https://doi.org/10.1038/nature09568) (cit. on p. 2).
- [Chou et al. 2005] C. W. Chou, H. de Riedmatten, D. Felinto, S. V. Polyakov, S. J. van Enk, and H. J. Kimble (2005). „Measurement-induced entanglement for excitation stored in remote atomic ensembles.“ *Nature* **438.7069**, pp. 828–832. ISSN: 1476-4679. DOI: [10.1038/nature04353](https://doi.org/10.1038/nature04353) (cit. on p. 155).
- [Christensen et al. 2014] S. L. Christensen, J. B. Béguin, E. Bookjans, H. L. Sørensen, J. H. Müller, J. Appel, and E. S. Polzik (2014). „Quantum interference of a single spin excitation with a macroscopic atomic ensemble.“ *Physical Review A* **89**, p. 033801. DOI: [10.1103/PhysRevA.89.033801](https://doi.org/10.1103/PhysRevA.89.033801) (cit. on pp. 5, 101, 156).
- [Christensen et al. 2013] S. L. Christensen, J. B. Béguin, H. L. Sørensen, E. Bookjans, D. Oblak, J. H. Müller, J. Appel, and E. S. Polzik (2013). „Towards quantum state tomography of a single polariton state of an atomic ensemble.“ *New Journal of Physics* **15.1**, p. 015002. DOI: [10.1088/1367-2630/15/1/015002](https://doi.org/10.1088/1367-2630/15/1/015002) (cit. on pp. 5, 101, 156).
- [Christensen 2012] S. L. Christensen (2012). *Generation of exotic quantum states in a cold ensemble of Caesium atoms*. MA thesis. URL: <http://quantop.nbi.ku.dk/publications/thesis/> (cit. on pp. 5, 76, 83, 85, 87, 106).
- [Combesure et al. 2012] M. Combesure and D. Robert (2012). *Coherent states and applications in Mathematical Physics*. Springer. ISBN: 9400701950 (cit. on p. 29).
- [Demtröder 2008] W. Demtröder (2008). *Laser Spectroscopy*. Vol. 2: Experimental Techniques. Springer Science & Business Media. ISBN: 3540749543 (cit. on p. 173).

Bibliography

- [Dicke 1954] R. Dicke (1954). „Coherence in Spontaneous Radiation Processes.“ *Physical Review* **93.1**, pp. 99–110. DOI: [10.1103/PhysRev.93.99](https://doi.org/10.1103/PhysRev.93.99) (cit. on pp. 33, 34).
- [Ding et al. 2010] L. Ding, C. Belacel, S. Ducci, G. Leo, and I. Favero (2010). „Ultralow loss single-mode silica tapers manufactured by a microheater.“ *Applied Optics* **49.13**, pp. 2441–2445. DOI: [10.1364/AO.49.002441](https://doi.org/10.1364/AO.49.002441) (cit. on p. 130).
- [Dowling et al. 1994] J. P. Dowling, G. S. Agarwal, and W. P. Schleich (1994). „Wigner distribution of a general angular-momentum state: Applications to a collection of two-level atoms.“ *Physical Review A* **49** (5), pp. 4101–4109. DOI: [10.1103/PhysRevA.49.4101](https://doi.org/10.1103/PhysRevA.49.4101) (cit. on pp. 27, 28).
- [Duan et al. 2001] L. M. Duan, M. D. Lukin, J. I. Cirac, and P. Zoller (2001). „Long-distance quantum communication with atomic ensembles and linear optics.“ *Nature* **414.6862**, pp. 413–418. DOI: [10.1038/35106500](https://doi.org/10.1038/35106500) (cit. on pp. 53, 58).
- [Dubost et al. 2012] B. Dubost, M. Koschorreck, M. Napolitano, N. Behbood, R. J. Sewell, and M. W. Mitchell (2012). „Efficient Quantification of Non-Gaussian Spin Distributions.“ *Physical Review Letters* **108.18**, pp. 1–5. DOI: [10.1103/PhysRevLett.108.183602](https://doi.org/10.1103/PhysRevLett.108.183602) (cit. on p. 125).
- [Efron et al. 1994] B. Efron and R. Tibshirani (1994). *An Introduction to the Bootstrap*. Chapman & Hall/CRC Monographs on Statistics & Applied Probability. Taylor & Francis. ISBN: 9780412042317 (cit. on p. 176).
- [Filip et al. 2011] R. Filip and L. Mišta (2011). „Detecting Quantum States with a Positive Wigner Function beyond Mixtures of Gaussian States.“ *Physical Review Letters* **106.20**, p. 200401. DOI: [10.1103/PhysRevLett.106.200401](https://doi.org/10.1103/PhysRevLett.106.200401) (cit. on p. 125).
- [Garrison et al. 2008] J. Garrison and R. Chiao (2008). *Quantum optics*. Oxford graduate texts. Oxford University Press. ISBN: 9780198508861 (cit. on pp. 9, 15).

- [Gerry et al. 2005] C. Gerry and P. Knight (2005). *Introductory Quantum Optics*. Cambridge University Press. ISBN: 9780521527354 (cit. on pp. 60, 161).
- [Giovannetti et al. 2011] V. Giovannetti, S. Lloyd, and L. Maccone (2011). „Advances in quantum metrology.“ *Nature Photonics* 5.4, pp. 222–229. DOI: [10.1038/NPHOTON.2011.35](https://doi.org/10.1038/NPHOTON.2011.35) (cit. on pp. 30, 31).
- [Grimm et al. 2000] R. Grimm, M. Weidemüller, and Y. B. Ovchinnikov (2000). „Optical Dipole Traps for Neutral Atoms.“ *Advances In Atomic, Molecular, and Optical Physics*. Ed. by B. Bederson and H. Walther. Vol. 44. Academic Press, pp. 95–170. DOI: [10.1016/S1049-250X\(08\)60186-X](https://doi.org/10.1016/S1049-250X(08)60186-X) (cit. on p. 68).
- [Hammerer et al. 2010] K. Hammerer, A. S. Sørensen, and E. S. Polzik (2010). „Quantum interface between light and atomic ensembles.“ *Reviews of Modern Physics* 82.2, pp. 1041–1093. DOI: [10.1103/RevModPhys.82.1041](https://doi.org/10.1103/RevModPhys.82.1041) (cit. on pp. 2, 26, 32, 56, 58, 119, 120, 129).
- [Hinkley et al. 2013] N. Hinkley, J. A. Sherman, N. B. Phillips, M. Schioppo, N. D. Lemke, K. Beloy, M. Pizzocaro, C. W. Oates, and A. D. Ludlow (2013). „An Atomic Clock with 10^{-18} Instability.“ *Science* 341.6151, pp. 1215–1218. DOI: [10.1126/science.1240420](https://doi.org/10.1126/science.1240420) (cit. on p. 50).
- [Hoffman et al. 2014] J. E. Hoffman, S. Ravets, J. A. Grover, P. Solano, P. R. Kordell, J. D. Wong-Campos, L. A. Orozco, and S. L. Rolston (2014). „Ultrahigh transmission optical nanofibers.“ *AIP Advances* 4.6, p. 067124. DOI: [10.1063/1.4879799](https://doi.org/10.1063/1.4879799) (cit. on p. 130).
- [Holstein et al. 1940] T. Holstein and H. Primakoff (1940). „Field Dependence of the Intrinsic Domain Magnetization of a Ferromagnet.“ *Physical Review* 58 (12), pp. 1098–1113. DOI: [10.1103/PhysRev.58.1098](https://doi.org/10.1103/PhysRev.58.1098) (cit. on p. 26).
- [Hume et al. 2013] D. Hume, I. Stroescu, M. Joos, W. Muessel, H. Strobel, and M. Oberthaler (2013). „Accurate Atom Counting in Mesoscopic Ensembles.“ *Physical Review Letters* 111.25, p. 253001. DOI: [10.1103/physrevlett.111.253001](https://doi.org/10.1103/physrevlett.111.253001) (cit. on p. 144).
- [Haas et al. 2014] F. Haas, J. Volz, R. Gehr, J. Reichel, and J. Estève (2014). „Entangled States of More Than 40 Atoms in an Optical Fiber

Bibliography

- Cavity." *Science* **344.6180**, pp. 180–183. ISSN: 1095-9203. DOI: [10.1126/science.1248905](https://doi.org/10.1126/science.1248905) (cit. on pp. [156](#), [157](#)).
- [Itano et al. 1993] W. M. Itano, J. C. Bergquist, J. Bollinger, J. M. Gilligan, D. J. Heinzen, F. L. Moore, M. G. Raizen, and D. J. Wineland (1993). „Quantum Projection Noise - Population Fluctuations in 2-Level Systems." *Physical Review A* **47.5**, pp. 3554–3570. DOI: [10.1103/PhysRevA.47.3554](https://doi.org/10.1103/PhysRevA.47.3554) (cit. on p. [38](#)).
- [Jensen et al. 2010] K. Jensen, W. Wasilewski, H. Krauter, T. Fernholz, B. M. Nielsen, M. Owari, M. B. Plenio, A. Serafini, M. M. Wolf, and E. S. Polzik (2010). „Quantum memory for entangled continuous-variable states." *Nature Physics* **7.1**, pp. 13–16. DOI: [10.1038/nphys1819](https://doi.org/10.1038/nphys1819) (cit. on p. [130](#)).
- [Ježek et al. 2011] M. Ježek, I. Straka, M. Mičuda, M. Dušek, J. Fíurášek, and R. Filip (2011). „Experimental Test of the Quantum Non-Gaussian Character of a Heralded Single-Photon State." *Physical Review Letters* **107.21**, p. 213602. DOI: [10.1103/PhysRevLett.107.213602](https://doi.org/10.1103/PhysRevLett.107.213602) (cit. on p. [125](#)).
- [Kenney et al. 1951] J. F. Kenney and E. S. Keeping (1951). *Mathematics of Statistics, Pt. 2*. Van Nostrand (cit. on p. [125](#)).
- [Kiesel et al. 2011] T. Kiesel, W. Vogel, M. Bellini, and A. Zavatta (2011). „Nonclassicality quasiprobability of single-photon-added thermal states." *Physical Review A* **83.3**, p. 032116. DOI: [10.1103/PhysRevA.83.032116](https://doi.org/10.1103/PhysRevA.83.032116) (cit. on p. [98](#)).
- [Kiesel et al. 2012] T. Kiesel, W. Vogel, S. L. Christensen, J. B. Béguin, J. Appel, and E. S. Polzik (2012). „Atomic nonclassicality quasiprobabilities." *Physical Review A* **86.4**, p. 042108. DOI: [10.1103/PhysRevA.86.042108](https://doi.org/10.1103/PhysRevA.86.042108) (cit. on pp. [4](#), [85](#), [96](#), [97](#)).
- [Kimble 2008] H. J. Kimble (2008). „The quantum internet." *Nature* **453.7198**, pp. 1023–1030. DOI: [10.1038/nature07127](https://doi.org/10.1038/nature07127) (cit. on pp. [1](#), [130](#)).
- [Kitagawa et al. 1993] M. Kitagawa and M. Ueda (1993). „Squeezed spin states." *Physical Review A* **47** (6), pp. 5138–5143. DOI: [10.1103/PhysRevA.47.5138](https://doi.org/10.1103/PhysRevA.47.5138) (cit. on pp. [30](#), [53](#)).

- [Kot et al. 2012] E. Kot, N. Grønbech-Jensen, B. M. Nielsen, J. S. Neergaard—Nielsen, E. S. Polzik, and A. Sørensen (2012). „Breakdown of the Classical Description of a Local System.“ *Physical Review Letters* **108**, pp. 1–5. DOI: [10.1103/PhysRevLett.108.233601](https://doi.org/10.1103/PhysRevLett.108.233601) (cit. on p. 100).
- [Krauter et al. 2013] H. Krauter, D. Salart, C. A. Muschik, J. M. Petersen, H. Shen, T. Fernholz, and E. S. Polzik (2013). „Deterministic quantum teleportation between distant atomic objects.“ *Nature Physics* **9.7**, pp. 400–404. DOI: [10.1038/nphys2631](https://doi.org/10.1038/nphys2631) (cit. on p. 130).
- [Kuzmich et al. 2003] A. Kuzmich, W. P. Bowen, A. D. Boozer, A. Boca, C. W. Chou, L. M. Duan, and H. J. Kimble (2003). „Generation of nonclassical photon pairs for scalable quantum communication with atomic ensembles.“ *Nature* **423.6941**, pp. 731–734. DOI: [10.1038/nature01714](https://doi.org/10.1038/nature01714) (cit. on p. 101).
- [Kuzmich et al. 2000] A. Kuzmich and E. S. Polzik (2000). „Atomic Quantum State Teleportation and Swapping.“ *Physical Review Letters* **85** (26), pp. 5639–5642. DOI: [10.1103/PhysRevLett.85.5639](https://doi.org/10.1103/PhysRevLett.85.5639) (cit. on p. 26).
- [Kyung 2010] S. C. Kyung (2010). *Testing the Volume Bragg Grating*. Tech. rep. (cit. on p. 146).
- [Lacroûte et al. 2012] C. Lacroûte, K. S. Choi, A. Goban, D. J. Alton, D. Ding, N. P. Stern, and H. J. Kimble (2012). „A state-insensitive, compensated nanofiber trap.“ *New Journal of Physics* **14.2**, p. 023056. DOI: [10.1088/1367-2630/14/2/023056](https://doi.org/10.1088/1367-2630/14/2/023056) (cit. on p. 132).
- [Le Kien et al. 2004] F. Le Kien, V. I. Balykin, and K. Hakuta (2004). „Atom trap and waveguide using a two-color evanescent light field around a subwavelength-diameter optical fiber.“ *Physical Review A* **70.6**, pp. 1–9. DOI: [10.1103/PhysRevA.70.063403](https://doi.org/10.1103/PhysRevA.70.063403) (cit. on p. 132).
- [Le Kien et al. 2005] F. Le Kien, S. Dutta Gupta, V. I. Balykin, and K. Hakuta (2005). „Spontaneous emission of a cesium atom near a nanofiber: Efficient coupling of light to guided modes.“ *Physical Review A* **72** (3), p. 032509. DOI: [10.1103/PhysRevA.72.032509](https://doi.org/10.1103/PhysRevA.72.032509) (cit. on p. 145).
- [Le Kien et al. 2013] F. Le Kien, P. Schneeweiss, and A. Rauschenbeutel (2013). „Dynamical polarizability of atoms in arbitrary light

Bibliography

- fields: general theory and application to cesium." *The European Physical Journal D* **67.5**, pp. 92–16. DOI: [10.1140/epjd/e2013-30729-x](https://doi.org/10.1140/epjd/e2013-30729-x) (cit. on p. 139).
- [Leonhardt 1997] U. Leonhardt (1997). *Measuring the Quantum State of Light*. Cambridge Studies in Modern Optics. Cambridge University Press. ISBN: 9780521497305 (cit. on pp. 13, 14, 97, 117).
- [Leroux et al. 2010] I. D. Leroux, M. H. Schleier-Smith, and V. Vuletić (2010). „Orientation-Dependent Entanglement Lifetime in a Squeezed Atomic Clock." *Physical Review A* **104** (25), p. 250801. DOI: [10.1103/PhysRevLett.104.250801](https://doi.org/10.1103/PhysRevLett.104.250801) (cit. on p. 2).
- [Lodahl et al. 2013] P. Lodahl, S. Mahmoodian, and S. Stobbe (2013). „Interfacing single photons and single quantum dots with photonic nanostructures." arXiv: [1312.1079v1](https://arxiv.org/abs/1312.1079v1) [quant-ph] (cit. on pp. 131, 145).
- [Louchet-Chauvet et al. 2010] A. Louchet-Chauvet, J. Appel, J. J. Renema, D. Oblak, N. Kjaergaard, and E. S. Polzik (2010). „Entanglement assisted atomic clock beyond the projection noise limit." *New Journal of Physics* **12.6**, pp. 1–17. DOI: [10.1088/1367-2630/12/6/065032](https://doi.org/10.1088/1367-2630/12/6/065032) (cit. on pp. 2, 4, 85, 92, 96).
- [Loudon 2000] R. Loudon (2000). *The Quantum Theory of Light*. Oxford science publications. OUP Oxford. ISBN: 9780198501770 (cit. on p. 43).
- [Lvovsky et al. 2009] A. I. Lvovsky and M. G. Raymer (2009). „Continuous variable optical quantum state tomography." *Reviews of Modern Physics* **81.1**, pp. 299–332. DOI: [10.1103/RevModPhys.81.299](https://doi.org/10.1103/RevModPhys.81.299) (cit. on pp. 97, 117).
- [Lvovsky et al. 2002] A. I. Lvovsky and J. H. Shapiro (2002). „Non-classical character of a statistical mixture of the single-photon and vacuum optical states." *Physical Review A* **65**, pp. 1–6. DOI: [10.1103/PhysRevA.65.033830](https://doi.org/10.1103/PhysRevA.65.033830) (cit. on p. 124).
- [Lücke et al. 2014] B. Lücke, J. Peise, G. Vitagliano, J. Arlt, L. Santos, G. Tóth, and C. Klempt (2014). „Detecting Multiparticle Entanglement of Dicke States." *Physical Review Letters* **112.15**, p. 155304. DOI: [10.1103/physrevlett.112.155304](https://doi.org/10.1103/physrevlett.112.155304) (cit. on p. 95).

- [Ma et al. 2011] J. Ma, X. Wang, C. P. Sun, and F. Nori (2011). „Quantum spin squeezing.“ *Physics Reports* **509.2-3**, pp. 89–165. DOI: [10.1016/j.physrep.2011.08.003](https://doi.org/10.1016/j.physrep.2011.08.003) (cit. on pp. [30](#), [155](#)).
- [MacRae et al. 2012] A. MacRae, T. Brannan, R. Achal, and A. Lvovsky (2012). „Tomography of a High-Purity Narrowband Photon from a Transient Atomic Collective Excitation.“ *Physical Review Letters* **109.3**, pp. 1–4. DOI: [10.1103/PhysRevLett.109.033601](https://doi.org/10.1103/PhysRevLett.109.033601) (cit. on pp. [101](#), [155](#)).
- [Mandel 1986] L. Mandel (1986). „Non-classical states of the electromagnetic field.“ *Physica Scripta* **1986**, p. 34. DOI: [10.1088/0031-8949/1986/T12/005](https://doi.org/10.1088/0031-8949/1986/T12/005) (cit. on p. [96](#)).
- [Mandel et al. 1995] L. Mandel and E. Wolf (1995). *Optical Coherence and Quantum Optics*. Cambridge University Press. ISBN: 9780521417112. DOI: [10.1017/CB09781139644105](https://doi.org/10.1017/CB09781139644105) (cit. on pp. [9](#), [12](#), [27–29](#), [33](#), [38](#), [49](#), [97](#)).
- [McConnell et al. 2013] R. McConnell, H. Zhang, S. Ćuk, J. Hu, M. H. Schleier-Smith, and V. Vuletić (2013). „Generating entangled spin states for quantum metrology by single-photon detection.“ *Physical Review A* **88.6**, p. 063802. DOI: [10.1103/PhysRevA.88.063802](https://doi.org/10.1103/PhysRevA.88.063802) (cit. on pp. [154](#), [155](#)).
- [Mitchell et al. 2012] M. W. Mitchell, M. Koschorreck, M. Kubasik, M. Napolitano, and R. J. Sewell (2012). „Certified quantum non-demolition measurement of material systems.“ *New Journal of Physics* **14.8**, p. 085021. DOI: [10.1088/1367-2630/14/8/085021](https://doi.org/10.1088/1367-2630/14/8/085021) (cit. on p. [54](#)).
- [Mitsch et al. 2014] R. Mitsch, C. Sayrin, B. Albrecht, P. Schneeweiss, and A. Rauschenbeutel (2014). „Directional nanophotonic atom—waveguide interface based on spin—orbit interaction of light.“ arXiv: [1406.0896](https://arxiv.org/abs/1406.0896) (cit. on p. [145](#)).
- [Neergaard-Nielsen et al. 2006] J. Neergaard-Nielsen, B. Nielsen, C. Hettich, K. Mølmer, and E. Polzik (2006). „Generation of a Superposition of Odd Photon Number States for Quantum Information Networks.“ *Physical Review Letters* **97.8**, p. 083604. ISSN: 1079-7114. DOI: [10.1103/physrevlett.97.083604](https://doi.org/10.1103/physrevlett.97.083604) (cit. on p. [2](#)).

Bibliography

- [Oblak 2010] D. Oblak (2010). *Quantum State Engineering in Cold Cesium Atoms*. PhD thesis. URL: http://www.nbi.ku.dk/english/research/phd_theses/phd_theses_2010/daniel_oblak/ (cit. on pp. 4, 9, 20, 21, 26, 65, 67, 68, 72, 76, 78, 81, 83, 85, 86, 90, 93, 153, 167).
- [O’Connell et al. 2010] A. D. O’Connell, M. Hofheinz, M. Ansmann, R. C. Bialczak, M. Lenander, E. Lucero, M. Neeley, D. Sank, H. Wang, M. Weides, and et al. (2010). „Quantum ground state and single-phonon control of a mechanical resonator.“ *Nature* **464.7289**, pp. 697–703. DOI: [10.1038/nature08967](https://doi.org/10.1038/nature08967) (cit. on p. 1).
- [Ourjoumtsev et al. 2007] A. Ourjoumtsev, H. Jeong, R. Tualle-Brouiri, and P. Grangier (2007). „Generation of optical Schrödinger cats from photon number states.“ *Nature* **448.7155**, pp. 784–786. DOI: [10.1038/nature06054](https://doi.org/10.1038/nature06054) (cit. on p. 2).
- [Peres 1995] A. Peres (1995). *Quantum theory: concepts and methods*. Vol. 72. Springer Science & Business Media. ISBN: 0792336321 (cit. on p. 1).
- [Petersen et al. 2014] J. Petersen, J. Volz, and A. Rauschenbeutel (2014). „Chiral nanophotonic waveguide interface based on spin-orbit interaction of light.“ *Science* **346.6205**, pp. 67–71. DOI: [10.1126/science.1257671](https://doi.org/10.1126/science.1257671) (cit. on p. 145).
- [Petrov 2006] P. Petrov (2006). *Quantum noise limited light interferometry*. PhD thesis (cit. on p. 153).
- [Pino et al. 2011] J. M. Pino, R. J. Wild, P. Makotyn, D. S. Jin, and E. A. Cornell (2011). „Photon counting for Bragg spectroscopy of quantum gases.“ *Physical Review A* **83.3**, p. 033615. DOI: [10.1103/PhysRevA.83.033615](https://doi.org/10.1103/PhysRevA.83.033615) (cit. on p. 135).
- [Poizat et al. 1994] J. P. Poizat, F. J. Rock, P. Grangier, and Roch (1994). „Characterization of quantum non-demolition measurements in optics.“ *Ann. Phys. Fr.* **19.3**, pp. 265–297. DOI: [10.1051/anphys:01994001903026500](https://doi.org/10.1051/anphys:01994001903026500) (cit. on p. 54).
- [Reitz et al. 2013] D. Reitz, C. Sayrin, R. Mitsch, P. Schneeweiss, and A. Rauschenbeutel (2013). „Coherence Properties of Nanofiber-Trapped

- Cesium Atoms." *Physical Review Letters* **110.24**, p. 243603. ISSN: 1079-7114. DOI: [10.1103/physrevlett.110.243603](https://doi.org/10.1103/physrevlett.110.243603) (cit. on p. 153).
- [Saffman et al. 2009] M. Saffman, D. Oblak, J. Appel, and E. S. Polzik (2009). „Spin squeezing of atomic ensembles by multicolor quantum nondemolition measurements." *Physical Review A* **79** (2), p. 023831. DOI: [10.1103/PhysRevA.79.023831](https://doi.org/10.1103/PhysRevA.79.023831) (cit. on pp. 20, 72).
- [Sagué et al. 2008] G. Sagué, A. Baade, and A. Rauschenbeutel (2008). „Blue-detuned evanescent field surface traps for neutral atoms based on mode interference in ultrathin optical fibres." *New Journal of Physics* **10.11**, p. 113008. DOI: [10.1088/1367-2630/10/11/113008](https://doi.org/10.1088/1367-2630/10/11/113008) (cit. on p. 132).
- [Schleier-Smith et al. 2010] M. H. Schleier-Smith, I. D. Leroux, and V. Vuletić (2010). „States of an Ensemble of Two-Level Atoms with Reduced Quantum Uncertainty." *Physical Review Letters* **104.7**, p. 073604. DOI: [10.1103/PhysRevLett.104.073604](https://doi.org/10.1103/PhysRevLett.104.073604) (cit. on p. 2).
- [Schmied et al. 2011] R. Schmied and P. Treutlein (2011). „Tomographic reconstruction of the Wigner function on the Bloch sphere." *New Journal of Physics* **13.6**, pp. 1–18. DOI: [10.1088/1367-2630/13/6/065019](https://doi.org/10.1088/1367-2630/13/6/065019) (cit. on p. 28).
- [Schwinger 1952] J. S. Schwinger (1952). *On angular momentum*. Report (U.S. Atomic Energy Commission). U.S. Atomic Energy Commission (cit. on p. 15).
- [Sewell et al. 2013] R. J. Sewell, M. Napolitano, N. Behbood, G. Colangelo, and M. W. Mitchell (2013). „Certified quantum non-demolition measurement of a macroscopic material system." *Nature Photonics*. DOI: [10.1038/nphoton.2013.100](https://doi.org/10.1038/nphoton.2013.100) (cit. on p. 54).
- [Sherson et al. 2006] J. F. Sherson, H. Krauter, R. K. Olsson, B. Julsgaard, K. Hammerer, I. Cirac, and E. S. Polzik (2006). „Quantum teleportation between light and matter." *Nature* **443.7111**, pp. 557–560. ISSN: 1476-4687. DOI: [10.1038/nature05136](https://doi.org/10.1038/nature05136) (cit. on p. 130).
- [Simon et al. 2007] J. Simon, H. Tanji, J. K. Thompson, and V. Vuletić (2007). „Interfacing Collective Atomic Excitations and Single Photons." *Physical Review Letters* **98.18**, p. 183601. ISSN: 1079-7114. DOI: [10.1103/physrevlett.98.183601](https://doi.org/10.1103/physrevlett.98.183601) (cit. on p. 1).

Bibliography

- [Sobelman 2006] I. I. Sobelman (2006). *Theory of atomic spectra*. Alpha Science International Ltd. ISBN: 9781842652039 (cit. on p. 43).
- [Steck 2010] D. A. Steck (2010). „Alkali D Line Data,“ pp. 1–31. URL: <http://steck.us/alkalidata/cesiumnumbers.pdf> (cit. on pp. 24, 25, 106).
- [Steck 2012] – (2012). *Quantum and Atom Optics*. Ed. by D. A. Steck. URL: <http://atomoptics.uoregon.edu/~dsteck/teaching/quantum-optics/> (cit. on p. 9).
- [Strobel et al. 2014] H. Strobel, W. Muessel, D. Linnemann, T. Zibold, D. B. Hume, L. Pezze, A. Smerzi, and M. K. Oberthaler (2014). „Fisher information and entanglement of non-Gaussian spin states.“ *Science* **345.6195**, pp. 424–427. ISSN: 1095-9203. DOI: [10.1126/science.1250147](https://doi.org/10.1126/science.1250147) (cit. on p. 157).
- [Sørensen et al. 2001] A. Sørensen and K. Mølmer (2001). „Entanglement and Extreme Spin Squeezing.“ *Physical Review Letters* **86.20**, pp. 4431–4434. DOI: [10.1103/PhysRevLett.86.4431](https://doi.org/10.1103/PhysRevLett.86.4431) (cit. on p. 31).
- [The Walkmen 2012] The Walkmen (2012). *We Can't Be Beat* (cit. on p. vii).
- [Thompson et al. 2006] J. K. Thompson, J. Simon, H. Loh, and V. Vuletić (2006). „A High-Brightness Source of Narrowband, Identical-Photon Pairs.“ *Science* **313.5783**, pp. 74–77. ISSN: 1095-9203. DOI: [10.1126/science.1127676](https://doi.org/10.1126/science.1127676) (cit. on p. 155).
- [Titulaer et al. 1965] U. M. Titulaer and R. J. Glauber (1965). „Correlation Functions for Coherent Fields.“ *Physical Review* **140** (3B), B676–B682. DOI: [10.1103/PhysRev.140.B676](https://doi.org/10.1103/PhysRev.140.B676) (cit. on p. 96).
- [Vetsch et al. 2010] E. Vetsch, D. Reitz, G. Sagué, R. Schmidt, S. T. Dawkins, and A. Rauschenbeutel (2010). „Optical Interface Created by Laser-Cooled Atoms Trapped in the Evanescent Field Surrounding an Optical Nanofiber.“ *Physical Review Letters* **104.20**, pp. 1–4. DOI: [10.1103/PhysRevLett.104.203603](https://doi.org/10.1103/PhysRevLett.104.203603) (cit. on p. 132).
- [Vogel 2000] W. Vogel (2000). „Nonclassical States: An Observable Criterion.“ *Physical Review Letters* **84.9**, pp. 1849–1852. DOI: [10.1103/PhysRevLett.84.1849](https://doi.org/10.1103/PhysRevLett.84.1849) (cit. on pp. 96–98, 100, 124).

- [Volz et al. 2011] J. Volz, R. Gehr, G. Dubois, J. Estève, and J. Reichel (2011). „Measurement of the internal state of a single atom without energy exchange.“ *Nature* **475.7355**, pp. 210–213. ISSN: 1476-4687. DOI: [10.1038/nature10225](https://doi.org/10.1038/nature10225) (cit. on p. 156).
- [Wal et al. 2003] C. H. van der Wal, M. D. Eisaman, A. Andre, R. L. Walsworth, D. F. Phillips, A. S. Zibrov, and M. D. Lukin (2003). „Atomic Memory for Correlated Photon States.“ *Science* **301.5630**, pp. 196–200. ISSN: 1095-9203. DOI: [10.1126/science.1085946](https://doi.org/10.1126/science.1085946) (cit. on p. 155).
- [Walls et al. 2008] D. F. Walls and G. J. Milburn (2008). *Quantum optics*. 2nd ed. Springer, Berlin : ISBN: 9783540285731 9783540285748 (cit. on p. 54).
- [Windpassinger 2008] P. J. Windpassinger (2008). *Non-destructive quantum state measurements and spin squeezing*. PhD thesis. URL: http://www.nbi.ku.dk/english/research/phd_theses/phd_theses_2008/patrick_windpassinger/ (cit. on pp. 4, 65, 67, 68, 75, 83, 85, 153).
- [Windpassinger et al. 2009] P. J. Windpassinger, M. Kubasik, M. Koschorreck, A. Boisen, N. Kjærgaard, E. S. Polzik, and J. H. Müller (2009). „Ultra low-noise differential ac-coupled photodetector for sensitive pulse detection applications.“ *Measurement Science & Technology* **20.5**, p. 055301. DOI: [10.1088/0957-0233/20/5/055301](https://doi.org/10.1088/0957-0233/20/5/055301) (cit. on pp. 75, 76).
- [Wineland et al. 1994] D. Wineland, J. Bollinger, and W. Itano (1994). „Squeezed atomic states and projection noise in spectroscopy.“ *Physical Review A* **50.1**, pp. 67–88. DOI: [10.1103/PhysRevA.50.67](https://doi.org/10.1103/PhysRevA.50.67) (cit. on pp. 31, 96).
- [Wu et al. 1986] L.-A. Wu, H. Kimble, J. Hall, and H. Wu (1986). „Generation of Squeezed States by Parametric Down Conversion.“ *Physical Review Letters* **57.20**, pp. 2520–2523. DOI: [10.1103/physrevlett.57.2520](https://doi.org/10.1103/physrevlett.57.2520) (cit. on p. 1).
- [Wuttke et al. 2013] C. Wuttke and A. Rauschenbeutel (2013). „Thermalization via Heat Radiation of an Individual Object Thinner than the Thermal Wavelength.“ *Physical Review Letters* **111.2**, p. 024301. ISSN: 1079-7114. DOI: [10.1103/physrevlett.111.024301](https://doi.org/10.1103/physrevlett.111.024301) (cit. on p. 6).

Bibliography

[Yurke et al. 1986] B. Yurke, S. McCall, and J. Klauder (1986). „SU(2) and SU(1,1) interferometers.“ *Physical Review A* **33.6**, pp. 4033–4054. DOI: [10.1103/physreva.33.4033](https://doi.org/10.1103/physreva.33.4033) (cit. on p. 9).

[Zhang et al. 2012] H. Zhang, R. McConnell, S. Čuk, Q. Lin, M. H. Schleier-Smith, I. D. Leroux, and V. Vuletić (2012). „Collective State Measurement of Mesoscopic Ensembles with Single-Atom Resolution.“ *Physical Review Letters* **109.13**, p. 133603. DOI: [10.1103/PhysRevLett.109.133603](https://doi.org/10.1103/PhysRevLett.109.133603) (cit. on pp. [142–144](#), [156](#)).

[Zhao et al. 2008] R. Zhao, Y. O. Dudin, S. D. Jenkins, C. J. Campbell, D. N. Matsukevich, T. A. B. Kennedy, and A. Kuzmich (2008). „Long-lived quantum memory.“ *Nature Physics* **5.2**, pp. 100–104. DOI: [10.1038/nphys1152](https://doi.org/10.1038/nphys1152) (cit. on p. [155](#)).

ACRONYMS

1D	one-dimensional
AFS	atomic Fock state
AOM	acousto optical modulator
AQQP	atomic quadrature quasi-probability
BEC	Bose–Einstein condensate
CAMOT	Carlos MOT controller
Cs	cesium
CSS	coherent spin state
DC	direct current
DIO	DIO64 pulsing unit
DLCZ	Duan, Lukin, Cirac and Zoller
ECDL	external cavity diode laser
FORT	far-off-resonant dipole trap
FWHM	full width half maximum
JA	Jürgen Appel
JB	Jean-Baptiste Béguin
JHM	Jörg H. Müller
LO	local oscillator
MIT	Massachusetts Institute of Technology
MOT	magneto-optical trap
MSE	mean squared error

Bibliography

MZI	Mach-Zehnder interferometer
NBI	Niels Bohr Institute
NI	National Instruments
NIST	National Institute of Standards and Technology
PBS	polarizing beam-splitter
PDH	Pound–Drever–Hall
QND	quantum-nondemolition
QPD	quasi-probability distribution
QUANTOP	Danish Center for Quantum Optics
RF	radio frequency
Rb	rubidium
SPCM	single-photon-counting module
SSS	spin-squeezed state
SNR	signal-to-noise ratio
SQL	standard quantum limit
UCPH	University of Copenhagen

COLOPHON

This document was typeset in L^AT_EX using the typographical look-and-feel of the `classicthesis` package. The graphics are generated using `pgfplots`, `pgf/tikz`, `Mathematica` and `Inkscape`. The bibliography is typeset using `biblatex`.

A printed and bound version can be purchased via www.lulu.com following this [link](#)

